

Master thesis in Acoustic

# Reciprocity calibration of ultrasonic piezoelectric disks in air

Kenneth Kirkeng Andersen

November 2015



Department of Physics and Technology

University of Bergen

*The human race, to which so many of my readers belong, has been playing at child's games from the beginning... The players listen very carefully and respectfully to all that the clever people have to say about what is to happen in the next generation. The players then wait until all the clever men are dead and bury them nicely. They then go and do something else. That is all. For a race of simple tastes, however, it is great fun.*

G. K. Chesterton



## Acknowledgements

The current master thesis is part of an ongoing project under the supervision of professor Per Lunde and co-supervisor professor emeritus Magne Vestrheim. PhD Jan Kocbach, Christian Michelsen Research (CMR), is also involved in the project as a co-supervisor.

I would like to express my gratitude to all three supervisors for bringing a surprising amount of patience to the table. There has been many, and sometimes long, meetings where, probably, the current author has had the most benefit. Gratitude is expressed to Per Lunde for allowing the current author to partake in two national conferences, the 37th and 38th Scandinavian Symposium on Physical Acoustics (SSPA), where a conference proceeding were written for the last conference, available in Appendix D, and the 2015 International Congress on Ultrasonics (ICU) in Metz, France.

The current thesis is based on work by Eivind Nag Moseland [1] and Rune Hauge [2]. A thank you to both for showing the ins and outs of the measurement system at the acoustic laboratory at the University of Bergen (UiB) in their spare time. A special thank you to Eivind for providing raw data of prior measurements.

Part of the work has been performed in collaboration with André Adelsten Søvik [3], where he submitted his master thesis in June 2015. Credit goes to André for recognizing how the Fourier transform could be used to extract the phase response of our measurement system.

Besides this, a thank you to Espen Storheim, Magne Aanes and Mathias Sæthre for discussions over e-mail, in the laboratories or a beer. To Halvor Hobæk, professor emeritus, for in-hall guidance regarding acoustic centers. A special gratitude is express to Patricia Ordóñez Cebrián for providing a useful article and insight as to the effect of material constants in FE-simulations. A thank you to staff engineers Per Heradstveit for help with soldering of cables to the piezoelectric disks used in the current thesis. And, definitely not lastly, gratitude is expressed to both machine shop employees, Roald Langøen and Leif Egil Sandnes for assistance with the changes made to the measuring cage.

A great hug is thrown across the North Sea pond to the exiled bear residing in Scotland. We will meet again. To the other part-time residents of office 277, Adrià Salvador Palau, Håkon Eidsvåg and Simen Askeland, gratitude is extended in buckets for making life at the University seem like a day in the park.

A last thank you goes out to my friends and family for support and encouragement during my stay in Bergen at the university of Bergen.

Kenneth K. Andersen  
Bergen, Nov. 2015



# Table of Contents

<b>1</b>	<b>Introduction</b>	<b>1</b>
1.1	Background and motivation . . . . .	1
1.2	Literature review . . . . .	2
1.2.1	Brief review of the calibration by the reciprocity method . . . . .	2
1.2.2	Reciprocity calibration to obtain the phase response of a transducer . . . . .	3
1.3	Objectives . . . . .	4
1.4	Previous work at UiB . . . . .	5
1.4.1	Distinction of own work from previous work at UiB . . . . .	6
1.5	Thesis outline . . . . .	7
<b>2</b>	<b>Theory</b>	<b>8</b>
2.1	System model . . . . .	8
2.1.1	Fourier analysis . . . . .	9
2.1.2	Transfer functions obtained from the system model . . . . .	10
2.1.3	Transfer function $H_{15open}^{VV}$ . . . . .	11
2.1.4	Magnitude and phase representation of $H_{15open}^{VV}$ . . . . .	11
2.1.5	Decomposition of $\theta_{15open}$ in its constituent components . . . . .	12
2.2	Slowly varying phase obtained from measurements . . . . .	12
2.2.1	Time shifting of a Fourier transformed signal . . . . .	12
2.2.2	Complete expression for $\theta_{15open}^{slow}$ . . . . .	13
2.3	Sound speed model . . . . .	14
2.4	Transmitting and receiving properties of electroacoustical transducers . . . . .	14
2.4.1	Transmitting voltage response, $S_V$ . . . . .	14
2.4.2	Receiving voltage sensitivity, $M_V$ . . . . .	15
2.4.3	Reciprocity parameter, $J$ . . . . .	15
2.4.4	Average pressure over a free-field area, $\langle p_4(d) \rangle$ . . . . .	15
2.5	Calibration by the three-transducer reciprocity method . . . . .	15
2.5.1	Measurement conditions . . . . .	16
2.5.2	Reciprocity calibration . . . . .	16
2.5.3	Receiving sensitivity obtained by reciprocity calibration, $M_V^{T_2}$ . . . . .	16
2.5.4	Phase considerations for $M_V^{T_2}$ . . . . .	18
2.5.5	Transmitting response obtained by reciprocity calibration, $S_V^{T_1}$ . . . . .	18
2.5.6	Phase considerations for $S_V^{T_1}$ . . . . .	19
2.5.7	Possible perturbations of the calibration by the reciprocity method . . . . .	19
2.6	Reciprocity check . . . . .	19
2.7	Simulation of transmitter and receiver transfer function . . . . .	20
2.7.1	Far-field model . . . . .	20
2.7.2	Near-field model . . . . .	21
2.8	Diffraction correction factor, $C_{dif}$ . . . . .	22
2.8.1	Baffled piston diffraction correction, BPDC . . . . .	22
2.8.2	Simplified Finite Element Diffraction Correction, SFDC . . . . .	22
2.8.3	Diffraction correction factor applicable to measurement . . . . .	23
2.9	Correction accounting for attenuation in air, $C_\alpha$ . . . . .	24
2.10	Cables and Electronics . . . . .	25

2.10.1	Cables . . . . .	25
2.10.2	Transmitting electronics . . . . .	26
2.10.3	Receiving electronics . . . . .	27
2.11	Impedance measurements with oscilloscope . . . . .	30
2.12	Finite Element Method . . . . .	31
<b>3</b>	<b>Experimental set up and measurement methods</b>	<b>32</b>
3.1	Acoustical measurement set up . . . . .	32
3.1.1	Description of the acoustical measurement set up . . . . .	32
3.1.2	Data acquisition . . . . .	34
3.2	Description of measurement equipment . . . . .	34
3.2.1	Function generator . . . . .	35
3.2.2	Oscilloscope . . . . .	35
3.2.3	Brüel & Kjær 2636 Measuring Amplifier and Krohn-Hite Signal Filter . . .	37
3.2.4	Environmental parameters . . . . .	37
3.2.5	Coaxial cables . . . . .	39
3.2.6	Piezoelectric Disks . . . . .	39
3.2.7	Keyence sensors and controller . . . . .	41
3.3	Alignment of piezoelectric transmitter and receiver pair . . . . .	42
3.4	Measurement distance, $d$ . . . . .	43
3.4.1	Repeatability of $z$ -axis translation . . . . .	43
3.5	Signal processing and the FFT sub-routine . . . . .	44
3.5.1	FFT-window effect . . . . .	47
3.6	Phase considerations . . . . .	48
3.6.1	Effect of sound speed on post-processing of slowly varying phase . . . . .	49
3.6.2	Wrapped phase spectra and implications for measurement of slowly varying phase . . . . .	49
3.6.3	Unwrapping in noisy environments . . . . .	50
3.7	Noise analyses . . . . .	52
3.7.1	Random and incoherent periodic noise . . . . .	52
3.7.2	Coherent electrical noise . . . . .	52
3.7.3	Measurement scheme to reduce coherent noise . . . . .	53
3.7.4	Signal to noise ratio, SNR . . . . .	54
3.8	Determining minimum burst length required for steady-state conditions . . . . .	55
3.9	Electrical measurements . . . . .	56
3.9.1	Impedance measurement . . . . .	56
3.9.2	Impedance measurements with oscilloscope . . . . .	57
3.9.3	Measurements on amplifier and filter . . . . .	58
3.10	Investigation of the coaxial cable parameters and input impedance of the B&K amplifier . . . . .	60
<b>4</b>	<b>Finite Element simulations</b>	<b>65</b>
4.1	FEMP . . . . .	65
4.2	Simulation problem . . . . .	65
4.3	Simulation parameters . . . . .	65
4.4	Material parameters . . . . .	66
4.5	Extension to FEMP . . . . .	67
<b>5</b>	<b>Calibration of laser distance measuring unit</b>	<b>68</b>
5.1	Measurement set up . . . . .	68
5.1.1	Calibration frame . . . . .	69
5.2	Measurement method . . . . .	69
5.2.1	Measurement scheme . . . . .	70
5.3	theory . . . . .	71
5.3.1	Thermal expansion of the calibration frame . . . . .	71
5.3.2	Equation for $d_x$ . . . . .	72
5.3.3	$d_x$ obtained by statistical means . . . . .	72

5.4	Measurement results . . . . .	72
5.5	Indication of validity of approach . . . . .	73
5.6	Measurement uncertainties . . . . .	74
5.6.1	Combined standard uncertainty, $u_c(d_x)$ . . . . .	74
5.6.2	Standard uncertainty of each located minima, $u(d_{x,i})$ . . . . .	74
5.6.3	Numerical result for the combined standard uncertainty, $u_c(d_x)$ . . . . .	76
5.7	Translation pole . . . . .	76
<b>6</b>	<b>Results</b> . . . . .	<b>79</b>
6.1	Impedance . . . . .	79
6.1.1	Impedance measurement with oscilloscope . . . . .	80
6.2	Parameters influencing the FE-simulations . . . . .	84
6.2.1	Effect of material data on FE-simulations . . . . .	84
6.2.2	Effect of disk dimension on FE-simulations . . . . .	85
6.2.3	Effect of the sound speed in air on FE-simulations . . . . .	86
6.2.4	Summary of the results on FE-simulations . . . . .	87
6.3	Signal-to-noise ratio . . . . .	87
6.3.1	Effect of Faraday shield on signal-to-noise ratio . . . . .	88
6.3.2	Noise as a function of distance . . . . .	88
6.4	Corrections performed on the recorded voltages . . . . .	90
6.4.1	Correction $H_{0m1}^{VV}$ and $H_{6open6}^{VV}$ . . . . .	91
6.4.2	Correction $H_{5open5'}^{VV}$ . . . . .	91
6.4.3	Correction $H_{5'6open}^{VV}$ . . . . .	92
6.4.4	Correction accounting for propagation losses in air, $C_\alpha$ . . . . .	92
6.4.5	Correction accounting for possible diffraction effects, $C_{dif}$ . . . . .	93
6.5	Acoustic measurements on the transfer function $H_{15open}^{VV}$ . . . . .	95
6.5.1	Non linearity in acoustical measurements . . . . .	96
6.5.2	Measurements performed at $d = 0.50$ m . . . . .	97
6.5.3	Reciprocity check . . . . .	102
6.5.4	Three transducer reciprocity calibration obtained at $d = 0.50$ m . . . . .	104
6.5.5	Measurements performed at $d = 0.85$ m . . . . .	107
6.5.6	Three transducer reciprocity calibration obtained at $d = 0.85$ m . . . . .	108
<b>7</b>	<b>Measurement uncertainties</b> . . . . .	<b>111</b>
7.1	Combined standard uncertainty of the measurement distance, $u_c(d)$ . . . . .	112
7.1.1	Numerical result, $u_c(d)$ . . . . .	112
7.2	Combined standard uncertainty of the impedance of a piezoelectric disk . . . . .	113
7.3	Standard uncertainty associated with the correction term accounting for attenuation in air, $u(C_\alpha)$ . . . . .	114
7.4	Standard uncertainty associated with FFT-subroutine . . . . .	114
7.5	Combined standard uncertainty, $u_c( H_{15open}^{VV} )$ . . . . .	115
7.5.1	Standard uncertainty, $u( V_6 )$ . . . . .	115
7.5.2	Standard uncertainty, $u( V_{0m} )$ . . . . .	116
7.5.3	Standard uncertainty, $u( H_{5'6open}^{VV} )$ . . . . .	117
7.5.4	Standard uncertainty, $u( H_{5open5'}^{VV} )$ . . . . .	119
7.5.5	Standard uncertainty, $u( C_{dif}^{SFDC} )$ . . . . .	123
7.5.6	Results for the standard uncertainty, $u_c( H_{15open}^{VV} )$ . . . . .	123
7.5.7	Comments on correlation and results . . . . .	124
7.6	Combined standard uncertainty $u_c( M_V )$ . . . . .	125
7.6.1	Comments on correlation and results . . . . .	126
7.7	Combined standard uncertainty $u_c( S_V )$ . . . . .	128
7.8	Repeatability of the measurement set-up . . . . .	128

<b>8</b>	<b>discussion</b>	<b>131</b>
8.1	Measurements on non-linearity in piezoelectric disks . . . . .	131
8.2	Piezoelectric disk properties and material constants used in FE-simulations . . . . .	131
8.3	FE-simulation of phase . . . . .	132
8.4	Measured phase always higher in value than simulation . . . . .	132
8.5	Uncertainties . . . . .	132
8.6	Uncertainty in measurement distance influence on the slowly varying phase . . . . .	133
8.7	Alignment of piezoelectric disks . . . . .	133
8.8	Atmospheric conditions influencing the measurements . . . . .	133
8.9	Reciprocity check . . . . .	134
<b>9</b>	<b>Conclusion and further work</b>	<b>135</b>
9.1	Conclusion . . . . .	135
9.2	Further work . . . . .	136
<b>A</b>	<b>GUM</b>	<b>145</b>
A.1	Evaluating standard uncertainty . . . . .	145
A.2	General statements . . . . .	145
A.2.1	The measurand . . . . .	145
A.2.2	Type A evaluation of standard uncertainty . . . . .	145
A.2.3	Type B evaluation of standard uncertainty . . . . .	146
A.2.4	Determining combined standard uncertainty . . . . .	146
<b>B</b>	<b>Source code</b>	<b>148</b>
B.1	MATLAB scripts, post-processing . . . . .	148
B.1.1	findPeakToPeak_FFT_k.m . . . . .	148
B.1.2	findPeakToPeak_FFT_phase_k.m . . . . .	149
B.1.3	compute_sensitivity_coefficients.m . . . . .	150
B.1.4	Khimunin_diffractioncorrection.m . . . . .	151
B.1.5	SpeedOfSound.m . . . . .	152
B.2	MATLAB scripts, data acquisition . . . . .	153
B.2.1	main_acoustic.m . . . . .	153
B.2.2	instruments.m . . . . .	156
B.2.3	init_instruments.m . . . . .	158
B.2.4	measurement_parameters.m . . . . .	159
B.2.5	adjustAmplitude.m . . . . .	163
B.2.6	adjustTime.m . . . . .	164
B.2.7	relative_translation.m . . . . .	165
B.3	FEMP structures and extension . . . . .	167
B.3.1	piezofluid . . . . .	167
B.3.2	Extension to pressureatreceiver . . . . .	168
<b>C</b>	<b>Data sheets</b>	<b>172</b>
<b>D</b>	<b>SSPA</b>	<b>175</b>

# Chapter 1

## Introduction

### 1.1 Background and motivation

The use of ultrasound in the industry motivates the study of calibration of precision measurement equipment operating in air in the frequency range 100-300 kHz. The techniques used to calibrate air coupled transducers can also be used on transducer pairs operating in e.g. water [4]. Industrial usages of ultrasound in this frequency range can be e.g. fiscal measurement of natural gas, therein multipath ultrasonic transit-time flow meters (USM) [5], measurements of the velocity of sound in the gas (VOS) [5], as well as quality measurements on natural gas [6]. Other applications can be e.g. air-coupled non-destructive testing (NDT) [7], airborne imaging [8] and distance ranging in air [9].

In the frequency range below 100 kHz calibrated condenser microphones can be used to characterize air-coupled transducers [10], but in the frequency range above 100 kHz other techniques to calibrate microphones must be used. Such techniques can be e.g. tone-burst testing [11], time-delay spectrometry (TDS) [12], vector calibration [13], dynamic pressure calibration [14], light/optical diffraction tomography [15, 16], polyvinylidene fluoride (PVDF) membrane hydrophone calibration [17, 18], as well as the reciprocity method for pressure [10, 19], diffuse-field [20, 21], and free-field [4, 22, 23]. For a more thorough review of the field of calibration see [24] by Nedzelnitsky and [25] by Frederiksen.

The number of different methods available to characterize, or calibrate, air-borne ultrasonic transducers testifies to the difficulty in obtaining accurate data in the high ultrasonic frequency range [15]. Further more, when precision measurements in e.g. gas is of demand [5] then the calibration of the measurement equipment becomes even more important, and the necessity to obtain the complex transmitting response or complex receiving sensitivity of the transducers increases.

Although magnitude calibrations are of primary interest to most microphone users [26], the phase response of a microphone or transducer is of interest in several applications. In USM accuracy of the measurement is dependent on the accuracy of the transit time measurement [5]. Thus, improper knowledge about the phase response of the transmitter and receiver might lead to deviations in the transit time that are attributed the media and not the phase response of the transducers. Accurate knowledge about the transmitter and receiver is thus imperative such that the corresponding time-delay the transmitter and receiver imposes on the signal can be corrected for.

Not only in transit time measurements are the phase response of importance. When broadband signals such as an impulse [15] is recorded, if the phase response of the hydrophone is not flat, phase delays may be introduced into the various frequency components of the signal, such that distortions in the time-domain signal might be the result [15] when this is attempted to be reconstructed. Impulses are e.g. used in geophysical surveying where air guns or possible explosions are used to form acoustic pulses. The phase response is also of importance for the beam forming in arrays [15, 26], sound source locating and filtering [26], and in general, the frequency response of a transducer is not known without knowledge about the phase response, as well as the magnitude response.

The phase response of a transducer is an important property of the transducer as it quantifies the time delay the transducer inflict on the transmitted or received signal. However, obtaining

the phase response of a transducer by calibration techniques such as the free-field reciprocity method, is often associated with more challenges than for the magnitude response. E.g. the American National Standard (ANSI) [4] provides only the equation for the receiving sensitivity of a transducer as a complex quantity. The remaining quantities of interest, the transmitting current and voltage responses, as well as the secondary calibration techniques, are all given exclusively as magnitude expressions.

The reoccurring challenge when attempting to obtain the phase response of a transducer by e.g. the reciprocity method is the lack of accurate knowledge about the distance between the transmitter and receiver [4, 27], the co-axial positioning of the transducers relative to one-another, as well as estimating the speed of sound in the media where the acoustic waves are propagating [28]. Deviations in the separation distance between the transmitter and receiver consequently leads to a frequency dependent deviation in the calibrated quantities as the acoustic wavelength decreases with increasing frequency. Thus the measured deviation in the distance will correspond to an increasing fraction of the acoustic wavelength. For example, at 100 kHz given a sound speed in air of 343 m/s, a deviation of only  $\pm 1$  mm in the measured distance between the transmitter and receiver, gives a phase deviation of  $\pm 105^\circ$ , and for 300 kHz the phase deviation is  $\pm 315^\circ$ .

Furthermore, for a speed of sound of 343 m/s, a  $\pm 0.1\%$  deviation in the estimation of the speed of sound and a separation distance of 0.50 m yields a phase deviation of  $\pm 53^\circ$ , given 100 kHz, and a phase deviation of  $\pm 158^\circ$  given 300 kHz. For a separation distance of 0.85 m, the phase deviation given 100 kHz is  $\pm 89^\circ$ , and  $\pm 267^\circ$  given 300 kHz.

## 1.2 Literature review

In the current section a brief literature overview of the calibration by the reciprocity method will be given. First a brief review of the reciprocity method will be given, where the latest contributors considering magnitude calibration are included. The section concludes with a short selection of techniques to overcome the challenges with the distance and the sound speed when the phase response is of interest.

### 1.2.1 Brief review of the calibration by the reciprocity method

According to Bobber [29], MacLean (1940) [30] and Cook (1941) [31] independently introduced the concept of how three transducers, one of which obey the reciprocity principle, can be used to make absolute calibration of microphones and speakers. However, the first mentioning of this technique is by Ballentine [32] in 1929. Among other topics Ballentine examined the reciprocity relations in a reversible electrophone and applied this to a method that determines the frequency characteristic of an electrophone or microphone. He coined this method, the "method of three electrophones," and mentioned that it can be used to calibrate carbon microphones. Not necessarily contradicting Bobber, Wathen-Dunn [33] gives credit to MacLean for showing and introducing the concept of calibration by the reciprocity technique, and refers to the technique as the "Ballentine-MacLean method."

Regardless of the origin, calibration by the reciprocity method was soon recognised as an accurate and reliable technique and Olsen (1941) [34] adopted the method of reciprocity and with the principle of similarity used this to calibrate velocity microphones in air up to 15 kHz. Moreover, the rise of Nazi Germany resulted in a rapid development of testing and evaluation of sonar transducers, such that at the end of World War II it was possible to calibrate small hydrophones from 2 Hz to 2.2 MHz under ambient environmental conditions [29], and Ebaugh and Mueser [35] (1947) gave an elaborate discussion of the the practical application of the calibration of underwater sound transducers.

During the war years, the calibration by the reciprocity technique was not only investigated with intent of being used on under water equipment. Other military applications, such as earphones and air microphones were in readily demand and the calibration of this equipment was sought after. Some of this work was carried out at the Bell Telephone Laboratories, the National Bureau of Standards and the Electro-Acoustic Laboratory at Harvard University. DiMattia and Wiener (1946) [36] presented the current "state of the art" of absolute pressure calibration of Western Electric Type 640-AA condenser microphones over the frequency range 50-5.000 Hz and 50-10.000



Hz. In the abstract, they claimed that the calibration had been "perfected and standardized to a gratifying degree of accuracy," and presented the estimated accuracy in the final calibration as  $\pm 0.1$  dB and  $\pm 0.2$  dB, respectively.

More relevant for the current thesis, Rudnick and Stein (1948) [37] described a procedure for a free-field calibration by the reciprocity theorem of W. E. 640AA transducers in the frequency range 1-100 kHz. They showed that by using a separation distance of 30 cm the transducers acted essentially as points, such that no corrections for diffraction were needed. Furthermore, due to the relatively high frequency range, they had to incorporate corrections for the absorption in air. To calculate the absorption coefficient in air, they utilized two transducer of the same make and aligned them facing each other. The output level was then measured as a function of the separation distance while the input voltage was held constant. They then evaluated the deviation from the inverse square law, and found the attenuation coefficient of air for 50, 70 and 90 kHz. The free-field calibration of the transducers were compared to that of pressure calibration obtained at the Bell Telephone Laboratories, and the different techniques were found to be generally consistent with the diffraction phenomena.

In [38] Matsuzawa (1978) calibrated transducers by what he refers to as the "reciprocity method". As a reference for the technique, he gives the *Encyclopedia of Physics, ed. S. Flügge (Springer-Verlag, Berlin, 1962) Vol. XI/2, Acoustics II, p. 70*. As of today it has not been possible to obtain this book, thus it has not been verified what method Matsuzawa actually used to calibrate his transducers. However, it seems fair to assume that he used the three-transducer calibration method, as described in e.g. [4, 22, 23] since he states that "the calibration of the microphones was performed according to the reciprocity method in a free sound field." Matsuzawa used corrections for the attenuation in air, though he states not whether he applied corrections for diffraction or not. However, the interesting point here is that Matsuzawa calibrated his transducers up to 500 kHz.

In [39] the three-transducer reciprocity calibration technique was used over the frequency range 100-500 kHz for transducers operating in air. Broadband electrostatic transducers were employed [39, 40] to obtain the receiving voltage sensitivity,  $M_V$ , and the transmitting voltage response,  $S_V$ . Challenges related to the use of the three-transducer calibration technique in air at such high frequencies were dealt with in form of corrections for diffraction and attenuation in air. Corrections for the signal filter were made, and it is stated [39] that parasitic current losses were less than 0.2 percent from the ideal open circuit conditions.

In [41], the aim was to use the reciprocity calibration method in a free-field to obtain the sensitivity of 1/4-inch condenser microphones in the frequency range 20–160 kHz. An anechoic room was utilized to prevent reflections interfering with the measurements, and one of the key challenges reported was electrical crosstalk. To correct for possible near-field effects, the acoustic center was taken into account.

Recent works at the acoustic group at the Technical University of Denmark, DTU, where the reciprocity method has been used to calibrate microphones, though not piezoelectric disks, include [21, 42, 43]. To the authors knowledge, in [21, 42, 43], no use of corrections due to diffraction are applied. Corrections due to possible near-field effects are corrected for by use of the acoustic center.

At the university of Bergen, the reciprocity method was used in [1] to calibrate piezoelectric disk by primary and secondary means. Possible diffraction effects and attenuation in air were corrected for. The calibrations of the disks were compared to FE-simulations and to secondary calibrations where a pre-calibrated microphone were used.

## 1.2.2 Reciprocity calibration to obtain the phase response of a transducer

In the literature, several works regarding the phase calibration of ultrasonic transducers can be found. Some of the newest, or most important works will be outlined below.

Luker and Van Buren [28] (1981) proposed a method to eliminate some of the difficulties with determining the distance between the transmitter and receiver by placing the transmitter, the reciprocal transducer and the microphone to be calibrated on a straight line, with the reciprocal transducer in the middle. The distances between the three transducers thus cancels and the

accuracy of the receiving sensitivity is limited only to by the accuracy of the phase measurements of the voltages and current [28].

Hayman and Stephen [27], National Physical Laboratory (NPL) UK used the alignment technique proposed by Luker and Van Buren [28] to phase calibrate three hydrophones with the reciprocity method up to 400 kHz. The phase calibration was compared to phase response measurements performed at Hngzhou Applied Acoustic Research Institute, China, obtained by the optical vibrometry method. The two results deviated with less than  $8^\circ$ . Hayman and Stephen reported Type A uncertainties of up to  $30^\circ$  at 400 kHz.

Van Neer et. al. [44] (2010) proposed a method utilizing a pulse-echo regime where only knowledge about the transducer diameter, the transmission frequency, and an estimate of the acoustic wave speed was needed. The results were showed for two transducers, one with a front matching layer, the other without, and were compared with simulations. The simulation and transducer without a front layer exhibited best agreement. The results was reported with a reproducibility of  $\pm 10^\circ$  given a signal-to-noise ratio greater than 40 dB.

Olivera et. al [45] (2013) elaborated on the method developed in [44] and compared their results with calibrations performed by the National Physical Laboratory (NPL) UK. The comparison of the two calibrations agreed well, and the results were reported with an uncertainty of  $6.7^\circ$  given a level of confidence of 95%. However, the calibration was only performed for one frequency, 3 MHz.

### 1.3 Objectives

In the current work the free-field reciprocity method [4,22,23] is used to obtain both the magnitude and phase response of piezoelectric disks in the frequency range 50–300 kHz. The quantities of interest are the transmitting voltage response,  $S_V$ , and the receiving voltage sensitivity,  $M_V$ , for both magnitude and phase.

However, to obtain the phase response for either  $S_V$  or  $M_V$ , the phase response of the transfer function relating the input voltage of the transmitter to the open circuit output voltage of the receiver have to be obtained. This transfer function is denoted  $H_{15open}^{VV}$  and is defined in Sec. 2.1.3. With respect to the reciprocity calibration, it is imperative that  $H_{15open}^{VV}$  is corrected for attenuation due to propagation losses in the media, possible diffraction effects, and that it is the open circuit output voltage at the receiver that is being used. In the current work this is obtained by applying corrections to the recorded voltages.

To be able to obtain the phase response of the piezoelectric disks, the separation distance between the transmitter and receiver have to be known to a high degree of accuracy. To aid in determining this distance, a laser measurement system was constructed. Two laser distance sensors, a manual XYZ-translation stage and an elevation mechanism had to be purchased. In addition, a linear z-axis translation stage had to be implemented into the measurement cage to allow for precise translation of the transmitter. To accommodate the new hardware, the measurement cage had to undergo a fair bit of changes, and new techniques to align the piezoelectric disks had to be investigated.

The phase angle of interest in the current thesis is the slowly varying phase. In Sec. 2.2 the slowly varying phase of the transfer function  $H_{15open}^{VV}$ , denoted  $\theta_{15open}^{slow}$ , is defined. The slowly varying phase is the accumulative phase of the transmitter and receiver pair, where the phase contribution from the plane wave component has been removed. The benefit of this representation of the phase is that the small variations in the phase is easier to appreciate. For example,  $\theta_{15open}^{slow}$ , given the frequency range investigated in the current thesis, is in the range  $-135^\circ$  to  $+360^\circ$ , whereas the phase contribution from only the plane wave component at 100 kHz, given a separation distance of 0.50 m, is approximately  $330 \cdot 10^3^\circ$ .

In the current work piezoelectric disks, rather than transducers, are used. Piezoelectric disks are generally easier to simulate than both commercial transducers or in-house built transducers due to insufficient knowledge about the various materials that make up the transducers, i.e. front and back layer, transducer house and possible epoxy or glue. Although better knowledge about the various materials can exist if the transducers are assembled in-house, the materials might still need to be characterized if e.g. the manufacturer do not provide accurate enough data. It should be pointed out that it is of interest to apply the methods developed in [1–3] and the current thesis to transducers, for both magnitude and phase.

Due to the use of piezoelectric disks with exposed electrodes a recurring challenge with the measurement system was electrical coherent noise. In [3] and the current thesis, methods to attenuate the electric coherent noise have been investigated and implemented, and consist of a Faraday shield placed around both the transmitter and receiver.

The piezoelectric disks exhibits non-linear properties around the series resonance frequencies. A method to measure the impedance of the disk using an oscilloscope and a signal generator has been investigated. The benefit of this is that the excitation voltage over the disk can be kept constant and excitation voltages exceeding 1.1 V RMS can be used. 1.1 V RMS is the highest excitation voltage of the impedance analyzers available at UiB. In the current thesis, 4 V peak-to-peak excitation voltage has been used to investigate the non-linear properties of a single piezoelectric disk using an oscilloscope and signal generator and resistors.

The use of FE-simulation in the current work is regarded as important as it provides a way to compare the measurement with theory. The FE-simulation tool used in the current thesis is FEMP [46,47] developed at UiB in cooperation with CMR. It will be pointed out in Sec. 3.6.2 that without the aid of FE-simulations an offset of  $360^\circ$  would exist in the measurements.

Frequencies up to 300 kHz are important in industrial applications where measurements in gas are of interest, e.g. USM. In the current thesis, the frequency range 50–300 kHz is investigated. The disks used in the current thesis have an approximate diameter of 20 mm and an approximate thickness of 2 mm, with a diameter to thickness ratio of 10. The first two radial modes are thus included within the selected frequency range. The radial modes can be important in industrial applications as USM where e.g. the thickness extension mode, TE-mode, can be difficult to use due the size of the transducers.

Two separation distances are investigated in the current work, 0.50 m and 0.85 m. The first separation distance is associated with a greater signal-to-noise ratio than the latter, due to the attenuation of sound per unit length [48], while the correction for diffraction effects are expected to be higher for the former than the latter. Two separation distances are of interest to verify that the measurement method for the phase developed in [3] and the current thesis can be utilized at various distances.

## 1.4 Previous work at UiB

The ultrasonic transmit-receive measurement system was initiated by Storheim [49] and Amundsen [50]. The measurement setup was further developed by Mosland and Hauge [1,2], and the measurement setup was further developed by [3] and the current author.

In [1] the focus was at utilizing the reciprocity method to calibrate piezoelectric disks in the frequency range 50-300 kHz. The calibrated quantities were the magnitude of the transmitting voltage response,  $S_V$ , and the receiving voltage sensitivity,  $M_V$ . The calibration was compared to FE-simulations and primary- and secondary calibration techniques utilizing a pre-calibrated microphone. The primary calibration of the pre-calibrated microphone yielded deviations within 1 dB in the frequency range 103–130 kHz. The secondary calibration of the piezoelectric disk using the pre-calibrated microphone yielded an agreement within 2 dB for the frequency range 80–130 kHz.

In [2] the focus was on developing a model for an ultrasonic transmit-receive measurement system. The model included transmission lines modeling the cables connecting the measurement hardware together, as well as the hardware it self. Measurements and corresponding simulations of the measurement system was compared, however only for magnitude.

In [3] the work initiated by [2] was further developed. In [3] the focus was on the phase response of the transmit-receive system, i.e. the transfer function. A method as to how this could be obtained using the available hardware at the laboratory and the Fourier transform was suggested, and implemented. However, due to insufficient means to measure the separation distance between the transmitter and receiver pair, the measured phase deviated from the simulated phase. These deviations were corrected for such that the measurement and simulation fitted better. The qualitative comparison showed fair agreement between the measured and simulated phase response.

### 1.4.1 Distinction of own work from previous work at UiB

In the current section the contributions by [1–3] is attempted to be distinguished from the contributions by the current author.

#### Phase

In [1, 2] only the magnitude was under investigation. Thus, the contribution on the measurement of the phase comes from [3] and the current author.

In [3] a method as to how the Fourier transform could be applied to the current measurement setup to extract the slowly varying phase of the transmitter and receiver pair was proposed. The current author has elaborated on the method and further developed the theoretical description of the measurement system. A theoretical description showing how the slowly varying phase is obtained by direct measurements is now proposed, c.f. Sec. 2.2.

The investigation and corresponding purchase of the two laser sensors from Keyence [51] was mainly performed by the current author. That includes the work on the calibration frame, the translation pole and associated changes made to the measurement cage.

Although Søvik [3] was involved in part of the process (e.g. discussion about calibration frame and what laser sensors to purchase) most of the work was performed by the current author.

In [3] the onset of the signal, or the plane wave component, was estimated by cross-correlation. This is no longer used as the estimator of the plane wave component. Rather, the plane wave component is estimated by the sound speed model proposed by Cramer [52] and the distance measurement on the distance between the transmitter and receiver.

In [3] a "correction" due to insufficient knowledge about the distance between the transmitter and receiver was performed. The correction was performed such that the measured phase corresponded better with the simulated phase. This correction is no longer used.

During the work, it was discovered that the simulation tool FEMP do not use the sound speed as given in the input by the user [49]. The difference is small, however for the simulation distances used in the current thesis, 1000 m, this has a great impact on the simulated phase values. This discrepancy is now corrected for in the post-processing routine. <sup>1</sup>

#### Signal-to-noise ratio

In [1, 2] the recorded noise used in the signal-to-noise ratio was recorded just before the onset of the acoustical signal. However, due to electrical coherent noise stemming from the electrical field generated by the transmitter this is deemed insufficient. In [3] and the current thesis a technique to attenuate the electrical coherent noise was investigated, and the recording of the noise is now performed at exactly the same position as where the FFT-window is applied to the acoustic signal, c.f. Sec. 6.3.

#### System model

The system model developed in [2] was modified in [3] where a new set of transfer function used to correct the recorded voltages to obtain  $H_{15open}^{VV}$ , were derived. However, deviations at especially 112 kHz, was observed when using the new corrections. <sup>2</sup> These deviations were not present in [1, 2].

A working hypothesis was that these deviations could stem from the electrical corrections, c.f. 2.10, and all electrical correction have thus been implemented anew by the current author.

These corrections are also used when investigating the measurement uncertainties.

#### Post-processing and the FFT-subroutine

In [1, 2] a FFT-subroutine was developed. However, the subroutine utilized constant upper and lower window bounds of the rectangular window, such that the signal was cut at random places

---

<sup>1</sup>This has been brought to the attention of Kocback [46, 47] such that in the next version of FEMP the simulated sound speed will resemble the sound speed given in the input by the user to a higher degree.

<sup>2</sup>Note that a different set of coaxial cables connecting the receiver to the amplifier was used, as well as a new transfer function for the amplifier and filter, c.f. Sec. 2.10.3.

relative to the signal period. However, this might lead to spectral leakage. In Sec. 3.5.1 a new FFT-subroutine is presented which utilizes a dynamic window position that attempts to cut the signal in the zero-crosses of the signal. This is implemented by the current author.

### **Calibration by the reciprocity method**

All phase calibration obtained by the reciprocity method are new to the current thesis. It is also recognized in the current thesis what measurement the reciprocity parameter,  $J$ , obtains its environmental parameters from, c.f. Sec. 2.5, 6.5.4 and 6.5.6.

### **Measurement uncertainties**

All investigation of the measurement uncertainties are new to the current thesis, c.f. Sec. 7.

### **Non-linear properties of the piezoelectric disks**

All investigation on the non-linear properties of the piezoelectric disks using an oscilloscope are new to the current thesis, c.f. Sec. 2.11 and Sec. 6.1.1.

## **1.5 Thesis outline**

A short outline of the thesis will follow. In **chapter 2** the theoretical basis of the thesis is presented. The focus is on showing how the slowly varying phase of a transmitter and receiver pair is obtained, and presenting the reciprocity calibration method. **Chapter 3** presents the measurement setup and further examines the implications for phase measurements. **Chapter 4** presents the simulation setup. **chapter 5** shows how the distance between the two laser distance sensors are calibrated, and examines the associated uncertainties. **Chapter 6** is devoted to the results. In **chapter 7** the measurement uncertainties for the measured open circuit loss-free transfer function is given, as well as measurements on the repeatability of the measurement set-up. In **chapter 8** and **chapter 9** the discussion followed by the conclusion and further works are presented, respectively. In the **Appendix** a brief summary of the theory used in the Guide to the Expression of Uncertainty in Measurement are presented. A selection of the source code is included in the appendix, and the paper submitted for the 38th Scandinavian Symposium on Physical Acoustics is included in the appendix.

# Chapter 2

## Theory

In the present chapter the theory used to describe the measurement system at hand will be given.<sup>1</sup> The theoretical background will begin with a description of the measurement system, denoted system model. Although the system model is not the main focus of the present thesis, it is intrinsic to the theoretical development of the various correction terms imposed on the measured quantities. The system model is described in [2, 3, 53–56].

From the system model the loss-free, open-circuit transfer function,  $H_{15open}^{VV}$ , describing the sound propagation from the transmitter to the receiver is derived. It will then be shown how the slowly varying phase of  $H_{15open}^{VV}$  is obtained.

The electroacoustical transmitter and receiver properties, such as the transmitting response and receiving sensitivity of a transmitter or receiver, respectively, and the reciprocity parameter will be defined. Thereafter, the calibration by the reciprocity technique will be presented and the receiving sensitivity of a transducer obtained by the reciprocity method will be derived. The equation for the transmitting response obtained by the reciprocity method will be presented.

A far-field model, obtained by FE-simulations, for  $H_{15open}^{VV}$  will be derived, and the equation for a near-field model will be presented. The far-field model is used throughout the thesis for comparison between measurements and simulations, while the near-field model is used in a formulation of the diffraction correction applicable to measurements.

The corrections used to correct the recorded voltages such that the loss-free open circuit transfer function  $H_{15open}^{VV}$  will then be presented. The technique used to measure the impedance of a piezoelectric disk using an oscilloscope, signal generator and a resistor will be presented, and the chapter ends with a short description of the simulation tool used throughout the thesis, FEMP.

Throughout, linear theory is used and the harmonic time dependency  $e^{i\omega t}$  is assumed and suppressed, where  $\omega = 2\pi f$ ,  $f$  is frequency and  $t$  is time. All quantities are attempted to be defined with the accompanying variable dependencies. However, when the quantities are thus defined the dependencies will be suppressed from future expressions if their inclusion is deemed superfluous. Furthermore, to simplify notation cylindrical coordinates are introduced,  $(r, z)$ , replacing the Cartesian coordinate system,  $(x, y, z)$ , where the radius  $r = \sqrt{x^2 + y^2}$ . Note that due to the axisymmetry of the system the azimuthal ( $\theta$ ) is suppressed from the cylindrical coordinates,  $(r, \theta, z)$ .

### 2.1 System model

The system model used in the current work is developed by Hauge [2] and further developed by Søyvik [3]. The notation used regarding the system model follows [3].

The purpose of the system model is to divide the signal propagation through the measurement set up in modules, c.f.3.1, such that each module can be handled individually, either by mathematical models or by measurements. The benefit of this is that the mathematical handling and analyses, as well as possible measurements of each module are more readily available than similar mathematical representations and corresponding analyses of the compounded measurement set up.

---

<sup>1</sup> Note that the use of the word transducer is intended when the discussion is on a general level, meaning both a transmitter or receiver, and the distinction transmitter or receiver, piezoelectric disk or microphone is attempted to be used when specific cases are discussed.

The system model is composed of several modules representing the various hardware used during an acoustical measurement, as well as the propagating medium. In Fig. 2.1 a block diagram of the system model is given. The modules are, from left to right: function generator, cable 1, transmitting piezoelectric disk, medium (air), receiving piezoelectric disk, cable 3, signal amplifier and filter, cable 4 and oscilloscope. In addition, cable 2 connects the function generator to the oscilloscope. Although more hardware is used during measurements these do not partake in the system model and the discussion of these are deferred to Chapter 3.

All quantities in Fig. 2.1 are given as the Fourier transform of the time-domain equivalents, cf. Sec. 2.1.1 and all frequency or spatial dependency is suppressed from the quantities in Fig. 2.1, e.g.  $V_n = V_n(f)$ , where  $n$  is any integer between 0 and 6. In Tab. 2.1 a description of the quantities involved in the system model is given.

In Fig. 2.2 a schematics of a transmitter and receiver pair is given. The radius,  $r = a$ , and area,  $A$ , of the transmitting disk is indicated. The transmitter is placed in the  $xy$ -plane with the front face at  $z = 0$  and its circular center in  $r = 0$ . The receiver is similarly placed in the  $xy$ -plane, with its circular center in  $r = 0$ . The principal, or acoustical axis, is assumed to be identical with the  $z$ -axis, and  $d$  denotes the separation distance between the facing surfaces of the transmitting and receiving disk.

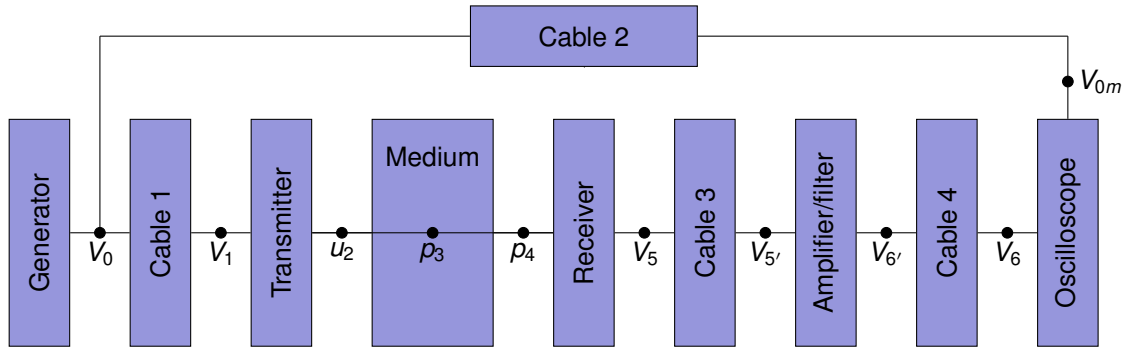


Figure 2.1: Functional block diagram of the system model where each block represents a module in the measurement set up. Schematics inspired by [3]

### 2.1.1 Fourier analysis

In the current work all measurements are performed in the time domain, whereas, in the system model, all quantities are given as the the frequency domain equivalents. A transformation from the time to the frequency domain is therefore needed. Throughout the theory section the quantities should be regarded as continuous. It is therefore implicit that they are transformed to the frequency domain by the continuous-time forward Fourier transform, Eq. 2.1 [58]<sup>2</sup>. For all measurements, however, where the measurand are sampled, the discrete Fourier transform (DFT) is used, Eq. 2.2.

$$\begin{aligned} H(f) &= \int_{-\infty}^{\infty} h(t)e^{-i2\pi ft} dt \\ &= \int_{-\infty}^{\infty} h(t)[\cos(2\pi ft) - i \sin(2\pi ft)] dt \end{aligned} \quad (2.1)$$

$$H\left(\frac{n}{NT}\right) = \sum_{k=0}^{N-1} h(kT)e^{-i2\pi nk/N}, \quad n = 0, 1, \dots, N-1 \quad (2.2)$$

where  $T$  is the sampling interval or period,  $N$  is the total number of samples within  $T$ ,  $n$  is the current sampling number under investigation, and  $k$  is the index of summation (not to be confused

<sup>2</sup>Note 1)  $i$  is used instead of  $j$  to denote the imaginary unit, 2)  $H$  is an arbitrary variable name and should not be confused with the transfer functions.

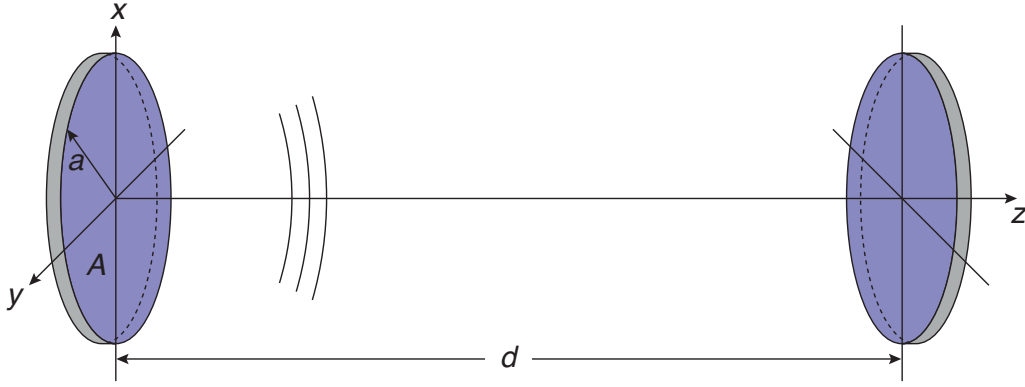


Figure 2.2: Schematics of a transmitter and receiver pair. The transmitting disk is given on the left, with radius  $r = a$  and the area of the front surface of the disk,  $A$ , is denoted. The receiving disk is given on the right. The separation distance,  $d$ , is indicated as the distance between the two facing surfaces of the transmitter and receiver.

Table 2.1: Electromechanical quantities involved in the system model.

Quantity	Description
$V_0 = V_0(f)$	output voltage at the terminals of the function generator
$V_{0m} = V_{0m}(f)$	recorded voltage given the electric signal transmission through cable 2
$V_1 = V_1(f)$	input voltage at the terminals of the transmitting disc
$u_2(r = 0, f)$	particle displacement at the center of the face of the transmitting disc
$p_3 = p_3(d_0, f)$	on-axis free- and far-field sound pressure at a reference distance $d_0 = 1$ m Note: if $d_0$ is not in the far-field of the transmitter, $p_3$ is extrapolated to the ref. distance from a pressure measured in the far-field [57]
$p_4 = p_4(r, d, f)$	free-field sound pressure at a separation distance $z = d$
$V_5 = V_5(f)$	output voltage voltage at the terminals of the receiving disc
$V_{5'} = V_{5'}(f)$	input voltage at the terminals of the amplifier
$V_{6'} = V_{6'}(f)$	output voltage at the terminals of the amplifier
$V_6 = V_6(f)$	input voltage at the terminals of the oscilloscope
Quantities not readily visible in Fig. 2.1	
$V_{5open} = V_{5open}(f)$	open-circuit output voltage at the terminals of the receiving disc
$V_{6open} = V_{6open}(f)$	open-circuit output voltage at the terminals of the amplifier
$V_{gen} = V_{gen}(f)$	peak-to-peak open-circuit generator voltage

with the wave number). From the last equality of Eq. 2.1 it is better appreciated that the phase angle of a Fourier transform equivalent is confined to the range  $\pm\pi$ . This is referred to as the *wrapped phase spectra*, contrary to the *phase spectra* where the phase angles are allowed any value between  $\pm\infty$ , c.f. Sec. 3.5..

### 2.1.2 Transfer functions obtained from the system model

From the schematics of the system model, Fig. 2.1 a series of complex voltage to voltage transfer functions can be defined. The corresponding transfer functions relate each module's output to the input of the same module. The voltage to voltage transfer function describing the ratio of the two recorded voltages,  $V_6$  and  $V_{0m}$ , is given in [3] as



$$H_{0m6}^{VV} \equiv \frac{V_6}{V_{0m}} = \frac{V_1}{V_{0m}} \cdot \frac{V_{5open}}{V_1} \cdot \frac{V_{5'}}{V_{5open}} \cdot \frac{V_{6open}}{V_{5'}} \cdot \frac{V_6}{V_{6open}}, \quad (2.3)$$

which can be re-written using transfer functions, as

$$H_{0m6}^{VV} = H_{0m1}^{VV} \cdot H_{15open}^{VV} \cdot H_{5open5'}^{VV} \cdot H_{5'6open}^{VV} \cdot H_{6open6}^{VV}. \quad (2.4)$$

The individual transfer functions are defined below:

$$H_{0m1}^{VV} \equiv \frac{V_1}{V_{0m}} = |H_{0m1}^{VV}| e^{i\theta_{0m1}}, \quad (2.5)$$

relates the input voltage at the terminals of the transmitting disk,  $V_1$ , to the recorded voltage,  $V_{0m}$ , and is estimated by transmission line theory [59]. The last expression shows the exponential representation of the transfer function, and  $||$  denotes magnitude.

$$H_{15open}^{VV} \equiv \frac{V_{5open}}{V_1} = |H_{15open}^{VV}| e^{i\theta_{15open}}, \quad (2.6)$$

relates the open-circuit output voltage at the terminals of the receiving disk,  $V_{5open}$ , to the input voltage at the terminals of the transmitting disk,  $V_1$ . Both measurements and transmission line theory will be used in estimating  $H_{15open}^{VV}$ .

$$H_{5open5'}^{VV} \equiv \frac{V_{5'}}{V_{5open}} = |H_{5open5'}^{VV}| e^{i\theta_{5open5'}}, \quad (2.7)$$

relates the input voltage at the terminals of the amplifier,  $V_{5'}$ , to the open-circuit output voltage at the terminals of the receiving disk,  $V_{5open}$ , estimated by transmission line theory.

$$H_{5'6open}^{VV} \equiv \frac{V_{6open}}{V_{5'}} = |H_{5'6open}^{VV}| e^{i\theta_{5'6open}}, \quad (2.8)$$

relates the open circuit voltage output voltage at the terminals of the amplifier,  $V_{6open}$ , to the input voltage at the terminals of the signal amplifier,  $V_{5'}$ , estimated by measurements and transmission line theory.

$$H_{6open6}^{VV} \equiv \frac{V_6}{V_{6open}} = |H_{6open6}^{VV}| e^{i\theta_{6open6}}, \quad (2.9)$$

relates the input voltage at the terminals of the oscilloscope,  $V_6$ , to the open-circuit output voltage at the terminals of the signal amplifier,  $V_{6'}$ , estimated by transmission line theory.

### 2.1.3 Transfer function $H_{15open}^{VV}$

Solving Eq. 2.4 with respect to  $H_{15open}^{VV}$ , and introducing necessary corrections terms, yields the loss-free open-circuit transfer function

$$H_{15open}^{VV} = \frac{V_6}{V_{0m}} \cdot \frac{1}{H_{0m1}^{VV} \cdot H_{5open5'}^{VV} \cdot H_{5'6open}^{VV} \cdot H_{6open6}^{VV}} \cdot C_\alpha \cdot C_{dif} \quad (2.10)$$

where  $C_\alpha$  is the correction term accounting for losses in air, Sec. 2.9, and  $C_{dif}$  is the correction term accounting for possible diffraction effects, Sec. 2.8. Note that the transfer function,  $H_{0m6}^{VV}$  is rather expressed by  $V_6$  and  $V_{0m}$ .

### 2.1.4 Magnitude and phase representation of $H_{15open}^{VV}$

The expression for the transfer function in Eq. 2.10 can be expressed as a complex exponential:

$$\begin{aligned} H_{15open}^{VV} &= |H_{15open}^{VV}| e^{i\theta_{15open}} \\ &= |H_{15open}^{VV}| e^{i[\theta_6 + \theta_{dif} - (\theta_{0m1} + \theta_{5open5'} + \theta_{5'6open} + \theta_{6open6})]}, \end{aligned} \quad (2.11)$$

where the notation  $\angle H_{15open}^{VV} = e^{i\theta_{15open}}$  will also be used to denote the phase angle. The correction term accounting for propagation losses in air is purely real and contributes nothing to the phase. From Eq. 2.10 we see that the magnitude  $|H_{15open}^{VV}|$  can be represented as the magnitude of the individual contributions, and from Eq.2.11 we see that the phase can be expressed by omitting the exponential notation, as

$$\theta_{15open} = \theta_6 + \theta_{dif} - (\theta_{0m1} + \theta_{5open5'} + \theta_{5'6open} + \theta_{6open6}). \quad (2.12)$$

### 2.1.5 Decomposition of $\theta_{15open}$ in its constituent components

It is of interest to decompose the phase  $\theta_{15open}$  in its constituent components to be able to distinguish the slowly varying phase from the plane wave component. From Eq.2.11 the phase  $e^{i\theta_{15open}}$  can be decomposed as [57, 59]

$$e^{i\theta_{15open}} = e^{i(\theta_{15open}^{slow} - kd)}, \quad (2.13)$$

where  $k = 2\pi f/c$ , and  $c$  is the speed of sound. Recognizing that both terms in the exponents have to be identical, and solving for  $\theta_{15open}^{slow}$ , we obtain the expression for the slowly varying phase, i.e.

$$\theta_{15open}^{slow} = \theta_{15open} + kd. \quad (2.14)$$

The  $kd$  term can be re-written and interpreted as that of a phase angle:

$$kd = \frac{2\pi f}{c}d = 2\pi \frac{t_p}{T} \quad (2.15)$$

where  $T = f^{-1}$  is the period time of a signal,  $t_p = d/c$ , is the time the plane wave have used to propagate  $d$  meters given a sound speed  $c$ .

## 2.2 Slowly varying phase obtained from measurements

In the current section the theoretical description as to how the slowly varying phase,  $\theta_{15open}^{slow}$ , is obtained from measurements will be derived. The derivation is based on [3], however the derivation in the current thesis differ from that in [3]. The derivation will show that by placing the FFT-window's lower bound at the estimated time-of-arrival,  $t_d$ , of the plane wave component of the propagating wave, the remaining quantity is  $\theta_{15open}^{slow}$ .

A generic description of the method follows, thereafter the derivation will be given.

In Fig.2.3 a schematics of a signal, or wave, traveling from left to right is given. The signal has originated in a transmitter at  $t = 0$  and is recorded by a receiver a time  $t$  later. A rectangular FFT-window is placed over the recorded signal, and the FFT is computed from the signal contained within the window, c.f. 3.5. The FFT-window's lower bound is calculated from  $t_p = d/c$ .  $\theta_p$  is the phase corresponding to the plane wave component, i.e. a linear phase term.  $\theta_6$  is the accumulative phase, i.e. it contains both the phase contribution from the plane wave, and the phase response of the transmitter and receiver. The phase  $\theta_6^{slow}$  quantifies the phase response of the signal that differs from the plane wave, i.e. the phase response of the transmitter and receiver.

### 2.2.1 Time shifting of a Fourier transformed signal

In the current section, it will be shown how a linear phase is obtained from a time shifted Fourier transformed signal. This phase will be used to obtain the slowly varying phase  $\theta_{15open}^{slow}$ . The transformation is shown for the time equivalent of  $V_6(f)$ , namely  $V_6(t)$ .

If  $V_6(t)$ , is shifted in time with a constant  $t_p$ , then by substituting  $s = t - t_p$  the Fourier transform becomes [58]

$$\begin{aligned}
\int_{-\infty}^{\infty} V_6(t - t_p) e^{-i2\pi f t} dt &= \int_{-\infty}^{\infty} V_6(s) e^{-i2\pi f (s+t_p)} ds \\
&= e^{-i2\pi f t_p} \int_{-\infty}^{\infty} V_6(s) e^{-i2\pi f s} ds \\
&= e^{-i\theta_p} V_6(f) \\
&= |V_6(f)| e^{i(\theta_6^{slow} - \theta_p)} \\
&= |V_6(f)| e^{i\theta_6}
\end{aligned} \tag{2.16}$$

where  $|V_6(f)|$  represents the magnitude of the Fourier transform,  $\theta_6 = \theta_6^{slow} - \theta_p$  is the accumulated phase response,  $\theta_p$  is the linear phase term given a time delay of  $t_p$ , and  $\theta_6^{slow}$  is the phase response remainder of the accumulative phase when the phase corresponding to the plane wave is subtracted from it. The linear phase term can be re-written as

$$\theta_p = 2\pi f t_p = 2\pi \frac{t_p}{T}. \tag{2.17}$$

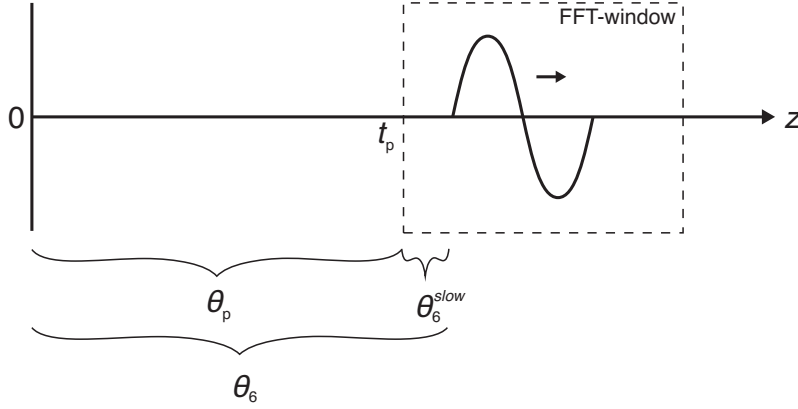


Figure 2.3: Schematics of a wave traveling from left to right, denoted signal. The signal has originated in a transmitter at  $t = 0$  and is recorded a time  $t$  later.  $t_p = d/c$  is the estimate of the arrival of the plane wave component.  $\theta_6 = \theta_6^{slow} - \theta_p$ . The minus sign is a consequence of a time delay in the Fourier domain.  $\theta_p$  is the linear phase term given a time delay,  $t_p$ .  $\theta_6^{slow}$  is the phase response of the signal that differs from the plane wave. The dashed rectangle indicates the FFT window.

### 2.2.2 Complete expression for $\theta_{15open}^{slow}$

Combining the expression for the phase angles obtained in Eq. 2.12 with that of Eqs.2.16 and 2.14 we get an expression for the slowly varying phase of the transfer function:

$$\theta_{15open}^{slow} = \theta_6^{slow} - \theta_p + kd + \theta_{dif} - (\theta_{0m1} + \theta_{5open5'} + \theta_{5'6open} + \theta_{6open6}) \tag{2.18}$$

Then, by expressing both propagation terms,  $-\theta_p$  and  $kd$ , by the equivalent expressions in Eqs. 2.17 and 2.15, respectively, we get

$$\begin{aligned}
\theta_{15open}^{slow} &= \theta_6^{slow} + \frac{2\pi}{T}(t_p - t_p) + \theta_{dif} - (\theta_{0m1} + \theta_{5open5'} + \theta_{5'6open} + \theta_{6open6}) \\
&= \theta_6^{slow} + \theta_{dif} - (\theta_{0m1} + \theta_{5open5'} + \theta_{5'6open} + \theta_{6open6}).
\end{aligned} \tag{2.19}$$

## 2.3 Sound speed model

The estimation of arrival of the plane wave component,  $kd$ , is partly dependent on the accuracy of the sound speed model. To the authors knowledge, the best estimate of the speed of sound in humid air is the sound speed model proposed by Cramer [52], where it is estimated that the uncertainty of the sound speed model is less than 300 ppm [52].<sup>3</sup>

The sound speed model proposed by Cramer takes into account the temperature in Kelvin,  $T_K$ , atmospheric pressure,  $p$ , humidity and CO<sub>2</sub> concentration, and is given in [52] as

$$c_0^2 = \gamma \frac{RT_K}{M} \left( 1 + \frac{2pB}{RT_K} \right) \quad (2.20)$$

where  $c_0$  is the zero frequency speed of sound,  $\gamma = C_p/C_v$  is the specific heat ratio where  $C_p$  and  $C_v$  are the specific heat at constant pressure and volume, respectively,  $R$  is the universal gas constant,  $M$  is the molecular mass and  $B$  is the second virial coefficient of state.

The expression in Eq. 2.20 can be expanded to account for dispersion due to the vibrational relaxation effects of oxygen and nitrogen, both of which are functions of frequency and are regarded as the greatest contributors to the absorption of sound by the atmosphere [60]. The speed of sound can then be estimated using a model, proposed by Morfey and Howell [61], which takes into account dispersion:

$$\frac{1}{c_0} - \frac{1}{c} = \frac{\alpha_{\nu N}}{2\pi f_{rN}} + \frac{\alpha_{\nu O}}{2\pi f_{rO}} \quad (2.21)$$

where  $c = c(f)$  is the estimated speed of sound at a frequency  $f$  including effects of dispersion,  $\alpha_{\nu N}$  and  $\alpha_{\nu O}$  are the plane wave attenuation coefficients due to vibrational relaxation of nitrogen and oxygen, respectively, and  $f_{rN}$  and  $f_{rO}$  are the relaxation frequencies for nitrogen and oxygen, respectively. In the current thesis, the speed of sound is estimated using a MATLAB function `SpeedOfSound.m` written by Søvik [3], also available in Appendix B.1.5.

## 2.4 Transmitting and receiving properties of electroacoustical transducers

In the following section the fundamental properties of acoustical transmitter and receiver pairs will be defined.

### 2.4.1 Transmitting voltage response, $S_V$

The complex transmitting voltage response relates the on-axis, free- and far-field pressure at a reference distance  $d_0 = 1$  m to the drive voltage over the transmitting transducers electrical terminals [59, 62]

$$S_V \equiv \frac{p_3(d_0)}{V_1} = |S_V| e^{i\theta_{S_V}} \quad (2.22)$$

where  $|S_V|$  is the magnitude and  $\theta_{S_V}$  is the phase of the transmitting voltage response. Since measurements are generally not performed at the reference distance Eq. 2.22 is rather expressed by  $p_4$ , as

$$S_V = \frac{p_4(0, d)}{V_1} \frac{d}{d_0} e^{ik(d-d_0)} \quad (2.23)$$

where  $d$  have to be great enough such that a far-field pressure is realized at  $d$ .

A corresponding transmitting current response,  $S_I$ , is defined as the quotient of the free- and far-field pressure at a reference distance  $d_0 = 1$  m to the current flowing at the terminals over the transmitting transducers electrical terminals [59, 62]

$$S_I \equiv \frac{p_3(d_0)}{I_1} = S_V Z_T \quad (2.24)$$

---

<sup>3</sup>The notation deviates from [52].

where  $I_1$  is the current flowing at the terminals of the transmitting disk. The last expression on the right hand side shows how  $S_I$  and  $S_V$  are related through the electrical input impedance,  $Z_T$ , of the transmitting transducer.

### 2.4.2 Receiving voltage sensitivity, $M_V$

The complex receiving voltage sensitivity is the quotient of the output open-circuit voltage at the electrical terminals of the receiving transducer to the on-axis free and far-field sound pressure at a distance  $d$  [59, 62]

$$M_V \equiv \frac{V_{5open}}{p_4(0, d)} = |M_V| e^{i\theta_{M_V}} \quad (2.25)$$

where  $|M_V|$  is the magnitude and  $\theta_{M_V}$  is the corresponding phase of the receiving voltage sensitivity.

### 2.4.3 Reciprocity parameter, $J$

For a passive and linear electroacoustical transducer, the lossless, complex reciprocity parameter is the quotient of the receiving transducers open-circuit voltage sensitivity to the transmitting transducers current response [62, 63]

$$J(\rho, f, c) \equiv \frac{M_V}{S_I} = \frac{M_V}{S_V Z_T} = \frac{2d_0}{i\rho f} e^{ikd_0} = |J| e^{i\theta_J} \quad (2.26)$$

where  $k = \omega/c$  is the wave number, and  $\rho$  is the density of the medium, the last expression on the right is a complex representation of  $J$ . The lossless reciprocity parameter is used to conform with the measurements criteria for the calibration by the reciprocity method, c.f. Sec.2.5.1.

For the reciprocity parameter to be valid, certain requirements have to be fulfilled [63]: 1) the transmitter generates a spherical sound field over the region occupied by the receiver, 2) the transmitter do not appreciably change the radiation impedance of the receiver, 3) the transmitter and receiver pair must be placed at such a distance such that the above conditions are satisfied. This implies that [63]

$$d \gg \frac{a^2}{\lambda} \quad \text{and} \quad d \gg a \quad (2.27)$$

where  $\lambda$  is the wavelength, and 4) the above requirements refer to a free-field scenario in a homogeneous isotropic medium.

### 2.4.4 Average pressure over a free-field area, $\langle p_4(d) \rangle$

The free-field pressure,  $p_4(r, d)$ , might be composed of spherically diverging waves, or for large  $d$ 's or small receivers, by plane waves, and it is intuitive that the pressure in a spherically diverging sound field will vary over a finite object. The average free-field pressure is defined as the sound pressure over an area of identical size as the receiver, referred to as the receiving area, divided by its area, i.e.

$$\langle p_4(d) \rangle = \frac{1}{A} \int_A p_4(r, d) dA \quad (2.28)$$

where the angle brackets,  $\langle \rangle$ , denote the average of the sound pressure,  $p_4$ .

## 2.5 Calibration by the three-transducer reciprocity method

In the present section the three transducer reciprocity method will be presented, referred to as reciprocity method. The derivation of the receiving sensitivity of a transducer,  $M_V$ , is based on [1], however the two derivations differ slightly. E.g. the reciprocity parameter is a function of both the density of the medium and the sound speed in the medium. However, although three measurements are performed, the reciprocity parameter only exist in the final equation once. Thus,

one needs to know what measurement  $J$  obtains its environmental dependencies from. In [1] this is not clarified, and the following derivation includes this aspect.

The derivation of the receiving sensitivity of a microphone, or disk, will be presented in full, however the derivation of the transmitting response of transducer, or disk, will be omitted for brevity, and the equation is merely presented. Four other possible quantities from the same measurement set up will be presented. These are derived in [1] and are included in the current thesis as future references of what measurement  $J$  obtains its environmental dependencies from.

### 2.5.1 Measurement conditions

To perform calibration by the reciprocity method, the following measurement conditions have to be fulfilled [4]

- Steady-state conditions have to be obtained, regardless if continuous wave or short-duration pulsed sinusoidal sound waves are used. In the current work, the latter is used.
- One of the transducers in the measurement set-up have to be reciprocal. A reciprocal transducer is a linear, passive, reversible electromechanical or electroacoustical transducer such that coupling is equal in either direction [62].
- The receiving transducer is in the far- and free-field of the transmitter, and the transmitter and receiver are aligned coaxially. The free-field pressure is defined as the pressure in a homogeneous, isotropic fluid medium without boundaries [62].
- The recorded voltage is the open-circuit output voltage of the receiver.
- There are no propagation losses in the medium.

To obtain the open-circuit output voltage of the receiver corrections obtained from the system model are applied, c.f. Sec2.10. Moreover, to correct for the propagation losses a correction  $C_\alpha$  is introduced, c.f. Sec.2.9, and to correct for possible diffraction effects a correction  $C_{dif}$  is introduced, c.f. Sec.2.8. Note that these corrections are applied directly to the recorded voltages such that propagation losses, as well as possible diffraction effects, are corrected for in the transfer function  $H_{15open}^{VV}$ .

In [4] there is also a condition that the distance between the transmitter and receiver is corrected for against possible deviations from the effective acoustic center. Deviations from the the effective acoustic center is regarded as a near-field effect. In the current thesis the near-field effects are accounted for by the diffraction correction factor, and this therefore do not apply.

### 2.5.2 Reciprocity calibration

In Fig. 2.4 the schematics of the measurement set-up is given. In the figure three piezoelectric disks are shown for three independent measurements. To distinguish the quantities obtained from the different measurements, a superscript is imposed on the variable names, e.g.  $p_4^{(1)}$  denotes the sound pressure  $p_4$  at the position of the receiver for the first measurement.

### 2.5.3 Receiving sensitivity obtained by reciprocity calibration, $M_V^{T_2}$

In Fig. 2.4, let  $T_2$  be the disk to be calibrated as a receiver, then for measurement 1, the  $T_1$  disk is employed as transmitter and the  $T_2$  disk is employed as receiver. The separation distance is  $d_1$ , the sound pressure at  $d_1$  is  $p_4^{(1)}$  and the open circuit output voltage is  $V_{5open}^{(1)}$ . For the second measurement,  $T_2$  is replaced by  $T_3$ , and for the third measurement the transmitter is the  $T_3$  disk and the receiver is again the disk to be calibrated,  $T_2$ .

Considering the first measurement, and applying appropriate notation of Fig. 2.4 to Eq.(2.23), while solving for  $p_4$ , yields

$$p_4^{(1)} = S_V^{T_1(1)} V_1^{(1)} \frac{d_0}{d_1} e^{ik(d_0-d_1)}, \quad (2.29)$$

where the superscript  $T_1$  superimposed on  $S_V$  denotes which transducer  $S_V$  is valid for. Note that this notation will be superimposed on  $M_V$ , too.

Applying the same procedure to Eq.(2.25), and solving for  $V_{5open}$ , yields

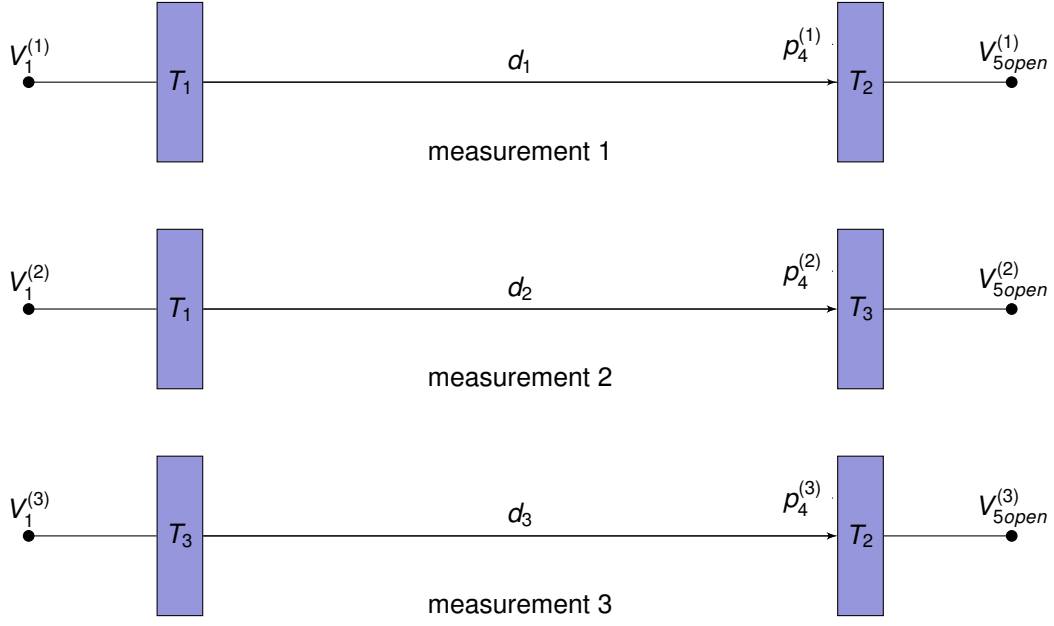


Figure 2.4: Schematics of the calibration by reciprocity method.

$$V_{5open}^{(1)} = M_V^{T_2(1)} p_4^{(1)}. \quad (2.30)$$

Inserting the expression for  $p_4^{(1)}$  from Eq.(2.29) in Eq.(2.30), results in the voltage to voltage transfer function for the first measurement

$$H_{15open}^{VV(1)} \equiv \frac{V_{5open}^{(1)}}{V_1^{(1)}} = M_V^{T_2(1)} S_V^{T_1(1)} \frac{d_0}{d_1} e^{ik(d_0-d_1)}. \quad (2.31)$$

A similar approach with respect to measurement 2 and 3, yields the transfer functions for measurement 2 and 3, respectively

$$H_{15open}^{VV(2)} \equiv \frac{V_{5open}^{(2)}}{V_1^{(2)}} = M_V^{T_3(2)} S_V^{T_1(2)} \frac{d_0}{d_2} e^{ik(d_0-d_2)}, \quad (2.32)$$

$$H_{15open}^{VV(3)} \equiv \frac{V_{5open}^{(3)}}{V_1^{(3)}} = M_V^{T_2(3)} S_V^{T_3(3)} \frac{d_0}{d_3} e^{ik(d_0-d_3)}. \quad (2.33)$$

Dividing Eq.(2.31) on Eq.(2.32) and solving for  $M_V^{T_2}$  yields

$$M_V^{T_2(1)} = M_V^{T_3(2)} \cdot \frac{H_{15open}^{VV(1)}}{H_{15open}^{VV(2)}} \frac{d_1}{d_2} e^{ik(d_1-d_2)}, \quad (2.34)$$

where the assumption that  $S_V^{T_1(2)}/S_V^{T_1(1)} = 1$  has been made. If the environmental parameters are essentially identical between the two measurements, then this assumption is valid. Though, deviations in  $S_V$  are expected if e.g. the temperature, relative humidity or the ambient pressure varies between measurement.

The next step involves expressing the reciprocal transducer,  $M_V^{T_3}$ , by the reciprocity parameter,  $J$ , and solving for  $S_V^{T_3}$ . From Eq.(2.26), we obtain

$$S_V^{T_3} = \frac{M_V^{T_3}}{JZ^{T_3}}. \quad (2.35)$$

This expression for  $S_V^{T_3}$  will replace  $S_V^{T_3(3)}$  in Eq.(2.33) and we have now obtain from what measurement the reciprocity parameter is valid for, namely measurement 3. Applying this to Eq.(2.33), yields

$$H_{15open}^{VV(3)} = M_V^{T_2(3)} \frac{M_V^{T_3(3)}}{J^{(3)} Z^{T_3}} \frac{d_0}{d_3} e^{ik(d_0-d_3)}, \quad (2.36)$$

giving

$$M_V^{T_3(3)} = \frac{1}{M_V^{T_2(3)}} H_{15open}^{VV(3)} J^{(3)} Z^{T_3} \frac{d_3}{d_0} e^{ik(d_3-d_0)}. \quad (2.37)$$

Assuming that  $M_V^{T_3(2)} = M_V^{T_3(3)}$  the last expression can replace  $M_V^{T_3(2)}$  in Eq.(2.34). The final expression for the receiving sensitivity of the  $T_2$  transducer is therefore

$$M_V^{T_2} = \left[ J^{(3)} Z^{T_3} \frac{H_{15open}^{VV(1)} H_{15open}^{VV(3)}}{H_{15open}^{VV(2)}} \frac{d_1}{d_0} \frac{d_3}{d_2} e^{ik(d_1+d_3-d_0-d_2)} \right]^{\frac{1}{2}}. \quad (2.38)$$

#### 2.5.4 Phase considerations for $M_V^{T_2}$

To obtain the phase of  $M_V^{T_2}$ , denoted  $\theta_{M_V}^{T_2}$ , it is important to recognize that it is the accumulative phase  $\theta_{15open}$  that is represented in Eq. (2.38). However, in Sec. 2.2 it was shown that it is the slowly varying phase  $\theta_{15open}^{slow}$  that is being measured. To resolve this, the  $kd$  term needs to be added to the slowly varying phase.

However, it is imperative to use the same  $k$  for every quantity in Eq. (2.38). As of yet, the  $k$  in Eq. (2.38) has not been specified for a certain measurement. Since the reciprocity parameter has obtained its environmental dependency from the third measurement, and  $J$  is it self associated with a  $k$ , then the rest of the  $k$ 's in Eq. (2.38) takes its environmental dependency from the third measurement. The expressions for the accumulative phase for the transfer function, is then

$$\theta_{15open}^{(n)} = \theta_{15open}^{(n)slow} - k^{(3)}d, \quad (2.39)$$

where  $\theta_{15open}^{(n)slow}$  denotes the slowly varying phase for the  $n$ 'th measurement and  $n = 1, 2, 3$ . The phase  $\theta_{M_V}^{T_2}$  is then expressed as

$$\theta_{M_V}^{T_2} = \frac{1}{2} [\theta_J^{(3)} + \theta_Z^{T_3} + \theta_{15open}^{(1)} + \theta_{15open}^{(3)} - \theta_{15open}^{(2)} + k^{(3)}(d_1 + d_3 - d_0 - d_2)]. \quad (2.40)$$

where  $\theta_Z^{T_3}$  denotes the phase of the impedance of the  $T_3$  disk. Note that  $\theta_{M_V}^{T_2}$  is not associated with an accumulative phase, thus it is superfluous to distinguish a slowly varying phase from  $\theta_{M_V}^{T_2}$ .

#### 2.5.5 Transmitting response obtained by reciprocity calibration, $S_V^{T_1}$

Using the same configuration as in Fig. 2.4, let  $T_1$  be the disk to be calibrated as a transmitter [4]. For measurement 1, the  $T_1$  disk is employed as transmitter and the  $T_2$  disk is employed as receiver. For the second measurement  $T_1$  is still employed as a transmitter while the  $T_3$  disk is employed as a receiver. For the third measurement, the transmitter is the  $T_3$  disk and the receiver is the  $T_2$  disk.

The equation for transmitting response obtained by reciprocity calibration is [1]

$$S_V^{T_1} = \left[ \frac{1}{J^{(3)} Z^{T_3}} \frac{H_{15open}^{VV(1)} H_{15open}^{VV(2)}}{H_{15open}^{VV(3)}} \frac{d_1}{d_0} \frac{d_2}{d_3} e^{ik(d_1+d_2-d_0-d_3)} \right]^{\frac{1}{2}} \quad (2.41)$$

where the reciprocity parameter,  $J$ , obtains its environmental dependencies from the third measurement.



### 2.5.6 Phase considerations for $S_V^{T_1}$

To obtain the phase of  $S_V^{T_1}$ , denoted  $\theta_{S_V}^{T_1}$ , an identical procedure as in Sec. 2.5.4 is adopted, i.e. the accumulative phase of  $S_V^{T_1}$ , can be expressed as

$$\theta_{S_V}^{T_1} = \frac{1}{2} [-\theta_J^{(3)} - \theta_Z^{T_3} + \theta_{15open}^{(1)} + \theta_{15open}^{(2)} - \theta_{15open}^{(3)} + k^{(3)}(d_1 + d_2 - d_0 - d_3)]. \quad (2.42)$$

Since  $S_V^{T_1}$  is associated with an accumulative and a slowly varying phase, a distinction of this must be made [57, 59], i.e.

$$\theta_{S_V}^{T_1, slow} = \theta_{S_V}^{T_1} + k^{(3)}d. \quad (2.43)$$

### 2.5.7 Possible perturbations of the calibration by the reciprocity method

Following the same procedure as above, a family of a total of six equations relating the receiving sensitivities and the transmitting responses of all three disks can be found. In [1] this was derived, and the derivations will not be repeated here. But, for future references and completeness, the remaining four equations will be presented with the notation for the reciprocity parameter identifying which measurement the reciprocity parameter obtains its environmental parameters from. It should be noted that to obtain the expressions for  $M_V^{T_1}$  and  $S_V^{T_2}$  the  $T_1$  or  $T_2$  transducer, respectively, have to be reciprocal. The equations are:

$$\begin{aligned} M_V^{T_1} &= \left[ \frac{J^{(3)}(Z_{T_1})^2}{Z_{T_3}} \frac{H_{15open}^{VV(1)} H_{15open}^{VV(2)}}{H_{15open}^{VV(3)}} \frac{d_1}{d_0} \frac{d_2}{d_3} e^{ik(d_1+d_2-d_0-d_3)} \right]^{\frac{1}{2}}, \\ M_V^{T_3} &= \left[ J^{(3)} Z_{T_3} \frac{H_{15open}^{VV(2)} H_{15open}^{VV(3)}}{H_{15open}^{VV(1)}} \frac{d_2}{d_0} \frac{d_3}{d_1} e^{ik(d_2+d_3-d_0-d_1)} \right]^{\frac{1}{2}}, \\ S_V^{T_2} &= \left[ \frac{Z_{T_3}}{J^{(3)}(Z_{T_2})^2} \frac{H_{15open}^{VV(1)} H_{15open}^{VV(3)}}{H_{15open}^{VV(2)}} \frac{d_1}{d_2} \frac{d_3}{d_0} e^{ik(d_1+d_3-d_0-d_2)} \right]^{\frac{1}{2}}, \\ S_V^{T_3} &= \left[ \frac{1}{J^{(3)} Z_{T_3}} \frac{H_{15open}^{VV(2)} H_{15open}^{VV(3)}}{H_{15open}^{VV(1)}} \frac{d_2}{d_0} \frac{d_3}{d_1} e^{ik(d_2+d_3-d_0-d_1)} \right]^{\frac{1}{2}}. \end{aligned} \quad (2.44)$$

## 2.6 Reciprocity check

To determine if a transducer is reciprocal, a check for reciprocity is necessary to conduct. The transducers investigated need to be placed as in Fig. 2.5, where  $I_1^{(1)}$  is the input current flowing at the terminals of the transmitting transducer for measurement 1, and  $V_{5open}^{(1)}$  is the open-circuit output voltage at the terminals of the receiving transducer for measurement 1. For measurement 2 the propagation direction is reversed, such that  $T_2$  is used as a transmitter and  $T_1$  is used as a receiver, then if the system is reciprocal [59]

$$\frac{V_{5open}^{(1)}}{I_1^{(1)}} = \frac{V_{5open}^{(2)}}{I_1^{(2)}}. \quad (2.45)$$

Substituting the current term with corresponding voltage and impedance terms, leads to

$$\frac{V_{5open}^{(1)}}{V_1^{(1)}} Z_{T_1} = \frac{V_{5open}^{(2)}}{V_1^{(2)}} Z_{T_2}, \quad (2.46)$$

which can be expressed by transfer functions, as

$$H_{15open}^{VV(1)} Z_{T_1} = H_{15open}^{VV(2)} Z_{T_2}. \quad (2.47)$$

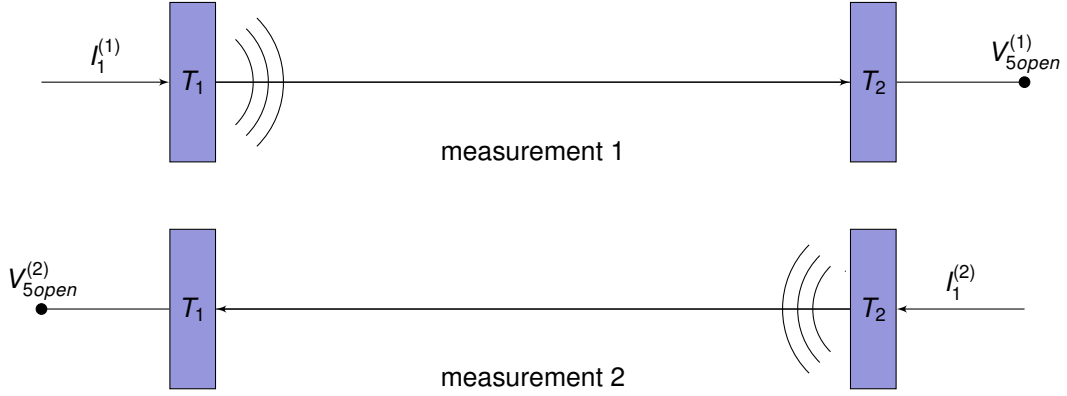


Figure 2.5: Schematics of reciprocity check.

## 2.7 Simulation of transmitter and receiver transfer function

It is of interest to develop a theoretical background applicable to Finite Element (FE) modeling, c.f. Sec. 2.12, such that simulations of the transmitter and receiver pair can be obtained. Simulations of this kind will be used to assess the measurements on the transfer function  $H_{15open}^{VV}$ , and the results obtained by the calibration equations.

In the present section two models for the transfer function,  $H_{15open}^{VV}$ , will be presented. One modeling a far-field scenario, the other a near-field scenario. The far-field model will be derived as this is used throughout the thesis to compare measurements with simulations. The near-field model, however, is not utilized extensively in the present thesis, and the step-by-step derivation will be omitted. Both derivations will be given without propagation losses in the medium.

### 2.7.1 Far-field model

A far-field model is derived to investigate the properties of sound propagation in the far-field. In Fig. 2.6 a schematics of the far-field model is presented. The far-field receiver is assumed to be a point receiver of no spatial extent, visualized in the figure as the black circle.  $z_{ff}$  denotes the distance to the far field, which in the present work is set to 1000 m. It is assumed that  $z_{ff}$  is sufficiently great such that the sound pressure amplitude decreases inversely with the distance [57].

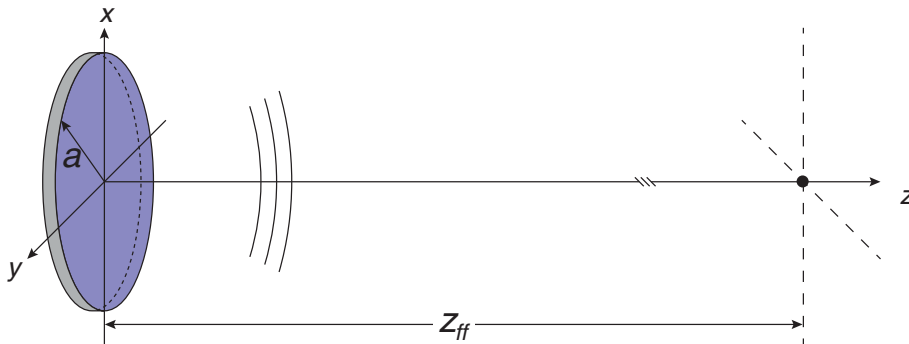


Figure 2.6: Schematics of the far-field model. The front face of the transmitting disk is placed in the  $xy$ -plane at  $z = 0$ . The receiver is assumed to be a point receiver in the far-field at a separation distance  $z = z_{ff} = 1000$  m.

Readily available in the FE-simulations is the simulated far-field quantity  $p_A(z_{ff})$ . It is of interest to express the simulated transfer function by this while extrapolate the simulated transfer function to a realistic measuring distance.

The loss-free, open circuit voltage to voltage transfer function at a separation distance  $d$  is defined as

$$\begin{aligned}
H_{15open}^{VV_{ff}}(d) &\equiv \frac{V_{5open}(d)}{V_1} \\
&= \frac{p_4(d)}{V_1} \cdot \frac{V_{5open}(d)}{p_4(d)} \\
&= p_4(d) \cdot M_V
\end{aligned} \tag{2.48}$$

where the superscript  $^{ff}$  denotes the far-field model,  $p_4(d)$  is the sound pressure at  $d$  given  $V_1 = 1$  V. It is further assumed that  $d$  is sufficiently great such that  $p_4(d)$  is in the far-field of the transmitter, allowing the last fraction to be expressed by  $M_V$ . The sound pressure  $p_4(d)$  is rather expressed by the simulated far-field pressure  $p_4(z_{ff})$ , i.e.

$$p_4(d) = p_4(z_{ff}) \frac{z_{ff}}{d} e^{ik(z_{ff}-d)}, \tag{2.49}$$

and  $M_V(d)$  can be expressed with the aid of Eq. (2.26), as

$$\begin{aligned}
M_V &= Z_T \cdot J \cdot S_V \\
&= Z_T \cdot \frac{2z_{ff}}{i\rho f} p_4(z_{ff}) e^{ikz_{ff}},
\end{aligned} \tag{2.50}$$

where the last expression is obtained by expressing  $J$  by the last equivalent in Eq. (2.26), and substituting  $S_V$  with an extrapolated far-field equivalent expressed by  $p_4(z_{ff})$ , i.e.

$$S_V = p_4(z_{ff}) \frac{z_{ff}}{d_0} e^{ik(z_{ff}-d_0)}. \tag{2.51}$$

The complete expression showing how the simulated far-field pressure,  $p_4(z_{ff})$ , is used to obtain  $H_{15open}^{VV_{ff}}$  at a separation distance  $d$ , is

$$H_{15open}^{VV_{ff}} = Z_T \cdot p_4^2(z_{ff}) \frac{2z_{ff}^2}{i\rho f d} e^{ik(2z_{ff}-d)}. \tag{2.52}$$

When there are no possibility for confusion, the superscript denoting far-field will be excluded.

The far-field model can be represented as a complex exponential, i.e.

$$H_{15open}^{VV_{ff}} = |H_{15open}^{VV_{ff}}| e^{\theta_{15open}^{ff}}. \tag{2.53}$$

From the accumulative phase  $\theta_{15open}^{ff}$  we obtain the slowly varying phase:

$$\theta_{15open}^{ffslow} = \theta_{15open}^{ff} + kd. \tag{2.54}$$

## 2.7.2 Near-field model

In [54] a near-field model of the transmitter/receiver pair is derived. Although this document is not public, the derivation of the near-field model given in [2, 3] is based on [54], where the second are publicly available. The derivation is therefore omitted in the current work, but ample explanation will be presented.

The voltage to voltage transfer function, accounting for near-field effects at a separation distance,  $d$ , is [54]

$$H_{15open}^{VV_{nf}}(d) = \frac{v_2^{eq,pist} \cdot \rho c e^{-ikd}}{V_1} \cdot J \cdot Z_T \cdot S_V \cdot H^{dif}(d) \tag{2.55}$$

where the subscript  $^{nf}$  denotes the near-field,  $v_2^{eq,pist}$  is the equivalent piston particle velocity, and  $H^{dif}(d)$  is the diffraction correction at a distance  $d$  defined in Sec. 2.8. The diffraction correction is not restricted to any formulations at this point, however, for Eq.(2.55) the SFDC formulation

will be used in the current thesis. The numerator in the fraction is recognized as that of a plane wave, given that the particle velocity is  $v_2^{eq,pist}$ .

The equivalent piston particle velocity,  $v_2^{eq,pist}$ , is defined as [54]

$$v_2^{eq,pist} \equiv \frac{2z_{ff}e^{ikz_{ff}}}{i\rho cka^2} \cdot p_4(z_{ff}) \quad (2.56)$$

Eq.(2.56) relates a far-field pressure,  $p_4(z_{ff})$ , to an equivalent piston particle velocity. In other words, the sound pressure at  $z_{ff}$  is assumed equal to the sound pressure that would have been generated by a piston source if the pistons particle velocity was  $v_2^{eq,pist}$ .

Note that the transfer function in Eq. (2.55) can not be spherically extrapolated as its far-field counterpart.

## 2.8 Diffraction correction factor, $C_{dif}$

In a sound field with spherically diverging waves, and a receiver of finite extend immersed in the sound field, the measured open-circuit output voltage of the receiver can differ in magnitude and phase compared to the same receiver being immersed in a sound field composed of ideal plane waves. This effect is referred to as diffraction, or geometrical losses [64].

The diffraction correction proposed by Khimunin [64], denoted BPDC (c.f. Sec.2.8.1), and the diffraction correction proposed by Lunde et al. [5], denoted SFED (c.f. 2.8.2), has been further investigated by Storheim [49]. In [2,3] the SFDC formulation was used to add diffraction effect to FE-simulations, and in [1] the objective was to obtain loss-free measurement conditions, thus the diffraction effect had to be corrected for. This was achieved using a correction factor denoted,  $C_{dif}$  (c.f. Sec.2.8.3), which was based on BPDC.

The objective of the current thesis is similar to that of [1], however, in [49] it is shown that a diffraction correction based on BPDC might be insufficient for the frequency range used in the current thesis. The SFDC formulation, where a piezoelectric disk is used as a transmitter, takes into account a more realistic vibration pattern of the active surface of the disk, and possible pressure waves generated by the edges of the disk. It is therefore of interest to compare the two formulations for the diffraction correction and investigate what effects the two formulations have on the measurements.

### 2.8.1 Baffled piston diffraction correction, BPDC

In Fig. 2.7 a schematics of the baffled piston diffraction correction (BPDC) is given. On the left, a plane circular and uniformly vibrating piston is mounted in a rigid baffle of infinite extent. At the separation distance,  $d$ , a free-field receiver area is coaxially aligned with the piston source.

The diffraction correction defined by Khimunin [64] is the quotient of the averaged sound pressure over the free-field area, to the plane wave pressure at the same separation distance as the free-field area, i.e.

$$H^{dif}(d) = \frac{\langle p_4(d) \rangle}{p^{plane}} = 1 - \frac{4}{\pi} \int_0^{\pi/2} e^{-ik(\sqrt{1+4(a/z)^2 \cos^2(\Theta)}-1)} \sin^2(\Theta) d\Theta, \quad (2.57)$$

where  $p^{plane}$  denotes a plane wave pressure at a distance  $d$ .

### 2.8.2 Simplified Finite Element Diffraction Correction, SFDC

In Fig. 2.8 a schematics of the simplified finite element diffraction correction (SFDC), proposed by Lunde et al. [5], is shown. The similarity to the BPDC is apparent, however the baffled piston source of the BPDC is replaced by a piezoelectric disk. The disk is placed with its front surface in the  $xy$ -plane at  $z = 0$ . At the separation distance,  $d$ , a free-field receiver area is coaxially aligned with the disk. The use of a piezoelectric disk, rather than a uniformly vibrating piston source, takes into account a more realistic vibration pattern of the surface of the disk, as well as possible pressure waves emanating from the edges of the disk.

The definition of SFDC is similar to that of BPDC [5,49]

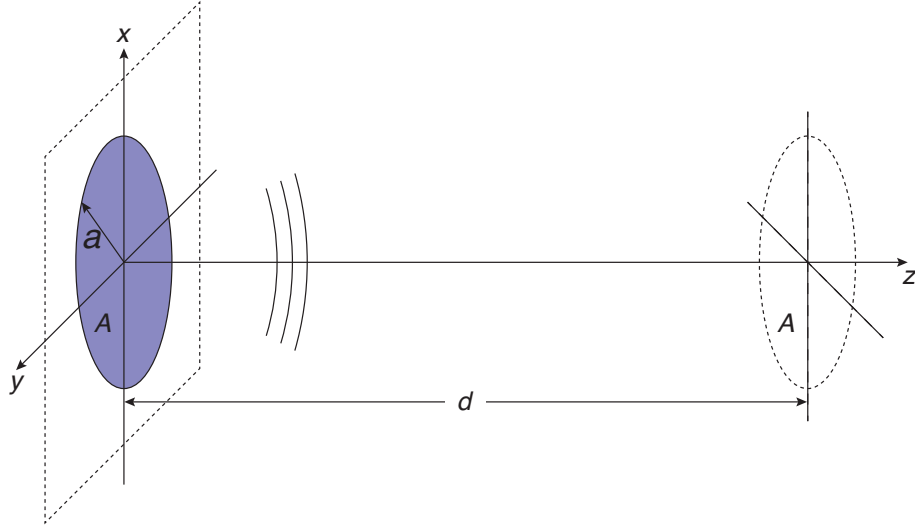


Figure 2.7: Schematics of a baffled piston source and free-field receiver area. The piston source is placed in the  $xy$ -plane at  $z = 0$ , and the integration area is of equal size as the piston and is placed coaxially aligned at  $z = d$ .

$$H^{dif}(d) \equiv \frac{\langle p_4(d) \rangle}{p_4^{eq,plane}(d)} = \frac{\langle p_4(d) \rangle}{p_{ff} 2z_{ff}} ika^2 e^{ik(d-z_{ff})}, \quad (2.58)$$

where  $p_4^{eq,plane}(d)$  is the plane wave pressure at distance  $d$  given the equivalent piston velocity,  $v_2^{eq,pist}$ , defined in Eq. 2.56, i.e.

$$p_4^{eq,plane}(d) = \rho c v_2^{eq,pist} e^{-ikd} = \frac{p_4(z_{ff}) 2z_{ff} e^{ik(z_{ff}-d)}}{ika^2}. \quad (2.59)$$

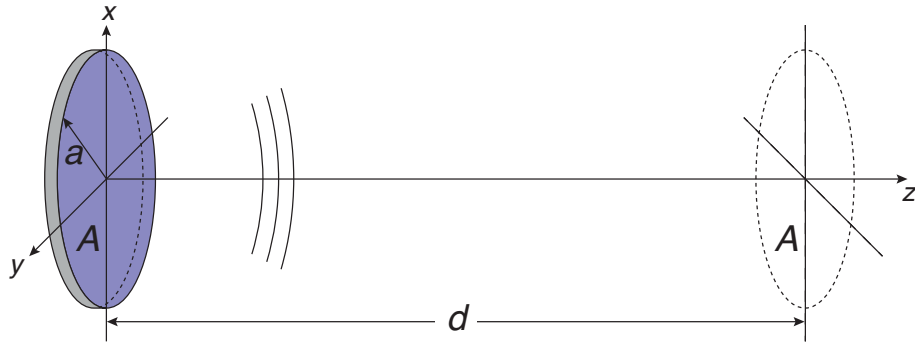


Figure 2.8: Schematics of the SFDC formulation. A transmitting disk, simulated in FE, is placed in the  $xy$ -plane at  $z = 0$ , and an free-field area of equal size as the transmitting disk is placed coaxially at  $z = d$ .

### 2.8.3 Diffraction correction factor applicable to measurement

In the following section two formulations for the diffraction correction factor,  $C_{dif}$ , used to correct measurement for possible diffraction effects will be presented. The first formulation, denoted  $C_{dif}^{BPDC}$ , is given in [1], and is based on BPDC. The second formulation, denoted  $C_{dif}^{SFDC}$ , is developed in the current thesis and is based on SFDC.

#### Diffraction correction factor, $C_{dif}^{BPDC}$

In [1] a formulation for correcting the measurement for possible diffraction effects, denoted  $C_{dif}^{BPDC}$ , was given as the quotient of the BPDC obtained at a far-field distance,  $z_{ff}$ , to the BPDC obtained

at the separation distance  $d$ , multiplied with the quotient of the far-field distance,  $z_{ff}$ , to the separation distance,  $d$ , i.e.

$$C_{dif}^{BPDF} = \frac{d_{z_{ff}} H^{dif}(z_{ff})}{d H^{dif}(d)}. \quad (2.60)$$

This formulation is used in the current work when the BPDC is under investigation. The BPDC is calculated using the MATLAB script `Khimunin_diffractioncorrection.m` implemented by Storheim [49] available in Appendix B.1.4.

### Diffraction correction factor, $C_{dif}^{SFDC}$

The following formulation for correcting the measurements for possible diffraction effects is based on an intuitive approach. Recognizing that the far-field model of Sec.2.7.1 do not model losses due to the geometry of the receiver, or losses due to the existence of spherically diverging waves over the surface of the receiver, whilst the near-field model of Sec.2.7.2 attempts to model these kind of losses, the diffraction correction factor can be stated as the the ratio of the far-field model to the near-field model, e.g.

$$C_{dif}^{SFDC} = \frac{H_{15open}^{VV_{ff}}(d)}{H_{15open}^{VV_{nf}}(d)} \quad (2.61)$$

Note that this approach is general and is not restricted to the far- or near-field models presented in the current thesis. However, at the time of writing, the available model taking into account near-field effects such as diffraction, is the near-field model of Sec.2.7.2. In Sec.2.7.2 it was stated that the diffraction correction embedded in the model would be obtained by the SFDC. Thus, the diffraction correction factor defined in the current section utilizes the SFDC formulation.<sup>4</sup>

## 2.9 Correction accounting for attenuation in air, $C_\alpha$

According to [48,59] the absorption of acoustical energy by the atmosphere can be modeled as

$$p_t = p_i e^{-0.1151\alpha_{dB/m} \cdot d} \quad (2.62)$$

where  $p_t$  is the sound pressure that decreases exponentially due to atmospheric absorption from its initial value  $p_i$  in accordance with the decay formula for a plane sound wave in free space,  $\alpha_{dB/m}$  is the absorption coefficient expressed in decibels per meter and  $d$  is the separation distance between the transmitter and receiver.  $\alpha_{dB/m}$  can be further expressed as [57]

$$\alpha_{dB/m} = \alpha_{cl} + \alpha_{rot} + \alpha_{vib,O} + \alpha_{vib,N} \quad (2.63)$$

where  $\alpha_{cl}$  is the classical absorption coefficient,  $\alpha_{rot}$  represents absorption due to rotational-relaxation,  $\alpha_{vib,O}$  represents absorption due to vibration-relaxation stemming from  $O_2$ -molecules and  $\alpha_{vib,N}$  represents absorption due to vibration-relaxation stemming from  $N_2$ -molecules. Although not explicit from Eq. 2.62, the absorption of acoustical energy in air is a strong function of temperature.

The correction term,  $C_\alpha$ , correcting the recorded voltage for attenuation due to absorption is the ratio of the initial sound pressure to the corrected sound pressure, i.e.

$$C_\alpha = \frac{p_i}{p_t} = e^{0.1151\alpha_{dB/m} \cdot d} \quad (2.64)$$

---

<sup>4</sup>The benefit of this formulation is that it yields an intuitive method as to how one can measure the diffraction effect. If the propagation losses in the media are adequately handled, a relative diffraction correction can be measured using Eq. 2.61. Although a separation distance of  $z_{ff} = 1000$  m is not practically realizable in laboratories, nor possible to perform in air for the frequencies investigated in the current thesis, an upper separation distances of  $\approx 0.85$  m is. Thus, a relative diffraction correction, relating the diffraction effects at a measurement distance of  $d < 0.85$  m to that of  $d = 0.85$  m should be realizable. Measurements performed thus can then be compared with the simulated diffraction correction,  $C_{dif}^{SFDC}$ , given in Eq. 2.61.

## 2.10 Cables and Electronics

In the present section, a theoretical description of the cables and electronics embedded in the transmit-receive system will be presented. This includes the coaxial cables connecting the various instruments together, as well as the coaxial cables connecting the piezoelectric disks to the function generator and amplifier. The instruments used in the measurement set up is given in Sec.3.2. The objective of the current section is to present the equations modeling the various transfer functions obtained from the system model, c.f. Eq.2.10.

In [1] the same system model as in [2] was used, however a different set of transfer functions were derived. In [3] the system model used in [2] was elaborated on, and a new set of transfer functions were derived.

The most fundamental change from [2] to [3] is the implementation of measurements on the magnitude and phase response of the amplifier and filter. In [1, 2] a constant gain of 60 dB was assumed, such that the gain was corrected for by dividing the received voltage with a factor of 1000. To correct for possible deviations from that of a perfect gain, measurements on the amplifier frequency response were conducted and normalized to the response at 50 kHz. However, not specified in [1, 2] was the settings for gain, input voltage, and filter used during the measurements. Thus it is not clear what settings the corrections are valid for. In [3] it is seen that the handling of the amplifier and filter as in [1, 2] might be insufficient for the frequency range used in the current thesis.

Both the current author and [3] observed fluctuations in the measured  $|H_{15open}^{VV}|$  at especially 112 kHz. These fluctuations were hardly visible in either [1, 2], and a hypothesis was that these deviations originated in the transfer functions derived by [3]. To investigate this, the current author derived and implemented the transfer functions anew, using the system model given in [3], c.f. Sec.2.1. However, the equations obtained by the current author are identical to that derived by [3], and except one deviation <sup>5</sup>, they are found to be identical to [2]. This is not shown in the current thesis, but should be easy to check, if necessary.

The equations derived by the current author will be presented with schematics of the individual transfer functions, however the step-by-step derivation will be omitted for brevity as they are found to be equivalent to [3]. Although they are equivalent, they differ in form. The equations presented in the current thesis are also used when investigating the measurement uncertainties, c.f. Sec.7.

### 2.10.1 Cables

The influence of the cables on the signal transmission through the electrical part of the measurement system has shown to be of significance [1–3]. Coaxial cables are used on the transmitting side to connect the function generator with both the transmitting disk (cable 1) and the oscilloscope (cable 2); on the receiving side, coaxial cables are used to connect the receiving disk with the amplifier (cable 3), and to connect the amplifier to the oscilloscope (cable 4). Two other cables are also in use, 1) trigger signal from function generator to oscilloscope, and 2) interconnection between amplifier and filter. Since these cables do not partake in any derivation, no further discussion regarding these will be conducted.

The coaxial cables are modeled as ideal, uniform transmission lines [59, 65, 66] using distributed elements, depicted in Fig. 2.9 as the impedances  $Z_a$  and  $Z_b$  terminating in a load impedance,  $Z_L$ , where  $Z_L$  is a general load representing either the input impedance of the transmitting disk,  $Z_T$ , the input impedance of the receiving disk,  $Z_T$ , the input impedance of the amplifier,  $Z_{amp,in}$ , and the input impedance of the oscilloscope,  $Z_{osc}$ .

Note that throughout the current thesis the electromotive force of the function generator will be given as a peak-to-peak voltage. This has been chosen to conform with the notation in [1, 2]. However, in [3] a peak voltage was used.

The transmission line impedances,  $Z_a$  and  $Z_b$ , are given as [59]

---

<sup>5</sup>The deviation is found in the transfer function  $H_{6open6}^{VV}$ . In the current thesis  $H_{6open6}^{VV}$  is given in Eq.(2.73), and in [3]  $H_{6open6}^{VV}$  is given in Eq.(2.77). These two equations are found to be identical, however when compared to the equivalent equation in [2] a deviation is found. In [2] a different notation is used, due to the difference in the system model notation, however, Eq.(2.110) in [2] is the equivalent to  $H_{6open6}^{VV}$  in the current thesis and in [3]. It is believed that there is a typo in the numerator in [2], such that  $Z_{A,out}$  should have been  $Z_S$ . Besides this, the three equations are identical.

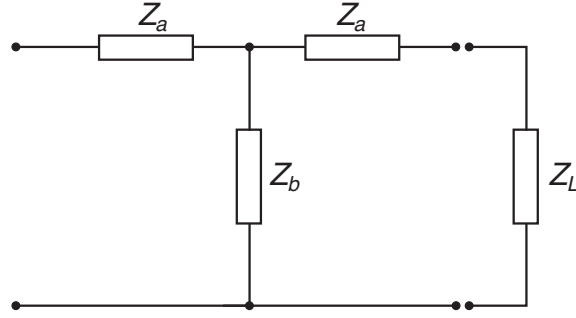


Figure 2.9: Schematics of a coaxial cables represented as an ideal transmission line using a distributed element model, also referred to as a two-port network or a four terminal model, terminated in an impedance,  $Z_L$ .

$$\begin{aligned} Z_a &= iZ_0 \tan(k_{em} \frac{l}{2}) \\ Z_b &= \frac{Z_0}{i \sin(k_{em} l)} \end{aligned} \quad (2.65)$$

where  $Z_0$  is the characteristic impedance of the the coaxial cable,  $k_{em}$  is the electromagnetic wave number, and  $l$  is the length of the coaxial cable.  $Z_0$  and  $k_{em}$  is defined as

$$\begin{aligned} Z_0 &= \sqrt{\frac{L_x}{C_x}} \\ k_{em} &= \omega \sqrt{L_x C_x} \end{aligned} \quad (2.66)$$

where  $\omega$  is the angular frequency,  $L_x$  and  $C_x$  are the the inductance and capacitance per meter, respectively. Following the notation introduced in [3], the subscript  $Z_{an}$  and  $Z_{bn}$ , where  $n = 1, 2, \dots, 4$ , will be used to denote the appropriate cables in Fig. 2.1.

### 2.10.2 Transmitting electronics

The transmitting electronics, c.f. Fig. 2.1, consists of the function generator connected to the transmitting disk through cable 1, and the function generator connected to the oscilloscope through cable 2. The transmitting electronics is modeled by the transfer function  $H_{0m1}^{VV}$ .

In Fig. 2.10 the schematics of the transmitting electronics is given. On the far left, the function generator, represented as a Thévenin equivalent circuit, is given.  $V_{gen}$  is the peak-to-peak electromotive force of the generator, and  $Z_{gen}$  is the internal output impedance of the function generator, set to  $50 \Omega$ . The upper branch represents cable 1 connected to the transmitting disk, whereas the lower branch represents cable 2 connected to the oscilloscope. The input impedance of the oscilloscope is denoted  $Z_{osc}$ .

The transfer function,  $H_{0m1}^{VV}$ , is found by dividing the expression for  $V_1$  on that of  $V_{0m}$ , i.e.

$$H_{0m1}^{VV} = \frac{V_1}{V_{0m}} \quad (2.67)$$

where  $V_1$  and  $V_{0m}$  are expressed by [3]

$$\begin{aligned} V_{0m} &= \frac{Z_{osc} Z_{b2}}{Z_{a2} Z_{b2} + (Z_{osc} + Z_{a2})(Z_{a2} + Z_{b2})} \cdot V_0 \\ V_1 &= \frac{Z_{b1} Z_T}{Z_{b1}(Z_{a1} + Z_T) + Z_{a1} Z_{b1} + Z_{a1}(Z_{a1} + Z_T)} \cdot V_0 \end{aligned} \quad (2.68)$$



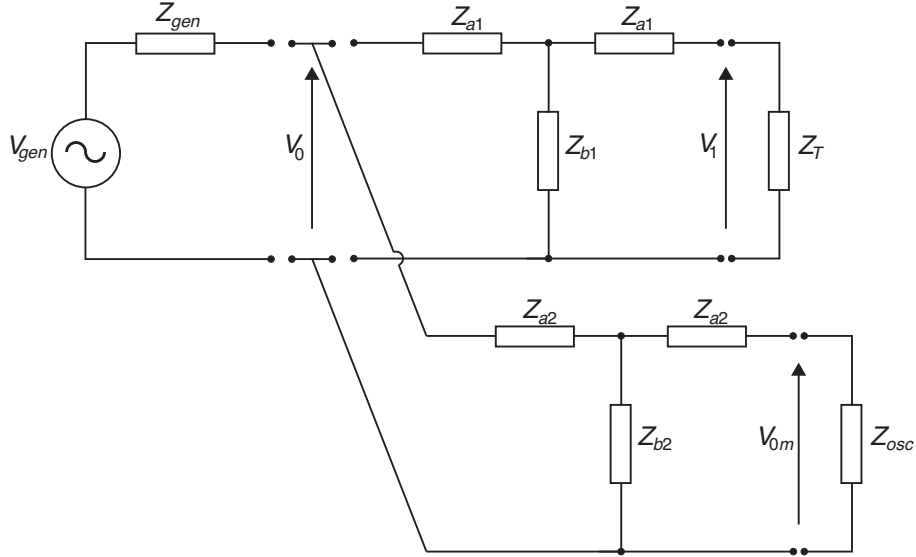


Figure 2.10: Schematics of the transmitting electronics where the function generator, represented as a Thévenin equivalent, is connected to the transmitting disk and oscilloscope through cable 1 and 2, respectively.

### 2.10.3 Receiving electronics

The receiving electronics, c.f. Fig. 2.1, is modeled by three transfer functions: 1) the receiving disk connected to the amplifier/filter through cable 3, represented by  $H_{5'open5'}^{VV}$ , 2) the amplifier/filter itself, represented by  $H_{5'6open}^{VV}$ , and 3) the amplifier/filter connected to the oscilloscope through cable 4, represented by  $H_{6open6}^{VV}$ . 1) and 3) are expressed using transmission lines, while 2) is found by measurements.

In the following, the three transfer functions will be presented. 1) and 3) follow the procedure used to determine the transmitting electronics, and 2) will be described a little more in detail below.

To emulate the measurements conditions used during the acoustical measurements, the gain of the amplifier is set to 60 dB when measuring the frequency response of the amplifier and filter. To avoid clipping in the amplifier, due to the large gain, the input voltage have to be sufficiently low. However, if the input voltage is too low, the corresponding digitization of the input signal is associated with large jumps due to the vertical resolution of the oscilloscope. To overcome this, a voltage divider is introduced when performing measurements on the amplifier and filter [3]. The output voltage of the generator is then great enough such that the the full range of the oscilloscope is utilized, and the input voltage to the amplifier is divided down such that clipping is not experienced.

#### Transfer function $H_{5'open5'}^{VV}$

The transfer function  $H_{5'open5'}^{VV}$  describes the signal transmission from the receiving disk to the input terminals of the amplifier/filter through cable 3. In Fig. 2.11 the equivalent circuit representation of the connection is given. The receiving disk is modeled as a Thévenin equivalent with an open circuit voltage,  $V_{5open}$  and an internal impedance,  $Z_R$ . The impedance is determined by electrical measurements on the specific disk used under acoustical measurements. Cable 3 is modeled as an ideal transmission line terminated in the input impedance of the signal amplifier and filter, denoted  $Z_{amp,in}$ .

The transfer function  $H_{5'open5'}^{VV}$  is given by [3]

$$H_{5'open5'}^{VV} = \frac{V_{5'}}{V_{5open}} = \frac{Z_{amp,in}Z_{b3}}{(Z_R + Z_{a3})Z_{b3} + (Z_{a3} + Z_{amp,in}) \cdot (Z_R + Z_{a3} + Z_{b3})} \quad (2.69)$$

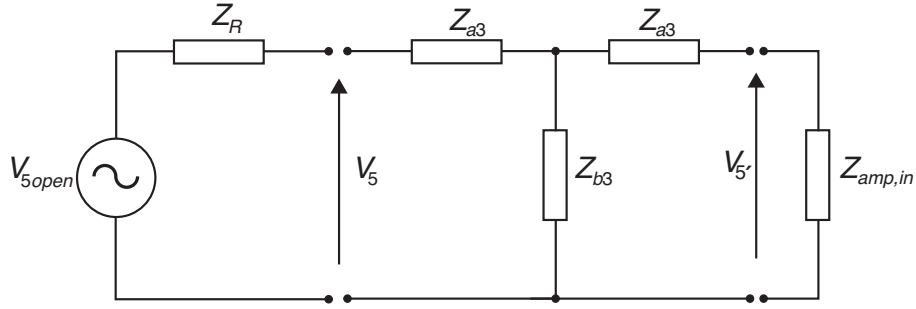


Figure 2.11: Schematics of transfer function  $H_{5'6open}^{VV}$ . The receiving disk is represented as a Thévenin equivalent, with  $Z_R$  denoting the impedance of the disk. Cable 3 is represented as an ideal transmission line terminated in the input impedance of the amplifier, denoted  $Z_{amp,in}$ .

### Transfer function $H_{5'6open}^{VV}$

To illustrate the use of the voltage divider employed to determine  $H_{5'6open}^{VV}$ , the system model is slightly modified. In Fig. 2.12 (a) the modified system model is given. The white blocks, generator and cable 5, do not partake in the derivation, and in (b) the schematics of the voltage divider is presented.  $Z_{vd1}$  and  $Z_{vd2}$  are the voltage divider impedances. Where applicable, the node and block names have been inherited from Fig. 2.1.

The input terminals of the voltage divider is branched off, connecting the voltage divider to the oscilloscope through cable 2. The output terminals of the voltage divider is connected to the input terminals of the amplifier. Connecting the voltage divider and oscilloscope thus, allows for less corrections to be made for cables in the circuit. The rest of the circuit is identical with Fig. 2.1. From the system model in Fig. 2.12 the following transfer functions are identified:

$$\begin{aligned} H_{0m6}^{VV} &\equiv \frac{V_6}{V_{0m}} = \frac{V_6}{V_{6open}} \cdot \frac{V_{6open}}{V_{5'}} \cdot \frac{V_{5'}}{V_0} \cdot \frac{V_0}{V_{0m}} \\ &= H_{6open6}^{VV} \cdot H_{5'6open}^{VV} \cdot H_{05'}^{VV} \cdot H_{0m0}^{VV} \end{aligned} \quad (2.70)$$

which can be solved for  $H_{5'6open}^{VV}$ , yielding

$$H_{5'6open}^{VV} = \frac{V_6}{V_{0m}} \cdot \frac{1}{H_{6open6}^{VV} \cdot H_{05'}^{VV} \cdot H_{0m0}^{VV}} \quad (2.71)$$

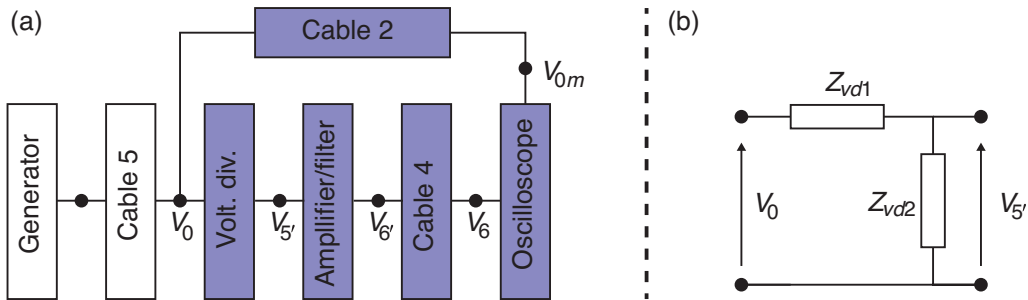


Figure 2.12: (a) Functional block diagram of the system model used to determine  $H_{5'6open}^{VV}$ . Note that the white blocks do not partake in the derivation, but is included in the schematics to give a correct representation of the measurement set-up. Cable 5 refers to any cable of appropriate length. (b) schematics of voltage divider.

In Fig. 2.13 the schematics used to determine  $H_{05'}^{VV}$  and  $H_{0m0}^{VV}$  is given. The lower branch is recognized as the same branch as in Fig. 2.10. The two transfer functions can be expressed as [3]

$$H_{05'}^{VV} = \frac{1}{\left(\frac{1}{Z_{vd2}} + \frac{1}{Z_{amp,in}}\right)Z_{vd1} + 1} \quad (2.72)$$

$$H_{0m0}^{VV} = \left[ \left( \frac{Z_{a2} + Z_{osc}}{Z_{b2}} + 1 \right) + 1 \right] \frac{Z_{a2}}{Z_{osc}} + 1$$

while  $H_{6open6}^{VV}$  is determined in the following section.

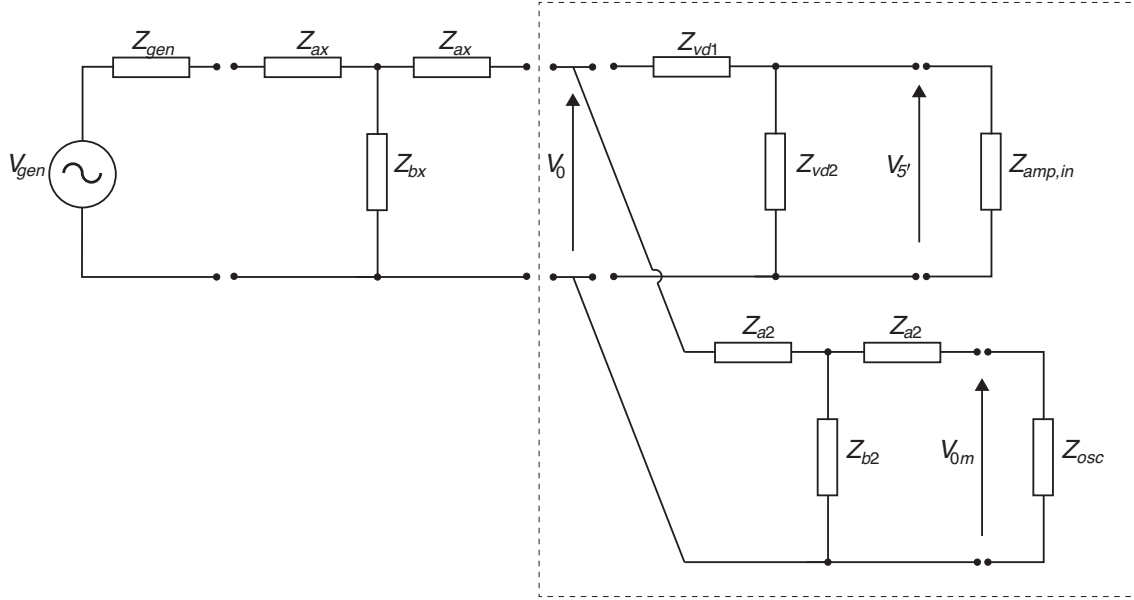


Figure 2.13: Schematics of the system model in Fig. 2.12 excluding the amplifier/filter and cable 4 blocks. The stippled square frames the part of the schematics involved in the derivation of the transfer function.

### Transfer function $H_{6open6}^{VV}$

The transfer function  $H_{6open6}^{VV}$  models the signal propagation from the output terminals of the amplifier to the oscilloscope through cable 4. In Fig. 2.14 the equivalent circuit is given. On the left, the output voltage of the amplifier is given as the Thévenin equivalent with open circuit voltage  $V_{6open}$ , and internal output impedance,  $Z_{amp,out}$ . Cable 4 is modeled using transmission lines terminated in the input impedance of the oscilloscope,  $Z_{osc}$ . The transfer function,  $H_{6open6}^{VV}$ , is given by [3]

$$H_{6open6}^{VV} = \frac{Z_{osc}}{\left(\frac{Z_{a4} + Z_{osc}}{Z_{b4}} + 1\right)(Z_{amp,out} + Z_{a4}) + Z_{a4} + Z_{osc}} \quad (2.73)$$

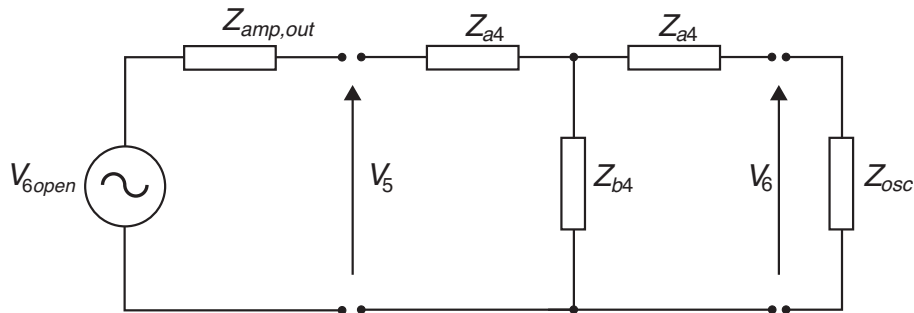


Figure 2.14

## 2.11 Impedance measurements with oscilloscope

Piezoelectric ceramic exhibits non-linear behavior when driven by sufficient large excitation voltages [67, 68]. The drive voltage applied to the piezoelectric disk in the current thesis is mainly 10 V. However, due to the internal output impedance of the function generator, the voltage at the terminals of the transmitting disk for the series resonance frequency can be as low as 4.5 V.

At UiB a commercial impedance analyzer, HP Model 4192A LF Impedance Analyzer [69], is available. However, this device outputs a maximum excitation voltage of 1.1 V root-mean-square (RMS) in a 50  $\Omega$  load.

Thus a large discrepancy is observed between the excitation voltage used during the acoustical measurements compared to the excitation voltage when the impedance of the piezoelectric disks is determined. It is therefore of interest to be able to determine the impedance with higher voltages. An attempt at measuring the impedance using a function generator, oscilloscope and various resistors have been made. In the current section the theory will be presented, and in Sec. 3.9.2 the measurement method is described.

In Fig. 2.15 a schematics of the measurement set-up is given.  $V_{gen}$  is the electromotive force of the function generator,  $Z_{gen}$  is the 50  $\Omega$  internal resistor of the function generator,  $V_{ch}^1$  and  $V_{ch}^2$  are the recorded voltages of the oscilloscope given input channel 1 and 2, respectively,  $Z_{osc}$  is the internal termination impedance of the oscilloscope,  $Z_{res}$  is the resistor connected in series between the two input channels of the oscilloscope, and  $Z_T$  is the impedance of the piezoelectric disk. In Fig. 2.16 a simplification of the schematics is given. Noteworthy is that both the impedance of the function generator and the termination impedance of channel 1 do not partake in the derivation. Given the schematics in Fig. 2.16, the following equations can be written using Kirchoff voltage law (KVL)

$$\begin{aligned} I_1 &= I_2 + I_3 \\ V_{ch}^2 &= Z_T I_3 \\ V_{ch}^2 &= I_2 Z_{osc} \\ V_{ch}^1 &= I_1 Z_{res} + I_2 Z_{osc} \end{aligned} \quad (2.74)$$

which can readily be solved by substitution, yielding

$$Z_T = \frac{V_{ch}^2 Z_{res} Z_{osc}}{Z_{osc}(V_{ch}^1 - V_{ch}^2) - V_{ch}^2 Z_{res}} \quad (2.75)$$

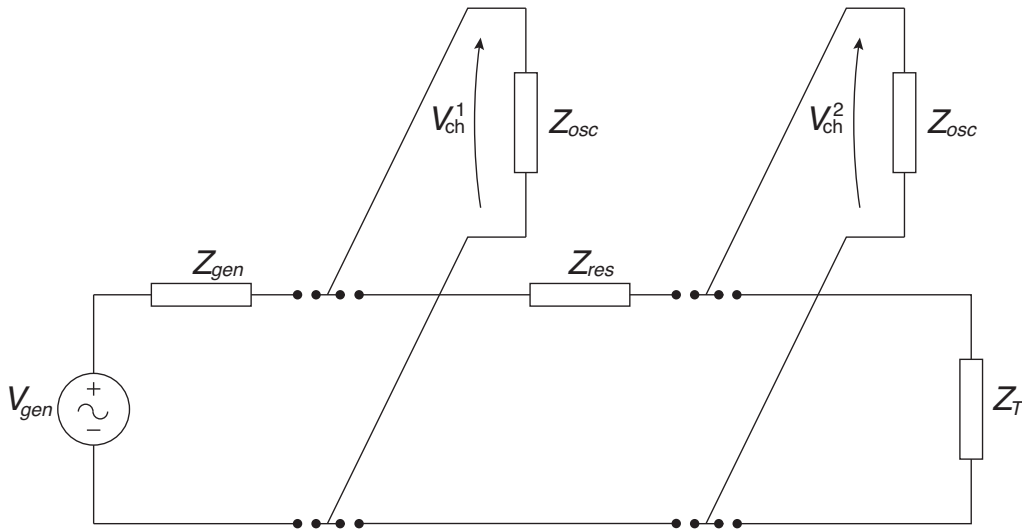


Figure 2.15: Set-up used to measure the impedance of the piezoelectric disk.

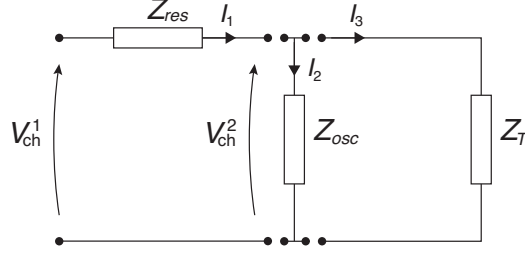


Figure 2.16: Simplification of Fig. 2.15.

## 2.12 Finite Element Method

All simulations in the current thesis are performed in the Finite Element (FE) software FEMP 5.0 or 5.1 [46, 47]<sup>6</sup>. FEMP has been developed at the acoustics department of UiB in cooperation with Christian Michelsen Research (CMR) [70]. and the theory behind FEMP is available in e.g. [46]. A full description of the theory is beyond the scope of the current thesis, but a few of the most important equations will be presented.

The simulations are modeled as axisymmetric problems where the piezoelectric disk is radiating into a fluid media of infinite extent. The finite element equations used in FEMP for a piezoelectric disk with an infinite fluid medium on  $H$ -form are [46]

$$-\omega^2 \begin{bmatrix} M_{uu} & 0 & 0 \\ 0 & 0 & 0 \\ 0 & 0 & -M_{\psi\psi} \end{bmatrix} \begin{Bmatrix} \hat{\mathbf{u}} \\ V \\ \hat{\psi} \end{Bmatrix} + i\omega \begin{bmatrix} 0 & 0 & C_{u\psi} \\ 0 & 0 & 0 \\ C_{\psi u} & 0 & 0 \end{bmatrix} \begin{Bmatrix} \hat{\mathbf{u}} \\ V \\ \hat{\psi} \end{Bmatrix} + \begin{bmatrix} H_{uu} & H_{u\phi} & 0 \\ H_{\phi u} & H_{\phi\phi} & 0 \\ 0 & 0 & -K_{\psi\psi} \end{bmatrix} \begin{Bmatrix} \hat{\mathbf{u}} \\ V \\ \hat{\psi} \end{Bmatrix} = \begin{Bmatrix} 0 \\ -I/i\omega \\ 0 \end{Bmatrix} \quad (2.76)$$

where  $[ \ ]$  and  $\{ \ }$  indicate a matrix or a vector, respectively,  $u$  is the displacement,  $\phi$  is the electrical potential,  $\psi$  is the velocity potential, and  $V$  is the electrical potential between the electrodes of the piezoelectric disk. The remaining quantities in Eq. 2.76 are defined in [46].

From the above expression, the electrical admittance of the piezoelectric disk can be found as [46]

$$Y = i\omega [\{H_{u\psi}\}^T + [D]^{-1} \{H_{u\phi}\} - H_{\phi\phi}] \quad (2.77)$$

where  $[D]$  is expressed as [46]

$$[D] = [H_{uu}] - \omega^2 [M_{uu}] + \omega^2 [C_{u\psi}] (-K_{\psi\psi} + \omega^2 [M_{\psi\psi}])^{-1} [C_{\psi u}] \quad (2.78)$$

And the relationship between the velocity potential,  $\psi$ , and the acoustic pressure in the fluid is given as [46]

$$p = -i\omega\rho\psi \quad (2.79)$$

where the velocity potential,  $\psi$  in the fluid is given as

$$\{\psi\} = -i\omega (-[K_{\psi\psi}] + \omega^2 [M_{\psi\psi}])^{-1} [C_{\psi u}] \{u\} \quad (2.80)$$

The electrical admittance,  $Y$ , is used to compare the measured admittance of the piezoelectric disks with the simulation, and is intrinsic to the far- and near-field models, c.f. Eq. (2.52) and (2.55). The acoustic pressure in the fluid,  $p$ , is used in e.g. Eq. (2.55) to simulate the far-field pressure  $p_A(z_{ff})$ .

<sup>6</sup>Both FEMP 5.0 or 5.1 are used, however for the functions used in the current thesis, there are no change between FEMP 5.0 and 5.1.

## Chapter 3

# Experimental set up and measurement methods

The current chapter present the experimental set up and measuring methods used to perform the acoustical, as well as electrical, measurements.

In Sec. 3.1 a description of the measurement set-up will be given. This is followed by a description of the measurement equipment, Sec. 3.2.

In Sec. 3.3 the method to alignment of the piezoelectric disks are described, followed by Sec. 3.4 where the description of how the measurement distance,  $d$ , is realized in the measurement set-up, is given. Both of these sections are important to the repeatability of the measurements.

In Sec. 3.5 the FFT-subroutine will be described, and an discussion on the importance of using a rectangular FFT-window that cuts the signal in the zero crossings of the signal is given.

In Sec. 3.6 several aspects of the phase measurements are discussed. Noteworthy is Sec. 3.6.2 where it is shown that without the aid of FE-simulations the measured phase would have an offset of  $360^\circ$ .

In Sec. 6.3 the noise observed in the measurement set-up is discussed and two formulations of the signal-to-noise ratio is given.

In Sec. 3.8 a discussion of the burst length versus steady-state conditions is given. And it is pointed out that for certain frequencies the choice of burst length might be too low to experience steady state conditions.

In Sec. 3.9 the electrical measurements are presented. This includes impedance measurement with a commercial impedance analyzer, impedance measurements with oscilloscope, and measurements on the amplifier and filter. The last is performed to verify the measurements performed by Søvik [3], and to obtain statistical data that are used in the uncertainty analysis, c.f. Sec. 7.

The chapter ends with Sec. 3.10 where an investigation of the coaxial cable parameters and input impedance of the amplifier is given.

### 3.1 Acoustical measurement set up

The current section describes the acoustical measurement set up. The acoustical measurement system is based on a measurement system developed by Hauge and Mosland [1,2] which work was based on Storheim and Amundsen [49,50]. The acoustical measurement set up has been further developed by Søvik [3] and the current author. Some of the changes are discussed in Sec. 3.1.1.

#### 3.1.1 Description of the acoustical measurement set up

In Fig. 3.1 a schematics of the acoustical measurement set up is given. The schematics is taken from [3] and the individual components are described in Sec. 3.2.

The function generator superimposes a single toned sinusoidal burst on the system, denoted  $V_0$ . This is recorded by the oscilloscope as  $V_{0m}(t)$ . The voltage superimposed on the terminals of the transmitting disk is denoted  $V_1$ . In Fig. 3.1 the transmitting disk is placed on the left. The sound pressure propagates through air from left to right and the receiving disk transforms

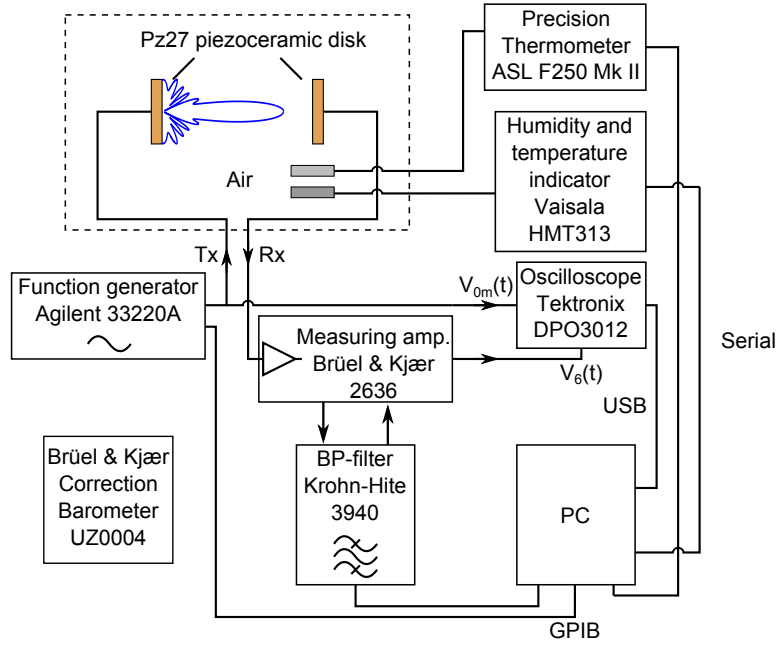


Figure 3.1: Schematics of the acoustical measurement set up. Schematics taken from [3].

the sound pressure to an electric potential. The open circuit electric potential at the terminals of the receiving disk is denoted  $V_{5open}$ . The received voltage is amplified and filtered, by the B&K measuring amplifier and Krohn-Hite digital filter, before it is recorded by the oscilloscope. The recorded "acoustical" signal is denoted  $V_6(t)$ . This process is repeated for each frequency under investigation.

The transmitter and receiver are placed inside a measurement cage which is covered in plastic sheets. The plastic sheets are used to prevent possible air currents which might disturb the acoustical measurement. This is indicated in Fig. 3.1 as the stippled line around the transmitter and receiver. The precision thermometer, ASL F250, is used to record the temperature during each measurement and the temperature probe is placed inside the cage in approximately the same height as the transmitter and receiver pair. The humidity is recorded by the Vaisala HMT313, and also this probe is placed inside the measurement cage.

### Changes made to the measurement set up

In [3] it was shown that the temperature measurements performed with the Vaisala temperature indicator was insufficient for the wanted precision of the phase response. The ASL F250 precision thermometer was therefore introduced in [3], and the ASL F250 is used throughout in the current work to estimate the temperature. In [1–3] the distance between the transmitter and receiver was measured with a measuring tape. The precision and associated uncertainty of this approach is rather high, and is deemed insufficient with respect to the accuracy wanted when the phase response of the system is estimated. To improve on this, short range, high resolution laser distance sensors was purchased, c.f. Sec. 5, and most of the work regarding this was performed by the current author in collaboration with [3]. The measurement cage had to undergo some changes to conform with the laser sensors. The legs of the cage was extended with approximately 0.30 m. And the pole corresponding to the transmitting side was extended with approximately 0.10 m. Both of these changes were performed to allow a vertical distance of approximately 0.50 m from the center of the piezoelectric disks to the top of the laser sensors, such as to prevent possible reflections.

The coaxial cables, Type RG-58, connecting the function generator to the transmitting disk, and the receiving disk to the amplifier in [1, 2] have been replaced by RG-178 B/U, c.f. Sec. 3.2.5. The latter is a thinner type of cable compared to the former.

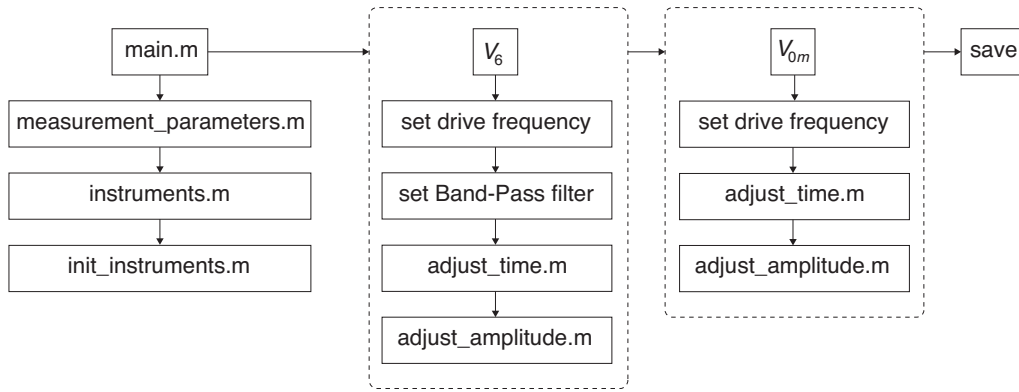


Figure 3.2: Flow-chart describing the acoustical measurement regime.

### 3.1.2 Data acquisition

In Fig. 3.2 a flow chart describing the acoustical measurement is given. `main.m` controls the measurement regime by first calling `measurement_parameters.m`, where the various measurement settings e.g. frequency vector, measurement voltage, are defined, the script `instruments.m` sets up the handles to each instruments, and `init_instruments.m` transfers the instrument settings to the respective instruments. When the handles to each instrument are set up, and the settings are successfully transferred to each instrument, the acoustical measurement can commence. The first quantity to be recorded is  $V_6$  for each frequency defined in `measurement_parameters.m`. This is performed by stepping through the frequencies one at a time, and superimposing the electromotive force  $V_{gen}$  on the system. The BP-filter is adjusted for each frequency, and `adjust_time.m` sets the time resolution according to  $b_l$ , such that the greatest sampling frequency is achieved without cutting the signal, and `adjust_amplitude.m` sets the vertical resolution of the oscilloscope, ensuring that the signal is not cut at peak, or valley.

All the scripts mentioned in the current section are available in the Appendix B.2.

## 3.2 Description of measurement equipment

In the current section a description of the measurement equipment used during the acoustical measurement will be given.

In Fig. 3.3 an overview of the acoustical laboratory is given, and in Tab 3.1 a list of the measurement equipment in Fig. 3.3 are: (a) plastic sheet covering the measurement cage - used to prevent possible air currents during acoustical measurements, (b, k) precision thermometer probe and precision thermometer, respectively, c.f. Sec. 3.2.4, (c, d) transmitter or receiver - interchangeable, c.f. Sec. 3.2.6, (e) z-axis stage - for translation of the transmitter or receiver along the acoustical axis (difficult to appreciate in image), (f) rotation stage - used to rotate the transmitter or receiver such that the front face of the transmitter or receiver is as best aligned with the xy-plane, (g) x- and y-translation stages - used to align the transmitter or receiver, (h) measurement cage - aluminium structure that is easy to assemble and expand on, (i) elevation mechanism - used to position the laser sensors between the transmitter and receiver (difficult to appreciate in image), c.f. Secs. SOMETHING, (j) controller for laser sensors, (l) function generator, c.f. Sec. 3.2.1, (m, n) signal amplifier, c.f. Sec. 3.2.3, (o) oscilloscope, c.f. Sec. 3.2.2, (p) laboratory PC running WINDOWS 7, all instruments are controlled by MATLAB.



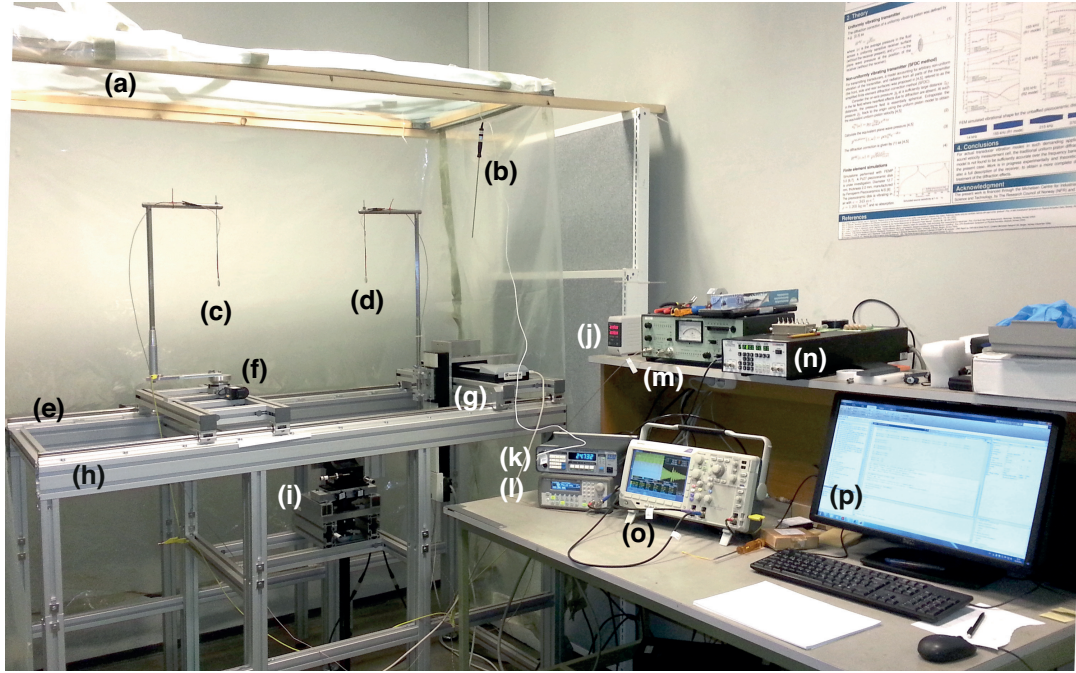


Figure 3.3: Overview of the measurement set-up. The components are partly listed in Table 3.1 and in the text.

### 3.2.1 Function generator

An Agilent 33220A function generator [79] is used to generate bursts consisting of single toned sinusoids. The frequency of the single toned sinusoids are denoted  $f_d$ <sup>1</sup>, and will often be referred to as drive frequency. The burst repetition period, denoted  $b_T$ , is set to 40 ms [1], such that 25 bursts are generated each second. The time duration of each burst, denoted  $b_t = 1.1$  ms, is used as a constant, c.f. Sec. 3.8, and the number of signal periods contained within each bursts, denoted  $b_N = f_d \cdot b_t$ , is thus adjusted according to the drive frequency.

The function generator outputs an electromotive force,  $V_{gen} = Ae^{i\omega t}$ , in the internal output impedance,  $Z_{gen} \approx 50 \Omega$ , c.f. Fig. 3.4 (a), where  $A$  is a constant determining the amplitude of the electromotive force,  $t$  is time and  $\omega = 2\pi f$ . Two values for  $A$  is used in the current work, 10 and 1 V.<sup>2</sup>

Due to the internal impedance,  $Z_{gen}$ , the voltage at the terminals of the transmitter becomes a function of the impedance of the transmitting disk. In Fig. 3.4 (b) this is exemplified for the frequency range 50–140 kHz where the voltage  $|V_{0m}|$  is plotted as a function frequency. The decrease in voltage is apparent for the frequency range 80–110 kHz. This corresponds with the decrease in impedance of the piezoelectric disk.

### 3.2.2 Oscilloscope

A Tektronix DPO3012 digital oscilloscope [80] is used as a digitizer of the analog signals  $V_{0m}$  and  $V_6$ . The oscilloscope is connected to the laboratory PC and the recorded voltages are transferred to MATLAB whereupon the recordings are saved. The oscilloscope is equipped with an input resistance of 1 M $\Omega$  in parallel with a capacitance of 11.5 pF. The received signals, electric and acoustic, are

<sup>1</sup>The notation  $f_c$  was adopted in [3] to denote both the center frequency of the filter and the frequency of the single toned sinusoidal signals. The notation is misleading when further adopted to the Fourier transform where it implies that the center frequency of the Fourier transformed spectrum is different from zero. The notation  $f_c$  is hereby used to denote the center frequency of the filter, but the notation  $f_d$  is adopted denoting the drive frequency of the single toned sinusoidal signals superimposed on the system. Although  $f_c = f_d$  the notation is used to avoid confusion.

<sup>2</sup>Note that this change in notation was implemented quite late in the current thesis. An attempt to correct all prior notation has been made. However, if e.g. 20 V peak-to-peak, or 2 V peak-to-peak, occurs in the current thesis, it should be understood that the intended meaning is 10 V and 1 V, respectively.

Table 3.1: Complete list of measurement equipment used. Physic Instrumente is abbreviated in the table as PI.

Make/Type	Type of equipment	Serial number
Physical measurements		
TESA DIGIT-CAL SI [71]	Digital caliper	4J09704
Mitutoyo MDH-25M [72, 73]	Digital micrometer	15229628
Electrical measurement		
HP 4192A [69]	Impedance analyzer	23423
Positioning stage		
PI M-535.22 [74]	Linear position stage (x-axis)	109040312
PI M-531.DG [75]	Linear position stage (y-axis)	-
PI miCos LS270 [76]	Linear position stage (z-axis)	414000926
SMC hydra TT [76]	2 axes Motion-Controller	1404-0153
PI M-037.PD [77]	Worm-Gear rotation stage	109040312
PI MS77E - C-843.41 [78]	Motor controller card	0095103296
Laser distance sensors		
KEYENCE LK-G32 [51]	2 x Sensor heads	2041141, 2041143
KEYENCE LK-G3001PV [51]	Controller with display	1741187
KEYENCE LK-H1W [51]	Software LK-Navigator	-
Acoustical measurement		
Agilent 33220A [79]	Function Generator	MY44023589
Tektronix DPO3012 [80]	Digital oscilloscope	195539
Vaisala HMT313 [81]	Humidity and temperature transmitter	F4850018
Brüel & Kjær 2636 [82]	Signal amplifier	1615638
Krohn-Hite 3940A [83]	Digital signal filter	AM2626
ASL Ltd., F250 Mk. 2 [84]	Precision thermometer	1365026993
- Isotech 935-14-61 Pt100	Platinum resistance thermometer	161076/1
Brüel & Kjær UZ0004	Correction barometer	1918465
Brüel & Kjær 4138-A-015 [85, 86]	Microphone system	2795107
- Brüel & Kjær 4138	1/8-inch pressure-field microphone	2784915
- Brüel & Kjær UA-160	Adaptor - microphone-preamplifier	-
- Brüel & Kjær 2670	Preamplifier	2799662
Elevation mechanism		
Gitzo Series 5	Geared centre column (long)	-

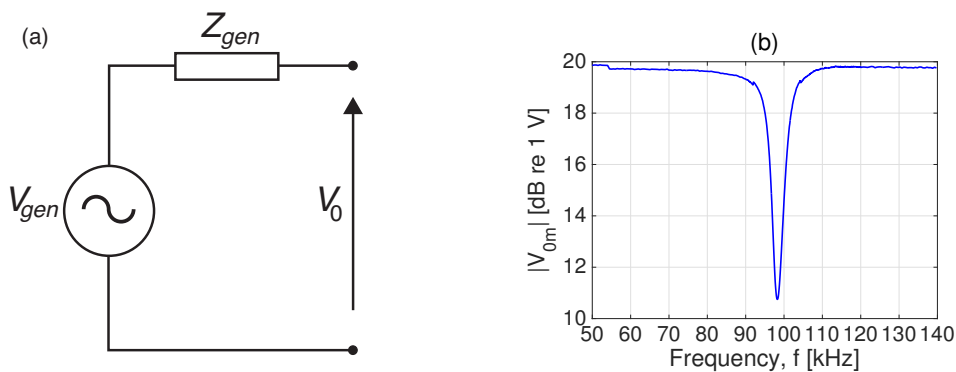


Figure 3.4: (a) Thévenin equivalent circuit of the electromotive force,  $V_{gen}$ , and the output impedance,  $Z_{gen}$ , of the function generator, (b) example of the recorded voltage,  $|V_{0m}|$ , showing the decrease in  $V_{0m}$ .

averaged 128 times in order to reduce the random noise present in the system. The oscilloscope has an 8-bit vertical resolution with a dynamic range  $20\log_{10}(2^8) \approx 48$  dB. To utilize the dynamic range, the vertical setting of the oscilloscope is adjusted according to the maximum value of the recorded signal. A MATLAB function, `adjustAmplitude` is written by [1,2], and further developed

Table 3.2: Selected features of the measuring amplifier.

1 V FSD Output	
Frequency range (without filters)	1 Hz to 200 kHz ( $\pm 0.5$ dB)
Overall Gain	from -30 dB to 100 dB in $10 \pm 0.05$ dB steps
Input Impedance	$1 \text{ M}\Omega \parallel 90 \text{ pF}$
Output Impedance	$\sim 100 \text{ }\Omega$ given 10 V peak into a max load of $10 \text{ k}\Omega \parallel 200 \text{ pF}$
Phase deviations	$\leq \pm 5^\circ$ (from 20 Hz to 20 kHz)

by the current author and [3]. `textttadjustAmplitude` is available in Appendix B.2.

According to [1,2] a minimum vertical scaling of 10 mV/div is necessary as not to lose important information of the acoustical signal. This setting is found to be accurate and is kept in the current work.

### 3.2.3 Brüel & Kjær 2636 Measuring Amplifier and Krohn-Hite Signal Filter

A B&K Measuring Amplifier [82], referred to as the amplifier, is used to amplify the received signal. In the current work the signal is amplified with a gain of 60 dB, where a gain of 40 dB is applied before the external filter (input) and 20 dB is applied after the external filter (output). Most of the gain is applied before the external filter such that any noise arising in the external filter, or in the amplifier itself, will not be amplified unnecessarily. The settings are inherited from [1,2].

A Krohn-Hite Model 3940 Multichannel Filter is used to filter out unwanted frequency components from the received acoustical signal. The filter is operated as a sliding bandpass (BP) filter with a center frequency,  $f_c$ , equal to the drive frequency,  $f_d$ . The BP-filter consist of a high-pass (HP) filter of type Butterworth with a cut off frequency  $f_{HP} = f_c/2$ , and a low-pass (LP) filter of type Butterworth with a cut off frequency  $f_{LP} = f_c \cdot 2$ . Both the BP- and LP-filter have an attenuation of 24 dB/Octave.

The amplifier is equipped with three possible outputs, (1) AC 1 V FSD, (2) AC 5 V FSD, (3) DC 5 V FSD. The AC Output of 1 V FSD is used in the current work. In Table 3.2 some selected features of the amplifier are given. In Fig. 3.7 a typical frequency response (magnitude) of the amplifier is given. On the far right it is observed that the AC Output of 1 V FSD is the superior output choice over the two other output possibilities, though also this output choice deviate from a flat frequency response when the frequency exceeds 200 kHz. In Fig. 3.6 the typical phase response of the amplifier is given. Although the amplifier exhibits a flat frequency response over a wide frequency range, the phase starts to lag at about 5-10 kHz.

In [3] measurements on the amplifier and filter was initiated to determine the magnitude and phase response of the amplifier and filter. This corresponds to the transfer function  $H_{5'6open}^{VV}$ . The magnitude measurements conducted by [3] was found to be within the uncertainties for the amplifier, and the phase was found to be comparable to the typical phase response shown in Fig. 3.6. In Sec. 3.9.3 the measurements performed by [3] has been repeated by the current author, and in Fig. 6.17 the results obtained in the current thesis are compared to those obtained in [3].

### 3.2.4 Environmental parameters

Recordings of the environmental parameters: relative humidity, temperature and atmospheric pressure is performed in order to be able to estimate the speed of sound. The temperature and relative humidity is recorded for each frequency, though the atmospheric pressure is treated as a constant through out the measurements and are read of an analog barometric indicator prior to a measurement.

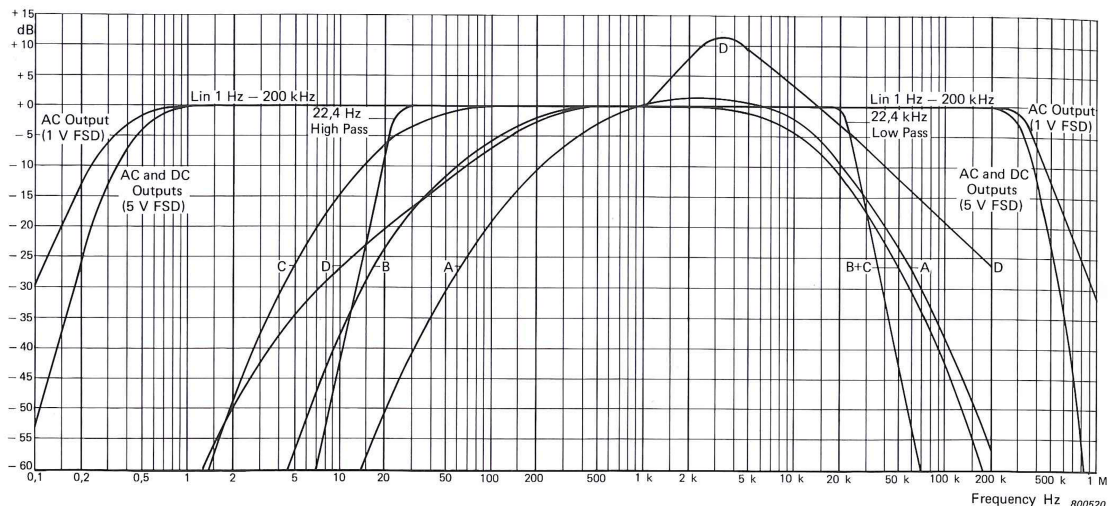


Figure 3.5: Typical overall frequency response (magnitude) of the B&K 2636 measurement amplifier [82]. The AC Output of 1 V FSD is used during measurements.

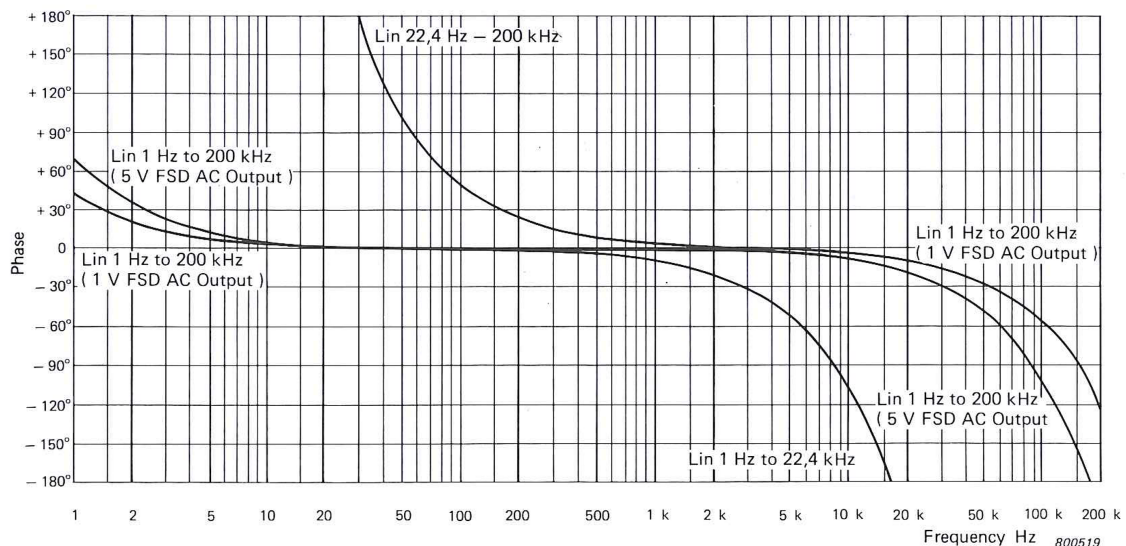


Figure 3.6: Typical overall phase response of the B&K 2636 measurement amplifier [82]. The AC Output of 1 V FSD is used during measurements.

### Temperature

In [3] the uncertainty of the Vaisala Humidity and Temperature Transmitter [81] was deemed to high for accurate predictions of the speed of sound. The temperature is therefore recorded using the ASL F250 MK II Precicion Thermometer [84] in combination with a Isotech 935-14-61 Semi Standard Pt100 platinum resistance thermometer. The temperature is recorded using the highest resolution of 0.001°C. The uncertainty of the ASL F250 MK II Precicion Thermometer, using the resolution of 0.001°C, is  $\pm 0.01^\circ$ .

### Humidity

The relative humidity of the acoustic laboratory is recorded using the Vaisala Humidity and Temperature Transmitter [81]. The humidity sensor is associated with a  $\pm 0.6\%$  uncertainty for a relative humidity lower than 40%, and  $\pm 1.0\%$  uncertainty for a relative humidity in the range 40-97%, both at a 95% confidence level, [87].

## Atmospheric pressure

The atmospheric pressure is read out from an analog Brüel & Kjær UZ0004 Correction barometer prior to an acoustical measurement. The duration of one measurement can vary from approximately 5-14 hours, and the atmospheric pressure is observed to be fairly constant during a measurement, though with increased deviations as the measurement time increases. However, the speed of sound is found to be rather independent of changes in the atmospheric pressure. E.g. for a temperature of 25°C and a relative humidity of 40% the change in the speed of sound is found to be 0.25 m/s given a change in the atmospheric pressure from 90-130 kPa. The range of atmospheric pressure presented are representative of the observed atmospheric pressure in the laboratory, though not for one measurement. The influence of the atmospheric pressure on the sound speed is therefore deemed lower.

### 3.2.5 Coaxial cables

Two types of coaxial cables are used in the current work. RG-178 B/U Mil-C 17 F [88] are used to connect the waveform generator to the transmitting disk, as well as the receiving disk to the amplifier. Interconnections between the electrical equipment are done with RG-58. See Table 3.3 for a list of features of the two types of cables <sup>3</sup>. Measurement on the impedance of the RG-178 cables have been performed to investigate the associated cable parameters, c.f. Sec. 3.10. Only the capacitance have shown important for the cable lengths used, and the corrected value is given in Table 3.3.

Table 3.3: Selected features of the coaxial cables.

Typical specifications			
Cable type	Impedance, $Z_0$	Inductance, L	Capacitance, C
RG-178 B/U	50±2 [Ω]	-	93 [pF/m] (at 1 kHz)
RG-58	50 [Ω]	250 [nH/m]	100 [pF/m]

Table 3.4: Overview of the coaxial cables used to connect the electrical equipment in the measurement set-up.

Cable nr.	From/To	Length [m]	Cable type
1	waveform generator / transmitter	2.97	RG-178 B/U
2	waveform generator / oscilloscope	0.975	RG-58
3	receiver / amplifier	2.97	RG-178 B/U
4	amplifier / oscilloscope	0.975	RG-58

### 3.2.6 Piezoelectric Disks

Circular Pz27 Piezoelectric disks are used as both transmitter and receivers of the sinusoidal bursts. The disks are of approximately diameter 20 mm and thickness 2 mm, with a D/T ratio of 10. In Table 3.5 the characteristic frequencies [89] for the piezoelectric disk used in the current thesis is given with definitions. The values are given for disk 11. It is worth noticing that for the R1-mode,  $f_s$  is concurrent with  $f_m$ , and  $f_p$  is concurrent with  $f_n$ . In Sec.6.1 a figure indicating the two modes and the characteristic frequencies  $f_m$  and  $f_n$  are given. Note that most discussion will be performed with respect to the series- and parallel resonance frequencies.

The piezoelectric disks used in the current thesis are of the same batch as those used by [1, 2], and are the exact same disks as those used by [3].

<sup>3</sup>The specific manufacturers of the coaxial cables of Type RG-58 have not been able to track down. Thus typical values for the specific cable are listed, and not the manufacturers specifications.



Table 3.5: Characteristic frequencies for the R1- and R2-mode. The stated values are for disk 11.

	R1-mode [kHz]	R2-mode [kHz]	Definition [89]
$f_s$	99.4	251.5	maximum conductance
$f_m$	99.4	251.2	maximum admittance
$f_p$	115.0	257.5	maximum resistance
$f_n$	115.0	257.9	maximum impedance

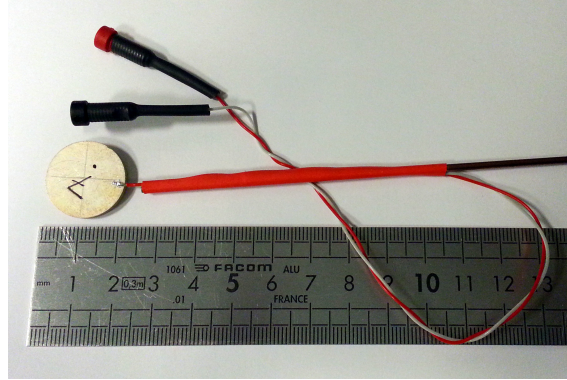


Figure 3.7: Image of a piezoelectric disk with wires soldered onto the electrodes. The welding rod is visible on the far right, and the red shrinking plastic is seen extending from the disk to the welding rod.

Prior work at UiB by e.g [90] on determining the piezoelectric material constants of Pz27 disks has yielded an adjusted material data set that are used during simulations, c.f. Sec. 4.4. The adjusted material data set is, however, not been adjusted for the current batch of disks, or for the individual disks. Deviations in the actual behavior of the disk compared to simulations are therefore expected. However, adjusting a set of material constants can be a timely affair which has not been prioritized in the current thesis. These deviations are discussed and exemplified in e.g. Secs.6.1 and 6.5.2.

### Soldering

To connect the piezoelectric disks to the coaxial cables, wires with a diameter of approximately 0.6 mm are soldered onto the electrodes near the edge of the disk. The soldering of the wires to the disk have been performed by Senior Engineer Per Heradstveit, and the soldering process and its implications are documented in [3]. The reader is hereby referred to [3] for a discussion of the soldering process [3] Sec.3.2.1, and its implications on the impedance measurements [3] Sec.5.3. The conclusion in [3] is that the soldering process alters the impedance of the piezoelectric disks which translates to both the electrical and acoustical measurements.

In Fig. 3.7 an image of a piezoelectric disk with wires soldered onto the electrodes are given. The welding rod is visible on the far right, and the red shrinking plastic is seen extending from the disk to the welding rod. The black dot indicates the polarization direction, and the straight lines drawn on the face of the disk indicates where the center of the disk is located.

### Measurements of dimensions

Accurate knowledge about the piezoelectric physical dimensions can be of important for the accuracy of the FE-simulations. Both thickness and diameter measurements of the disks have therefore been performed. The thickness is measured with a Mitutoyo MDH-25M digimatic micrometer [91] and the diameter of the piezoelectric disks are measured using a TESA DIGIT-CAL SI digital caliper [71]. Each disk have been measured 10 times in both the thickness and diameter dimension and the average of the measurements have been used during the FE-simulations.

A list of the measurements of element 04, 07, 11, 12, 13, 14 and 19 is provided in [3] for both

thickness and diameter, and will not be repeated here. Rather, a list of the elements mean and associated uncertainties calculated according to [92] for the disk used in the current thesis, 04, 07, 11, 13, will be presented. The calculation are of both type A and B, c.f. Sec. 7.

Note that simulations of e.g. the impedance of the disks in Table 3.6 have shown that the simulated impedance are rather independent of the different sizes tabulated. Thus, the simulated impedance and sound pressure of one disk is deemed valid for all disks and a distinction between the various simulations will not be made.

Table 3.6: List of dimensions for the piezoelectric disk with associated uncertainties.

Disk no.	Diameter [mm]	Thickness
04	$20.20 \pm 0.04$	$2.0265 \pm 0.0005$
07	$20.20 \pm 0.05$	$2.0410 \pm 0.0010$
11	$20.20 \pm 0.04$	$2.0234 \pm 0.0005$
13	$20.24 \pm 0.04$	$2.0288 \pm 0.0008$

### 3.2.7 Keyence sensors and controller

To be able to determine the distance between the transmitter and receiver two short range, high resolution laser distance sensors of type LK-G32 from Keyence [51] as well as a controller, LK-G3001PV, have been purchased. The laser distance sensors will hereafter be referred to as laser sensors or sensors. The sensors measure an absolute distance from the front face of the sensor to an object. To measure the distance between the transmitter and receiver the two sensors have to be mounted in opposite direction. A consequence of this is that the distance between the two front faces of the sensors are unknown. This distance is denoted  $d_x$ . In Sec. 5 the calibration of the distance  $d_x$  is given, and in Fig. 3.8  $d_x$  is indicated.

In Fig. 3.8 the two lasers are shown mounted in opposite directions. The width of each sensor is 76 mm. In front of each sensor are the measurement ranges indicated. The measurement range is 10 mm, spanning from 25 mm to 35 mm from the front face of the sensor. Measurements beyond the indicated range is not possible.

When a distance measurement is performed, the distance obtained from the sensor is referenced to the reference distance,  $d_{ref} = 30$  mm. If the distance to the object is larger than  $d_{ref}$ , then the distance obtained from the sensor is negative, and if the distance to the object is lower than  $d_{ref}$ , then the distance obtained from the sensor is positive. In Fig. 3.8 the distance from the front face of laser 1 to the object to be measured is denoted  $d_1$ , the distance obtained from the sensor is denoted  $d_1'$ , and the reference distance is denoted  $d_{ref}$ . The distance from the front face of sensor 1 to the object is:  $d_1 = d_{ref} - d_1'$ . A similar relationship exist for laser 2, i.e.  $d_2 = d_{ref} - d_2'$ .

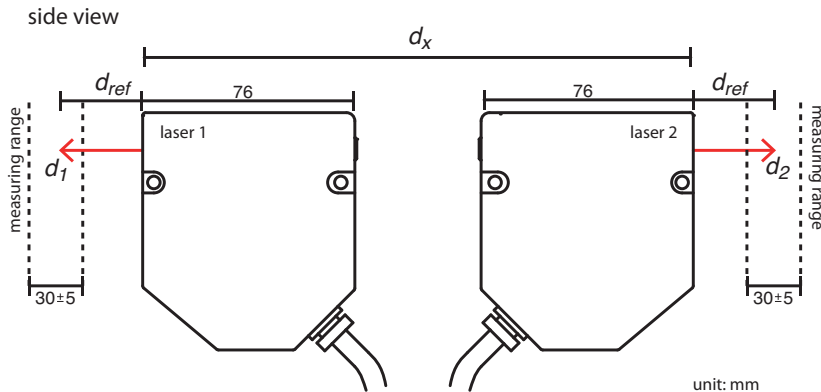


Figure 3.8: Schematics of LK-G32 shown with measuring ranges indicated.

In Table 3.7 a selection of some of the important features of the sensor are given. In Appendix C a surface scan and linearity plot provided by Keyence showing an example of a measurement on

a white ceramic material is given.

Table 3.7: Selected features of the LK-G32 laser sensor [51]. In the table the abbreviation std. is used for standard deviation.

LK-G32 laser sensor	
Reference distance, $d_{ref}$	30 mm
Measurement range	$\pm 5$ mm
Spot diameter	Approx. $\phi 30$ $\mu\text{m}$
Linearity (assuming one std. level)	$\pm 0.05\%$ of full scale (full scale = $\pm 5$ mm )
Repeatability (assuming one std. level)	0.05 $\mu\text{m}$
Resolution (assuming one std. level)	0.1 $\mu\text{m}$
Light source	650 nm (visible light)

### 3.3 Alignment of piezoelectric transmitter and receiver pair

The alignment of the piezoelectric disks front face with the  $xy$ -plane, and the coaxially alignment of the disks with the  $z$ -axis, is of significant importance when attempting to obtain repeatable measurements. The front faces of both disks should be as best parallel with the  $xy$ -plane, and the center of each disk should be as best placed in  $x = y = 0$ . Another important factor is the alignment of the disk's polarization direction. Such as not to introduce a phase shift of  $180^\circ$ , the polarization direction of both disks have to be facing one another, c.f. Fig. 3.9.

To align the piezoelectric disks parallel with the  $xy$ -plane the manual XYZ-translation stage from Thorlabs and the rotation stage, c.f. Sec. 5.1, are employed. In Fig. 3.9, the transmitter is placed on the left hand side, and the receiver is placed on the right hand side. For the transmitter, the center of the front face of the disk is placed in  $x = y = z = 0$ . This is indicated on the figure with the  $x$ - $y$ - $z$ -axes. The center of the front face of the receiver is placed in  $x = y = 0$  and  $z = d$ .

The alignment of the transmitter is first performed in the vertical direction. The laser sensor is first placed in  $x = y = 0$ , the laser spot is then moved along the  $x$ -axis by the XYZ-translation stage. Close to the top of the disk, the distance from the laser sensor to the front face of the disk is read out. Next, the laser spot is moved in the opposite  $x$ -direction, to the bottom of the disk, and the distance from the laser sensor to the front face of the disk is read out. The two distance readings are then compared. If the alignment is not satisfactorily, the disk is adjusted by lightly pushing on the bottom edge in either direction. This process is repeated until the deviation in distance along the  $x$ -axis is within satisfaction. A maximum deviation of approximately 20  $\mu\text{m}$  has been employed throughout the thesis. To align the transmitting disk with the  $y$ -axis, the rotation stage is employed to rotate the disk until deviations along the  $y$ -axis are less than 20  $\mu\text{m}$ .

For the receiver, the alignment technique is similar. However, since the receiver is not mounted on a rotation stage, the alignment of the receiver with the  $y$ -axis is performed by loosening the screw that holds the welding rod in place and by rotating the welding rod.

This technique to align the disks with the  $x$ - $y$ -plane are timely, but yields fair results. Maximum deviations along the  $x$ - and  $y$ -axis of 5-20  $\mu\text{m}$  are experienced. It should be noted that measurements on the deviations both before and after the acoustical measurements have been performed. The disks have then been suspended for a time period of e.g. 10-14 hours. There are observable differences in the deviations along the  $x$ - and  $y$ -axis from before to after an acoustical measurement. This is explained by tension in the cables welded onto the the disks that results in slight movements, and possible due to the translation of the transmitter to the measurement distance. The observed differences are assumed negligible, as they have been found to be less then 20  $\mu\text{m}$ . However, larger deviations have been experienced, though the implication of this on the measured phase has not been investigated.



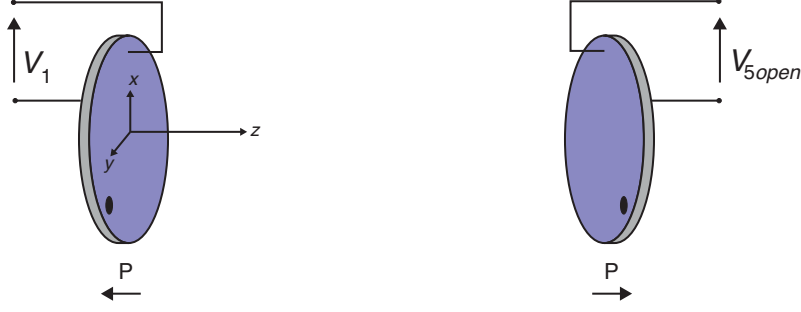


Figure 3.9: Schematics of the alignment of the piezoelectric disk with respect to polarization direction, and z-axis. The left disk's front face, i.e. the transmitter, should be aligned parallel with the xy-plane in  $x = y = z = 0$ . On the right hand side, the receiving disk's front face, aligned coaxially at  $z = d$ , should also be aligned parallel with the xy-plane in  $x = y = 0$ . The polarization direction is indicated with the arrows and the capital P, as well as the little black dot on each disk's face. In the laboratory, the black dots are marked on the disk's faces.

### 3.4 Measurement distance, $d$

The following section will describe how the measurement distance,  $d$ , is realized. The measurement distance  $d$  is treated as a constant, where  $d = 0.50$  m and  $0.85$  m have been utilized in the current thesis. The following section will also include the measurements on the repeatability of the  $z$ -axis translation needed to obtain  $d$ .

In Fig. 3.10 a schematics of the measurement set-up is given. The transmitting disk is indicated with  $T_x$  and the receiving disk is indicated with  $R_x$ . The distances  $d_1$  and  $d_2$  are the distances between laser 1 and the transmitter, and between laser 2 and the receiver, respectively.  $d_{rel}$  is the distance the transmitter have to move to obtain the separation distance  $d$ . The position of the transmitter after translation is indicated with the stippled disk on the far left. The distance  $d_x$  is the distance between the two front faces of the laser sensors. This distance is obtained in Sec. 5, where it was shown that  $d_x = 182.5692$  mm with a combined standard uncertainty  $u_c(d_x) = 2.6$   $\mu\text{m}$ , at 68.3% confidence level for a temperature  $T_{cal} \approx 24^\circ$ . The 5 mm aluminium plate, which the sensors are attached to, is indicated behind the two laser sensors. The aluminium plate is expected to exhibit thermal expansion if the temperature,  $T_c$ , during a distance measurement varies from  $24^\circ$ . Thus, the calibrated distance  $d_x$  can differ from the actual distance between the two front faces. This is corrected for by assuming that the aluminium plate will expand similar to that of a rod in the  $z$ -direction, c.f. Sec. 5.3.1.

The distance the transmitter have to move is obtained by

$$d_{rel} = d - d_{xe} - d_1 - d_2, \quad (3.1)$$

where  $d_{xe}$  is the calibrated distance,  $d_x$ , corrected for possible thermal expansion of the aluminium plate, and  $d_{xe}$  is given by

$$d_{xe} = d_x(1 + \alpha_{Al}\Delta T), \quad (3.2)$$

where  $\alpha_{Al}$  is the thermal expansion coefficient for aluminum, and  $\Delta T = T_c - T_{cal}$ .

When the laser sensors are placed in between the transmitter and receiver, the distances  $d_1'$  and  $d_2'$  are measured and saved to a .csv file which are loaded to a MATLAB script `relative_translation.m` that calculates  $d_{rel}$ . `relative_translation.m` is available in Appendix B.2.7.

#### 3.4.1 Repeatability of $z$ -axis translation

When  $d_{rel}$  in Sec. 3.4 is determined, the disks are positioned approximately 0.24 m apart. The shortest measurement distance used in the current thesis is 0.50 m. Thus, the transmitting disk have to be translated to the appropriate measurement distance. This translation is performed with the  $z$ -axis translation stage, and is associated with an uncertainty. Measurements have been performed attempting to determine this uncertainty.

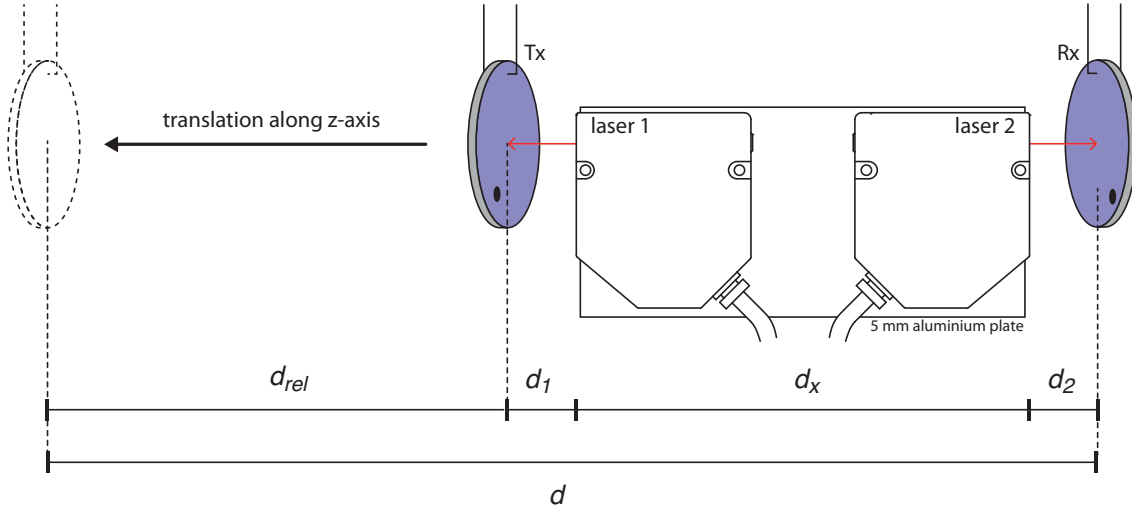


Figure 3.10: Schematics of a measurement on the distance between the piezoelectric disks, with the position for the transmitting disk indicated with the stippled disk on the far left.

The measurements have been performed by first measuring the distances,  $d_{1'}$  and  $d_{2'}$ . The transmitter has then been moved to  $d = 0.50$  m before being returned to the same position as before, whereupon a new measurement of  $d_{1'}$  and  $d_{2'}$  are performed.

Three measurement series, each consisting of ten measurements have been performed. The standard deviation have been calculated for each measurement series, and are given in Table 3.8. The measured standard deviations associated with  $d_{1'}$ , denoted laser 1 in the table, indicate that the transmitter is returned to approximately the same position after the translation. The deviations observed for  $d_{2'}$ , denoted laser 2 in the table, are understood by vibrations in the measurement cage stemming from the translation of the transmitter. These vibrations cause small deviations in the position of the suspended receiver.

It is observed that the largest value for laser 1 is found in the second measurement series, and in the first measurement series for laser 2.

In Appendix ?? a measurement performed by PI micos on the position error of the translation stage is given. The measurement is performed with laser interferometry, on a granit-base with a maximum error of  $1.6 \mu\text{m}$ , suspended  $40 \text{ mm}$  above the slider. The position error of the translation is therefore relative to the distance measurement obtained with the laser interferometry over the distance range  $0$  to approximately  $0.85 \text{ m}$ . It is observed that the position error is in the range  $+6$  to  $-10 \mu\text{m}$ . This is in fair agreement with what is obtained in the acoustical laboratory at UiB.

Table 3.8: Values on the repeatability of the z-axis translation stage.

meas. series	repeatability [ $\text{m} \cdot 10^{-6}$ ]	
	laser sensor 1	laser sensor 2
1	3.7	4.5
2	9.6	2.3
3	3.5	3.4

### 3.5 Signal processing and the FFT sub-routine

All measurements are performed in the time domain, however, and especially, the acoustical signal is associated with noise. A common technique to reduce noise is by transforming the time domain signal to the frequency domain [93], also referred to as the spectrum. The quantities to be transformed are the two recorded voltages,  $V_{0m}(t)$  and  $V_6(t)$ .

In Sec. 2.1.1 the Fourier transform for the continuous- and discrete-time (DTF) was given. The DFT forms the basis for the Fast Fourier Algorithm (FFT), which is used in the current thesis to estimate the spectra of the recorded voltages. The FFT algorithm used in the current thesis is the inbuilt FFT algorithm in MATLAB.

It is of interest to obtain both the magnitude and phase response of the recorded voltages, and these two quantities have to be estimated by slightly different approaches. The estimate of the magnitude is based on [1, 2], however an extension of their work has been implemented, c.f. Sec. 3.5.1. The estimation of the phase response is based on [3], however, as was pointed out in Sec. 2.2, the phase is handled differently in the current thesis compared to [3].

In the Appendix B.1.1 and B.1.2 the two script used to calculate the magnitude and phase spectra is given, respectively.

In Table 3.9 a list of the rectangular FFT-window's lower and upper boundaries, stated as both sample number and as time.

Table 3.9: List of the rectangular FFT-window's lower and upper boundaries, stated as both sample number and as time.

	FFT-window	
	lower bound	upper bound
$ V_{0m} $	20000 [sample nr.]	50000 [sample nr.]
$\angle V_{0m}$	$t = 0$ [s]	50000 [sample nr.]
$ V_6 $	30000 [sample nr.]	60000 [sample nr.]
$\angle V_6^{slow}$	$t_p$ [s]	60000 [sample nr.]

### Estimation of magnitude spectra for $V_{0m}(t)$ and $V_6(t)$

The estimation of the magnitude spectra for  $V_{0m}(t)$  and  $V_6(t)$  is similar for both signals, thus for the current section both  $V_{0m}(t)$  and  $V_6(t)$  will be referred to by  $V(t)$ .

The estimate of the magnitude spectra of the recorded voltages are referred to the steady state part of the time domain bursts. If the recorded bursts have not reached steady state conditions, the estimation will reflect this deviation. The time domain bursts are recorded independently for each drive frequency, denoted  $f_d$ , and the spectra are independently estimated from each time-domain burst. The FFT algorithm returns a double sided complex frequency spectrum, such that the magnitude of the frequency components are divided between the positive and negative frequencies. To compensate for this, the magnitude spectra have to be multiplied with 2. The FFT algorithm also returns a peak voltage level, such that to obtain a peak-to-peak voltage level the magnitude spectra once again have to be multiplied with 2.

In Fig. 3.11 (a) an example of a time domain burst of the recorded voltage  $V_6(t)$  is given. The drive frequency  $f_d = 100$  kHz, the burst time  $b_t = 1.1$  ms,  $V_{gen} = 10$  V, the onset of the electrical pulse is at  $t = 0$  and the recording of the received voltage has begun at  $t \approx 1.3$  ms, and the measurement distance  $d = 0.50$  m. In the figure there are two red vertical lines. The dotted line, at approximately  $t = 1.4$  ms, indicated the lower bound of the FFT-window when the phase spectra is estimated, and the dashed line, at approximately  $t = 1.9$  ms, indicated the lower bound of the FFT-window when the magnitude spectra is estimated. The black dashed line indicate the upper bound of the FFT-window for both magnitude and phase spectra estimations.

The aforementioned window, is a rectangular window, that cuts the signal in the position of the bounds. However, for the magnitude spectra estimation the upper and lower bounds are adjusted such that they cut the signal in the zero crossings of the signal, c.f. Sec. 3.5.1. Only the time-domain signal contained within the lower and upper bounds of the FFT-window are used in the estimate of the magnitude spectra. This shorter signal is referred to as a sub-signal with a corresponding signal length denoted,  $N_{sub}$ . The length of the sub-signal refers to the number of sample points contained within the lower and upper bounds of the FFT-window.

When a sub-signal of a time domain burst have been extracted, the sub-signal is padded with trailing zeros, denoted  $V_{pad}^{zro}(t)$ . The complex spectra is then estimated from the zero-padded signal,

i.e.

$$V(f_{FFT}) \stackrel{\text{FFT}}{\leftarrow} V_{pad}^{zro}(t) \quad (3.3)$$

where  $\stackrel{\text{FFT}}{\leftarrow}$  denote the fast-Fourier transform (FFT) algorithm of MATLAB,  $V(f_{FFT})$  is the complex spectrum of the zero-padded signal,  $V_{pad}^{zro}(t)$ , and  $f_{FFT}$  is the frequency vector associated with the transformation. Since we are only interested in the magnitude associated with the drive frequency,  $f_d$ , this frequency is located in  $f_{FFT}$  and the corresponding magnitude value is obtained by

$$|V(f_d)| = |V(f_{FFT} \equiv f_d)| \cdot \frac{2 \cdot 2}{N_{sub}} \quad (3.4)$$

where  $||$  denotes magnitude, multiplication by  $2 \cdot 2$  is performed to obtain the single-sided magnitude spectra and peak-to-peak voltage level, and the spectra is normalized with the length of the sub-signal,  $N_{sub}$ .

When  $|V(f_d)|$  has been extracted, the remaining frequency components of  $V(f_{FFT})$  are discarded. If the frequency components of  $f_{FFT}$  do not correspond with  $f_d$ , the magnitude  $|V(f_d)|$  is located by linear interpolated between the two surrounding frequencies in  $|V(f_{FFT})|$ . This process is repeated for each recorded time burst, and the cumulative magnitude spectra is stored in a vector.

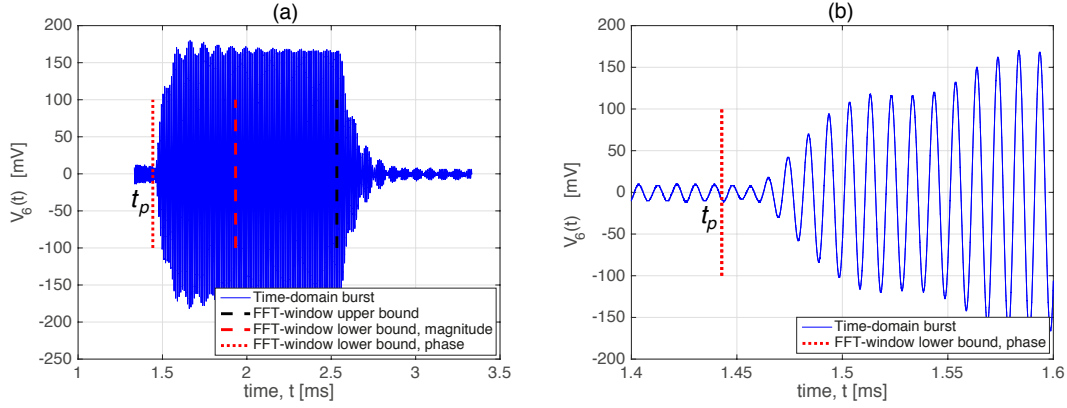


Figure 3.11: (a) example of a recorded electrical pulse with the FFT-window bounds denoted in the legend. (b) a close up of (a) showing the estimate of the arrival of the plane wave component,  $t_p$ .

### Estimation of phase spectra for $V_6$

When estimating the phase spectra of the slowly varying phase,  $\angle V_6^{slow}$ , of the recorded acoustical burst,  $V_6$ , the FFT-window is no longer referred to the steady-state part of the recorded signal. Instead, the lower bound of the FFT-window is attempted to be positioned in the onset of the arrival of the plane wave component, c.f. Sec. 2.2. The estimate of the arrival of the plane wave component is

$$t_p = \frac{d}{c(f)} \quad (3.5)$$

where  $t_p$  is the time the plane wave component has propagated given a separation distance  $d$ , c.f. Sec. 3.4 and a speed of sound  $c(f)$ .  $c(f)$  is the frequency dependent speed of sound accounting for dispersion, c.f. Sec. 2.3.

In Fig. 3.11 (a)  $t_p$  is indicated next to the red dotted line, and in (b) the onset of the signal is magnified. In (b) it is observed that the estimate of the plane wave component,  $t_p$ , is placed before any noticeable change in the recorded voltage is observed. This is explained by inertia and a low sound pressure, such that several signal periods are needed before any discernible output voltage is observed. The upper bound of the FFT-window used for phase calculations is identical as that for magnitude, indicated in Fig. 3.11 (a) as the stippled black line.

Given the FFT-window's lower bound is placed in  $t_p$  and the FFT-window's upper bound is placed in a zero crossing, a sub-signal is extracted from the time-domain burst. A zero-padded signal,  $V_{pad}^{zro}(t)$ , is obtained by appending zeros to the sub-signal and the complex spectrum of the zero-padded time burst,  $V_{pad}^{zro}(t)$ , is estimated by Eq. 3.3. The phase spectrum of the slowly varying phase is estimated by

$$\angle V_6^{slow}(f_{FFT}) = atan\left(\frac{V_{Im}(f_{FFT})}{V_{Re}(f_{FFT})}\right) \quad (3.6)$$

where  $\angle V_6^{slow}(f_{FFT})$  denotes the slowly varying phase spectrum,  $atan$  is the inverse of the trigonometric function tangent,  $V_{Re}(f_{FFT})$  and  $V_{Im}(f_{FFT})$  denotes the real and imaginary parts of the complex spectrum, respectively. The phase value corresponding to the drive frequency,  $f_d$ , is located in  $\angle V_6^{slow}(f_{FFT})$ , i.e.

$$\angle V_6^{slow}(f_d) = \angle V_6^{slow}(f_{FFT} \equiv f_d) \quad (3.7)$$

where  $\angle V_6^{slow}(f_d)$  denotes the phase corresponding to the single frequency component  $f_d$ . If the frequency components of  $f_{FFT}$  do not correspond with  $f_d$ , the phase  $\angle V_6^{slow}(f_d)$  is obtained by linear interpolated between the two surrounding frequencies in  $\angle V_6^{slow}(f_{FFT})$ .

### Estimation of phase spectra for $V_{0m}$

The estimation of the phase spectra  $\angle V_{0m}$  is similar to that of  $\angle V_6^{slow}$  with the one exception being that the FFT-window's lower bound is placed in  $t = 0$ .

#### 3.5.1 FFT-window effect

In [1, 2] a rectangular FFT-window was placed at a constant position for all frequencies under investigation. The position of the window was determined empirically from observation in the time-domain [1, 2] and in the frequency domain with the aid of a spectrogram plot [3]. However, it is observed that a constant rectangular window results in so-called spectral leakage. Spectral leakage comes about when the signal contained within the FFT-window is not periodic, i.e. the number of periods contained within the FFT-window are not an integer number such that the signal exhibits discontinuities at the boundaries of the window [94]. To handle this, windows of different types can be used. But applying a windowing function leads to handling of corrections due to the window itself [95]. Thus, a quadratic window, which requires no such handling, seems like a good place to begin.

In the present work, an algorithm to position the rectangular FFT-window in the zero crossings of the signal has been developed. The algorithm works as follows:

- For the time domain signal under investigation, define lower and upper boundaries for the FFT-window. At this point the boundaries are random with respect to the zero crossings, but should still be positioned where the signal is assumed to have obtained steady-state conditions.
- A list of all the zero crossings of the signal is generated. This is done using the MATLAB function `crossing.m`.<sup>4</sup>
- Given the lower and upper boundaries of the rectangular FFT-window, the first positive peak within one period of the boundaries are located.
- Using the generated list of zero crossings, the first zero cross before the positive peak is located.

This process ensures that the window boundaries are fixed in a zero crossing. Furthermore, if the SNR is large, i.e. a strong signal is under investigation, the algorithm finds an integer number of periods contained within the window. However, if the SNR is low non-integer number of periods might be contained within the window.

In Fig. 3.12 the procedure in [1, 2], denoted *random*, is compared to the procedure developed in the current work, denoted *zero*. In (a) and (b) the magnitude of the recorded voltages  $V_{0m}$

<sup>4</sup> `crossing.m` is written by Steffen Brueckner, 2002-09-25, revised in 2007-08-27. The function has in part been revised by, and is available to download at, MATLABCENTRAL File Exchange: <http://www.mathworks.com/matlabcentral/fileexchange/2432-crossing/content/crossing.m>

and  $V_6$ , respectively, are given. The recording have been performed using the following settings: Measurement distance: 0.5 m. Measurement burst time,  $b_t = 1$  ms. Sampling rate: 100 MS/s. Frequency range: 10-300 kHz.  $V_{gen} = 10$  V. Transmitter: element 11. Receiver: element 04. FFT-window lower boundary: 50.000. FFT-window upper boundary: 80.000.

The blue curves are found using the MATLAB function `findPeakToPeak_FFT.m` given in [1, 2] and the red curves are found using the procedure developed in the current work, the corresponding MATLAB script, `findPeakToPeak_FFT_k.m`, is found in the Appendix B.1.1.

In Fig. 3.12 (a) the largest deviation between the two procedures is observed. This is due to the strong SNR experienced in the electric signal such that any discontinuities at the boundaries of the FFT-window becomes significant. In the acoustic signal, however, where the noise level might be more prominent than the discontinuities, the effect of the discontinuities seem to be less dominant. However, even in the acoustic signal a difference is observed. This is magnified in (b) where we see periodic undulations, which is the expected result given a constant rectangular window size and a signal with a changing frequency.

At e.g. 145 kHz the frequency step is reduced. A reduction in the frequency step is sometimes performed to reduce measurement time. In Fig. 3.12 (a) the effect of changing the frequency step is apparent for the blue curve. This is magnified in the center of the figure. Although not clear from the figure, the blue fuzzy area is strictly periodic. Magnified in the lower left hand side of (a) the strict periodicity is better observed. These strict periodic fluctuations are not observed for the red curve.

In Fig. 3.12 (a) for the range 10–50 kHz, random, fluctuations are observed for the blue curve. This is explained by an increase in the period time as the frequency decreases. Thus, fewer and fewer signal periods will be contained within the FFT-window and any discontinuities at the boundaries will become more prominent. At the lower frequency bound where  $f = 10$  kHz there is only 10 periods contained within the whole signal. Furthermore, since the lower and upper boundaries on the FFT-window is 50.000 and 80.000, respectively, there is approximately only 3 signal periods contained within the FFT-window. It is observed that the fluctuations are not present in the red curve.

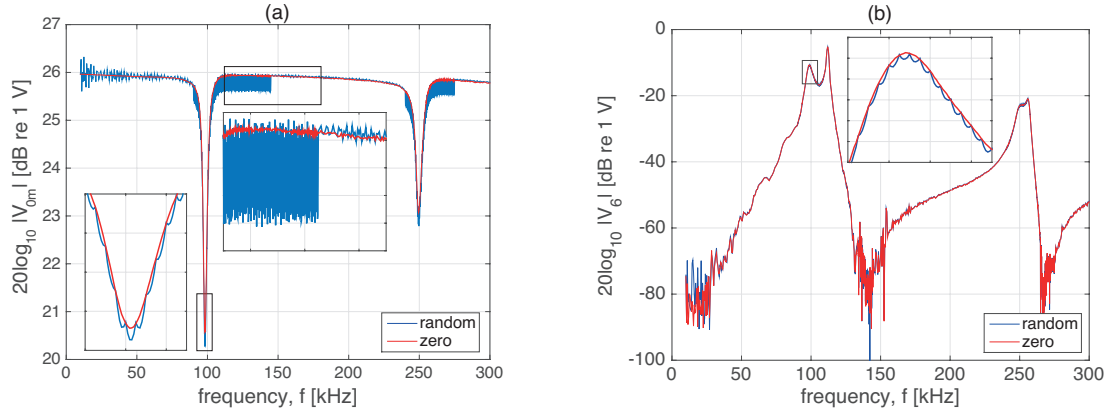


Figure 3.12: Example of the effect the rectangular FFT-window has on measurements. (a) magnitude of the recorded electric signal,  $|V_{0m}|$ . (b) magnitude of the recorded acoustic signal,  $|V_6|$ . For both (a) and (b) the blue curve represents a random placement of the FFT-window whereas the red curve shows the effect of placing the windows lower and upper boundaries in a zero crossing.

### 3.6 Phase considerations

In the current section several factors that are important in obtaining the slowly varying phase of the transfer function will be discussed.

### 3.6.1 Effect of sound speed on post-processing of slowly varying phase

The sound speed used as an input to the material file in FEMP is not used directly as the sound speed during simulations [49]. Rather, the sound speed used during simulations is calculated from the quantity  $\beta = \rho_0 c^2$  where  $c$  is the input sound speed provided by the user when the material file is created, and  $\rho_0$  is the density of air. The sound speed itself is not stored in the material file. The two quantities that are stored in the material file are  $\beta$  and  $\rho_0$ .

The rest of the discussion is better appreciated with a numerical example. Given an input sound speed of  $c = 343$  m/s and an air density of  $1.205$  kg/m<sup>3</sup>, then  $\beta = 141767$  kg/ms<sup>2</sup>. Using  $\beta$  to calculate the speed of sound, we obtain  $c = 342.9999455620972$  m/s.

The small deviations in the input sound speed versus the sound speed used during simulations become a factor when the simulated quantity, e.g.  $p_4$ , is obtained in the far-field. The far-field simulation distance,  $z_{ff}$ , in the current thesis is set to  $1000$  m. To obtain the slowly varying phase, the plane wave component,  $k \cdot z_{ff}$ , is corrected for in the accumulative phase, i.e.  $\angle p_4^{slow} = \angle p_4 + k \cdot z_{ff}$ .

In Fig. 3.13 the effect of using the input sound speed in the post-processing calculations (red dashed) versus the exact simulation sound speed (blue) is exemplified. The example is given for the slowly varying phase  $\angle H_{15open}^{VV}$ . Note that the exact value for  $c$  stated above is used in the calculations. It should also be mentioned that using the approximate sound speed in the legend will result in deviations in approximately the same order of magnitude as the deviations observed in Fig. 3.13.

There is clear linear dependency of the deviation with respect to frequency. This is understood by the  $k \cdot z_{ff}$  term. If the sound speed used to determine  $k$  is slightly wrong, but constant, then the deviations should increase with increasing frequency. Which is what is observed. For  $f = 100$  kHz a deviation of  $33^\circ$  is observed, and for  $f = 225$  a deviation of approximately  $75^\circ$  is observed.

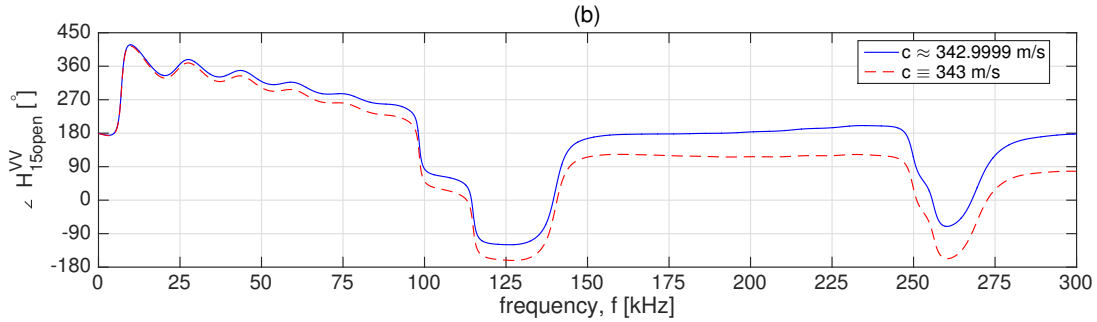


Figure 3.13: Example of the simulated slowly varying phase of  $H_{15open}^{VV}$  for element 07 where two different values for the speed of sound has been utilized. The simulation is performed at a far-field distance  $z_{ff} = 1000$  m. The approximate distance in the legend is not used in the calculation, and should also not be used. Rather the exact values stated in the text should be used when calculating the slowly varying phase.

### 3.6.2 Wrapped phase spectra and implications for measurement of slowly varying phase

The associated phase spectra obtained by the Fourier transform is referred to as the wrapped phase spectra. The word "wrapped" refers to the phase range possible to obtain directly by the Fourier transform, which is  $\pm\pi$  or  $\pm 180^\circ$ . In the current section the implication of this for the measurement set up used in the current thesis will be discussed. It will be shown that without the aid of FE-simulations, the phase angle would have an offset of  $360^\circ$ .

To aid in the discussion, a definition of the phase ranges experienced is deemed helpful. The phase range  $\pm 180^\circ$  is denoted the principal phase range. If the phase angle exceed this value, i.e. the phase angle is in the range  $180-540^\circ$ , this is denoted the first positive phase range. Similarly, if the phase angle recedes the principal phase range, i.e. the phase angle is in the range  $-180- -540^\circ$ , this is denoted the first negative phase range. Formally, this can be states as

$$\theta = \theta_w + N_w \cdot 2\pi, \quad N_w = 0, \pm 1, \pm 2, \dots, \pm\infty \quad (3.8)$$

where  $\theta$  is the "true" unwrapped phase angle corrected for possible deviations from the principal phase range,  $\theta_w$  is the wrapped phase as obtained by the Fourier transform, and  $N_w$  is an integer accounting for the number of  $2\pi$  multiples the wrapped phase deviates from the unwrapped phase.

In Fig. 3.14 (a) the slowly varying phase,  $\angle V_6^{slow}$  of the recorded and simulated voltage  $V_6$  is given. The simulation of  $V_6$  requires that the correction terms discussed in Sec. 2 are applied to the simulated quantity, rather than the measured quantity. It should be sufficient to state that the comparison of the two quantities in Fig. 3.14 (a) are performed for identical nodes in the system model. The simulation is performed in the frequency domain, such that no transformation to obtain the frequency response of the simulated quantity is necessary, thus in Fig. 3.14 (a) the simulated angle, exhibits no wrapping. The two quantities that are being compared are thus of different spectra, namely the wrapped spectrum (measurement) and spectrum (simulation).

The simulation has been performed from  $f = 1$  Hz, while the measurement has commenced from  $f = 10$  kHz. The horizontal black stippled lines indicate the  $\pm 180^\circ$  limits. For the lower frequencies, the measured phase angle exhibits a great deal of noise (10–30 kHz). The phase angle in this range is deemed to be associated with that of the noise, and not of the signal,  $V_6$ . Thus, the phase angles in this range should not be used for unwrapping, for discussion on unwrapping in noisy environments c.f. Sec 3.6.3.

For the lowest frequency,  $f = 1$  Hz, the simulated phase angle is located in the principal phase range at approximately  $+90^\circ$ . No significant change occurs before approximately 5 kHz. In between 5–10 kHz the simulated phase exceed the principal phase range and is located in the first positive phase range until approximately 50–52 kHz. At 50–52 kHz the simulated phase recedes back to the principal phase range.

Exceeding 30 kHz the measured phase angle  $\angle V_6^{slow}$  seems to be able to discern from that of the noise, and comparing the phase angles of the simulation and the measurement for the frequency range 30–50 kHz, it is observed that the measured phase angle is approximately  $360^\circ$  lower in value.

When the frequency exceed that of 50–52 kHz, a shift of  $+360^\circ$  is observed for the measured phase angle, as the simulated phase angle returns to the principal phase range, and a fair agreement between the simulated and measured phase angle is observed.

The agreement seems to hold until approximately 110–115 kHz where, again, the measured phase angle shifts with  $+360^\circ$  as the simulated phase angle decrease to the first negative phase range. When the simulated phase returns to the principal phase range, at approximately  $f = 140$  kHz, the measured phase shifts by  $-360^\circ$ , and the effect of the positive and negative phase shifting have canceled each other out.

Returning to the low frequency range, and the simulated phase, it was observed that the phase angle exceeded the principal phase range between 5–10 kHz, and was located in the first positive phase range until approximately 50–52 kHz. Any excess of the simulated phase angle from the principal phase range to the first positive phase range, should be associated with a negative phase shift of the measured phase angle. However, as already discussed, reliable phase measurement lower than  $\approx 30$  kHz, do not seem possible. Thus, to compensate for the lack of a measurement in the lowest frequency ranges, the phase angle have to be corrected with  $+360^\circ$ . The positive sign is to compensate for the expected negative phase shift associated with the simulated phase exceeds the principal phase range at 5–10 kHz.

In Fig. 3.14 (b) the effect of unwrapping the measurement in (a) is shown. The unwrapping has been performed from  $f = 30$  kHz, avoiding the noisy frequency range. The red stippled line is uncompensated for the expected  $-360^\circ$  offset, while the red solid line is compensated for the offset by adding  $+360^\circ$  to the unwrapped value. Clearly, the red solid line shows fair agreement with the simulation.

### 3.6.3 Unwrapping in noisy environments

All unwrapping of phase angles in the current thesis is performed using the inbuilt MATLAB function `unwrap`. The unwrapping is performed by looking at the absolute deviations between neighboring values of the phase angle. If a deviation larger than  $|180|^\circ$  is observed a multiple of  $\pm 360^\circ$  is added or subtracted to the remaining phase angles.

It is, however, not uncommon for noise to be associated with large phase jumps. Any unwrapping in these noisy frequency ranges is deemed unfavorable and should be avoided. In the



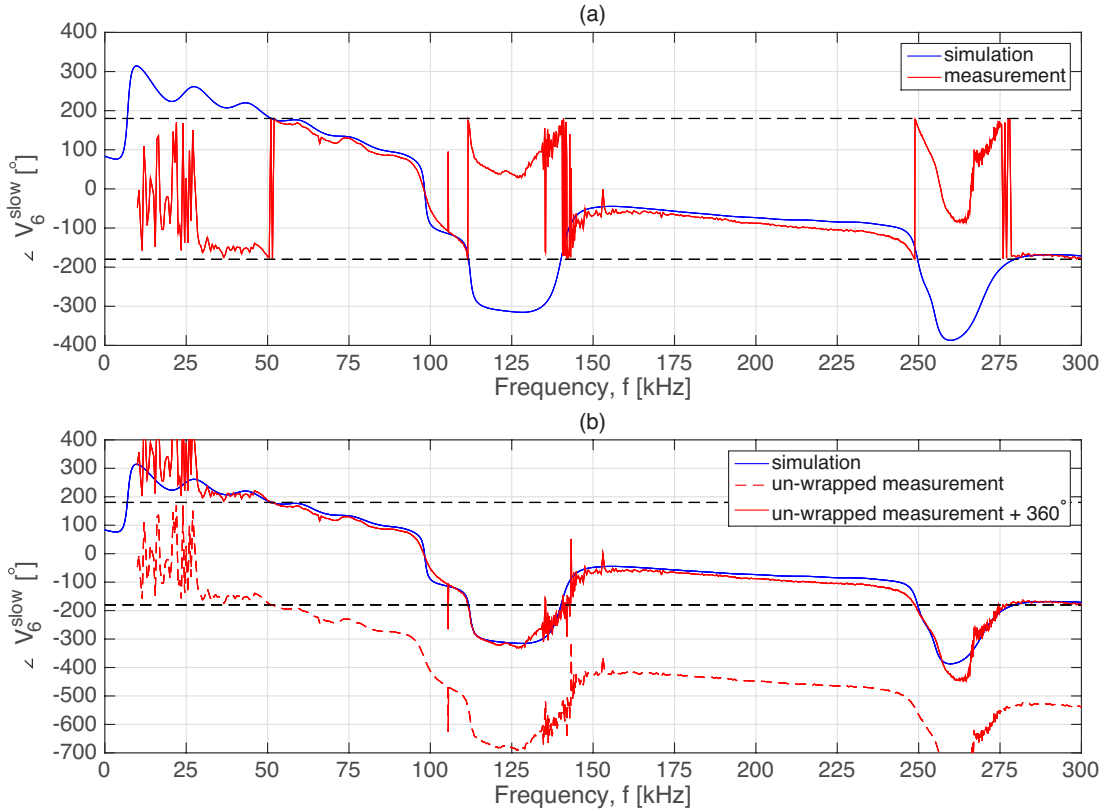


Figure 3.14: (a) example of the slowly varying phase  $\angle V_6^{slow}$  for simulation (blue) and measurement (red). The measurement is shown in the wrapped-phase spectra. (b) simulation (blue) identical as in (a), red stippled line shows the uncompensated, unwrapped phase angle  $\angle V_6^{slow}$ , red solid line shows the compensated unwrapped phase angle  $\angle V_6^{slow}$ . Compensation is performed by adding  $+360^\circ$  to the unwrapped phase angle.

frequency ranges up to 30 kHz, between 135–145 kHz, and 260–375 kHz the phase angle is observed to be quite noisy, and possible deviations larger than  $|180|^\circ$  can be observed. These deviations can sometimes be attributed the noise and not the signal. The result of this is that unwrap adds or subtracts one or more multiple(s) of  $\pm 360^\circ$  "wrongfully" to the remaining phase values.

Moreover, in the frequency ranges  $\approx 135$ –145 kHz, and  $\approx 260$ –275 kHz, the phase angle exhibits a steep incline. If the frequency resolution in these ranges are too great, then, regardless of any contribution from noise, the difference between two neighboring phase angles can be quite large. Thus, in the presence of noise, both these factors can together result in a false deviation between neighboring phase angles larger than  $|180|^\circ$ .

One attempt to resolve this is to increase the frequency resolution in the noisy frequency ranges. A frequency resolution of 100 Hz is observed to be sufficient such as not to experience any  $\pm 360^\circ$  offsets for  $d = 0.50$  m. However, at  $d = 0.85$  m  $\pm 360^\circ$  offsets are still a challenge.

### Unwrapping scheme

To resolve the challenges with the unwrapping in the noisy ranges, an unwrap scheme has been used: If an offset of  $\pm 360^\circ$  (or larger) in the slowly varying phase,  $\angle V_6^{slow}$ , is observed, and this offset occurs in the noise, the remaining phase values will be referenced to a phase value just prior to the noise.

Let  $A_w = [a_1, a_2, \dots, a_n]$  be a vector which represent the wrapped phase values, and  $n$  is an integer equal to the length of  $A_w$ . Let  $a_{10}$  and  $a_{11}$  represent the frequency ranges associated with noise. Then, in pseudocode,

$$\begin{aligned}
A_{uw1} &= \text{unwrap}(a_1, a_2, \dots, a_{11}) \\
A_{unw2} &= \text{unwrap}(a_9, a_{12}, \dots, a_n) \\
&\text{delete entry } a_9 \text{ from } A_{uw2} \\
A_u &= [A_{un1}, A_{unw2}]
\end{aligned} \tag{3.9}$$

where  $A_{uw}$  is a vector with length equal to  $A_w$ , the square braces,  $[\ ]$ , denote concatenation of the two vectors  $A_{uw1}$  and  $A_{uw2}$ . The implication of this scheme is that  $a_{12}$  is hereby referred to an unwrapped value not associated with noise. To use this scheme it is imperative that the expected value of  $a_9$  and  $a_{12}$  are located within the principal phase range or the same sub-phase range.

It should be noted that this scheme is only necessary to execute if there are observable  $\pm 360^\circ$  offsets stemming from a noisy frequency range. To be specific, in Sec. 6.5.2 where 16 measurements on the transfer function  $H_{15open}^{VV}$ , for  $d = 0.50$  m, are presented, only four measurements had to be corrected thus.

## 3.7 Noise analyses

Due to the piezoelectric disks operating with the electrodes exposed, it is observed that disks are rather susceptible to electrical energy, as well as acoustical energy. This was investigated by the current author in [96] for two separation distances  $d = 0.40$  m and  $d = 0.77$  m. Some of the discussion in [96] will be repeated here.

The acoustical measurements are associated with three types of noise, 1) random noise, 2) incoherent periodic noise, and 3) coherent noise. These will be briefly discussed below.

### 3.7.1 Random and incoherent periodic noise

Random noise is defined as any disturbance that is not associated with the transmitted signal and which do not exhibit any kind of periodicity. This can be of either acoustical or electrical origin [62]. If the noise is strictly random, it will be removed by averaging. Random noise can originate in the measurement equipment itself e.g. as thermal noise [97].

However, the noise in a measurement set-up will generally not tend to zero, regardless of the amount of averaging. The energy that still present after enough averaging is performed, which can not be attributed to the transmitter, will be referred to as incoherent periodic noise. An example of this can be vibrations in the foundation leading to vibrations in the transmitter or receiver.

No attempts to distinguish the random noise from the incoherent noise has been performed, and for the remainder of the thesis, the noise spectrum for both random and incoherent noise will be denoted  $V_r = V_r(f)$ . Measurements to determine  $V_r$  has been performed by setting  $V_{gen} = 0$ , and the recorded noise is transformed to the frequency domain according to Sec. 3.5. Note that the FFT-window is placed at exactly the same place as it would be for  $V_6$ . Measurements on  $V_r$  has shown that the noise level is approximately -90 dB to -80 dB.

### 3.7.2 Coherent electrical noise

Coherent noise is defined as any undesired disturbance [62] of either electrical or acoustical origin that exhibits periodicity. In the current section, only electrical coherent noise will be discussed. In Sec. 3.8 acoustical coherent noise is discussed.

The coherent electrical noise originates in the transmitting disk which sets up an electrical field when the sinusoidal signal,  $V_1$ , is present at the terminals of the disk. The noise spectrum for the coherent electrical noise is denoted  $V_c = V_c(f)$ .

To investigate the coherent electrical noise a technique to separate the coherent electrical noise from the signal is introduced. A 5 mm thick acrylic plate is mounted in between the transmitter and receiver to block the acoustical signal from propagating to the receiver. An image of the set up is shown in Fig. 3.15 (a) where orange dashed lines are drawn around its edges to better appreciate the acrylic plate. In the image, a Faraday shield is also seen. This is discussed in Sec. 3.7.3. The recorded energy can thus not be associated with the acoustical signal. In Fig. 3.15

(b) two recordings of the coherent electrical noise is given. The two blue curve corresponds to a recording where the Faraday shield is not used. It is observed that the coherent noise is largest around 112 kHz. This corresponds to the frequency where the piezoelectric disk is most sensitive as a receiver.<sup>5</sup>

The acrylic plate is attempted to be positioned as far away from the transmitter as possible, such as not to induce standing waves in between the transmitter and acrylic plate. It is thought, but not investigated, that standing waves might interfere with the transmitter and alter the electric field.

### 3.7.3 Measurement scheme to reduce coherent noise

To reduce the magnitude of the coherent electrical noise the current author in collaboration with Søvik [3] introduced cylindrical Faraday shields to the acoustical measurement set up. In Fig. 3.15 (a) behind the acrylic plate the Faraday shield for the receiver is shown. A similar Faraday shield is used for the transmitter (not shown). Each Faraday shield is of approximate diameter 0.40 m and 0.50 m, with a length of 0.19 m and 0.37, respectively. The former Faraday shield has a meshing of approximate size 4x4 mm, while the latter has a meshing of approximate size 12x12 mm. The use of different meshing sizes are due to available materials at location. Both shields are made of galvanized steel netting that are conductors, and both shields are grounded during measurements.

In Fig. 3.15 (b) a measurement on the coherent noise,  $V_c$ , is given. The measurement has been performed using the acrylic plate. The measurement has been conducted at  $d = 0.50$  m, with  $V_{gen} = 10$  V.

The red curve, corresponding to a measurement with the Faraday shield, is approximately 15 dB lower in value then the blue curve which corresponds to a similar measurement performed without the Faraday shield. It is observed that for the lower frequencies,  $f < 90$  kHz, the noise level is approximately -90–-80 dB. Similar to that of random noise. This is understood by the piezoelectric disk is not susceptible to electric energy in this frequency range.

It is thus seen that by using the Faraday shield the coherent electrical noise is reduced in the frequency range 100–125 kHz, but outside of this frequency range the Faraday shield do not seem to have much impact on the measurements.

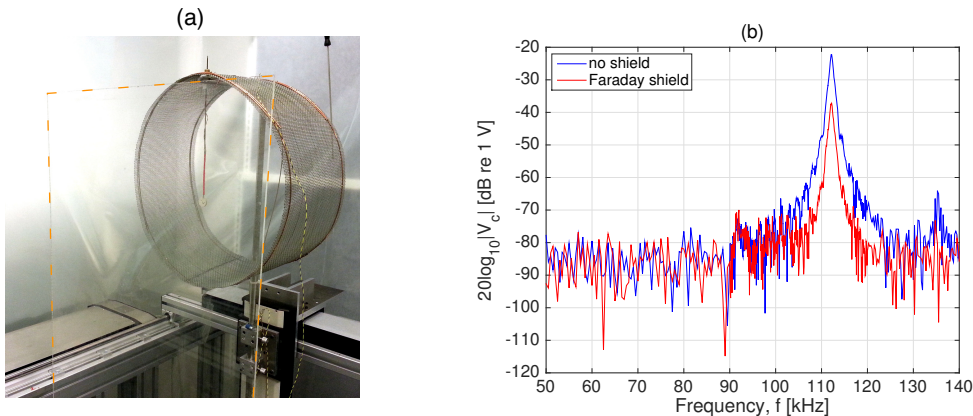


Figure 3.15: (a) image showing the Faraday shield surrounding the receiver and the 5 mm plexiglass plate mounted in front of the receiver, (b) coherent noise,  $V_c$ , for a separation distance of 0.50 m and a generator voltage  $V_{gen} = 10$  V with (red) and without (blue) the use of the Faraday shield.

In Fig. 3.16 the effect of the Faraday shield on the frequency 112 kHz is investigated. The figures can be difficult to understand, such that an ample explanation will be provided.

At  $t = 0$  the generator voltage,  $V_{gen}$ , is turned on. The receiver is placed 0.50 m from the transmitter and the transmitted sound waves uses  $t \approx 1.4$  ms to arrive at the receiver. This is indicated in both figures with the vertical stippled line.

<sup>5</sup>To be precise, the frequency where the piezoelectric disk is most sensitive as a receiver is approximately 114.8 kHz. However, the recordings shown in Fig. 3.15 (b) are uncorrected, i.e. it is the recorded voltage  $V_6$ , such that the deviations are explained by the measurement equipment's influence on the signal.

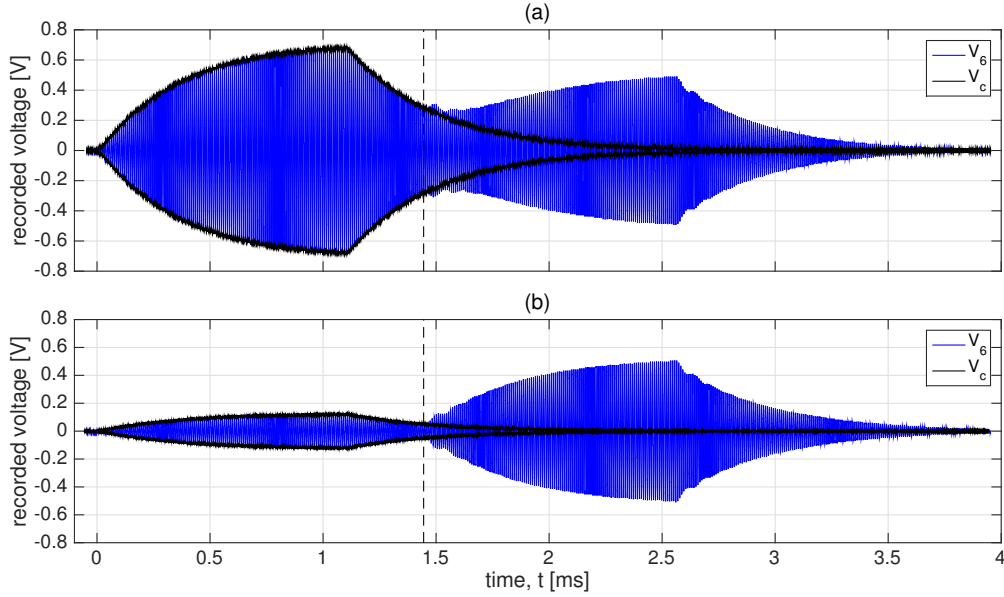


Figure 3.16: Examples of recorded bursts for  $f = 112$  kHz,  $d = 0.50$  m. For (a) and (b) the blue curve represents the recorded voltage  $V_6$ , and the black curve represents the enclosure curve of the recorded coherent noise,  $V_c$ . The vertical black stippled line denotes the estimate of the onset of the acoustical signal. In (a) the Faraday shield has been utilized, while not in (b).

In both figures, two recordings are presented.  $V_6$  is recorded without the use of the acrylic plate, and  $V_c$  is recorded using the acrylic plate.  $V_c$  is shown as the Hilbert enclosure curve to better appreciate how  $V_6$  and  $V_c$  are overlapping until  $t \approx 1.4$  ms. The recorded energy in the range  $t = 0$  to  $t \approx 1.4$  ms is associated with electrical coherent noise. At  $t \approx 1.4$  ms the sound waves are perceived by the receiver.  $V_6$  then diverge from  $V_c$ .

The difference between Fig. 3.16 (a) to (b) is that the Faraday shield has been used in (a) while not in (b). Comparing the magnitude of the coherent electrical noise from (a) to (b) at  $t = 1.1$  ms a reduction from 0.7 V to 0.2 V is observed. And at  $t = 2$  ms the coherent electrical noise in (b) is almost reduced to zero, whereas in (a) is still has a significant magnitude at  $t = 2$  ms. The last point is important since this is where the FFT-window's lower bound would be placed. Thus, the influence of the coherent electrical noise in (b) on the spectra is expected to be less than in (a).

### 3.7.4 Signal to noise ratio, SNR

The signal to noise ratio (SNR) is an important ratio in a measurement system as it yields information about the strength of the signal compared to the intrinsic noise present in the system, or in the measurement itself. The SNR discussed in the current thesis is actually that of signal-plus-noise to noise ratio [4], and is given by

$$\begin{aligned} \text{SNR}_r &= 20 \log_{10} \left( \frac{V_6}{V_r} \right) \\ \text{SNR}_c &= 20 \log_{10} \left( \frac{V_6}{V_c} \right) \end{aligned} \quad (3.10)$$

where  $\text{SNR}_r$  is the signal to noise ratio given random and incoherent periodic noise, and  $\text{SNR}_c$  is the signal to noise ratio given coherent electrical noise.

### 3.8 Determining minimum burst length required for steady-state conditions

Two factors contribute to the choice of burst length used during measurements: separation distance between transmitter and receiver and coherent noise.

As shown in Sec. 6.3 the magnitude of the coherent noise can be significant. In addition to using a Faraday shield, the coherent noise can be reduced by either moving the transmitter and receiver further apart, this is shown in Sec. 6.3.2, or by reducing the burst length. However, reducing the burst length might result in a lack of steady-state conditions, and moving the transmitter and receiver further apart is associated with a decrease in SNR, as well as the physical limitations in the laboratory.

The optimal burst length should allow for steady-state conditions while minimizing the coherent noise.

#### Interference from suspension

Measurements have shown that reflections from the receiver suspension will influence the received bursts with constructive and destructive interference. The distance between the receiver and the part of the suspension where the reflections occur is approximately 0.19 m, and the sound waves have to travel twice this length to be perceived by the receiver for the second time. This double length corresponds to a burst time,  $b_t$ , of approximately 1.1 ms. This value for  $b_t$  is used throughout the thesis.

#### Time domain investigation of number of burst cycles

In Fig. 3.17 four time-domain bursts obtained with different burst times are given for two frequencies, (a) 100 kHz, and (b) 112 kHz. The bursts are given as the Hilbert transformation, yielding only the envelope curves. For both frequencies the burst times are 0.4 ms, 0.8 ms, 1.2 ms and 1.6 ms. In both figures, the number of burst cycles are indicated next to the respective curves. The vertical dashed line corresponds to a burst time of 1.1 ms.

Clearly, in (a) the receiving transducers transient response dies out much faster than in (b). Moreover, in (b), it seems that the transient response does not die out before after the dashed line. Also noticeably, is the coherent noise in (b). The blue curve which correspond to a burst length of 180 cycles is visibly higher in amplitude at the onset of the received burst compared to the lilac curve. If the separation distance were reduced the coherent noise observed in (b) would be higher.

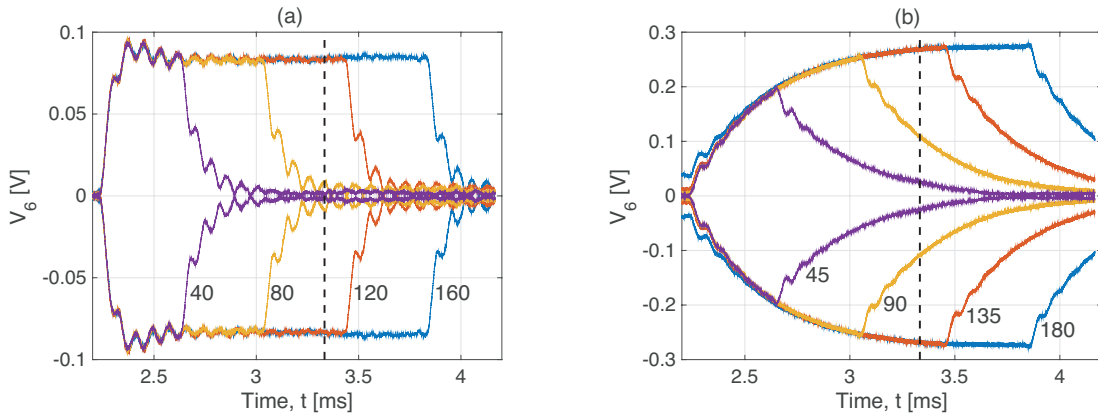


Figure 3.17: Four different bursts for two different frequencies, (a) 100 kHz, (b) 112 kHz. The numbers in both figures denote the number of burst cycles used during measurement.

#### Frequency domain investigation of steady-state conditions

In the current section steady-state conditions of the received acoustic burst are investigated in the frequency domain. The investigation is performed using a burst time of 1.1 ms, and the frequencies

under investigation is 100 and 112 kHz. The burst time 1.1 ms is used throughout the thesis.

To aid in the analysis a method to swipe the rectangular FFT-window over the time domain burst has been developed: The lower bound of the FFT-window is placed in a zero crossing close to the onset of the signal, and the FFT-window's upper bound is placed in a zero crossing an integer number of signal periods later. The FFT is then computed, and the window is moved one signal period later in time. The FFT is again computed. This process is repeated until the FFT-window's upper boundaries exceed the length of the signal.

The result of such a swipe is given in Fig. 3.18 where in (a)  $f = 100$  kHz, and in (b)  $f = 112$  kHz. In both (a) and (b) four integer number of signal periods are plotted for each frequency: 10, 20, 40 and 60 signal periods<sup>6</sup>. The time on the x-axis refers to where the FFT's lower boundary was positioned. The dashed line is inherited from 3.17.

In Fig. 3.18 (a) it is observed that all curves tend to the same value, though there are deviation. The general observation is that a longer FFT-window yields less fluctuations. This indicates the use of a longer FFT-window to reduce the fluctuations, however a FFT-window shorter than 60 signal periods can be applied.

In Fig. 3.18 (b) it is observed that the lilac curve do not converge, rather a parabola with a distinct peak is observed. The curve that seems to converge most is the blue curve, which contain only 10 signal periods. However, neither this has converged. This implication of this is that a longer burst should be used. However, applying a longer burst will result in reflections from the suspension, as discussed in Sec. 3.8.

The conclusion therefore is that the suspension should be made longer, allowing for longer burst without resulting in reflections. However, increasing the burst length will increase the coherent noise. Note that these changes have not been implemented during the current work. Thus deviations from steady-state conditions might exist, especially at 112 kHz.

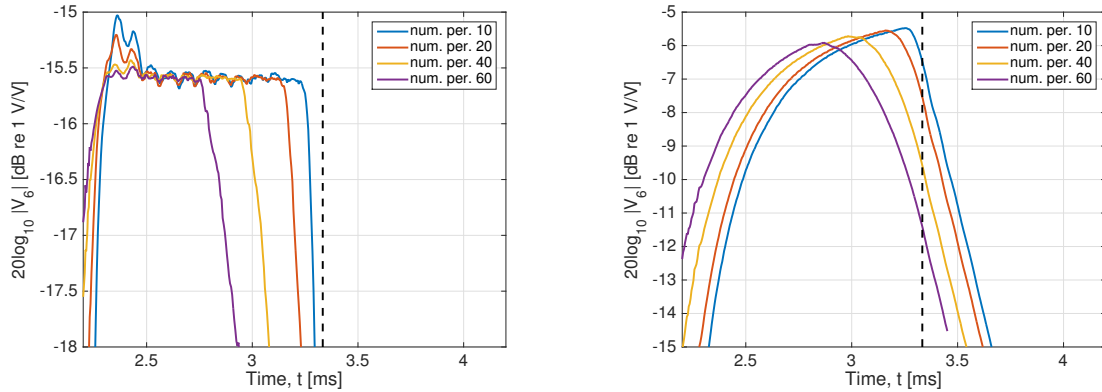


Figure 3.18: Examples of a frequency swipe for (a) 100 kHz, and (b) 112 kHz. In both (a) and (b) a signal corresponding to a burst time of 1.1 ms is used. The integer number of signal periods contained within the FFT-window is denoted in the legends.

## 3.9 Electrical measurements

In the current section the impedance measurement method performed with a commercial impedance analyzer, the HP 4192A impedance analyzer [69], and the impedance measurement method performed with an oscilloscope, will be presented. The measurements performed on the amplifier and filter to determine the transfer function  $H_{5'6open}^{VV}$  will also be presented.

### 3.9.1 Impedance measurement

The impedance of the piezoelectric transmitter and receiver are input parameters to the correction terms  $H_{0m1}^{VV}$  and  $H_{5open5'}^{VV}$ , respectively. The implication of this is that the accuracy of the correction

<sup>6</sup>A burst time of 1.1 ms corresponds to 60 and approximately 70 signal periods being contained within the FFT-window for 100 kHz and 112 kHz, respectively.



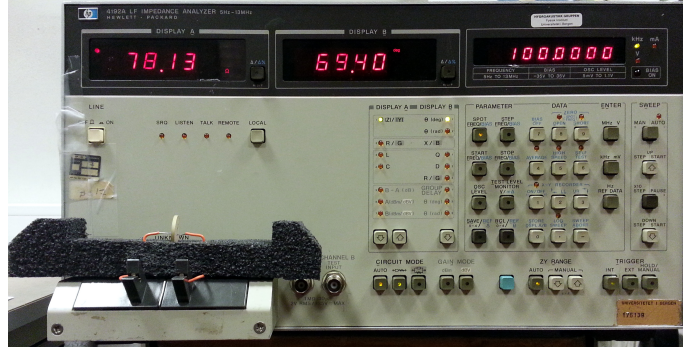


Figure 3.19: Image of the HP-impedance analyzer. On the left the black styrofoam holder is seen with a piezoelectric disk in place for measurement. The orange cables are connecting the electrodes of the disk to the in- and output terminals of the analyzer. The zero offset adjustment is, in this case, performed on the orange cables, such that the impedance associated with these are compensated for during measurement.

terms are dependent on the accuracy of the estimate of the impedance of the piezoelectric disk.

The impedance of the piezoelectric disks are measured with a HP 4192A impedance analyzer [69], referred to as the HP. The measurements have been performed as either conductance,  $G_T$ , and susceptance,  $B_T$ , or as the magnitude of the impedance,  $|Z_T|$ , and corresponding phase angle,  $\theta_T$ . The equations used to obtain the complex impedance are:

$$Z_T = |Z_T|e^{i\theta_T} = \frac{1}{Y_T} = \frac{1}{G_T + iB_T} \quad (3.11)$$

The HP is connected to the laboratory PC via a General Purpose Interface Buss (GPIB) and a USB interface. A MATLAB script `impanel.m`<sup>7</sup> is used to record and save the impedance measurements. The instrument is allowed a warm up time of minimum 30 minutes before use. A styrofoam holder has been cut out of available material, and a small indent is used to keep the piezoelectric disk in place, c.f. Fig. 3.19, and approximately 5 cm semi-stiff wires are pushed onto both sides of the elements. If the wires have been soldered onto the electrodes of the disk, the impedance measurements have been performed through the wires.

### Zero offset adjustment

Prior to measurements the HP-impedance analyzer is adjusted for possible impedance offset associated with the cables connecting the in- and output terminals of the impedance analyzer to the terminals of the piezoelectric disk. The zero offset is performed according to [69] utilizing a frequency of 1 MHz, and is conducted for both open-circuit and short-circuit conditions.

### 3.9.2 Impedance measurements with oscilloscope

In the present section a method to measure the impedance of a piezoelectric disk with an oscilloscope, a function generator and resistors of various impedance will be presented. In Sec. 2.11 the equations and motivation for this investigation was given.

The measurements have been performed on element 13 with cables soldered onto the electrodes. The measurements have been performed through the cables, such that the impedance are not necessarily valid for a free-standing piezoelectric disk. The signal processing is performed according to Sec. 3.5 such that the FFT is used to obtain both the magnitude and phase of the recorded voltages.

In Fig. 3.20 (a) the laboratory set-up is shown. The measurement set-up consist of a function generator (not shown in the image) connected to input channel 1 of the oscilloscope, a resistor,  $Z_{res}$ , connected to both input channels of the oscilloscope, and the piezoelectric disk connected to input channel 2. The resistor is connected in series with the piezoelectric. Connecting the resistor thus simplifies the set-up as no corrections for cables are necessary. The resistors are soldered onto the BNC-connectors, and in Fig. 3.20 (a), top right, a close up of one of the resistors is shown.

<sup>7</sup>`impanel.m` is documented in e.g. [1–3]

Three different resistors, 10, 100 and 1000  $\Omega$ , have been used for  $Z_{res}$ , these are indicative values only, and measurements on the impedance of the resistors have been performed. The need for different resistors with different impedance are due to the frequency dependent impedance of the disk. Depending on the frequency, the voltage over the disk will be shifted between the disk and the resistor. If e.g. the impedance of the resistor is much larger than the impedance of the disk, then  $V_{ch}^1 \approx V_{ch}^2$ , and the impedance of the disk is difficult to determine using the FFT method. In Table 3.10 the frequency ranges where the different resistors have been used are given.

Since it is of interest to examine the non-linear properties of the impedance of the piezoelectric disks, a method to keep the voltage drop over the piezoelectric disk constant, has been implemented. During measurement, the input voltage at channel 2 is monitored and if  $V_{ch}^2$  falls below or rise above a given threshold the generator voltage,  $V_{gen}$ , is increased or decreased accordingly.

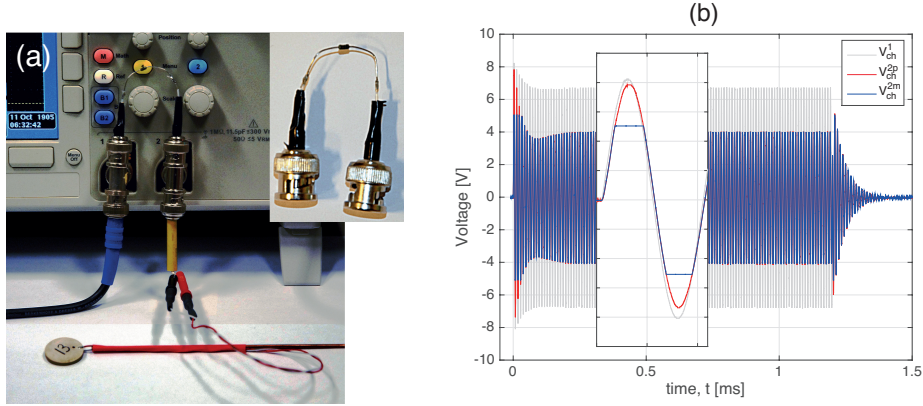


Figure 3.20: (a) image of the oscilloscope with  $Z_{res}$  connected in between input channel 1 and 2. The piezoelectric disk 13 is seen connected to the input channel 2. On the top right, a close up of a resistor soldered on to the BNC connectors is shown. (b) examples of recorded bursts. The grey curve is the recorded voltage at channel 1, the red and blue curves are the recorded voltages at channel 2. The first period is magnified.

Table 3.10: List of frequency ranges with associated values for  $Z_{res}$ .

Frequency range [kHz]	50-82	82-96.5	96.5-99.6	99.6-105	105-192	192-255	255-300
$Z_{res}$ [ $\Omega$ ]	1000	100	10	100	1000	100	1000

In Fig. 3.20 (b) an example of a recorded waveform using the 10  $\Omega$  resistor and a 100 kHz sinusoidal signal with  $V_{gen} = 10$  V is given. The first signal period is magnified. The grey curve is the recorded input voltage at channel 1, and the red and blue curve are the recorded input voltages at channel 2. The difference between the red and the blue curves are the vertical setting of the oscilloscope. It is observed in the magnification that the blue curve is cut at both peak and valley. Since the phase is calculated using the transient and steady-state part of the signal, a truncation of the peak and valley might lead to a deviation in the phase. Thus, the red curve is used for phase calculations, denoted  $V_{ch}^{2p}$  in the legend. Since the transient part of a signal is not used in the magnitude calculations, any truncation in the onset of the signal is irrelevant. The blue curve is used for magnitude calculations, denoted  $V_{ch}^{2m}$  in the legend. The benefit of this, is that the blue curve has twice as high vertical resolution than the red curve.

### 3.9.3 Measurements on amplifier and filter

Measurements on the B&K amplifier and KrohnHite filter have been conducted to determine the transfer function  $H_{5'6open}^{VV}$ . The measurements have been initiated by S ovik [3], and the current author have contributed by verifying the measurements for magnitude and phase. Moreover, the phase response have, by the current author, been calculated by two methods, 1) by the FFT method (used by [3]), and 2) by the zero cross method. The results obtained by the zero cross



method is not shown, however it should suffice to state that the two methods yielded comparable results.

All measurements on the B&K amplifier and KrohnHite filter in the current thesis, follow the measurement procedure outlined in [3] and the actual measurement set-up and method will not be repeated here. However, in [3] the frequency response of the amplifier and filter had to undergo "smoothing" to remove "spikes" with a magnitude of  $\pm 0.1$  dB. The presence of the spikes was in [3] explained as a consequence of the vertical scaling of the oscilloscope. However, an alternative explanation utilizing an example will follow.

In Fig. 3.21 (a) an example of a recording of  $V_6$  is presented for a measurement on the amplifier and filter. The aforementioned spikes are clearly visible. The figure shows the magnitude of the peak-to-peak voltage,  $|V_6|$ , as a function of frequency for the frequency range 10-300 kHz. The two circles indicate the frequencies 84 kHz (blue) and 86 kHz (red), which are plotted as the recorded time domain bursts in Fig. 3.21 (b). It should be mentioned that the spike level is larger in Fig. 3.21 (a) than what was reported in [3], however, the number of spikes in Fig. 3.21 (a) are significantly reduced from that in [3]. This is believed, but not investigated, to be due to the use of different FFT-subroutines.

During measurements of  $V_6$  the vertical scaling of the oscilloscope was 2 V/div, such that a voltage range of 20 V was realized. The oscilloscope has an 8-bit vertical resolution which yields 256 discrete voltage levels. Thus, 20 V/256 levels  $\approx 0.078$  V/level which corresponds to  $\approx -22.1$  dB/level. A large discrepancy between the discrete voltage levels and the experienced spike level is therefore observed, and this indicates that the spikes are not induced by the vertical scaling of the oscilloscope.

In Fig. 3.21 (b) an explanation as to the presence of the spikes is seen. In (b) the two time-domain bursts, corresponding to the indicated frequencies in (a), are juxtaposed. The burst lengths are approximately 0.9 ms long. The blue burst corresponds to  $f = 84$  kHz where no spike is observed, and the red burst corresponds to  $f = 86$  kHz where a spike is observed. It is observed that the magnitude of the blue burst exhibits a flat, steady-state response almost exclusively throughout the burst, with a peak voltage of  $\approx 8.24$  V. However, the red curve does not exhibit a steady-state response. Rather, the burst shows signs of amplitude modulation with a signal of lower frequency.

However, if the burst was amplitude modulated then a Fourier transform of the burst should separate the two frequency components, and the magnitude of the 86 kHz burst should not be affected. A Fourier transform has been conducted (not shown here) and the frequency component corresponding to 86 kHz shows a decline in value corresponding to the spike level in (a), which is in contrast to what is expected if the burst was amplitude modulated. Other time domain bursts corresponding to frequencies with spikes have been investigated. All investigated bursts exhibit the same periodic swings, where the frequency of the lower "signal", or "interference", is approximately 200 Hz. It should also be mentioned that the spikes are independent of frequency, i.e. that for two independent measurements on the frequency response of the amplifier and filter, the number of spikes will vary and the spikes will occur at different frequencies.

The reason as to the presence of the low frequency signal has not been investigated, and any corresponding hypothesis are elusive at this stage as it does not seem to be caused by amplitude modulation. However, it thus seems fair to remove the spikes by linear interpolation of neighboring points, as was performed in [3]. In APENDIX the Matlab script `remove_spikes.m` is given. The script uses a simple threshold check to locate the spikes to be removed.

### Effect of spikes on the mean of repeated measurements

It is of interest to conduct repeated measurement in order to obtain statistical data on the frequency response of the amplifier and filter. This has been performed by 10 repeated measurements over a frequency range 10–300 kHz with a frequency resolution of 2 kHz. In Fig. 3.21 (c) the measurements are given as the colored lines. The thicker, black line represents the mean of the ten measurements. It is observed that the mean exhibits fluctuations. In Fig. 3.21 (d) the same measurements as in (c) is presented, though in (d) the spikes have been removed. In (d) the thicker, black line represents the mean of the ten measurements after the spikes have been removed. The mean in (d) is generally higher in value than the mean in (c), and the fluctuations in (c) is severely reduced in (d).

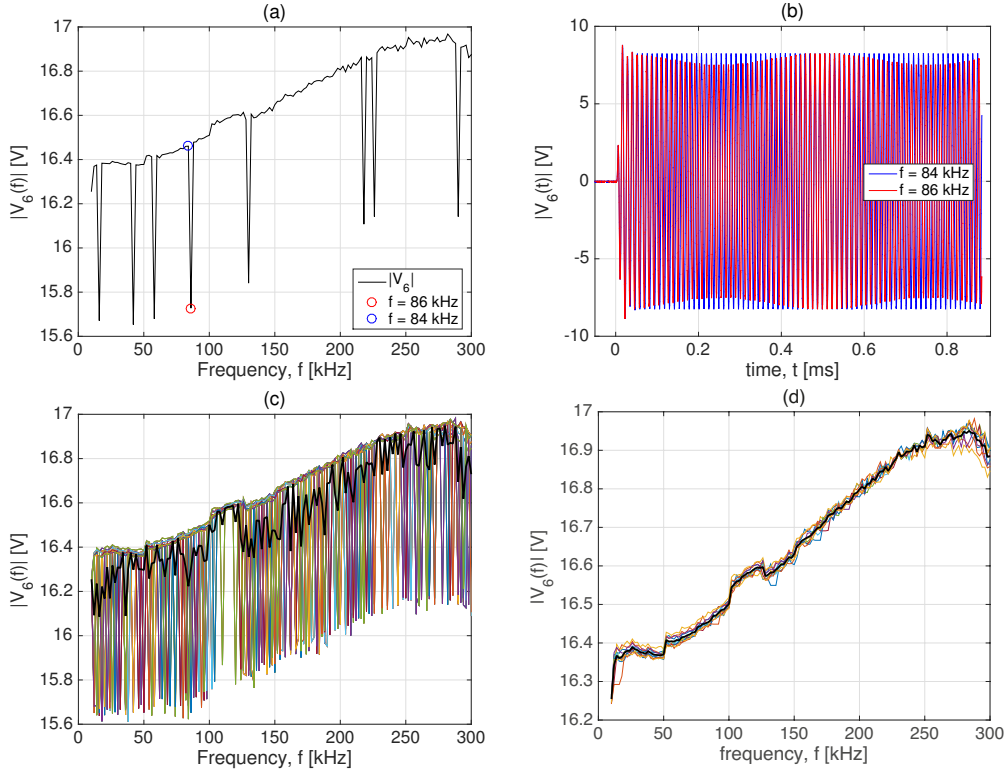


Figure 3.21: (a) example of a recording for the frequency characterization of the amplifier and filter. The recorded voltage exhibits spikes. The blue and red circle indicate the frequencies 84 and 86 kHz, respectively. (b) time-domain representation of the indicated frequencies in (a). (c) same as (a) but for ten repeated measurements represented as the colored lines; the black, thick line represents the mean of the ten measurements. (d) same as (c) but after removal of the spikes.

### 3.10 Investigation of the coaxial cable parameters and input impedance of the B&K amplifier

In Sec. 2.10 it was pointed out that both the current author and [3] observed fluctuations in the measured  $|H_{15open}^{VV}|$  at especially 112 kHz. In Sec. 2.10 a hypothesis was that these deviations originated in the implementation of the corrections itself, however, this was refuted. A second hypothesis as to the origin of these fluctuation are deviations in the parameters for the coaxial cable and input impedance of the amplifier, as stated in the data-sheets [82,88]. To investigate this, measurements have been performed on the coaxial cable of type RG-178, and the input impedance of the B&K signal amplifier. In Table 3.11 the data-sheet values and the adjusted values are given.

Table 3.11: Datasheet and adjusted values for the coaxial cable's capacitance per meter,  $C_x$ , input resistance,  $R_{amp,in}$ , and capacitance,  $C_{amp,in}$ , of the amplifier.

	Coaxial cable	Amplifier input impedance: R     C	
	$C_x$ [pF/m]	$R_{amp,in}$ [M $\Omega$ ]	$C_{amp,in}$ [pF]
data-sheet values	nom. 93	1	90
adjusted values	100	0.95	96

All measurements have been performed with the HP-impedance analyzer. Prior to measurements, a zero offset adjustment of the HP-impedance analyzer has been performed, as described in Sec. 3.9.1.

## Zero gain

For the measurements in the current section the Gain of the amplifier has been set to zero. This allows for a higher output voltage from the HP-impedance analyzer. The voltage has been set to 1 V RMS given a termination load of 50  $\Omega$ . The measurements have been compared to simulations of the measurement set-up using transmission line theory, as described in Sec. 2.10.

The measurements have been performed in three stages: a) an impedance measurement on a resistor is performed. b) when the impedance of the resistor is determined, a measurement on the coaxial cable 1 terminated in the resistor is performed. c) when the impedance of the coaxial cable 1 is determined, a measurement on cable 1 terminated in the amplifier is performed.

In Fig. 3.22 the schematics of the three measurements are shown, and the equations modeling the measurement set-up are:

$$\begin{aligned} Z_{in}^{(b)} &= Z_{a1} + Z_{b1} \parallel (Z_{a1} + Z_{res}) \\ Z_{in}^{(c)} \Big|_{Gain=0} &= Z_{a1} + Z_{b1} \parallel (Z_{a1} + Z_{amp,in}) \end{aligned} \quad (3.12)$$

where  $\parallel$  is used to denote a parallel circuit, and the superscript (b) and (c), refers to the schematics in Fig. 3.22.

The measurements and corresponding simulations are compared, and the associated cable or amplifier input impedance parameters have been adjusted such that a better fit between the measurements and the simulations have been achieved.

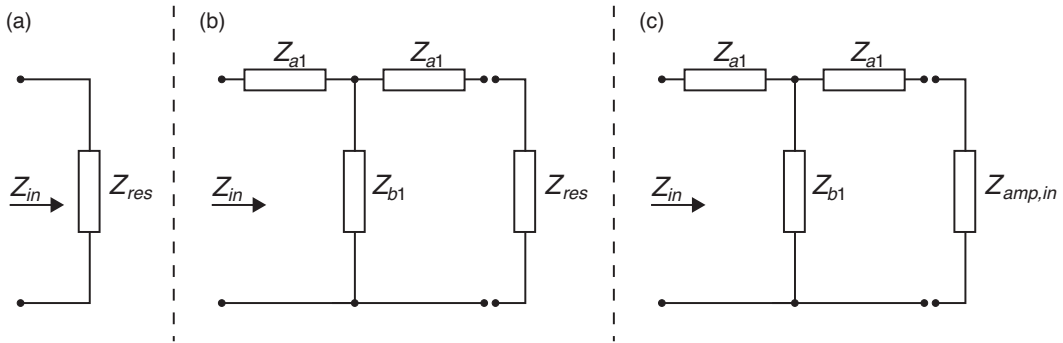


Figure 3.22: Schematics of the three measurements performed in order to investigate the cable parameters and input impedance of the amplifier.

In Fig. 3.23 the results of the measurement and simulation of the input impedance,  $Z_{in}^{(b)}$ , of the coaxial cable 1 terminated in  $Z_{res}$  are given for (a) magnitude, and (b) phase. In both (a) and (b) the simulation using the adjusted values agrees well with the measurement, while deviations are observed for the simulation using the data sheet values and the measurement.

In Fig. 3.24 the results of the measurement and simulation of the input impedance,  $Z_{in}^{(c)}$ , of the coaxial cable 1 terminated in the input impedance of the amplifier,  $Z_{amp,in}$ , given 0 dB Gain, are given for both (a) magnitude and (b) phase. In (a) the simulation obtained with the adjusted values agree well with the measurement. However, deviations are observed comparing the measurement with the simulation using the data-sheet values. In (b) however, a deviation around 50 kHz is observed between both simulations and the measurement. The deviation, or jump in value, is assumed a consequence of the internal switching between measurement ranges of the HP-impedance analyzer [69]. However, this has not been investigated further.

## 60 dB Gain

When the coaxial cable and amplifier input parameters have been adjusted according to the preceding section, a final measurement have been performed where the Gain of the amplifier has been set to 60 dB. The output voltage of the HP-impedance analyzer have been set to 250 mV RMS given a termination load of 50  $\Omega$ . The same voltage divider as described in Sec. 2.10.3 has been utilized to emulate the magnitude of the observed voltage at the input terminals of the amplifier

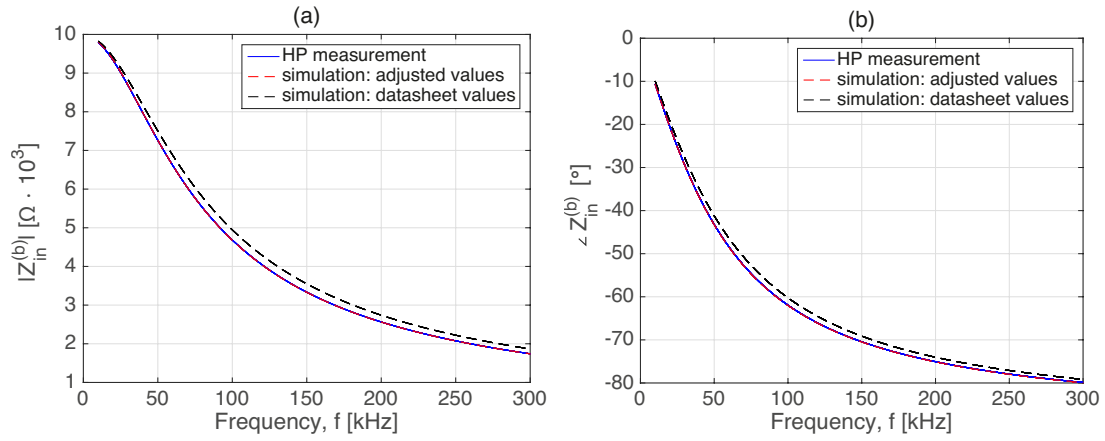


Figure 3.23: (a) magnitude of the input impedance,  $Z_{in}^{(b)}$ , of the coaxial cable 1 terminated in  $Z_{res}$  for measurements with the HP-impedance analyzer (blue), and two simulations where the datasheet values (stippled black) and adjusted values (stippled red) have been used. (b) same as (a) but for the phase angle associated with  $Z_{in}^{(b)}$ .

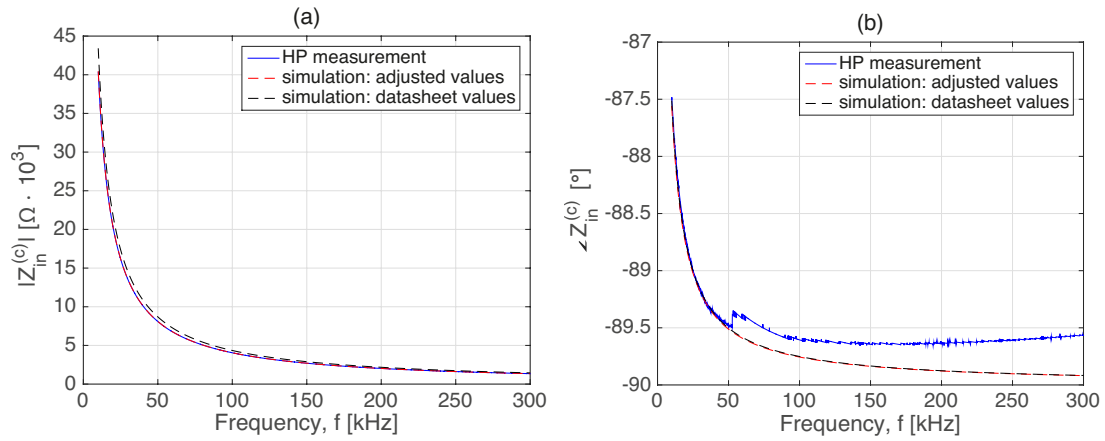


Figure 3.24: (a) magnitude of the input impedance,  $Z_{in}^{(c)}$ , of the coaxial cable 1 terminated in the amplifier, given a Gain of 0 dB. The blue curve is measured with the HP-impedance analyzer, the black stippled curve is obtained by simulations given the values in the datasheets, and the red stippled curve is obtained by the adjusted values. (b) same as (a) but for the phase angle associated with  $Z_{in}^{(c)}$ .

during the acoustical measurements. In Fig. 3.25 the schematics of the measurement is given, and the equation modeling the set-up is

$$Z_{in} \Big|_{Gain=60} = Z_{a1} + Z_{b1} \parallel \{Z_{a1} + Z_{vd1} + (Z_{vd2} \parallel Z_{amp,in})\} \quad (3.13)$$

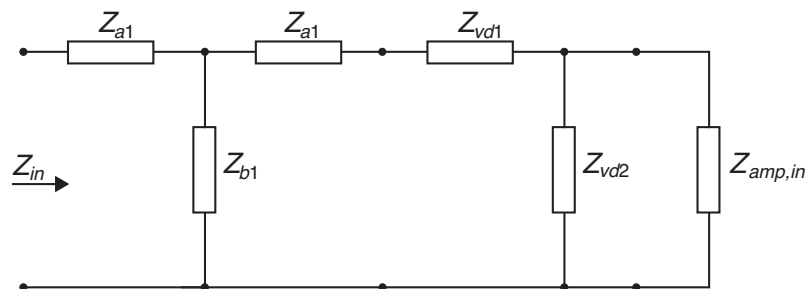


Figure 3.25: Schematics of the measurement set up with 60 dB Gain and voltage divider.

In Fig. 3.26 the results of the measurement and simulation of the coaxial cable 1 terminated in the input impedance of the amplifier,  $Z_{amp,in}$ , given 60 dB Gain are given for both (a) magnitude and (b) phase angle. In (a) the first thing to take notice of is that the input impedance is in a different order of magnitude. This is explained by the more complex impedance network used to be able to measure thus. Another thing to notice is that the measurement (blue) is quite noisy. This is explained by the relative low signal output amplitude of the HP-impedance analyzer. However, the simulation obtained with the adjusted values tend to agree fairly well with the measurement, while the simulation obtained with the data-sheet values are throughout larger in magnitude.

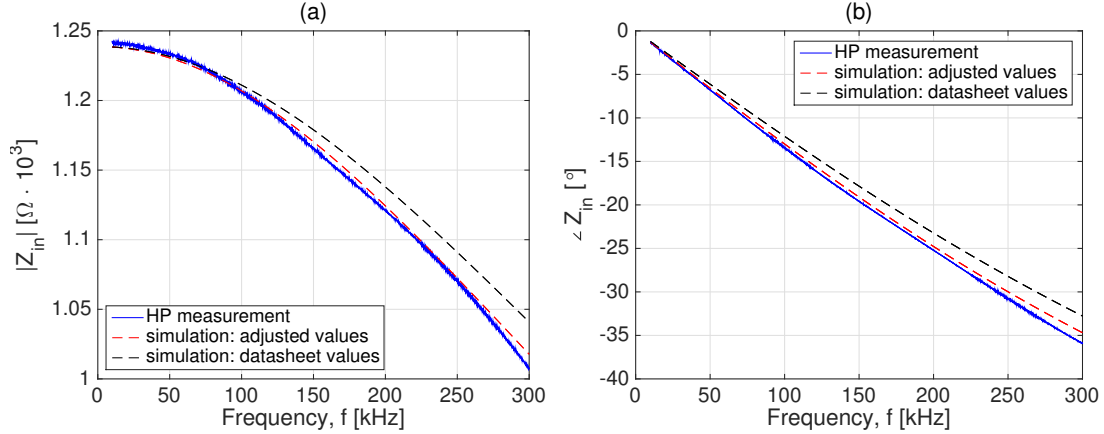


Figure 3.26: (a) magnitude of the input impedance,  $Z_{in}$ , of the coaxial cable 1 terminated in the amplifier, given a Gain of 60 dB. The blue curve is measured with the HP-impedance analyzer, the black stippled curve is obtained by simulations given the values in the data-sheets, and the red stippled curve is obtained by the adjusted values. (b) same as (a) but for the phase angle associated with  $Z_{in}$ .

### Effect of adjusted values on $|H_{15open}^{VV}|$

In Fig. 3.27 an example of the frequency range with challenges is shown for the magnitude of the open circuit transfer function,  $|H_{15open}^{VV}|$ . The blue curve corresponds to a simulation, the red curve corresponds to a measurement where the data-sheet values have been used in the corrections, and the black curve corresponds to a measurement where the adjusted values have been used in the corrections. The corrections are defined in Sec. 2.10. The measurement is performed at 0.50 m, using 10 V, the transmitter is disk 11, and the receiver is disk 04.

In the figure, a slight difference between the measurements using the different data values are observed. The measurement using the adjusted values exhibit less fluctuations than the measurement using the data-sheet values, however the difference is not conclusive.

For the remainder of the thesis, the adjusted values are used. Moreover, the adjusted values compared to the data-sheet values are used in the uncertainty analysis, c.f. Sec. 7, to obtain an estimate of the standard uncertainties where the manufacturer has not provided any data on the uncertainties.

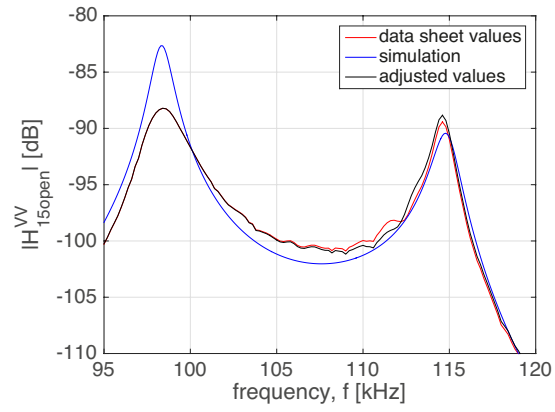


Figure 3.27: Magnitude of the open circuit transfer function,  $|H_{15open}^{VV}|$  for a simulation (blue), and with the use of data-sheet values (red) and use of adjusted values (black) in the corrections.

## Chapter 4

# Finite Element simulations

The Finite Element (FE) method is used to simulate the piezoelectric disk and corresponding radiated sound field. In this chapter, a brief description of the FE-simulation tool and corresponding simulation set up will be given.

### 4.1 FEMP

The FE-modeling program used in the current thesis is Finite Element Modeling of Piezoelectric Transducers FEMP 5.1 [46, 47, 98]. FEMP was originally developed in a cooperation between UiB and CMR by Kochbach [46, 47], and has since been further developed by researchers and students at UiB and CMR. FEMP is implemented in MATLAB which allows users to extend on the code, e.g. by adding new functionality to the Femp code base.

### 4.2 Simulation problem

For an axisymmetric simulation problem, the simulation is defined in the  $rz$ -plane c.f. Fig. 4.1. The 3D solution is obtained by assuming symmetry about the  $z$ -axis. The simulation problem is solved using a direct harmonic analysis, with the transducer immersed in a fluid. The simulation problem is divided into a region of finite elements and a region of infinite elements. The finite element region consists of the piezoelectric disk as well as the fluid loading, and is solved using 8 node isoparametric elements. The infinite element region consists of the infinite elements which are solved using 12<sup>th</sup> order conjugated Astley-Leis infinite elements.

The geometry of the simulation problem is defined in `read_in_project.m`. A new geometry, `piezofluid`, was defined for the current work. The geometry of `piezofluid` consists of a single piezoelectric disk radiating in air, c.f. Fig. 4.1 where the geometry of `piezofluid` is shown. The input parameters to `piezofluid` are defined in a text file `piezofluid.inn`. `piezofluid.inn` is available in the Appendix B.3.1.

### 4.3 Simulation parameters

It has been shown [46, 47, 49] that the accuracy in the FE-simulations is a function of the number of elements used per wavelength,  $N_\lambda$ . In addition, the distance at which the infinite elements are applied,  $r_{inf}$ , is important for the accuracy. Both  $N_\lambda$  and  $r_{inf}$  influence the simulation size and corresponding simulation time significantly.  $N_\lambda$  and the meshing frequency,  $f_{mesh}$ , determine the meshing density of the simulation. The wavelength used in the calculations of the meshing density is determined by the shortest wavelength of either the shear wavelength,  $\lambda_s = c_s/f$ , or the longitudinal wavelength,  $\lambda_l = c_l/f$ , where  $c_s$  and  $c_l$  are the shear and longitudinal sound speeds, respectively [46, 47], and  $f$  is frequency.

Convergence test (not shown here) to determine  $N_\lambda$  and  $r_{inf}$  have been conducted. The values used throughout the thesis are predominantly  $N_\lambda = 9$ , while also simulations obtained utilizing

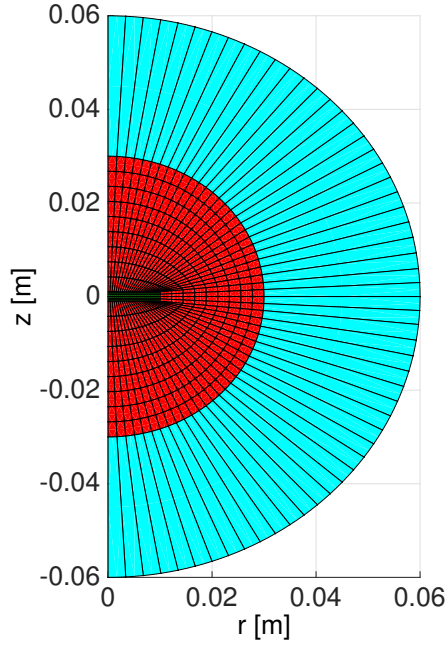


Figure 4.1: Example of a mesh of a simulation problem for the structure piezofluid. The piezoelectric disk is represented by the green elements, the fluid is represented by the red elements, and the infinite elements are represented by the cyan elements. Note that the meshing density is reduced significantly to be able to appreciate the element division.

$N_\lambda = 7$  will occur. However, this will not be stated alongside the simulations. And,  $r_{inf} = 0.03$  m is utilized throughout the thesis.

## 4.4 Material parameters

The material constants needed to simulate a piezoelectric disk in FEMP are the elastic stiffness constants  $c_{11}^E$ ,  $c_{12}^E$ ,  $c_{13}^E$  and  $c_{14}^E$ , the piezoelectric constants  $e_{31}$ ,  $e_{33}$  and  $e_{15}$ , and the permittivity at constant strain  $\epsilon_{11}^S$  and  $\epsilon_{33}^S$ . The dielectric, elastic and piezoelectric losses in the piezoelectric material are included by using complex material constants. The material data set provided by Ferroperm includes mechanical and dielectric losses in terms of the mechanical quality factor  $Q_m$  and the loss tangent  $\delta_e$ , respectively [99].

To be able to compare measurements with FE-simulations, the material constants used in the simulations have to accurately describe the physical relationship of the material that are being simulated. The material data provided by the manufacturers of e.g. piezoelectric disks, can be associated with relatively large uncertainties, and the actual properties of the physical disks can vary within production batches and also from disk to disk within the same production batch.

In the current thesis, piezoelectric disks of type Pz27 from Meggit Ferroperm [99] are used. The dielectric material constants provided by Meggit Ferroperm are associated with an uncertainty of  $\pm 10\%$ , the electromechanical material constants are associated with an uncertainty of  $\pm 5\%$ , and the mechanical material constants are associated with an uncertainty of  $\pm 2.5\%$ .

Previous work at UiB have resulted in several adjusted material data sets for the piezoelectric disks, where the adjusted material data sets have shown to yield better comparison with measurements [90, 100]. The adjusted data sets differ slightly, and the current author has chosen a set developed by Knappskog [90] due to recommendations in [2]. In Tab.4.1 the material parameters are given for the Ferroperm data and the adjusted data set.



Table 4.1: Material data for the piezoelectric disks of type Pz27. The adjusted data set is used throughout the thesis.

Parameter	Unit	Ferroperm [99]	Adjusted data set [90]
$c_{11}^E$	[10 <sup>10</sup> Pa]	14.70	$11.874(1 + i\frac{1}{95.75})$
$c_{12}^E$	[10 <sup>10</sup> Pa]	10.50	$7.430(1 + i\frac{1}{71.24})$
$c_{13}^E$	[10 <sup>10</sup> Pa]	9.37	$7.425(1 + i\frac{1}{120.19})$
$c_{33}^E$	[10 <sup>10</sup> Pa]	11.30	$11.205(1 + i\frac{1}{120.19})$
$c_{44}^E$	[10 <sup>10</sup> Pa]	2.30	$2.110(1 + i\frac{1}{120.19})$
$e_{31}$	[C·m <sup>-2</sup> ]	-3.09	$-5.40(1 - i\frac{1}{166})$
$e_{33}$	[C·m <sup>-2</sup> ]	16.00	$16.0389(1 + i\frac{1}{323.177})$
$e_{15}$	[C·m <sup>-2</sup> ]	11.60	$11.20(1 - i\frac{1}{200})$
$\epsilon_{11}^S$	[10 <sup>-9</sup> ]	10.0005	$8.110044(1 - i\frac{1}{50})$
$\epsilon_{33}^S$	[10 <sup>-9</sup> ]	8.0927	$8.14585(1 - i\frac{1}{86.28})$
$\rho$	[kg · m <sup>-3</sup> ]	7700	7700
$Q_m$	-	80	-
$\tan \delta$	-	0.017	-

## 4.5 Extension to FEMP

Intrinsic to the diffraction correction SFDC is the average sound pressure over a free-field area of equal size as the receiver. This sound pressure is possible to read out from FEMP at a given separation distance,  $d$ , using the function `pressureatreceiver`. However, `pressureatreceiver` is only written for one separation distance, thus a sweep of the average free-field area for different positions along the  $z$ -axis is not possible.

To resolve this, an extension was written and implemented to the FE-software FEMP. The extension allows the user to input a vector of distances along the  $z$ -axis from where the average free-field area will be calculated. This is then done for each frequency, and the resulting average free-field areas are saved in a matrix. The extension is given in the Appendix B.3.2. Note that to be able to display the whole code, some of the code lines had to be continued on the next line. This is indicated with three dots: "...".

## Chapter 5

# Calibration of laser distance measuring unit

The current chapter describes how the distance between the two laser distance sensors are calibrated. The sensors were described in Sec. 3.2.7, however, for completeness part of the description will be repeated here. To measure the distance between the transmitter and receiver, prior to an acoustical measurement, the two laser sensors have to be mounted in opposite direction. A consequence of this is that the distance between the two front faces of the sensors are unknown. This distance is denoted  $d_x$ . To aid in the determination of  $d_x$  a calibration frame were manufactured by CMR Prototech [101] and the inner distance of the calibration frame were measured by CMR Prototech to a high degree of accuracy.

Furthermore, prior to an acoustical measurement, the two sensors have to be positioned in between the transmitter and receiver such that the distance between the transmitter and receiver can be measured. A mechanism allowing the sensors to be moved thus had therefore to be constructed.

The objective of the current chapter is to present the measurement set-up used to determine  $d_x$ , and present the mechanism used to move the sensors in position for the distance measurement. The associated measurement uncertainties of  $d_x$  will be developed.

### 5.1 Measurement set up

In Fig. 5.1 (a) and (b) the laboratory equipment used to determine  $d_x$  are given. The sensors are attached to a manual XYZ-translation stage of type LT3/M from Thorlabs [102] via a 5 mm thick aluminium plate. The XYZ-translation stage are mounted on a manual rotation stage, PR01, also from Thorlabs [102], via a 8 mm aluminium plate. The 8 mm thick aluminium plate is only used during the calibration, however, the 5 mm thick aluminium is present during the distance measurement prior to an acoustical measurement. Lastly, the rotation state is mounted to a faceplate. The calibration frame (c.f. Sec. 5.1.1 for details) rests upon two and two parallel-blocks. In Tab. 5.1 the sizes and estimated unevennesses of the faceplate and parallel-blocks are given.

Movement of the XYZ-translation stage in the  $x$ - $y$ - $z$ -direction can be done by turning one of two knobs. There are two knobs for each direction: one revolution of the coarse knob results in a translation of approximately 1.4 mm and one revolution of the fine knob yields a translation of approximately 0.25 mm.

The laser sensors are aligned with the faceplate with a technique referred to as *clocking*. In Fig. 5.2 (b) an image of the clocking device is given. The clocking device is equipped with an analog dial of 0.01 mm resolution. The clocking device has a needle sensors that is placed upon the top surface of the laser sensor. When the clocking device is pushed across the faceplate, any deviations in the parallelity of the faceplate and the top of the laser sensor will result in a movement of the clock hand. Both laser sensors have been adjusted such that they are at best parallel with the faceplate by the employee(s) at the machine shop at UiB.

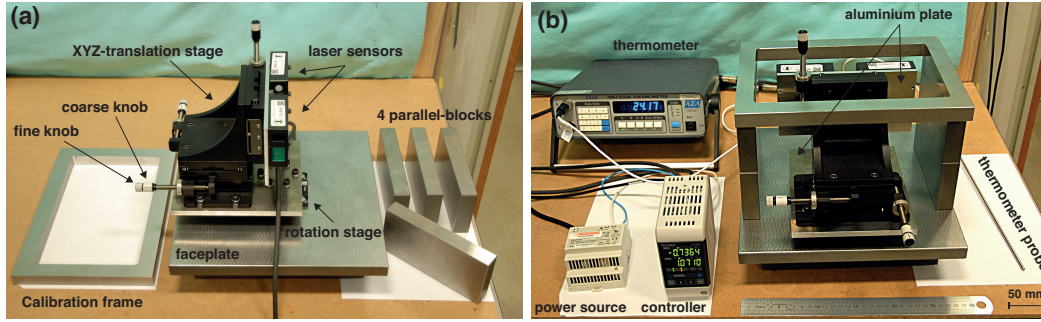


Figure 5.1: (a) image of the dismantled laboratory set up. (b) image of the laboratory set up as used during measurements. The controller and the power source as well as the precision thermometer, all of which are used during measurements, are shown in the image.

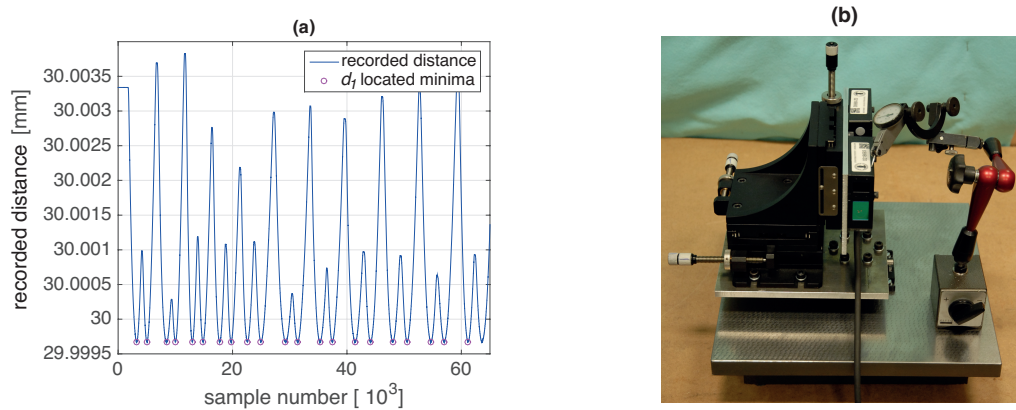


Figure 5.2: (a) plot of recorded distances for laser sensor 1 with located minima,  $d_1$ , indicated as magenta circles, (b) image of laser sensors with the clocking device used for aligning the sensors parallel with the faceplate.

Table 5.1: Selected features of the faceplate and parallel-blocks.

Unit	size in mm (length x width x height)	Tolerance standard	permissible deviation
Faceplate	300 x 300 (height not applicable)	DIN 876/2	26 $\mu\text{m}$
Parallel-block	160 x 24 x 80	DIN 7168 medium	$\pm 0.3$ mm

### 5.1.1 Calibration frame

A calibration frame, c.f. Figure 5.3 and 5.1, has been employed to determine  $d_x$ . The calibration frame has been cut out of a stainless steel plate of thickness 20 mm, and the edges are approximately 20x20x20 mm. Treatment of two of the opposite inner edges have been performed by CMR Prototech and the inner distance,  $D$ , have been measured with an uncertainty,  $u(D_{CMR}) = \pm 0.3$   $\mu\text{m}$ .

In Tab. 5.2 some of the most important features of the calibration frame are given.  $T_{diff}$  is the difference between the temperature sensor used by CMR Prototech and the temperature sensor ASL F250, which is also used during the acoustical measurements at UiB. To obtain the difference in the measured temperature, the two sensors were placed in the same room at CMR Prototech's location in Bergen. The two temperature readings were:  $T_{Prototech} = 21.373^\circ\text{C}$ , and  $T_{F250} = 21.384^\circ\text{C}$ .

## 5.2 Measurement method

The sensors and the XYZ-translation stage are mounted on a rotation stage, thus they can be rotated by pushing on either side of the bottom aluminium plate. When the laser sensors are

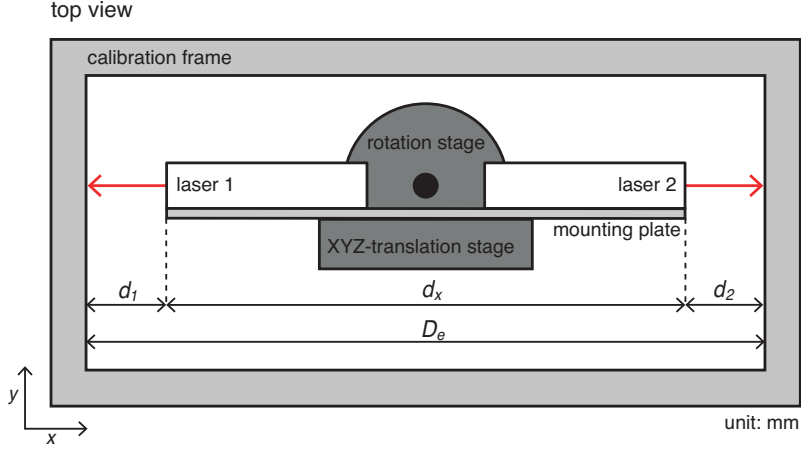


Figure 5.3: Schematics of calibration frame.

Table 5.2: Selected features of the calibration frame.

Calibration frame	
Material	Stainless steel grade 316
$D$ , Measured inner distance	242.192 mm
$u(D_{CMR})$ , uncertainty of meas. dist. by CMR Prototech [103]	$\pm 0.3 \mu\text{m}$
$T_{CMR}$ , temp. during measurement, CMR Prototech	$19.952^\circ\text{C}$
$T_{diff}$ calibrated temp. difference	$0.011^\circ\text{C}$
$\alpha_s$ , thermal expansion coefficient, steel 316	Approx. $16 \cdot 10^{-6} \text{K}^{-1}$

rotated thus, the laser beam will scan the inside of the calibration frame. The shortest distance from the front face of the sensors to the inside of the calibration frame is at normal incidence. The measurement task is to locate such minima and use this information to calculate  $d_x$ . The located minima are denoted  $d_1$  for sensor 1 and  $d_2$  for sensor 2.

In Fig. 5.2 (a) an example of a measurement for sensor 1 is given. The recorded distances are given in blue and the located minima,  $d_1$ , are indicated as magenta circles.<sup>1</sup>

When the minima are located, the mean of these are calculated and used as the estimate of the distance  $d_1$ . The bar signifying a mean is omitted for brevity, such that, to be perfectly clear,  $d_1$  and  $d_2$  are given by

$$d_1 = \bar{d}_1 = \frac{1}{n} \sum_{j=1}^n d_{1,j} \quad \text{and} \quad d_2 = \bar{d}_2 = \frac{1}{n} \sum_{j=1}^n d_{2,j} \quad (5.1)$$

where  $j$  denotes the  $j$ 'th minima of the recorded distances, and  $n$  is the total number of located minima.

### 5.2.1 Measurement scheme

The current section describes the measurement scheme used to overcome a challenge with the alignment of the laser sensors.

In Fig. 5.4 (a) the laser sensors are put in a coordinate system. The center of the rotation stage is defined as the position where  $x = y = 0$ , the x-axis is defined as the axis that runs parallel with the longest edge of the calibration frame, and the y-axis is defined as the axis that is parallel with the shortest edge of the calibration frame.

Aligning the laser sensors such that the laser spots are parallel with the  $x$ -axis and positioned in  $y = 0$  is challenging as this have to be done by visual inspection. Further more, if the laser

<sup>1</sup>Note that the last minimum is omitted. This is done to prevent possible errors stemming from a "fake minimum." So called fake minimum can be located when the sampling ends before a minimum has been scanned. This is only a problem at the end of a measurement.

spots are not positioned in  $y = 0$  the sensors will move towards or away from the calibration frame during rotation, resulting in a lower minima then if the sensors were positioned in  $y = 0$ . In Fig. 5.4 (b) this is visualized.

To overcome this, a measuring scheme has been employed. First, the laser spots are as best positioned in  $y = 0$ . This is possible to do within  $\pm 0.5$  mm. The sensors are then moved along the negative  $y$ -axis to approximately  $y = -1.0$  mm. This is performed by four revolutions of the small knob on the XYZ-translation stage. The objective is to perform 9 measurement, as describe in Sec. 5.2, while for each measurement the laser sensor is re-positioned by 0.25 mm in the positive  $y$ -direction. The first measurement is thus performed at  $y \approx -1.0$  mm, and the second is performed at  $y \approx -0.75$  mm. This is repeated until the ninth measurement is performed at  $y \approx 1.0$  mm. One process like this, with 9 measurements, is referred to as a measurement series.

The expected result of a measurement series just explained is that of a parabola where the minima of the parabola reflects the position when the sensors are at best aligned with  $y = 0$ . This distance reflects the shortest distance from the laser front face of the laser sensors to the calibration frame.

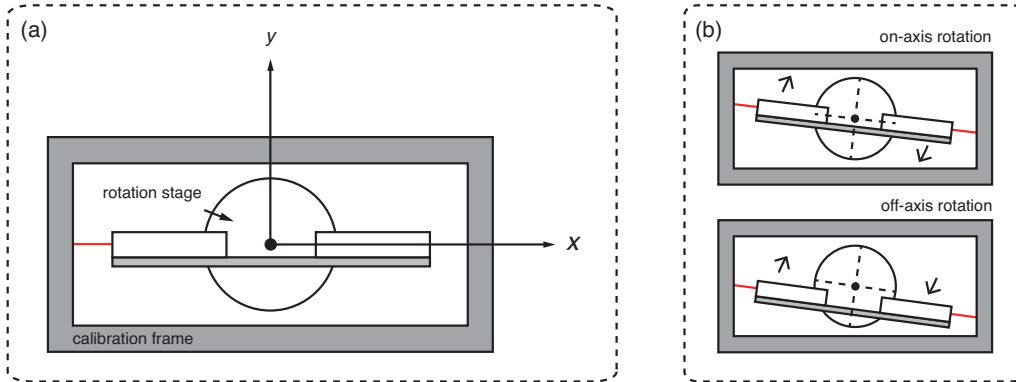


Figure 5.4: (a) schematics of rotation stage and calibration frame with both sensors pointing in opposite directions. The center of the rotation stage is defined as the origin. (b) (top) on-axis rotation, i.e. rotation when the laser beam is positioned in  $y = 0$ , (bottom) off-axis rotation, i.e. rotation when the laser beam is positioned in  $y \neq 0$ .

## 5.3 theory

In the current section the equations used to obtain  $d_x$  will be presented.

### 5.3.1 Thermal expansion of the calibration frame

Compensation for the thermal expansion of the calibration frame has been performed. The expansion is due to the temperature difference between the measurements performed by CMR Prototech and the measurements performed at UiB. It is assumed that the expansion is linear and that the calibration frame can be simplified to that of a rod with initial length equal to the inner distance,  $D$ , of the calibration frame, c.f. Fig. 5.5. The equations are [104]

$$\Delta D = D\alpha_s\Delta T \quad (5.2)$$

$$D_e = D(1 + \alpha_s\Delta T) \quad (5.3)$$

where  $\Delta D = D_e - D$  is the expansion or contraction of the inner distance of the calibration frame,  $D_e$  is the inner distance of the calibration frame after expansion or contraction,  $D$  is the inner distance of the calibration frame as measured by CMR Prototech given the temperature  $T_{CMR}$ ,  $\alpha_s$  is the linear thermal expansion coefficient for steel grade 316 and the change in temperature is given by

$$\Delta T = T - T_{diff} - T_{CMR} \quad (5.4)$$

where  $T$  is the temperature during calibration,  $T_{CMR}$  is the temperature measured by CMR Prototech during the measurement of  $D$ , and  $T_{diff}$  is the difference in the temperature readings of the two thermometers, c.f. Sec. 5.1.1.

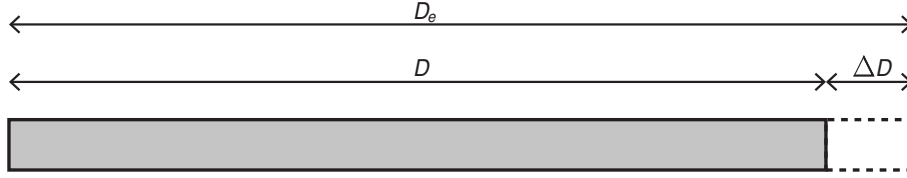


Figure 5.5: Schematics of thermal expansion of calibration frame simplified as a rod.

### 5.3.2 Equation for $d_x$

The distance between the two front faces of the laser sensor,  $d_x$ , is found by

$$\begin{aligned} d_x &= D_e - d_1 - d_2 \\ &= D(1 + \alpha_s \Delta T) - d_1 - d_2 \end{aligned} \quad (5.5)$$

where  $d_1$  and  $d_2$  are the mean of the located minima, c.f. Sec 5.2.

### 5.3.3 $d_x$ obtained by statistical means

Following the measurement scheme in Sec. 5.2.1, a total of ten measurement series have been conducted. The ten located minima of each measurement series will be denoted  $d_{x,i}$ , where  $i$  refers to the located minima of the  $i$ 'th measurement series. With this approach,  $d_{x,i}$  is treated as a random variable and the estimate of  $d_x$  is found by the mean of the ten located minima, i.e.

$$d_x = \bar{d}_{x,i} = \frac{1}{n} \sum_{i=1}^n d_{x,i}. \quad (5.6)$$

The estimate of  $d_x$  is then obtained by repeated measurement, and it is the mean of the ten located minima, that are used as the estimate of  $d_x$  in Eq. (3.2).

## 5.4 Measurement results

Two times ten measurement series were performed. The first ten measurement series were performed in a basement laboratory at UiB, where the temperature of the room was attempted to be controlled by a temperature guard and a floor standing convector such that it would resemble the temperature during the measurement on  $D$  performed by CMR Prototech. Thus, little or no expansion or contraction of the calibration frame should occur. The temperature during the measurements in the basement laboratory was found to be fairly constant around 20-21°C.

The second ten measurement series was performed at the acoustic laboratory at UiB. The temperature in this laboratory was fairly constant around 24°C. For both measurement series, corrections for thermal expansion were performed.

In Fig. 5.6 the results are presented. In (a) and (c) the results obtained in the basement laboratory are given, and in (b) and (d) the results obtained in the acoustic laboratory are given. In (a) and (b) the 10 measurement series are juxtaposed, and in (c) and (d) the selected minima,  $d_{x,i}$  are plotted with error-bars. Each colored curve in (a) and (b) corresponds to the same color in (c) and (d), respectively. The horizontal, dashed line in (c) and (d) represents the mean of the ten selected minima,  $d_x = \bar{d}_{x,i}$ , and the shaded, grey area represents the combined standard uncertainty,  $u_c(d_x)$ , associated with the mean of the selected minima.

The calibrated distance,  $d_x$ , obtained in the the basement laboratory is 182.5541 mm with a combined standard uncertainty  $u_c(d_x) = 2.6 \mu\text{m}$ . The calibrated distance,  $d_x$ , obtained in the acoustic laboratory is 182.5692 mm with a combined standard uncertainty  $u_c(d_x) = 2.6 \mu\text{m}$ .

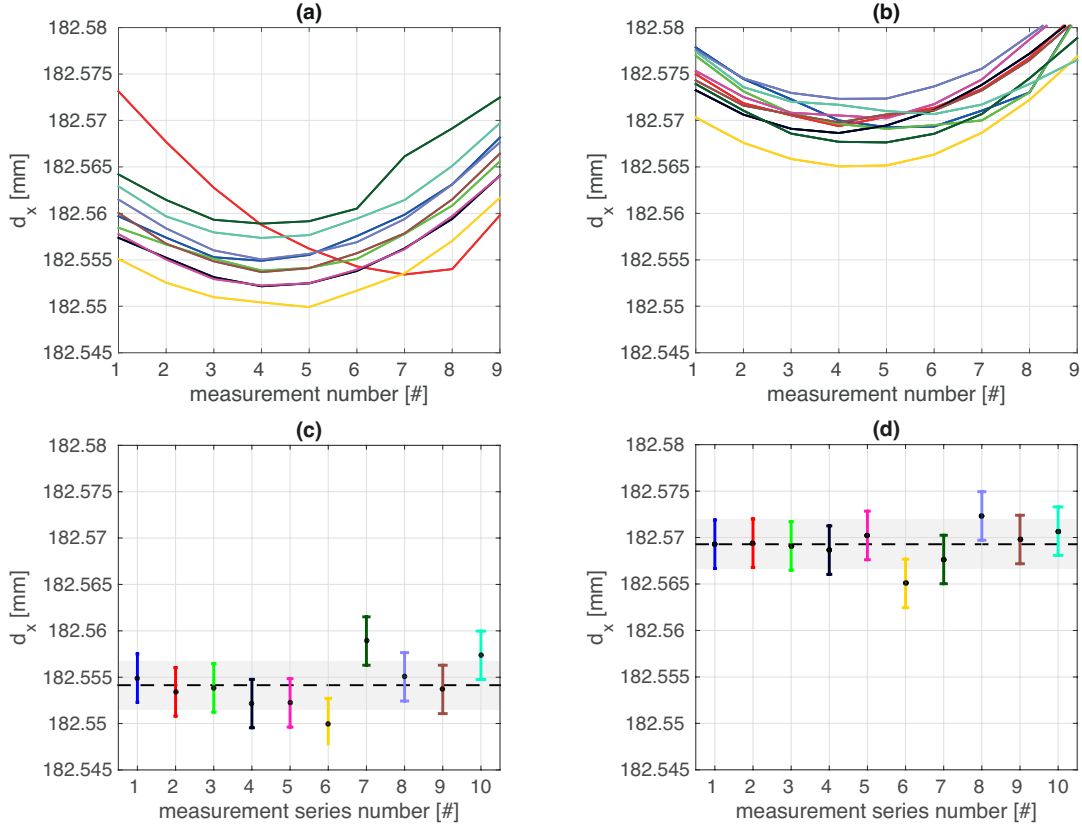


Figure 5.6: Measurement results for the measurement series performed in the basement laboratory, (a) and (c), and the acoustic laboratory, (b) and (d). In (a) and (b) the results of the ten measurement series are given. In (c) and (d) the selected minima from (a) and (b), respectively, are given with uncertainties as error bars. The dashed line in (c) and (d) represents  $d_x = \bar{d}_{x,i}$ , and the shaded, grey area represents the combined standard uncertainty  $u_c(d_x)$ , c.f. Sec. 5.6.3.

## 5.5 Indication of validity of approach

To quantify if the approach used yields fair results, a check can be performed where the values obtained for  $d_x$  in the basement and the acoustical laboratory are compared. If we let the distance  $d_x$  obtained in the basement laboratory be denoted  $d_{x,b}$ , and the distance  $d_x$  obtained in the acoustical laboratory be denoted  $d_{x,a}$ , and expressing Eq. 5.3 with respect to  $d_{x,a}$  as a function of  $d_{x,b}$ , we get

$$d_{x,a} = d_{x,b}(1 + \alpha_{Al}\Delta T_{a,b}) \quad (5.7)$$

where  $\alpha_{Al}$  is the linear thermal expansion coefficient for aluminium, and  $\Delta T_{a,b} = T_a - T_b$  is the temperature difference between the two laboratories,  $T_a$  is the temperature in the acoustical laboratory, and  $T_b$  is the temperature in the basement laboratory.

Since the temperature in the basement laboratory varied from about 20-21°C it is not given which temperature to use in the calculation. A simple approach is to present both. In Tab. 5.3 the values are given. On the right, the difference between the values obtained from Eq. 5.7 and the result for  $d_x$  obtained in the acoustical laboratory is presented. It is appreciated that the difference is rather small, and this indicates that the approach followed in the present chapter seem fair.

Table 5.3: Difference between the result obtained in the basement laboratory and the acoustic laboratory when the result from the basement laboratory has been corrected for thermal expansion, denoted with a subscript e.

$\Delta T_{a,b}$	$d_{x,a}$	$d_{x,a} - d_x$ (ac. lab.)
3 K	182.5672 mm	-1.956 $\mu\text{m}$
4 K	182.5716 mm	2.42 $\mu\text{m}$

## 5.6 Measurement uncertainties

Investigation into the measurement uncertainties associated with the estimate of  $d_x$  are important as any uncertainty in  $d_x$  will propagate to the uncertainty of the calibrated quantities. The uncertainty analysis has shown that the associated uncertainty of  $d_x$  is rather independent of the temperature difference between the basement and the acoustical laboratory, and is thus assumed valid for both.

### 5.6.1 Combined standard uncertainty, $u_c(d_x)$

The combined standard uncertainty associated with the estimate,  $d_x$ , is evaluated as a type A and type B uncertainty. From Eq. (5.6) the standard variance is [92]

$$u_c^2(d_x) = s^2(\bar{d}_{x,i}) + u_c^2(d_{x,i}), \quad (5.8)$$

where  $s^2(\bar{d}_{x,i})$  is the experimental variance of the mean [92], and  $u^2(d_{x,i})$  is the variance associated with each located minima,  $d_{x,i}$ . The experimental variance of the mean is found by [92]

$$s^2(\bar{d}_{x,i}) = \frac{1}{n(n-1)} \sum_{i=1}^n (d_{x,i} - \bar{d}_{x,i})^2. \quad (5.9)$$

The values for the experimental variance of the mean obtained in the basement and acoustical laboratory are  $(0.26 \cdot 10^{-6} \text{ m})^2$  and  $(0.19 \cdot 10^{-6} \text{ m})^2$ , respectively.

The uncertainty associated with the located minima will be dealt with in the following sections.

### 5.6.2 Standard uncertainty of each located minima, $u(d_{x,i})$

The standard uncertainty,  $u(d_{x,i})$ , is evaluated as a type A and type B uncertainty.  $d_1$  and  $d_2$  are obtained with different laser sensors of the same make, however they are still assumed uncorrelated. And although  $\alpha_s$  can be dependent on temperature, it is assumed constant for the temperature range in the current work. Allowing  $d_x$  of Eq. 5.5 to be written as the  $i$ 'th located minima,  $d_{x,i}$ , then the standard uncertainty associated with each located minima is the positive square root of the combined standard variance [92]

$$u^2(d_{x,i}) = (1 + \alpha_s \Delta T)^2 u^2(D) + (D \Delta T)^2 u^2(\alpha_s) + (D \alpha_s)^2 u^2(\Delta T) + u^2(d_1) + u^2(d_2) \quad (5.10)$$

### Uncertainty of the inner distance of the calibration frame, $u(D)$

The standard uncertainty,  $u(D)$ , associated with the inner distance of the calibration frame,  $D$ , is evaluated as a Type B uncertainty.

The standard uncertainty  $u(D)$  depends upon two factors, 1) the stated uncertainty associated with the measurement of the distance,  $D$ , performed by CMR Prototech, denoted  $u(D_{CMR})$ , and 2) calculable deviations from the distance  $D$  due to possible tilt of the calibration frame, denoted  $u(D_{tilt})$ .

In [103] a formula to calculate the associated uncertainty of a measurement performed by CMR Prototech is provided. The formula is:  $\pm(0.50 + 0.00025 \cdot D) \mu\text{m}$ , where  $D$  is the measured distance in millimeters, and the formula is valid for a coverage factor  $k = 2$ . The uncertainty associated with the measured distance is therefore  $u(D_{CMR}) = 0.28 \mu\text{m}$ , with a coverage factor of 1.



The possible tilt of the calibration frame stems from possible unevennesses in the parallel-blocks and faceplate, c.f. Table 5.1. The implication of this is that the distance between the two inner surfaces of the calibration frame might be experienced as greater than if there were no tilt of the frame.

The uncertainty associated with the possible tilt of the calibration frame is calculated as a "worst case" scenario. If the left hand side of the calibration frame is associated with the lowest permissible height, i.e. the faceplate is assumed to be in zero and the height of each of the two parallel-blocks are 80-0.3 mm, and if the right hand side of the calibration frame is associated with the maximum permissible height, i.e. the faceplate is assumed to be 26  $\mu\text{m}$  higher than that on the left hand side, and the height of each of the two parallel-blocks are 80+0.3 mm, then the difference between  $D$  and  $D_{tilt}$  is approximately 3.2  $\mu\text{m}$ . Note that this number can only be positive. i.e.  $D_{tilt} \geq D$ . Thus,  $u^2(D_{tilt}) = \left(\frac{3.2\mu\text{m}}{\sqrt{3}}\right)^2$ , where a rectangular distribution has been assumed.

The standard uncertainty associated with the inner distance distance of the calibration frame,  $D$ , is the positive square root of the variance

$$u^2(D) = u^2(D_{CMR}) + u^2(D_{tilt}) \approx u^2(D_{tilt}) \approx (1.9 \mu\text{m})^2. \quad (5.11)$$

#### Uncertainty of the thermal expansion coefficient, $u(\alpha_s)$

The standard uncertainty associated with the thermal expansion coefficient is evaluated as a Type B uncertainty. No information regarding the uncertainty of this coefficient is present at the time of writing. It is assumed that the uncertainty is better than  $\pm 2 \mu\text{K}^{-1}$ , where K is the temperature in Kelvin. Furthermore, a rectangular distribution is assumed such that the standard uncertainty is the positive square root of the variance:

$$u^2(\alpha_s) = \left(\frac{2.0\mu\text{K}^{-1}}{\sqrt{3}}\right)^2 \approx (1.2 \mu\text{K}^{-1})^2. \quad (5.12)$$

#### Uncertainty of the temperature difference, $u(\Delta T)$

The standard uncertainty associated with the temperature difference,  $\Delta T$ , is evaluated as a Type B uncertainty. The ASL F250 has a calibrated uncertainty given as  $\pm 0.01^\circ\text{C}$  [84].

Since no information regarding the temperature measuring unit at CMR Prototech is available at the time of writing it is assumed that the associated uncertainty with the temperature measuring unit is equal to that of the ASL F250. Therefore the same standard uncertainty will be used for both. The standard uncertainty associated with the the temperature measurement, is the positive square root of the variance, when a rectangular distribution is assumed [92]

$$u^2(T) = \left(\frac{0.01 \text{ K}}{\sqrt{3}}\right)^2 \approx (5.8 \cdot 10^{-3} \text{ K})^2. \quad (5.13)$$

Since  $T_{diff}$  is found by measurements with both instruments, the standard variance of the temperature difference,  $u^2(\Delta T)$ , is 4 times the standard variance  $u^2(T)$ , i.e.

$$u^2(\Delta T) \approx 4 \cdot (5.8 \cdot 10^{-3} \text{ K})^2 = (11.5 \cdot 10^{-3} \text{ K})^2. \quad (5.14)$$

#### Uncertainty of the measured distances, $u(d_1)$ and $u(d_2)$

The associated uncertainties of the measured distances,  $d_1$  and  $d_2$ , are regarded as identical, thus only the development for  $u(d_1)$  will be presented. The evaluation of  $u(d_1)$  is of both Type A and type B. The standard variance can then be expressed as

$$u^2(d_1) = s^2(\bar{d}_1) + u^2(d_{rep}) + u^2(d_{lin}) + u^2(d_{res}), \quad (5.15)$$

where  $s^2(\bar{d}_1)$  is the experimental variance of the mean,  $u(d_{rep})$  is the standard uncertainty reflecting the repeatability of the sensor,  $u(d_{lin})$  is the standard uncertainty reflecting the linearity of the sensor,  $u(d_{res})$  is the standard uncertainty reflecting the resolution of the sensor, c.f. Tab. 3.7.

$s^2(\bar{d}_1)$  is found to be in the range 0.01-0.03  $\mu\text{m}$ , and is regarded as negligible. The uncertainties associated with the repeatability and resolution are also regarded as negligible. Thus, Eq. 5.15 simplifies to

$$u^2(d_1) \approx u^2(d_{lin}) \approx (1.4 \mu\text{m})^2, \quad (5.16)$$

where a rectangular distribution of the linearity of the laser sensor has been assumed.

### Numerical results, $u(d_{x,i})$

Inserting the obtained values in Eq. (5.10) yields  $u(d_{x,i}) = 2.6 \mu\text{m}$ . It is recognized that the largest contributors to this uncertainty is the possible tilt of the calibration frame,  $u^2(D_{tilt})$  and the linearity of the laser sensor  $u(d_{lin})$ . The uncertainty associated with the thermal expansion coefficient,  $u(\alpha_s)$  contributes, however little, and the uncertainty associated with the temperature difference,  $u(\Delta T)$ , is negligible.

### 5.6.3 Numerical result for the combined standard uncertainty, $u_c(d_x)$

Inserting the values for  $u(d_{x,i})$  and  $s^2(\bar{d}_{x,i})$  in Eq. 5.8 reveals that  $s^2(\bar{d}_{x,i})$  is negligible from the combined standard uncertainty  $u_c(d_x)$ , i.e.  $u_c(d_x) \approx u(d_{x,i}) = 2.6 \mu\text{m}$ .

## 5.7 Translation pole

To be able to perform a distance measurement on the distance between the transmitter and receiver, a translation mechanism to allow the laser sensors to be positioned in between the transmitter and receiver had to be constructed. The construction of the mechanism was in large performed by the employees at the machine shop at UiB, in close cooperation with the current author. The objective was to obtain a mechanism that would contribute as little as possible to the uncertainty of the measured distance between the transmitter and receiver.

In Fig. 5.7 (a) the mechanism is shown elevated to the measurement position. The mechanism consists of a pole with a crank from Gitzo [105]. The pole and crank is originally designed to be used in photography. In Fig. 5.7 (b) the two sensors and the XYZ-translation stage are seen mounted on top of the pole in position for a distance measurement. In Fig. 5.7 (c) the translation mechanism is seen attached to the measuring cage.

To stabilize the mechanism, a steel block is mounted to the pole below the crank. A slit is crafted just below the crank such that when the pole is elevated, the steel block enters into the slit and is wedged in between the edges of the slit. There is a knob behind the slit that locks the pole in position.

To further stabilize the pole, just above the crank, two steel blocks are mounted around the pole. One of the steel block are fastened to the mechanism, while the other steel block is adjustable by two knobs. When the knobs are tightened, the adjustable steel block pushes the pole towards the fastened steel block. The purpose of this is to suspend the pole in exactly the same position each time the mechanism is elevated.

### Repeatability of the translation mechanism

To obtain data on the repeatability of the translation mechanism, four measurement series of each ten measurements have been conducted. In Fig. 5.8 (a) the calibration frame is shown suspended inside the measurement cage by two vices. It should be noted that it was not possible to suspend the calibration frame at the height of the piezoelectric disks. The maximum translation height was therefore approximately 0.11 m lower than the translation height used prior to the acoustical measurement. The implication of this is that the expected repeatability should be higher in value than what is found in the current section.

Prior to measurements, care has been taken to assure that the calibration frame is as best horizontally aligned with the measurement cage, and that the x-axis of the calibration frame is parallel with the laser beam. The measurements are performed by first lowering the mechanism to its lowest position, and thereafter translating it to the measurement position. After translation,

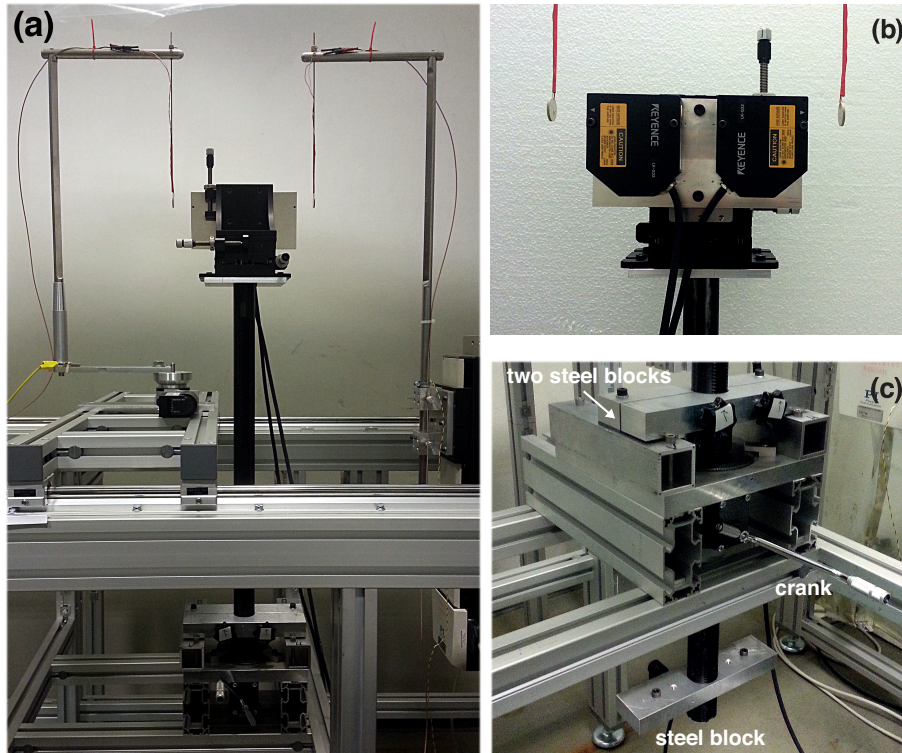


Figure 5.7: (a) the translation mechanism shown in its most elevated position, i.e. identical as it would be during a distance measurement prior to an acoustical measurement. (b) close up of the laser sensors and the XYZ-translation stage in between the transmitter and receiver, mounted on top of the pole. (c) close up of the translation mechanism. The lower steel block slides into a slit under the crank. The two steel blocks can be tightened around the pole by turning the knobs on the front.

there are observable vibrations in the measurement cage which are allowed to attenuate before a measurement is conducted. This process is repeated 10 times per measurement series. Before a new measurement series, the laser spots are moved to a new position by the XYZ-translation stage.

In Fig. 5.8 the results are shown as the standard deviation of ten measurements per measurement series. The largest value of the standard deviation is approximately  $27 \mu\text{m}$  for both sensors for the first measurement, and the lowest value is approximately  $10 \mu\text{m}$ , corresponding to the second measurement. Deviations in the repeatability between the four measurement series can partly be explained by the unevenness of the surface of the inside of the calibration frame. However, it is believed that most of the deviations should be associated with the translation mechanism itself.

The greatest value of the standard deviation will be associated with the repeatability of the translation mechanism. This is denoted  $u(\text{pole})$ . Note that dividing down with  $\sqrt{n}$  is not performed on  $u(\text{pole})$ .

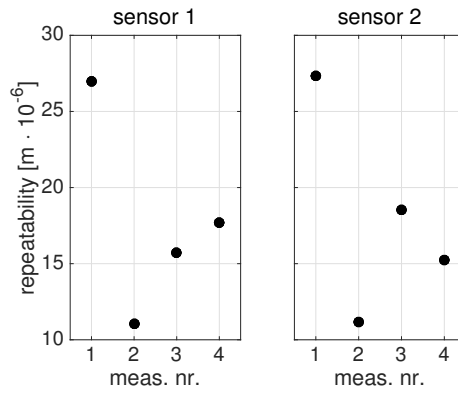
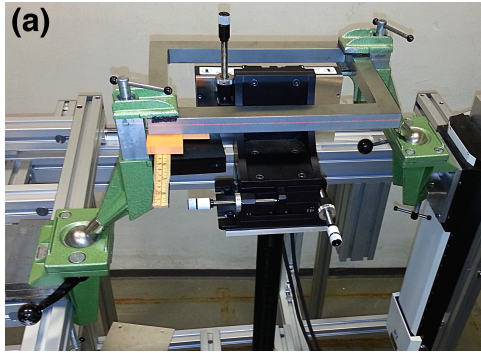


Figure 5.8: (a) image shows how the calibration frame has been suspended inside the measurement cage by two vices such that measurements on the repeatability of the elevation mechanism could be performed. (right) results for sensor 1 and 2 given as standard deviations obtained by 10 repeated measurements per measurement series.

# Chapter 6

## Results

In the present chapter the results obtained in the present work is presented. The results consist of the impedance measurement of the piezoelectric disks, as well as the impedance measurements performed with an oscilloscope. This will be presented in Sec. 6.1.

In Sec. 6.2.3 three parameters that might influence the FE-simulations are discussed.

Sec. 6.3 examines the SNR for two distances: 0.50 m and 0.85 m and the SNR discussion ends with recordings of noise as a function of distance.

In Sec. 6.4 the corrections used to obtain the open circuit loss-free transfer function  $H_{15open}^{VV}$  are presented for both magnitude and phase. If it is deemed insightful the corrections will be exemplified on either simulations of  $H_{15open}^{VV}$  or measurements.

In Sec. 6.5 the acoustic measurements are presented. The section begins with the measurements for  $H_{15open}^{VV}$  obtained at 0.50 m. In total there are four transmitter and receiver pairs that each have been measured four times. All 16 measurements are shown for both magnitude and phase. From the 16 measurements four are selected and from these four measurements two of the piezoelectric disks are calibrated according to the reciprocity method. The disks that are calibrated are denoted 04 and 07. The calibrated quantities are the receiving voltage sensitivity  $M_V$  and the transmitting voltage response  $S_V$ .

The chapter ends with Sec. 6.5.6 where the acoustic measurements performed at 0.85 m is presented. The four measurements on  $H_{15open}^{VV}$  that are used to calibrate the disks 04 and 07 are presented, and, as was the case for the calibrations at 0.50 m, the quantities that are obtained by calibration are  $M_V$  and  $S_V$ .

### 6.1 Impedance

In the present section the results of the impedance measurements on the piezoelectric disks used in the current thesis, disk 04, 07 and 11, will be presented. The measurements will be compared to FE-simulations. Simulations of the impedance of the various disks have shown to yield comparable results (not shown here), thus only one simulation of the impedance will be presented and this will be regarded comparable to all measurements. The measurements have been performed as given in Sec.3.9.1, and an excitation voltage of 0.1 V RMS is used for the impedance measurements. 0.1 V RMS is chosen such as not induce non-linear behavior in the disks. Investigation of the non-linearity of the piezoelectric disks are deferred to Sec.6.1.1.

For the disks used in the current thesis, the first radial mode, R1 or the R1-mode, is found around 90–125 kHz, and the second radial mode, R2 or the R2-mode, is found around 240–260 kHz. In Table 3.5 four of the characteristic frequencies were given for the R1- and R2-mode, and it was pointed out that for the R1-mode the frequency  $f_s$  is concurrent with  $f_m$ , and that the frequency  $f_p$  is concurrent with  $f_n$ . In Fig. 6.1 the  $f_m$  and  $f_n$  frequencies are indicated. Note that the discussions will be given with respect to the series- and parallel resonance frequencies.

In Fig. 6.1 the following quantities are presented: (a) magnitude of the admittance  $|Y_T|$ , (b) magnitude of the impedance  $|Z_T|$ , (c) phase of the admittance  $\angle Y_T$ , (d) phase of the impedance  $\angle Z_T$ . Fig. 6.1 presents the results for the full frequency range investigated in the current thesis, 50–300 kHz, and in Fig. 6.2 (a) and (c) the frequency range 95–105 of Fig. 6.1 (a) and (c) are

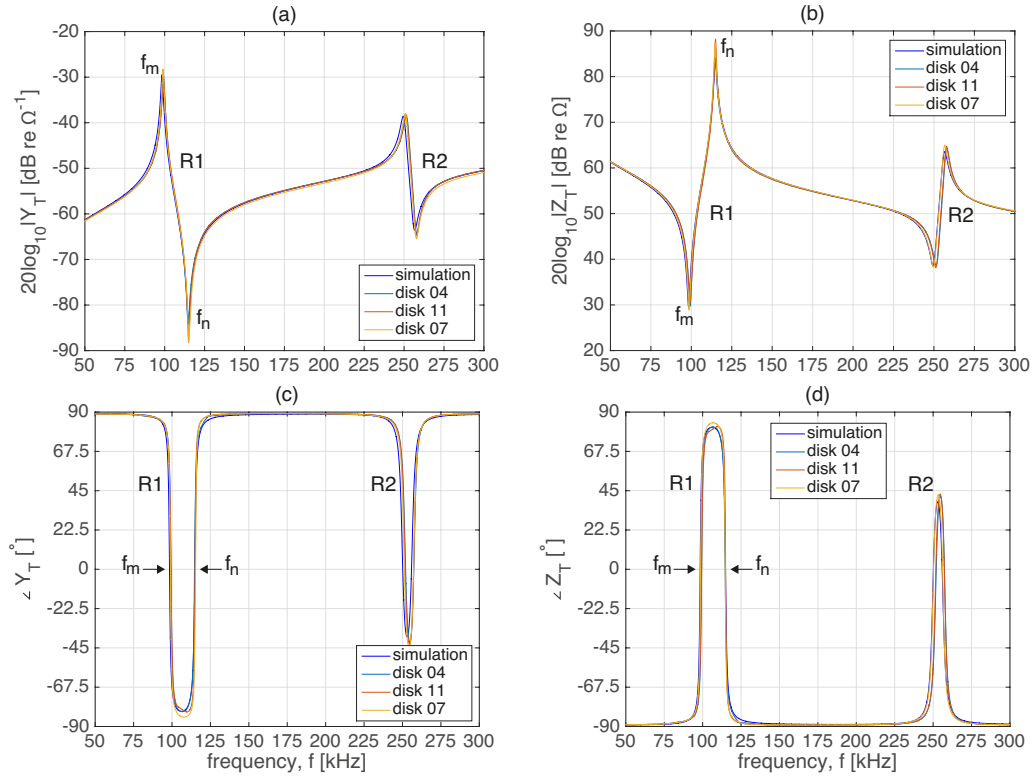


Figure 6.1: Admittance and impedance of the piezoelectric disks 04, 07 and 11, compared to FE-simulation. (a) magnitude of the admittance  $|Y_T|$ . (b) magnitude of the impedance  $|Z_T|$ . (c) phase of the admittance  $\angle Y_T$ . (d) phase of the impedance  $\angle Z_T$ . The two modes, R1 and R2, are indicated as well as the characteristic frequencies  $f_m$  and  $f_n$ .

given. In Fig. 6.2 (b) and (d) the frequency range 110–120 of Fig. 6.1 (b) and (d) are given.

In Fig. 6.1 a good overall agreement between the various measurements and simulations are seen. However, deviations are observed for especially the R2-mode and also for the R1-mode for both magnitude and phase. Outside the R1- and R2 modes slight deviations are observed, however these will not be discussed. The deviations are better appreciated in Fig. 6.2.

In Fig. 6.2 (a) disks 04 and 11 exhibit a fair agreement, while disk 07 deviates in both peak magnitude and for what frequency the peak occurs. The simulation is shifted down in frequency with 0.9 kHz compared to disks 04 and 11, and 0.6 kHz compared to disk disk 07. These frequency deviations are also observed in Fig. 6.2 (c), where the disks 04 and 11 tend to agree well, and the disk 07 shows a downwards shift in frequency. For  $f_s$  the simulation is shifted down in frequency with 0.9 kHz compared to disks 04 and 11, and 0.6 kHz compared to disk 07.

In Fig. 6.2 (b) slight deviations in the frequency corresponding to the peaks are observed. The simulation and disk 11 are comparable, while disk 04 and 07 are comparable. Disk 04 and 07 are shifted down in frequency with 0.3 kHz. A maximum deviation of 4.7 dB is observed between disk 11 and the simulation, and a deviation between disk 11 and disk 04 of 4 dB is observed.

In Fig. 6.2 (d) frequency deviations in the order of 0.4 kHz are observed between the measurements and simulations. As in (b) disk 11 exhibits the greatest value and disk 04 agrees best with the simulation.

In conclusion, it is observed that the disks used in the current thesis exhibits slightly different properties for the resonance frequencies investigated. The deviations discussed here translates to the acoustical measurements discussed in e.g. Sec.6.5.2 and Sec.6.5.5.

### 6.1.1 Impedance measurement with oscilloscope

In the present section the results of the impedance measurement performed with an oscilloscope will be presented, c.f. Sec. 2.11. The measurements have been performed on element 13, and the results are compared to that of the HP-impedance analyzer (HP). All measurements have been

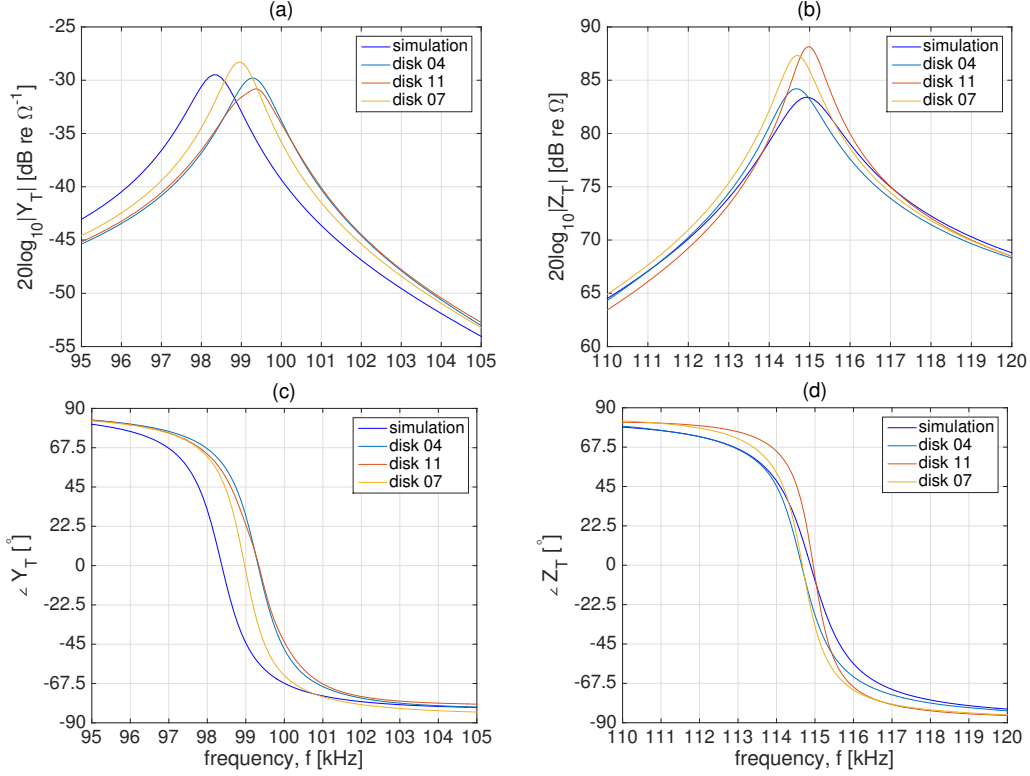


Figure 6.2: Same as Fig. 6.1 but for (a) and (c) 95–105 kHz; (b) and (d) 110–120 kHz.

performed through the cables, such that the impedances presented will not necessarily reflect the impedance of a free standing disk. Further more, the wires have been soldered onto the electrodes, c.f. Sec.3.2.6, such that the impedance of the disk might have been altered due to the heating process.

The investigation in the present section is performed to gain knowledge about the non-linear properties of the piezoelectric disks. A similar investigation was performed at the UiB by [100] and similar investigation can be found in the literature, e.g. [106].

Two different voltages have been used during the measurements with the oscilloscope, 60 mV and 4.0 V. The 60 mV measurement is used to compare the method with the results from HP, while the 4.0 V measurement is used to investigate the non-linear properties of the piezoelectric disk.

The actual voltage the terminals of the piezoelectric disk has been monitored during measurements, and attempted to be kept constant. With the standard laboratory equipment at hand, a perfectly constant voltage has not been practically realizable. Instead, an upper and lower voltage bound has been utilized. For the measurement with 60 mV, the recorded voltage at the terminals of the piezoelectric disk has a mean with a one standard deviation of  $59.1 \pm 0.28$  mV, and a corresponding maximum and minimum value of 59.8 and 58.0 mV, respectively. Similarly, the measurement with 4.0 V has a mean and a one standard deviation of  $4.004 \pm 0.0412$  V, and a corresponding maximum and minimum value of 4.05 and 3.97 V, respectively. Note that these values have been calculated in the Fourier domain.

To compare the HP measurement with the 60 mV oscilloscope measurement, the voltage at the terminals of the piezoelectric disk should be equal for all frequencies for both measurements.

However, the HP is equipped with an internal  $50 \Omega$  impedance in series with the load, such that the voltage at the terminals of the piezoelectric disk will be a function of the impedance of the disk. The HP outputs a  $V_{RMS}^{HP}$  given a termination of  $50 \Omega$ . Since the piezoelectric disk is expected to exhibit its most non-linear tendencies when the impedance tends to zero, the corresponding voltage drop over the piezoelectric disk is calculated using the impedance of the series resonance, which is found to be  $\approx 30 \Omega$ . The output voltage of the HP which corresponds to a peak voltage of 60 mV at the terminals of the piezoelectric disk given an impedance of  $30 \Omega$  is:  $V_{RMS}^{HP} \approx 115$  mV



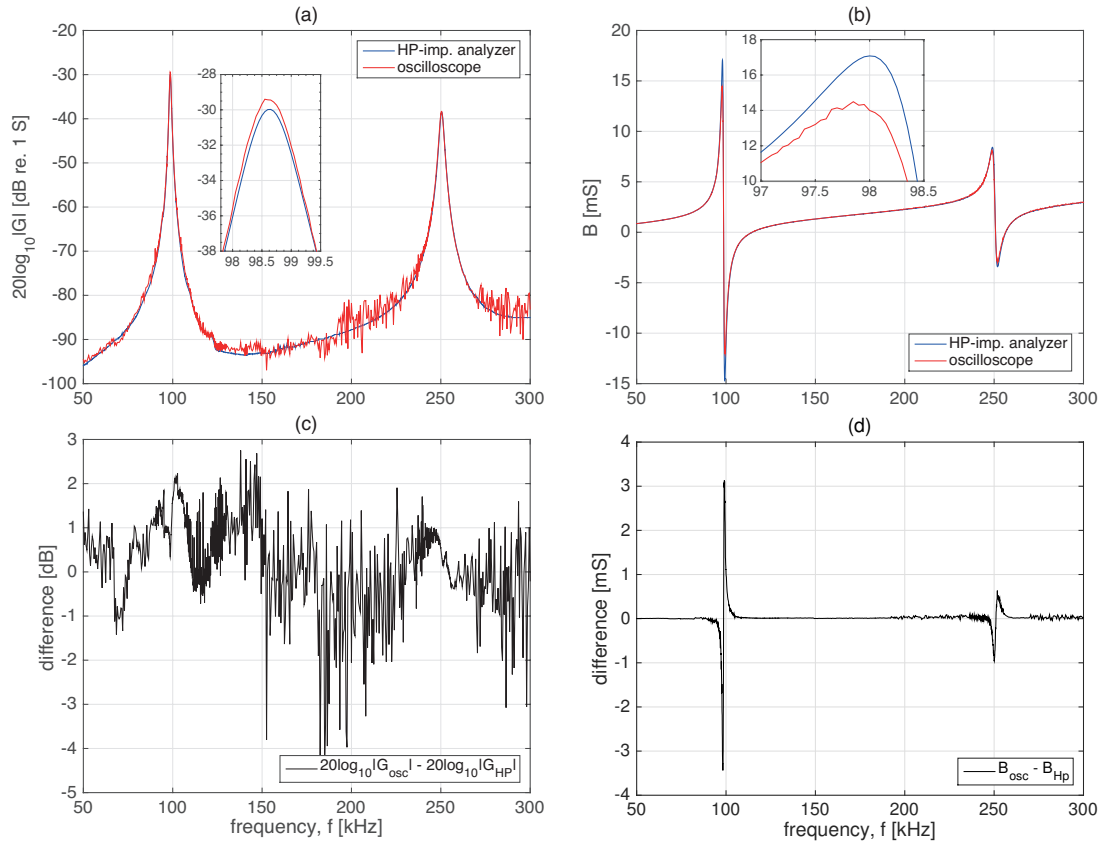


Figure 6.3: Comparison of the measurement on the impedance of a piezoelectric disk performed with an oscilloscope and the HP impedance analyzer. (a) conductance, (b) susceptance, (c) difference between the two measurements on conductance, (d) difference between the two measurements on susceptance.

RMS.

### Comparison of oscilloscope and HP-impedance analyzer measurements

In Fig. 6.3 the admittance (a) and susceptance (b) measured with the oscilloscope are compared to the HP measurement of the same quantities. In (c) and (d) the differences between the juxtaposed measurements in (a) and (b), respectively, are given. The oscilloscope measurements has utilized an approximate constant voltage at the terminals of the disk of 60 mV, and the HP measurement has utilized a comparable voltage at the terminals of the piezoelectric disk of 115 mV RMS.

In (a) a good overall agreement between the two measurements is observed, though the oscilloscope measurement shows a significantly more noisy tendency, especially in the lower decibel ranges. In the close up, an approximate deviation of 0.5 dB for the series resonance frequency is observed. In (c) it is observed that the deviations are mostly in the range  $\pm 2$  dB, though with some spikes extending as far as +3 dB and -4 dB. This general agreement is also observed in (d). However, for the R1- and R2-mode in (b), the agreement tends to disagreement, and an approximately  $\pm 3.2$  mS deviations are observed around the R1-mode, while approximately +0.5 and -1.0 mV deviations are observed around the R2-mode.

An alternative realization of the measurement in Fig. 6.3 is given in Fig. 6.4 as (a) impedance and (b) phase, with the differences of (a) and (b) given in (c) and (d), respectively. In (a) it is observed that the noise seen in Fig. 6.3 (a) is not as prominent. Also in (a) it is observed that a slight shifting of the frequency has occurred. This is enhanced in (c) around the parallel-resonance frequency (114-115 kHz) as the flipping from a positive value to a negative value. In (b) and (c) the same frequency shifting is observed. Although not readily appreciated in (b), but in the frequency range 50-98.65 kHz, the oscilloscope measurement is larger in value than the HP-impedance measurements. At 98.65 kHz this relationship is reversed, rendering the HP-impedance



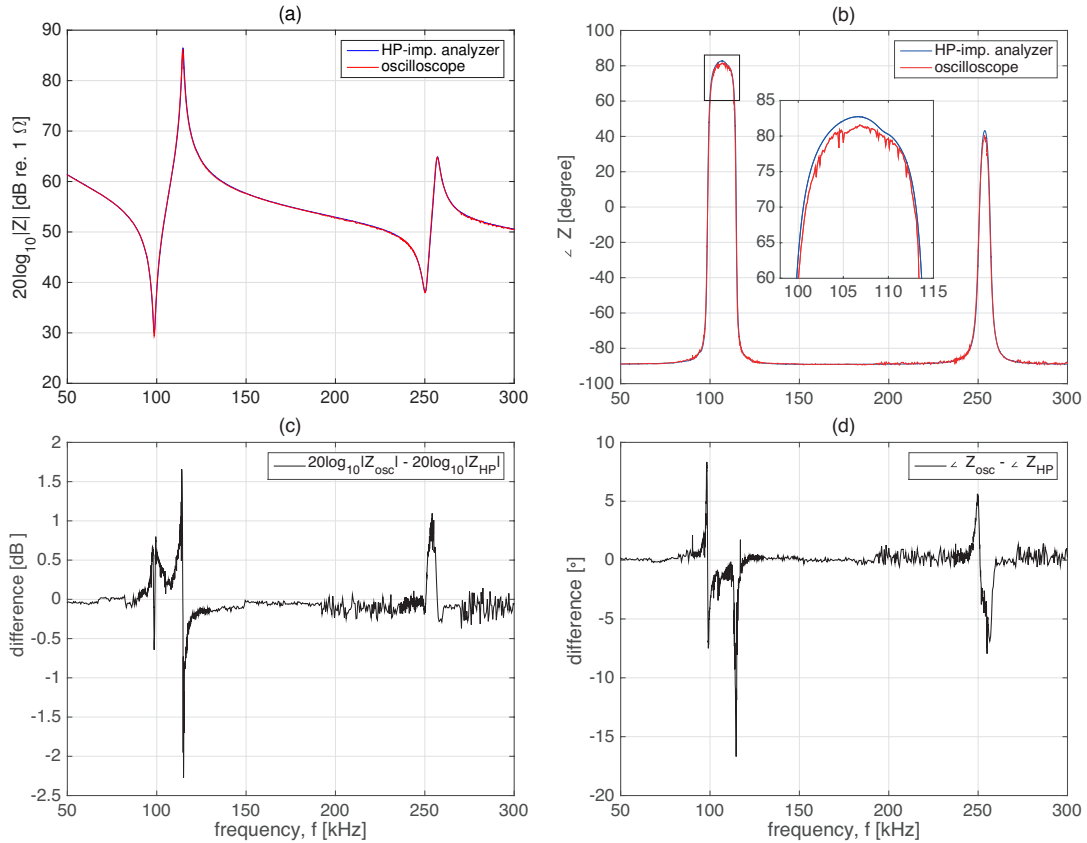


Figure 6.4: Same measurements as in Fig. 6.3 presented as (a) impedance, (b) phase of the impedance, (c) difference between the two measurements on the impedance, (d) difference between the two measurements on the phase .

measurement larger in value until approximately 120 kHz, from where the two curves are nearly indistinguishable, until the R2 mode.

Although the measurement with the oscilloscope has yielded quite fair results, and for most frequencies the difference is negligible, this is not necessarily so for the most important frequency range 90-110 kHz. In this range, the conductance shows a 0.5-2 dB deviation and the susceptance shows a relative large deviation of nearly 20%. The comparison between the impedances, and the corresponding phases, yields a similar discussion.

### Investigation of non-linearity in piezoelectric disk utilizing oscilloscope measurements

In Fig. 6.5 (a) the conductance, (b) susceptance, (c) and (d) the difference between the two oscilloscope measurements in (a) and (b), respectively, are given. To appreciate the non-linear tendency of the piezoelectric disk better, only a frequency range spanning R1 is presented. In both (a) and (b), the measurement with the HP-impedance analyzer is shown in green for comparison.

In (a) it is observed that the red curve tends to asymmetry while both the green and blue curve seem to be fairly symmetric about  $f_s$ . The peak magnitude of the 4.0 V measurements is reduced by 4.4 dB and the peak is shifted down in frequency with 0.85 kHz compared to the 60 mV measurement. This deviation is regarded as an effect of the non-linearity of the disk.

In (b) it is observed that the 4.0 V measurement has dropped off noticeably from the the 60 mV measurement. Although it seems fair to attribute this difference to non-linearity, the deviation between the HP and the 60 mV measurement renders any conclusion regarding the susceptance elusive.

In Fig. 6.6 (a) the impedance, (b) phase, (c) and (d) the difference between (a) and (b), respectively, are given. In (a) a fair agreement is observed between all three curves for the lower and upper frequencies. However, approaching  $f_s$  a clear deviation between the red and blue curve

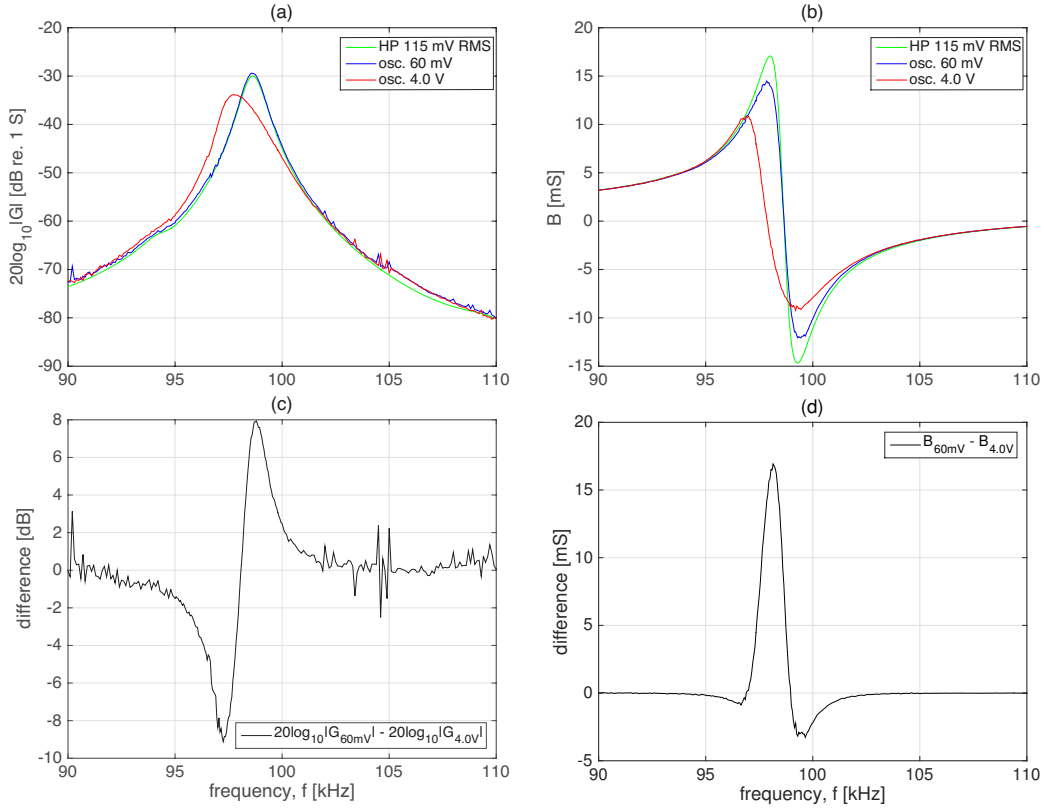


Figure 6.5: Comparison of the impedance measurement with oscilloscope for two excitation voltages, 60 mV and 4.0 V. The HP measurement with 115 mV RMS is juxtaposed in (a) and (b) for comparison. (a) conductance, (b) susceptance, (c) and (d) the difference between the two oscilloscope measurements in (a) and (b), respectively.

is observed. As in Fig. 6.5 (a) and (b) this deviation is attributed to the non-linear properties of the piezoelectric disk. The measurement with 4.0 V is shifted down in frequency with 0.85 kHz compared to the 60 mV measurement, and the dip exhibits an increase in magnitude of approximately 5 dB. In (c) a peak difference of +2.5 dB and -6.5 dB are observed.

In (b), although a slight difference between the 60 mV and HP measurement is observed, the difference between the 4.0 V and 60 mV measurement tends to dominate. Also here, a clear downward shift of approximately 1 kHz in frequency is observed for  $f_s$  at the R1-mode. In (d) a peak difference of -47.3° is observed for 97.8 kHz.

It is worth taking notice of that no significant deviations are observed for both magnitude and phase below 95 kHz and above 150 kHz. These frequency limits are used in Sec.6.5.1.

## 6.2 Parameters influencing the FE-simulations

Various parameters can influence the FE-simulation. Three parameters will be investigated in the current section, 1) material data sets, 2) the dimensions of the piezoelectric disks, and 3) the speed of sound used during simulations. Throughout the section the comparisons are performed with respect to the transfer function  $H_{15open}^{VV}$  for both magnitude and phase.  $H_{15open}^{VV}$  is obtained by simulations in the far-field, utilizing a far-field distance  $z_{ff} = 1000$  m, before being extrapolated to a realistic measurement distance  $d = 0.50$  m. For all simulations 7 elements per wavelength are used, such that the simulations have converged.

### 6.2.1 Effect of material data on FE-simulations

The material data set provided by Meggit Ferroperm [99], referred to as Ferroperm for short, is compared to the adjusted material data set used throughout the thesis. It is observed that there are differences between the results obtained with the data set from Meggit Ferroperm and the adjusted material data set developed at UiB [90].

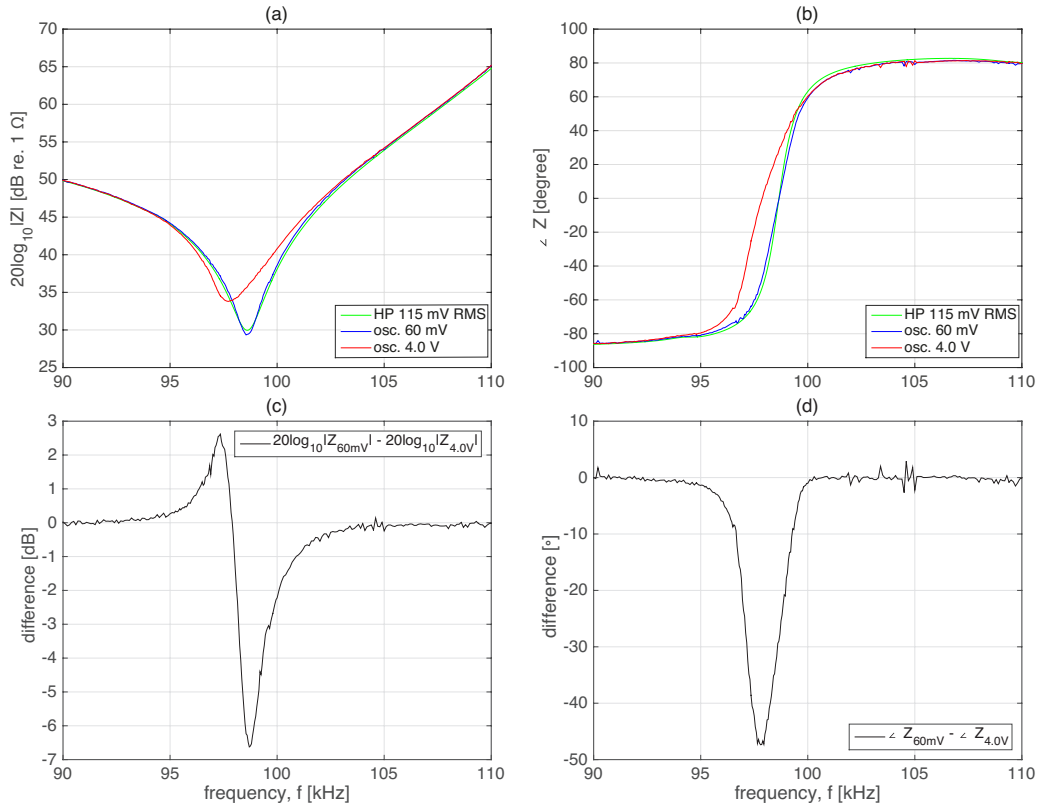


Figure 6.6: Same measurements as in Fig. 6.3 presented as (a) impedance, (b) phase of the impedance, (c) and (d) the difference between the two oscilloscope measurements in (a) and (b), respectively.

In Fig. 6.7 (a) the magnitude,  $|H_{15open}^{VV}|$ , and (b) the phase,  $\angle H_{15open}^{VV}$ , is given for both data sets for the transfer function  $H_{15open}^{VV}$ . In (a) it is observed that the adjusted material data set predicts a reduction in magnitude for the first peak of the R1-mode ( $\approx 100$  kHz) of approximately 2 dB, and a downwards shift in frequency of approximately 0.5 kHz. For the second peak of the R1-mode the reduction in magnitude is approximately the same, however the downwards frequency shift is now approximately 0.9 kHz. Interestingly, for the first peak of the R2-mode the frequency shifting has switched. The adjusted material data set is now shifted upwards of approximately 3.5 kHz compared to the Ferroperm data set, while approximately the same reduction in magnitude is observed.

In (b) the adjusted and Ferroperm data sets seem to agree fairly well for the R1-mode, however, large differences are observed for 1) the lower frequency ranges: 0–75 kHz, 2) the middle frequency ranges: 135–150 kHz, and 3) the high frequency ranges: 235–265 kHz. It is also observed that the frequency shifting of the magnitude and phase corresponds to one another.

## 6.2.2 Effect of disk dimension on FE-simulations

The influence the dimensions of the piezoelectric disks have on the FE-simulations are investigated. The investigation is only shown for two disks, but should be regarded as valid for all disks used in the current thesis as the estimated dimensions of the disks are comparable.

In Fig. 6.8 disk 07 (solid blue) and disk 12 (dashed red) are compared. The associated disk dimensions are given in Tab. 3.2.6. It is observed that the measurements of the dimensions have little influence on the FE-simulations of the two disks. Although not shown here, this is the observed tendency regarding all disks used in the current thesis.

The implications of this is that simulations of one disk is deemed representative for other disks of approximately the same dimensions.

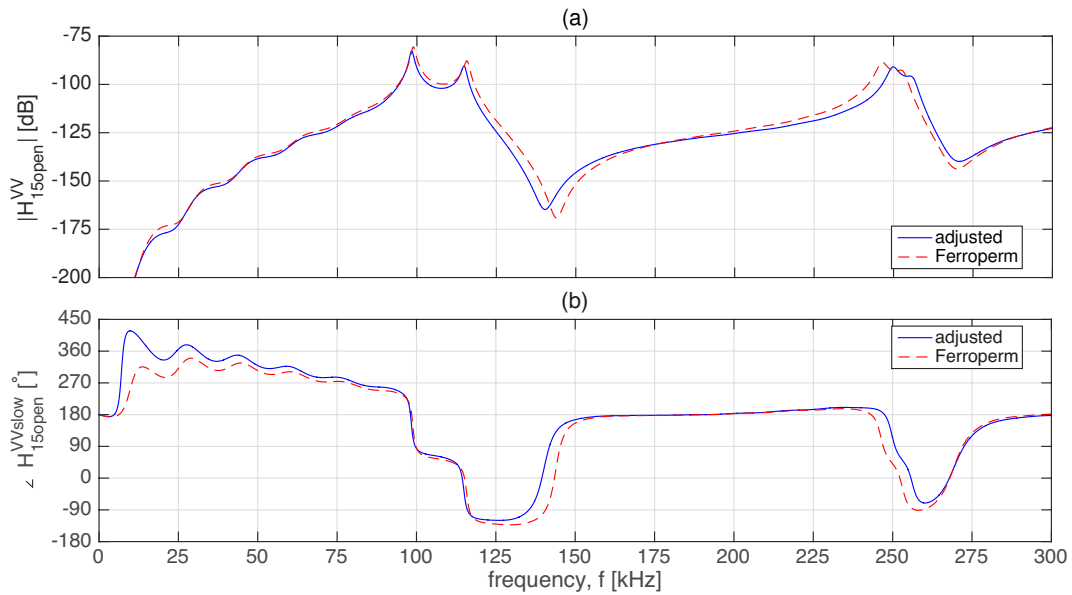


Figure 6.7: Comparison of a simulation of disk 07 for the adjusted (solid blue) and Ferroperm material data set. (a) magnitude, (b) phase.

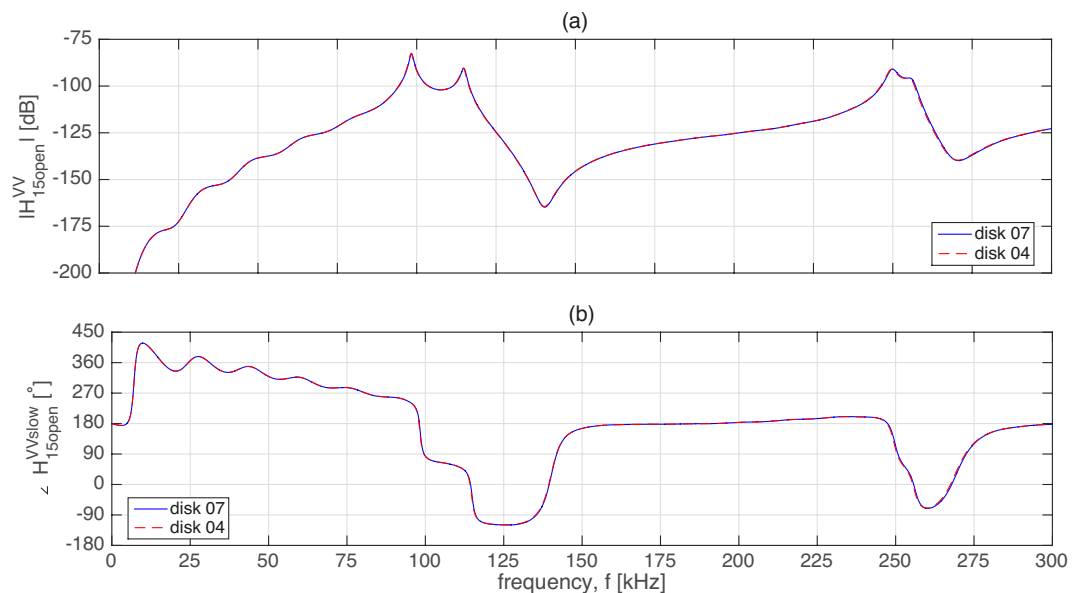


Figure 6.8: Comparison of the simulation of disk 07 (solid blue) and disk 04 (red dashed). The difference between the simulations are the estimates of the disk dimensions. (a) magnitude, (b) phase.

### 6.2.3 Effect of the sound speed in air on FE-simulations

The influence sound speed in air have on the FE-simulation are compared for two different sound speeds,  $c = 346.5$  m/s and  $c = 343$  m/s. The former represents a sound speed as it is observed in the acoustical laboratory during measurements, while the latter corresponds to the speed of sound in dry air at 20°C.

In Fig. 6.9 the results are given for (a) magnitude, and (b) phase. In both (a) and (b) it is observed that there are practically no difference between the two simulations. In the interference pattern stemming from the superposition of the sound waves emanating from the front surface of the disk and the side edges of the disk the largest deviations are seen (25–75 kHz). Interference as this is observed in the lower frequency ranges where the sound waves are expected to diffract more than in the higher frequency ranges. The deviations observed at 60 kHz for the magnitude

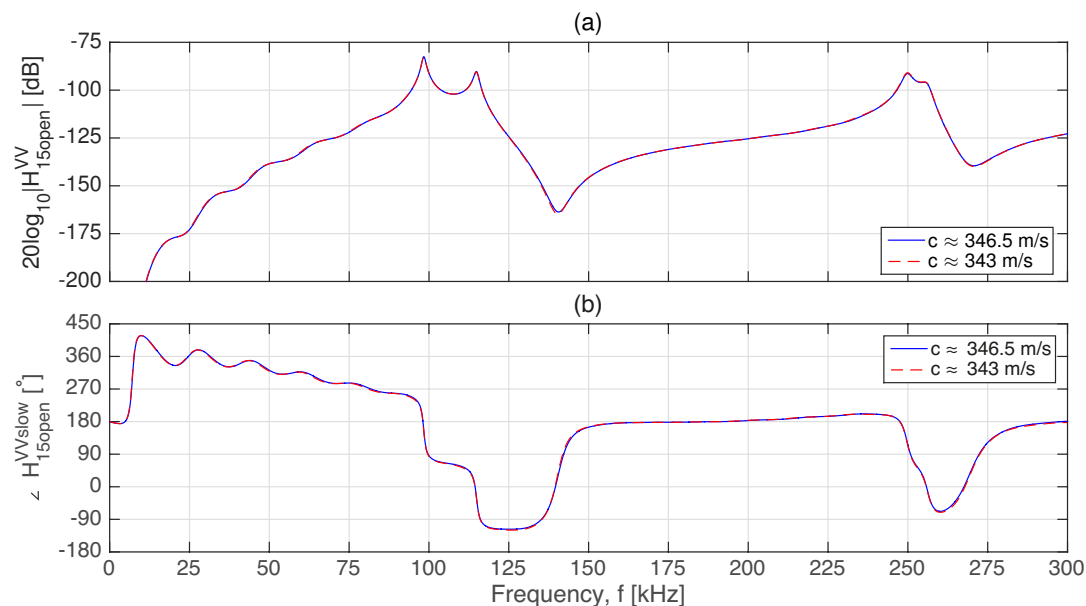


Figure 6.9: Comparison of the simulation of disk 07 given  $c \approx 346.5$  m/s (solid blue), and  $c \approx 343$  m/s (dashed red).

is approximately 0.5 dB, and for the phase a maximum deviation of  $3.3^\circ$  is observed at 64 kHz.

The implications of this is that the experienced fluctuations in the sound speed at the laboratory, do not need to be addressed in the FE-simulations.

#### 6.2.4 Summary of the results on FE-simulations

For the variations in the input parameters investigated, it is observed that neither the piezoelectric disk dimensions nor the speed of sound influence the FE-simulations noticeably. Although the material data sets investigated influence the FE-simulations, there exist a frequency range where the simulated phase seems to be unaffected by the material data set. In Fig. 6.7 (b) comparing the phase obtained with the Ferroperm data set and the adjusted data set, little or no deviations are observed for the frequency range 175–225 kHz. This frequency range is thus deemed valuable when comparing measurements with simulations, since it seems to be invariant of the three parameters investigated in the current section.

### 6.3 Signal-to-noise ratio

In the current section the results on the signal-to-noise ratio will be presented. The quantities under investigation are the signal-to-noise ratio given random and incoherent periodic noise,  $\text{SNR}_r$ , the signal-to-noise ratio given coherent electrical noise,  $\text{SNR}_c$ , c.f. Sec. 3.7.4. Both quantities will be investigated for for the frequency range 50–140 kHz and for two distances, 0.50 m and 0.85 m. Moreover, two excitation voltages, 10 V and 1 V, will be used, and both quantities will be investigated with and without the use of the Faraday shield.

The noise will also be investigated as a function of distance.

In [4] it is stated that a SNR larger than 20 dB yields an error of about  $\pm 1$  dB. This translates to about  $\pm 10\%$  error. In the context of calibration an error of about  $\pm 10\%$  is regarded as quite large, thus a criterion of SNR larger than 40 dB will be discussed, which corresponds to approximately  $\pm 1\%$  error. This does not guaranty that the calibrated quantities will be given with  $\pm 1\%$  error.

### 6.3.1 Effect of Faraday shield on signal-to-noise ratio

#### Separation distance 0.50 m

In Fig. 6.10 the results obtained for the separation distance  $d = 0.50$  m are presented. In (a) and (c) the signal-to-noise ratio given random and incoherent periodic noise,  $\text{SNR}_r$ , obtained with and without the Faraday shield is presented for (a) 10 V, and (c) 1 V. While in (b) and (d) the signal-to-noise ratio given coherent electrical noise,  $\text{SNR}_c$ , obtained with and without the Faraday shield is presented for (b) 10 V, and (d) 1 V.

In Fig. 6.10 (a) it is observed that the use of the Faraday shield do not seem to have any significant influence on the  $\text{SNR}_r$ . It is also observed that a  $\text{SNR}_r > 40$  dB is achieved for the frequency range 70–125 kHz.

In Fig. 6.10 (b), however, the effect of the Faraday shield is apparent. The two curves seem to be overlapping from 50–100 kHz, and from 125–140 kHz. However, for  $f = 112$  kHz<sup>1</sup> an increase of approximately 15 dB in  $\text{SNR}_c$  is observed when the Faraday shield is used.

In (a) the  $\text{SNR}_r \approx 70$  dB given  $f = 112$  kHz, for both curves. Comparing this value with the  $\text{SNR}_c$  in (b) given no Faraday shield, a reduction of approximately 50 dB is observed. The same comparison, now with respect to the measurement with the Faraday shield, yields a reduction of approximately 35 dB. Moreover, for the shielded case in (b), it is observed that, except the 3 dB dip at 112 kHz, a  $\text{SNR}_c > 40$  dB is achieved for a frequency range 75–125 kHz.

In Fig. 6.10 (c) and (d) it is observed that no significant distinction between the measurements with and without the Faraday shield is observed. It is also observed that a  $\text{SNR} > 40$  dB is achieved for the frequency range 90–105 kHz, except some minor deviations around 90–92 kHz for both (c) and (d).

The frequency range 70–125 kHz is thus deemed to be associated with a  $\text{SNR} > 40$  dB given that the Faraday shield is used.

#### Separation distance 0.85 m

In Fig. 6.11 the results obtained for the separation distance  $d = 0.85$  m are presented. In (a) and (c) the signal-to-noise ratio given random and incoherent periodic noise,  $\text{SNR}_r$ , obtained with and without the Faraday shield is presented for (a) 10 V, and (c) 1 V. While in (b) and (d) the signal-to-noise ratio given coherent electric noise,  $\text{SNR}_c$ , obtained with and without the Faraday shield is presented for (b) 10 V, and (d) 1 V.

Comparing Fig. 6.11 (a) and (b) it is observed that no significant deviations can be made for the four curves, except in (b) for the measurement without a Faraday shield. For 110–120 kHz a dip in value is observed. This dip is attributed the coherent noise. It is observed that a  $\text{SNR} > 40$  dB is achieved for the frequency range 80–115 kHz.

Fig. 6.11 (c) and (d) no significant deviations between the four curves are seen, and a  $\text{SNR} > 40$  dB is achieved for the frequency range 95–105 kHz.

### 6.3.2 Noise as a function of distance

It is of interest to investigate the distance dependency of the random and incoherent periodic noise,  $V_r$ , and coherent electrical noise,  $V_c$ . If e.g.  $V_c \approx 0$  for a given distance, then this distance should be used as a measurement distance,  $d$ , if only the SNR was taken into account.

The distance dependency of the noise is recorded by moving the receiver from  $d = 0.50$  m to 0.85 m, in steps of 0.005 m. The acrylic plate is mounted in between the transmitter and receiver when  $V_c$  is recorded, and  $V_{gen} = 0$  when  $V_r$  is recorded, c.f Sec.6.3. The results are given in Fig. 6.12 for (a) 100 kHz, and (b) 112 kHz. The results are given in decibels and are valid for a generator voltage  $V_{gen} = 10$  V. Note that the results in Fig. 6.12 are obtained without the use of the Faraday shield, c.f. Fig. 6.13 for a comparison of the use of the Faraday shield.

In Fig. 6.12 (a) no significant difference between  $V_c$  and  $V_r$  is observed, and the noise level tend to approximately -80 dB. In (b), however, a difference between  $V_c$  and  $V_r$  is observed. It is

---

<sup>1</sup>Note that the 112 kHz corresponds well with the parallel resonance frequency,  $f_p$ , discussed in Sec.6.5.2. However, in Sec.6.5.2 it was stated that  $f_p \approx 114.6$  kHz. This discrepancy is understood by the influence of the transfer function  $H_{5open5'}^{VV}$  discussed in Sec.6.4.2.  $H_{5open5'}^{VV}$  influences the recorded voltages, such that the peak observed at 114.6 kHz is shifted to approximately 112 kHz.

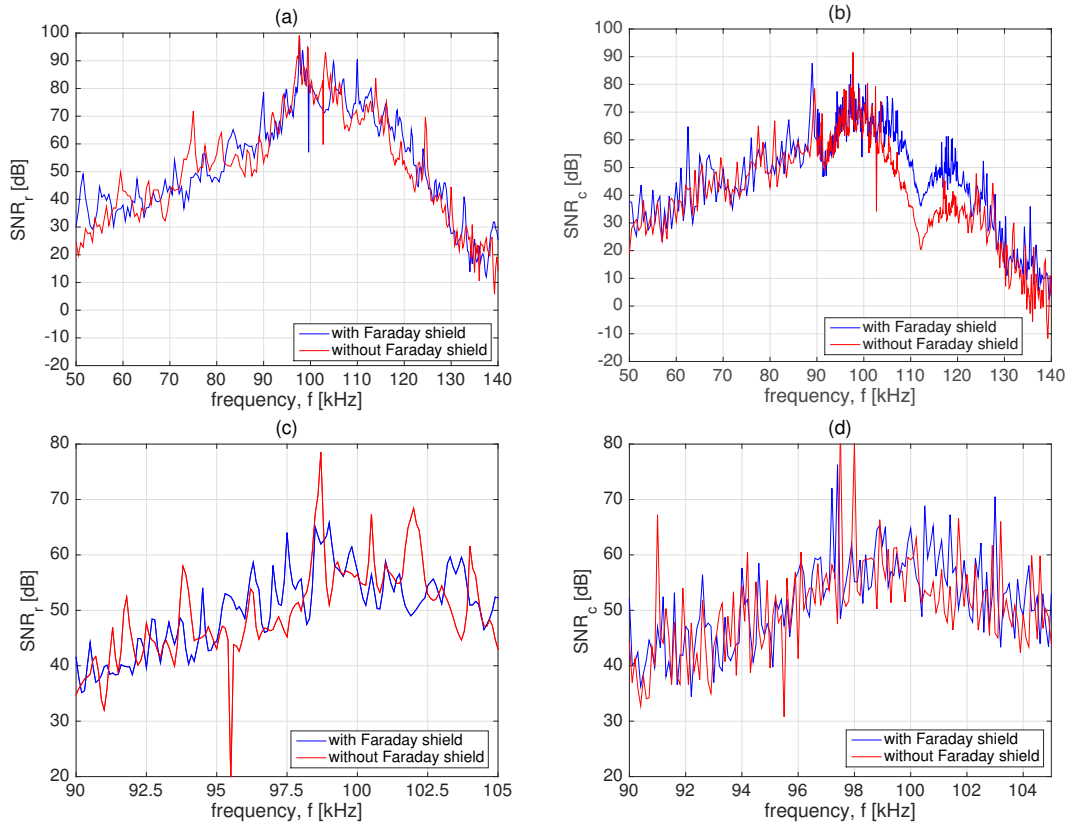


Figure 6.10: SNR given random and incoherent periodic noise (a) and (c), and coherent electric noise (b) and (d). In (a) and (b) an excitation voltage of 10 V has been utilized, while in (c) and (d) an excitation voltage of 1 V has been utilized. In all figures the blue curve corresponds to measurements where the Faraday shield has been used, and the red curve corresponds to measurements where the Faraday shield has not been used. For all figures a separation distance of 0.50 m has been utilized.

observed that the coherent noise decays exponentially as a function of distance. In the figure this is seen as a linear decay due to the logarithmic scaling. Another aspect that is interesting, is that  $V_r$  in (b) tends to approximately -65 dB. That is approximately 15 dB higher than in (a). This is understood by comparing the frequencies:  $\approx 112$  kHz corresponds well with the frequency where the disk is at it most sensitive as a receiver, and  $\approx 110$  kHz corresponds well with the frequency where the disk is at its most responsive as a transmitter.

A comparison of  $V_r$  and  $V_c$  where the Faraday shield has been utilized is performed. The comparison is only given for  $f = 112$  kHz as the coherent noise do not seem to be present when  $f = 100$  kHz. In Fig. 6.13 the results are presented. The solid blue and red curves are inherited from Fig. 6.12 (b), the blue curve with squares is  $V_c$  given a measurement with a Faraday shield, and the red curve with squares is  $V_r$  given measurements with a Faraday shield.

Comparing the coherent electric noise first, it is observed that the by utilizing a Faraday shield a decline in the noise level of 11-12 dB is achieved.<sup>2</sup>

It is observed that  $V_r$  has declined by approximately 10 dB after introducing the Faraday shield. This is understood if some of the noise can be attributed electromagnetic fluctuations in the laboratory. Thus, the receiver is also shielded from these disturbances with the use of the Faraday shield.

<sup>2</sup>Note that in Fig. 3.15 (b) a difference of approximately 15 dB was observed for  $d = 0.50$  m. This deviation is explained by a slightly different position of the Faraday shield. If the Faraday shield on the transmitting side is positioned closer to the receiver, i.e. it is moved along the positive z-axis, a decline in the coherent noise is observed, however, this can possibly also lead to reflections that are perceived as interference. The measurements in the current section has utilized a position of the Faraday shield's front at  $z \approx 0.05$  m, while the measurements in Fig. 3.15 (b) has utilized a position of the Faraday shield's front at  $z \approx 0.08$  m. Some deviations are thus expected.

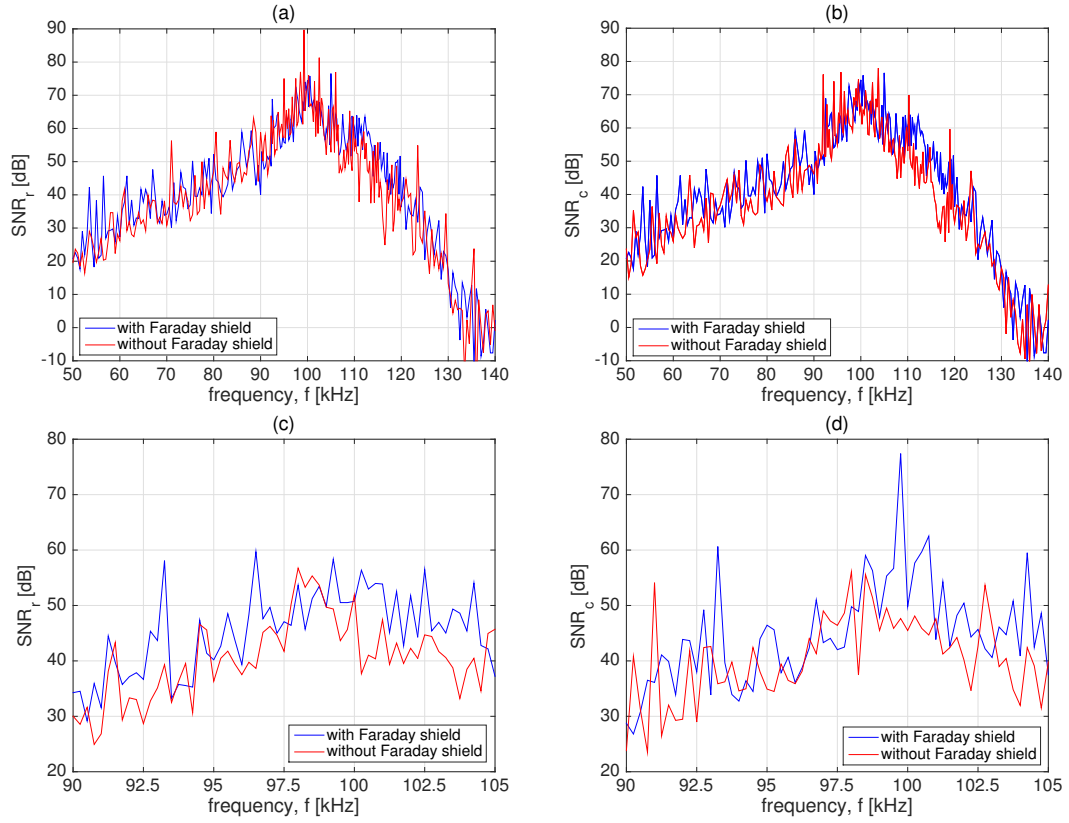


Figure 6.11: SNR given random and incoherent periodic noise (a) and (c), and coherent electric noise (b) and (d). In (a) and (b) an excitation voltage of 10 V has been utilized, while in (c) and (d) an excitation voltage of 1 V has been utilized. In all figures the blue curve corresponds to measurements where the Faraday shield has been used, and the red curve corresponds to measurements where the Faraday shield has not been used. For all figures a separation distance of 0.85 m has been utilized.

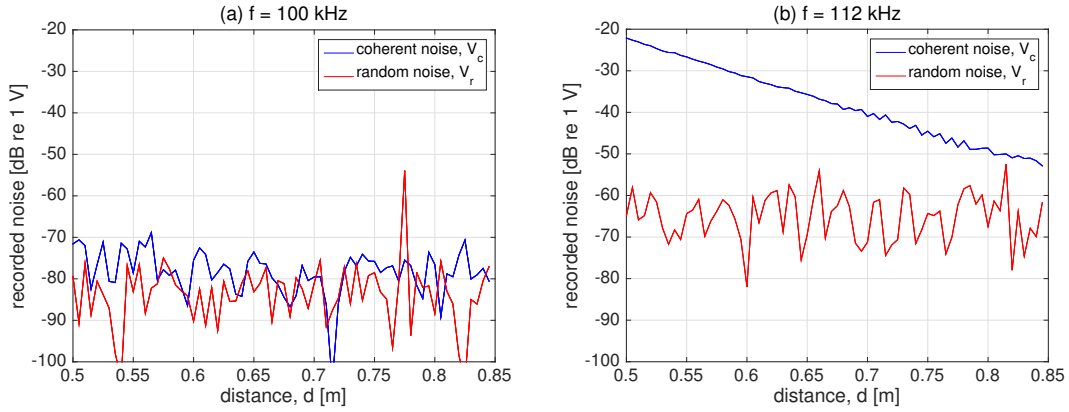


Figure 6.12: Random and incoherent periodic noise,  $V_r$ , and coherent electric noise,  $V_c$  as a function of distance. (a) 100 kHz, (b) 112 kHz. The receiver has been moved from  $d = 0.50$  m to  $d = 0.85$  m in steps of 0.005 m. Note that these results are obtained without the use of the Faraday shield.

## 6.4 Corrections performed on the recorded voltages

In the current section the corrections performed on the recorded voltages to obtain the open circuit, loss free transfer function  $H_{15open}^{VV}$  will be presented. The corrections refer to the transfer functions defined in Sec.2.1.2. A short description of the corrections will be presented.

$H_{0m1}^{VV}$  is referred to as the transmitting electronics. This includes the function generator, the coaxial cable 1 connecting the function generator the transmitting disk and the coaxial cable 2



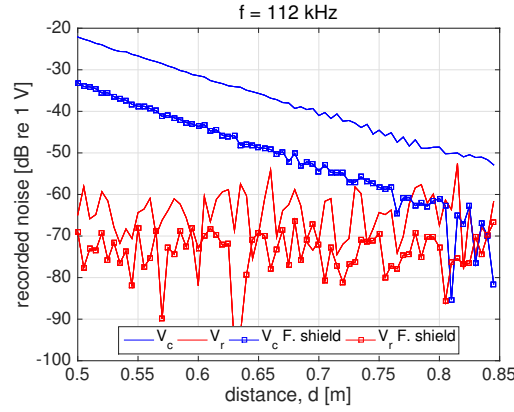


Figure 6.13: Random and incoherent periodic noise,  $V_r$ , and coherent electric noise,  $V_c$  as a function of distance compared to the use of the Faraday shield and without the use of the Faraday shield for  $f = 112$  kHz. The solid blue and red curves are inherited from Fig. 6.12 (b), and the blue curve with squares is the coherent noise,  $V_c$ , given measurement with a Faraday shield, and the red curve with squares is the random noise,  $V_r$ , given measurements with a Faraday shield

connecting the function generator to the oscilloscope, as well as the impedance of the transmitting disk.

$H_{5open5'}^{VV}$  models the signal propagation from the output of the receiving disk to the input of the amplifier. This includes the coaxial cable 3 connecting the receiver and the amplifier, and the impedance of the transmitting disk is a part of the correction.

$H_{5'6open}^{VV}$  is the amplifier and filter transfer function, obtained by measurements.

$H_{6open6}^{VV}$  models the signal propagation from the output of the amplifier to the oscilloscope. This includes the coaxial cable 4.

$C_\alpha$  is the correction accounting for attenuation losses in air.

$C_{dif}^{SFDC}$  and  $C_{dif}^{BPDC}$  are the corrections for possible diffraction effects.

In [2] the above correction were shown for magnitude, and in [3] a thorough review of  $H_{5'6open}^{VV}$  was given for both magnitude and phase for different Gain and filter settings.

#### 6.4.1 Correction $H_{0m1}^{VV}$ and $H_{6open6}^{VV}$

In Fig. 6.14 the transfer functions  $H_{0m1}^{VV}$  and  $H_{6open6}^{VV}$  are given for (a) magnitude and (b) phase. It is observed that both transfer functions for magnitude tend to 0 dB, and the phase tend to  $^\circ$ . For the magnitude, it is observed that the greatest sum of both transfer functions are in the range -0.06 to +0.09 dB. Excluding both transfer functions would thus lead to a deviation of approximately  $\pm 1\%$ . For the phase, the greatest sum of both transfer functions are experienced for  $f = 250$  kHz, and is approximately  $-1.7^\circ$ . Both transfer functions are regarded as negligible, though they are included in the corrections throughout the thesis.

#### 6.4.2 Correction $H_{5open5'}^{VV}$

In Fig. 6.15 the transfer function  $H_{5open5'}^{VV}$  is given for (a) magnitude and (b) phase. For  $|H_{5open5'}^{VV}|$  the correction exhibits its peak values for  $f = 112$  kHz, and the value is in the range -12.5 to +10 dB. For the phase, the correction is constant and equal to zero for most frequencies, however, around the R1- and R2-mode the correction takes on the peak values  $-120^\circ$  and  $-40^\circ$ , respectively.  $H_{5open5'}^{VV}$  is regarded as an important correction in the system model.

Although Fig. 6.15 yields important insight into  $H_{5open5'}^{VV}$ , it is of interest to see how the correction influences the transfer function  $H_{15open}^{VV}$ . To show this,  $H_{15open}^{VV}$  is multiplied with the correction  $H_{5open5'}^{VV}$ . In Fig. 6.16 (a) the magnitude of the transfer function  $H_{15open}^{VV}$  (solid blue) is juxtaposed with the magnitude of the transfer function  $H_{15open}^{VV}$  given  $H_{5open5'}^{VV}$  is multiplied with  $H_{15open}^{VV}$ . The greatest effect of the correction is for  $f = 112$  kHz, where it is observed that the second peak is shifted 2.7 kHz down in frequency. In Fig. 6.15 (b), where the same configuration

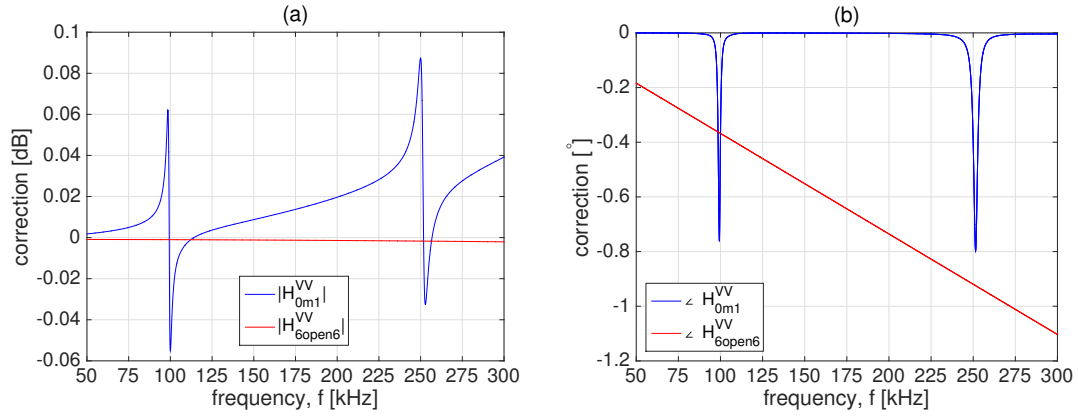


Figure 6.14: (a) magnitude of the transfer functions  $|H_{0m1}^{VV}|$  and  $|H_{6open6}^{VV}|$ . (b) phase of the transfer functions  $\angle H_{0m1}^{VV}$  and  $\angle H_{6open6}^{VV}$ .

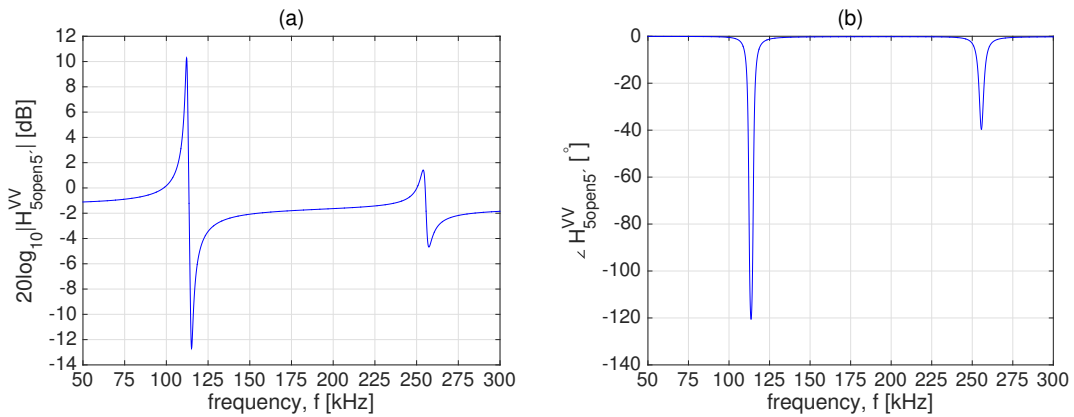


Figure 6.15: (a) magnitude of the transfer function  $|H_{5open5'}^{VV}|$ . (b) phase of the transfer function  $\angle H_{5open5'}^{VV}$ .

as in (a) is given, though for the phase the same downwards shift in frequency is experienced. Noticeably, is that the first peak of the R1-mode seem to be unaffected by the correction.

#### 6.4.3 Correction $H_{5'6open}^{VV}$

In Fig. 6.17 the transfer function  $H_{5'6open}^{VV}$  is given for (a) magnitude and (b) phase. The solid blue curves in both (a) and (b) are the results of the measurement on the transfer function  $H_{5'6open}^{VV}$  obtained in the current thesis by the mean of ten repeated measurements, c.f. Sec.3.9.3. In Fig. 3.21 (d) the ten repeated measurements for the magnitude is shown. In Fig. 6.17 (a) the solid red curve, and the red dashed curve in (b) are the results obtained by Søvik [3]. For the phase, no noticeable deviations are observed, however there is a slight deviation in the magnitude. For  $f = 60$  kHz, a deviation of 0.6% is observed, where the results obtained in the current thesis is larger in value. Moreover, the blue curve tends to exhibit a more noisy tendency. This is attributed the use of different FFT-subroutines and different regimes to remove the spikes, c.f. Sec.3.9.3.

The influence the magnitude  $|H_{5'6open}^{VV}|$  has on the transfer function  $H_{15open}^{VV}$  will not be shown, however, the influence the phase  $\angle H_{5'6open}^{VV}$  has on  $H_{15open}^{VV}$  is given in Fig. 6.19. As in Sec.6.4.2, the effect the correction has on  $H_{15open}^{VV}$  is shown by multiplying  $H_{15open}^{VV}$  with the correction. Clearly,  $\angle H_{5'6open}^{VV}$  has great influence on  $\angle H_{15open}^{VV}$ , and the transfer function  $H_{5'6open}^{VV}$  is regarded as an important correction in the system model.

#### 6.4.4 Correction accounting for propagation losses in air, $C_\alpha$

The correction accounting for propagation losses in air,  $C_\alpha$ , is exemplified in Fig. 6.19 where the simulated magnitude of the transfer function  $|H_{15open}^{VV}|$  is given for the two separation distances

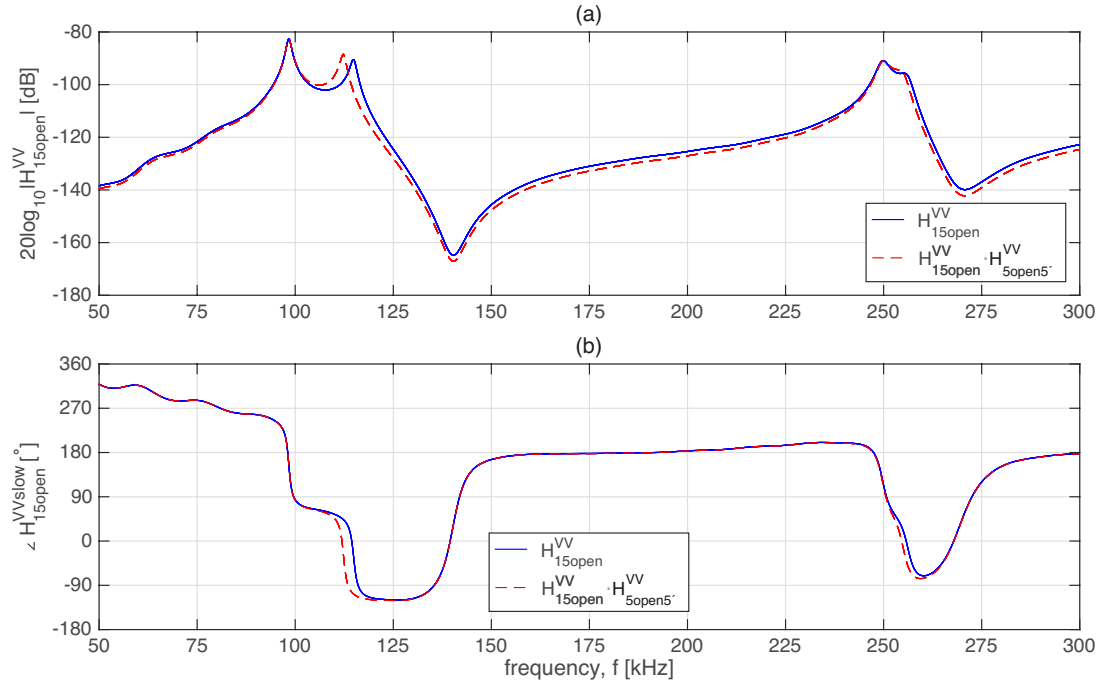


Figure 6.16: (a) (solid blue) magnitude of the transfer function  $H_{15open}^{VV}$ , (dashed red) magnitude of the transfer function  $H_{15open}^{VV}$  given  $H_{5open5'}^{VV} = 0$ . (b) same as (a) but for phase the slowly varying phase.

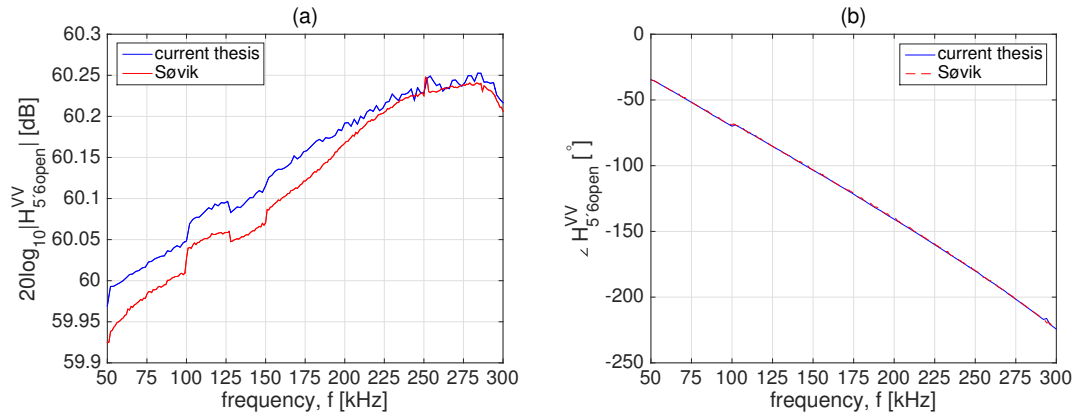


Figure 6.17: (a) magnitude of the transfer function  $|H_{5'6open}^{VV}|$  for the results obtained in the current thesis (blue) compared to the results obtained by Søvik [3]. (b) same as (a) but for phase  $\angle H_{5'6open}^{VV}$ .

used in the current thesis (a)  $d = 0.50$  m, and (b)  $d = 0.85$  m. The solid blue line shows  $|H_{15open}^{VV}|$  without propagation losses, and the dashed red line shows  $|H_{15open}^{VV}|$  with propagation losses. Since  $C_\alpha$  corrects for possible propagation losses, the inverse of the correction is multiplied with the loss free transfer function  $|H_{15open}^{VV}|$  to show the effect of the propagation losses. As expected the propagation losses is a strong function of frequency [57], and the propagation losses for  $f \approx 250$  kHz is 1.42 dB given  $d = 0.50$  m, and 2.42 dB given  $d = 0.85$  m.

#### 6.4.5 Correction accounting for possible diffraction effects, $C_{dif}$

In the current section the two different formulations for the diffraction correction used to correct the measurements for possible diffraction effects will be presented. In Fig. 6.20 the two models are juxtaposed for (a) magnitude, and (b) phase for the separation distances  $d = 0.85$  m (solid line)  $d = 0.50$  m (dash dotted line). In both figures, the blue curves corresponds to  $C_{dif}^{SFDC}$ , and the red curves corresponds to  $C_{dif}^{BPDC}$ . An overall agreement between the two models are observed for

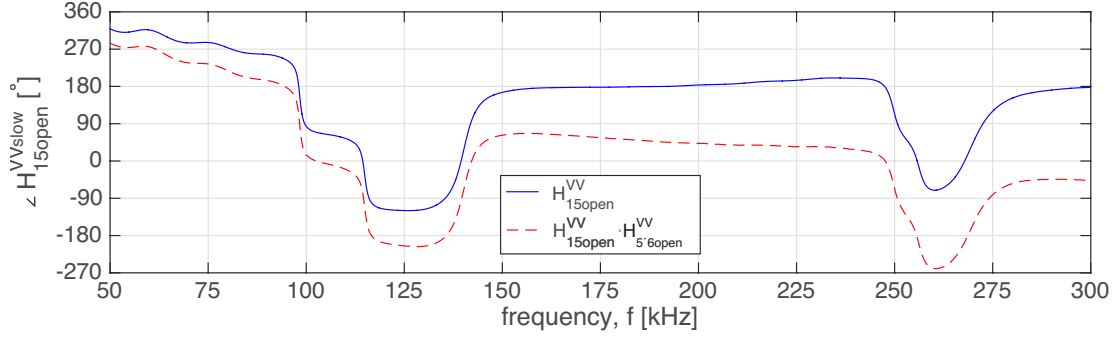


Figure 6.18: Phase of the transfer function  $H_{15open}^{VV}$  (solid blue) and phase of the transfer function  $H_{15open}^{VV}$  given  $H_{5'6open}^{VV} = 1$ .

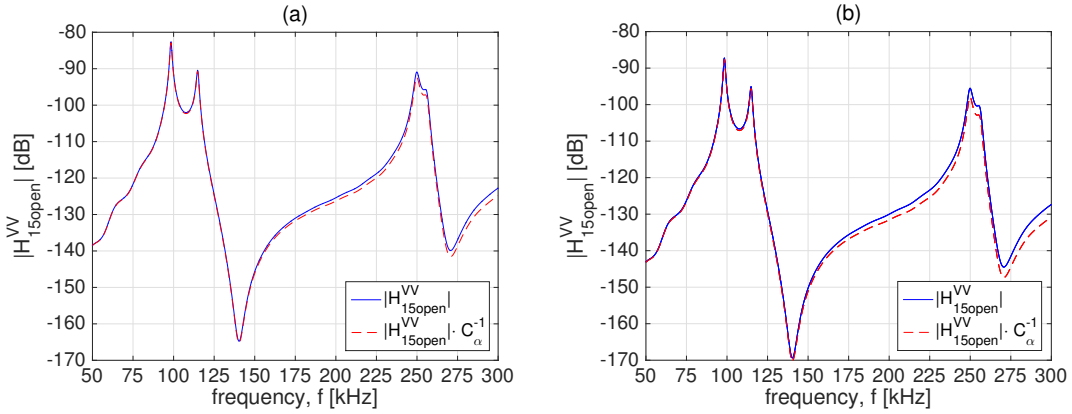


Figure 6.19: Simulation of the magnitude of the transfer function,  $|H_{15open}^{VV}|$ , without propagation losses (solid blue) and with propagation losses (dashed red). The transfer function is simulated at (a)  $d = 0.5$  m, and (b)  $d = 0.85$  m.

both magnitude and phase, however  $C_{dif}^{SFDC}$  exhibits strong fluctuations for certain frequencies, while the  $C_{dif}^{BPDFC}$  appears to exhibit a linear change. In (a) it is worth noticing that the SFDC predicts a correction lower than 1. The physical reason behind this is not investigated, however, in Fig. 6.21 an explanation as to the origin of the decrease is observed.

In Fig. 6.21 the transfer function,  $H_{15open}^{VV}$  is simulated utilizing the near-field model (solid blue) and the far-field model (dashed red) defined in Secs.2.7.2 and 2.7.1, respectively, for (a) magnitude and (b) phase.

In 6.21 (a) deviations between the two models are seen especially at 140 and 270 kHz. The lower frequency range 70–75 kHz is magnified. In this frequency range it is observed that the near-field model predicts a magnitude higher in value than the far-field model. The near-field model utilizes a free-field integration area of equal size as the receiver to obtain the sound pressure at a separation distance  $d$ . Although, the free-field integration area is placed in the far-field of the receiver, one can expect small deviation due to spherical waves over the free-field integration area. This should be associated with a decrease in magnitude compared to an integration over the same free-field area given plane waves. However, in 6.21 (a) an increase is predicted.

In Fig. 6.22 the two formulations for the diffraction correction are exemplified on a phase measurement of the transfer function  $\angle H_{15open}^{VVslow}$  conducted at 0.50 m. The excitation voltage is 10 V throughout the frequency range, thus non-linear behavior is expected at the R1- and R2-modes, the transmitter is disk 11 and the receiving disk is 04.

In the figure the simulation is shown in blue, the black curve corresponds to a measurement that has not been corrected for diffraction, the green curve corresponds to a measurement where the correction  $C_{dif}^{SFDC}$  has been applied to the measurement, and the brown curve corresponds to a measurement where the correction  $C_{dif}^{BPDFC}$  has been applied to the measurement.

Noteworthy is it that the simulation and the uncorrected measurement (black) tend to agree

throughout the frequency range, except for the highest frequencies where deviations of  $15^\circ$  is observed. The deviations between the uncorrected measurement and the two corrected measurements diverge accordingly to what Fig. 6.20 predicts. As an example, at 200 kHz, in Fig. 6.20  $\angle C_{dif}^{SFDC} = 28^\circ$ , and  $\angle C_{dif}^{BPDC} = 21^\circ$ . In Fig. 6.22 the deviations from the uncorrected measurement and the one corrected with  $\angle C_{dif}^{SFDC}$  is  $28^\circ$ , and for the measurement corrected with  $\angle C_{dif}^{BPDC}$  the deviation is  $21^\circ$ .

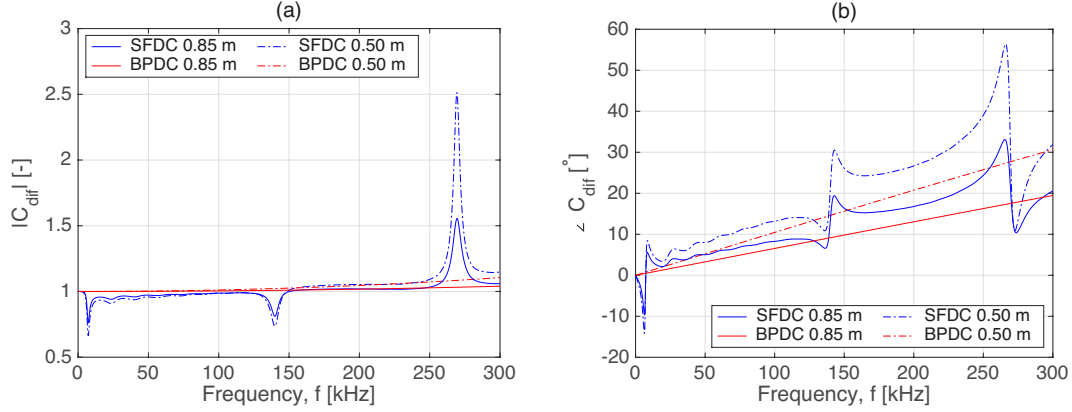


Figure 6.20: Correction accounting for possible diffraction effects,  $C_{dif}$ . In both figures, the blue curves corresponds to  $C_{dif}^{SFDC}$ , and the red curve corresponds to  $C_{dif}^{BPDC}$ . (a) magnitude, and (b) phase for the separation distances  $d = 0.85$  m (solid line)  $d = 0.50$  m (dash dotted line)

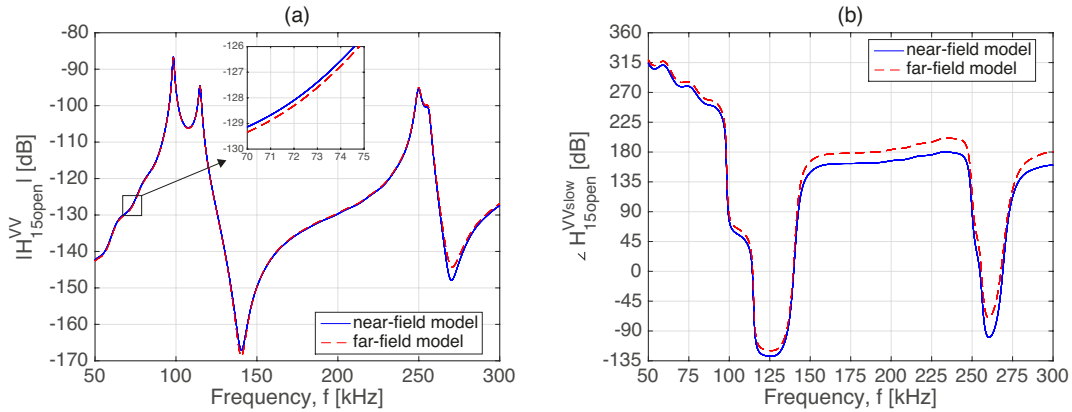


Figure 6.21: Simulation of the magnitude of the transfer function  $H_{15open}^{VV}$  using a near-field model (solid blue) and far-field model (dashed red) for (a) magnitude and (b) phase.

## 6.5 Acoustic measurements on the transfer function $H_{15open}^{VV}$

In the present section the acoustic measurements on the transfer function  $H_{15open}^{VV}$ , given that piezoelectric disks are used as both transmitter and receiver, will be presented.

Both magnitude and phase of the transfer function will be presented, and two separation distances,  $d = 0.50$  m and  $d = 0.85$  m, are investigated. Two separation distances are used to investigate if the method developed to measure the slowly varying phase is scalable. Moreover, increasing the measurement distance reduces the correction term used to correct the measurement for possible diffraction effects. Thus, in this respect, a larger measurement distance is desired.

For all measurements in the current section, the diffraction correction term  $C_{dif}^{SFDC}$  is used. Referring to Sec.6.2.4 the frequency range 175–225 kHz will often be used to compare the measurements with simulations since this frequency range is deemed invariant of the three simulation parameters investigated in Sec.6.2.4.

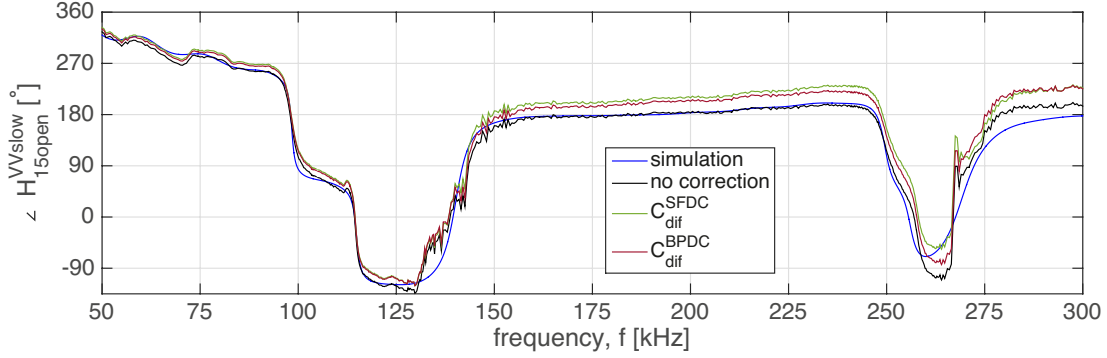


Figure 6.22: Slowly varying phase  $\angle H_{15open}^{VVslow}$  shown for simulation (blue), no correction for possible diffraction (black), diffraction correction  $C_{dif}^{SFDC}$  (green), and diffraction correction  $C_{dif}^{BPDC}$  (brown).

The measurements presented for the separation distance  $d = 0.50$  are used in the reciprocity calibrations.

3

### 6.5.1 Non linearity in acoustical measurements

In the present section observed non linearity in the acoustical measurements will be investigated. The observed non linearity is considered to stem from the piezoelectric disks and is observed mainly around the R1-mode ( $f \approx 100$  kHz) and R2-mode ( $f \approx 250$  kHz), however only the observed non linearity at the R1-mode will be investigated. In Fig. 6.23 (a) and (b) the magnitude and phase, respectively, for the transfer function  $H_{15open}^{VV}$  are presented. Only the frequency range 85–110 kHz is shown. In both figures the blue curve corresponds to the simulation of the transfer function, the black curve corresponds to a measurement with 10 V, while the red curve corresponds to a measurement with 1 V. The frequency range where the non linearity is expected is determined from the results in Sec. 6.1.1, and is assumed to exist mainly within the frequency range 90–105 kHz. The measurements in the present section is performed using element 07 as a transmitter and element 04 as a receiver.

In Fig. 6.23 (a) it is observed that the magnitude of the simulation and the 1 V measurement are comparable. However, a frequency shift of approximately 0.4 kHz is observed, where the 1 V measurement has its maximum at a higher frequency than the simulation. This frequency shifting is deemed a result of the material constants that are not adjusted for the specific batch of piezoelectric disks or the individual disks. Comparing the 10 and 1 V measurements, a frequency shift of 1 kHz is observed, where the 1 V measurement has its maximum at a higher frequency than the 10 V measurement. A decrease in amplitude of  $\approx 5.5$  dB is observed, where the 10 V measurement is lower in value than the 1 V measurement.

In Fig. 6.23 (b) it is observed that the slope of the two measurements are slightly different: the 1 V measurement begins to decrease at a higher frequency, and it decreases with a higher rate, than the 10 V measurement. As in Fig. 6.23 (a) the 1 V measurement is slightly larger in value compared to the simulation, and a frequency shift of approximately 0.4 kHz is observed. Generally, the simulation and the 1 V measurement show better agreement than the simulation and the 10 V measurement.

Throughout the thesis, the 1 V measurement will be used instead of the 10 V measurement in the frequency range 90–105 kHz. For the R2-mode and a separation distance 0.50 m, no measurements with a 1 V excitation voltage were performed. Thus, in Sec. 6.5.2 a deviation due to non-linearity is observed at the R2-mode. This deviation is also observed in Sec. 6.5.4.

<sup>3</sup>Note that there are some unresolved challenges with the Krohn-Hite Model 3940 digital filter [83]. The challenges are sudden loss of the signal. The sudden loss of signal results in sudden jumps, or spikes, for the quantity under investigation. For the transfer function presented in the current section, the spikes have not been removed. However, for the calibrated quantities  $M_V$  and  $S_V$ , the spikes have been removed. It should be noted that the loss of signal occurs at random places, and that not every measurement is associated with loss of signal.

For the separation distance 0.85 m, c.f. Secs. 6.5.5 and 6.5.6 measurements with 1 V were performed for both the R1- and R2-mode.

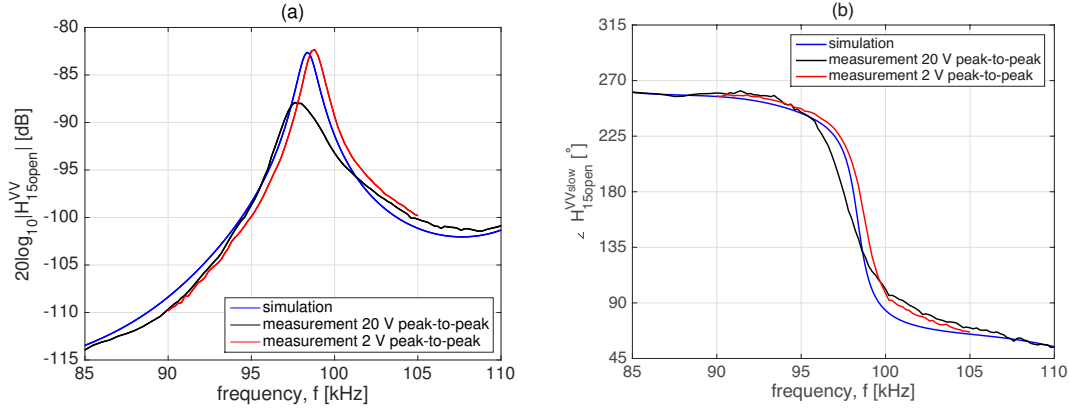


Figure 6.23: (a) comparison of the R1 mode for the frequency range 85–110 kHz for the magnitude of the transfer function,  $|H_{15open}^{VV}|$ , given simulation (blue), measurement with 10 V (black), and measurement with 1 V (red). (b) same as (a) but for phase of the transfer function,  $\angle H_{15open}^{VV}$ .

### 6.5.2 Measurements performed at $d = 0.50$ m

In the current section the measurements on the transfer function  $H_{15open}^{VV}$  given  $d = 0.50$  m will be presented for both magnitude and phase. The measurements will be compared to FE-simulations of the same transfer function.

Four transmitter and receiver pairs have been investigated and each transmitter and receiver pair have been measured four times. In Table 6.1 the transmitter and receiver pairs are denoted, where e.g. the notation 1(2) is adopted to denote the transmitter and receiver pair nr. 1, and measurement 2 out of 4. This notation is also present in the corresponding figures. The fourth transmitter and receiver pair is used to investigate the reciprocity of the measurement system (c.f. Sec. 8.9), and to calibrate the disk 07 (c.f. Sec. ??).

Table 6.1: Transmitter and receiver pairs, abbreviated tr. and rec., respectively, used to obtain the transfer function  $H_{15open}^{VV}$ .

tr. and rec. pairs (meas. nr.)	tr.	rec.
1(1,2,...,4)	11	04
2(1,2,...,4)	11	07
3(1,2,...,4)	07	04
4(1,2,...,4)	04	07

### Re-alignment of the piezoelectric disks

For the transmitter and receiver pair nr. 1, the piezoelectric disks have been re-aligned in between measurement 1 and 2. Comparing measurement 1(1) with 1(2,3,4) yields information about the reproducibility of the measurement system, while comparing measurement 1(2,3,4) among themselves yield information about the repeatability of the measurement system. For the transmitter and receiver pair nr. 2 and 3, the re-alignment have been performed in between measurement 2 and 3, such that comparing 2(1,2) with 2(3,4), and 3(1,2) with 3(3,4), yields information about the reproducibility of the measurement system, while comparing measurement 2(1,2), 2(3,4), 3(1,2) and 3(3,4) among themselves yield information about the repeatability of the measurement system. For the transmitter and receiver pair nr. 4 no re-aligned in between measurement have

been performed. Thus, 4(1,2,...,4) yields information about the repeatability of the measurement system.

### General observations

For Figs. 6.24 – 6.27 the following general observations are made, and will not be repeated during the discussion of the individual figures:

For the disks used in the current thesis, the first radial mode, R1 or the R1-mode, is found around 90–125 kHz, and the second radial mode, R2 or the R2-mode, is found around 240–260 kHz. Note that the discussions will be given with respect to the series- and parallel resonance frequencies.

1. In Table 3.5 four of the characteristic frequencies were given for the R1- and R2-mode for disk 11. It was pointed out that for the R1-mode the frequency  $f_s$  is concurrent with  $f_m$ , and that the frequency  $f_p$  is concurrent with  $f_n$ . In Fig. 6.1 the  $f_m$  and  $f_n$  frequencies are indicated for the R-1 mode on admittance and impedance plots. In Fig. 6.24 the first radial mode, R1-mode, and the second radial mode, R2-mode, are indicated for the transfer function  $H_{15open}^{VV}$ .

The two characteristic peaks of  $H_{15open}^{VV}$ , are denoted "first" and "second" peaks. In Fig. 6.24, for the R1-mode, the first and second peaks are indicated. The first peak of the R1-mode is observed in the frequency range 98.4–99.2 kHz, and the second peak of the R1-mode is observed in the frequency range 114.6–114.7 kHz. The first peak corresponds well with both  $f_s$  and  $f_m$ , and the second peak corresponds well with both  $f_p$  and  $f_n$ . However, the notation first and second peak are adopted for  $H_{15open}^{VV}$  to distinguish the observed peaks from the characteristic frequencies. This notation is adopted for both the R1- and R2-mode.

2. For the magnitude of the transfer function, the first peak of the R2-mode can exhibit non-linear behavior of up to 5 dB for an excitation voltage of 10 V [1]. However, in the current section, no measurements using 1 V were performed for the R2 mode. Thus, the deviation experienced for the first peak of the R2-mode can partly be explained by non linearity.

3. The frequency ranges 130–150 kHz and 260–275 kHz are associated with a low signal-to-noise ratio, thus unwrapping the phase in these frequency ranges can result in fluctuating phase values. If this is experienced, the unwrapping is handled as discussed in Sec. 3.6.3. Note that this unwrapping scheme has only been necessary to use in 4 out of 16 measurements.

4. For the frequency 267 kHz a jump in value is observed for the phase, and a great dip in value is observed for the magnitude. This jump and dip was first believed to be due to an insufficient frequency resolution of 0.5 kHz in the frequency range 260–275 kHz. However, increasing the frequency resolution has shown not to be associated with any significant change in the jump or dip. However, increasing the measurement distance to 0.85 m has resulted in an significant change in the jump and dip, c.f. Sec.6.5.5. The reason why this jump and dip is observed at  $d = 0.50$  m and is not so pronounced at  $d = 0.85$  m is not investigated, but is thought to be due to the beam pattern of the disk and corresponding narrow major lobes. However, it should be clarified, that this is only hypothesized and is not investigated.

5. For all figures, the solid blue curve is the simulated equivalent transfer function  $H_{15open}^{VV}$ , and the black crosses at  $f = 90$  kHz and  $f = 105$  kHz denotes where the 1 V measurements are used in stead of the 10 V measurements, c.f. Sec.6.5.1.

6. For magnitude and phase, although some discussion regarding the repeatability will be given in the current section, this is deferred to Sec. 7.8.

### Transmitter and receiver pair nr. 1

In Fig. 6.24 (a) and (b) the measurements on the magnitude and phase, respectively, of the transfer function  $H_{15open}^{VV}$  for the transmitter and receiver pair nr. 1 is given, i.e. transmitter: disk 11, receiver: disk 04.

In Fig. 6.24 (a) it is observed that there is a good overall agreement between the measurements and simulation. For the R1-mode a frequency shift of 0.8 kHz is observed between the first peak where the simulations are shifted down in frequency compared to the measurements. For the second peak of the R1-mode a decrease in magnitude of approximately 1 dB is observed. For the second peak of the R2-mode the simulation is shifted down in frequency with approximately 1.7 kHz.



Comparing the measurements among themselves, except for the noisy frequency ranges, the four measurements tend to agree well, and there seem to be little that distinguishes the reproducibility from the repeatability.

In Fig. 6.24 (b) there is also a fair agreement between the measurements and the simulation. However, for all measurements the phase is larger in value than the simulated phase. The best agreement between the measurements and simulation is experienced in measurement 3, where a deviation of  $20^\circ$  is observed for  $f = 200$  kHz. The greatest deviation between the measurements and simulation is experienced in measurement 2, where a deviation of  $48^\circ$  is observed for  $f = 200$  kHz.

Comparing the measurements with one another, it is observed that measurement 1, 2 and 4 deviates with approximately  $15^\circ$  given  $f = 200$  kHz, and measurement 3 is approximately  $20^\circ$  lower than the mean of the three measurements, 1,2 and 4.

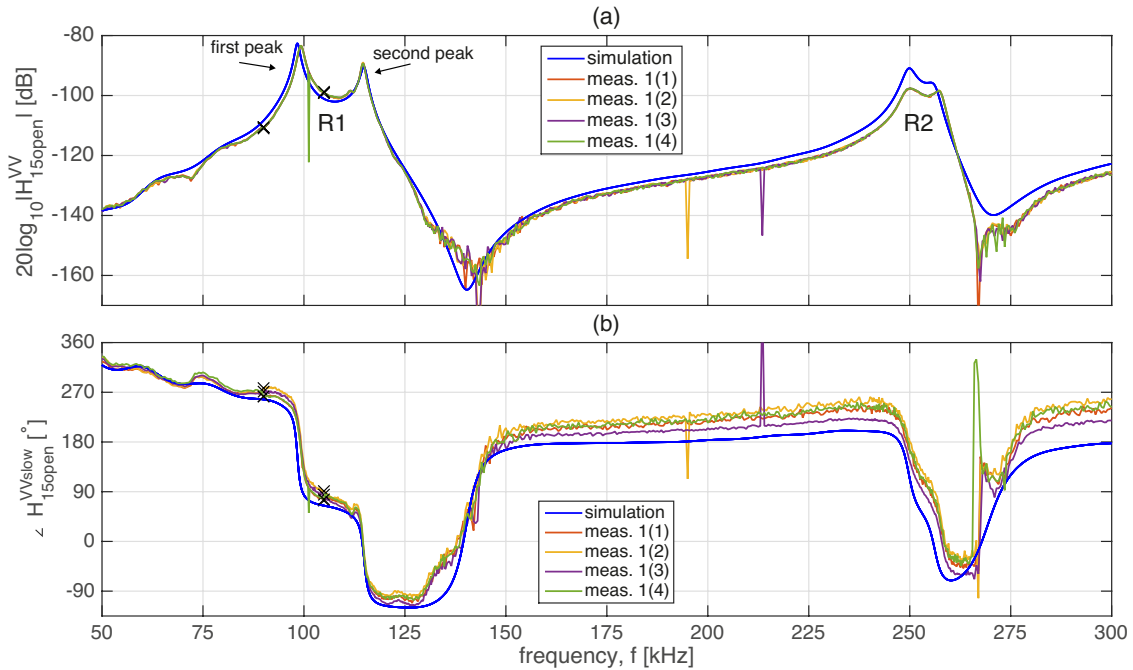


Figure 6.24: (a) magnitude of the transfer function  $|H_{15open}^{VV}|$  for transmitter and receiver pair nr. 1, for measurement 1–4. (b) same as (a) but for phase of the transfer function  $\angle H_{15open}^{VV}$ .

### Transmitter and receiver pair nr. 2

In Fig. 6.25 (a) and (b) the measurements on the magnitude and phase, respectively, of the transfer function  $H_{15open}^{VV}$  for the transmitter and receiver pair nr. 2 is given, i.e. transmitter: disk 11, receiver: disk 07.

In Fig. 6.25 (a) similar deviations for the first peak of the R1-mode are experienced as in Fig. 6.24 (a). This is the expected result as the same transmitter is used. For the second peak of the R1-mode a deviation of approximately 4.4 dB is experienced between the measurements and simulation. The second peak at the R2-mode show fair agreement between all measurements and simulations. Comparing the magnitude measurements among themselves, no noticeable deviations are observed throughout the frequency range.

In Fig. 6.25 (b) a similar trend as in Fig. 6.24 (b) is observed: for all measurements the phase is larger in value than the simulated phase. The measurements that corresponds best with the simulation are measurement 3 and 4. For  $f = 200$  kHz a deviation between measurement 3 and the simulation of  $24^\circ$  is observed. The greatest deviation between the measurements and simulation is observed for measurement 1, where a deviation of  $47^\circ$  is experienced.

Measurement 3 and 4 tend to agree throughout the entire frequency range, while measurement 1 and 2 deviates with  $17^\circ$  given  $f = 200$  kHz. Both measurements 1 and 2 are larger in value than measurement 3 and 4. Though, measurement 2 tends to agree better with measurement 3 and 4.

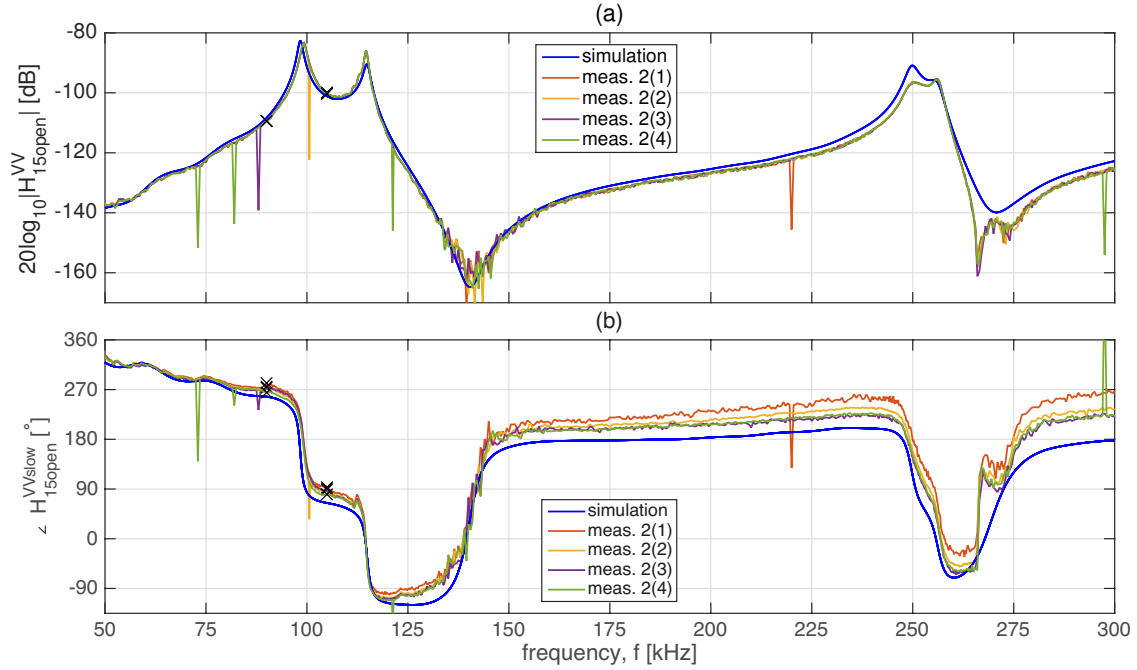


Figure 6.25: (a) magnitude of the transfer function  $|H_{15open}^{VV}|$  for transmitter and receiver pair nr. 2, for measurement 1–4. (b) same as (a) but for phase of the transfer function  $\angle H_{15open}^{VV}$ .

### Transmitter and receiver pair nr. 3

In Fig. 6.26 (a) and (b) the measurements on the magnitude and phase, respectively, of the transfer function  $H_{15open}^{VV}$  for the transmitter and receiver pair nr. 3 is given, i.e. transmitter: disk 07, receiver: disk 04.

In Fig. 6.26 (a) a good overall agreement between measurements and simulation is observed. The best agreement is observed at the R1-mode, where for both the first and second peak the measurements and simulation curves are partly overlapping. For the first peak of the R2-mode the measurements are approximately 7.3 dB lower in magnitude than the simulations, and the second peak is approximately 4.5 dB lower in magnitude. The second peak of the R2-mode is shifted up in frequency with 1.7 kHz compared to the simulation. Comparing the magnitude measurements among themselves, no noticeable deviations are observed throughout the frequency range.

In Fig. 6.26 (b) a good overall agreement between measurements and simulation is observed. The best agreement between the measurements and simulation is observed for the 4th measurement where a deviation of  $12^\circ$  is observed given  $f = 200$  kHz. The greatest deviation between measurements and simulations is observed for the first measurement, where a deviation of  $35^\circ$  is observed for the same frequency.

Comparing the measurements among themselves, it is observed that measurements 1, 2 and 3 corresponds best with each other. For  $f = 200$  kHz a maximum deviation of  $11^\circ$  is observed among measurement 1, 2 and 3. The 4th measurement is approximately  $20^\circ$  lower in value than the measurement 1, 2 and 3.

### Transmitter and receiver pair nr. 4

In Fig. 6.27 (a) and (b) the measurements on the magnitude and phase, respectively, of the transfer function  $H_{15open}^{VV}$  for the transmitter and receiver pair nr. 4 is given, i.e. transmitter: disk 04, receiver: disk 07.

In Fig. 6.27 (a) for the first peak of the R1-mode, the measurements compared to the simulation are shifted upward in frequency with 0.9 kHz, while the amplitude is decreased with less than 0.5 dB. For the second peak of the R1-mode the measurements compared to the simulation are shifted down in frequency with approximately 0.2 kHz, while an increase in magnitude of 4.5 dB is observed. For the second peak of the R2-mode the measurements compared to the simulation

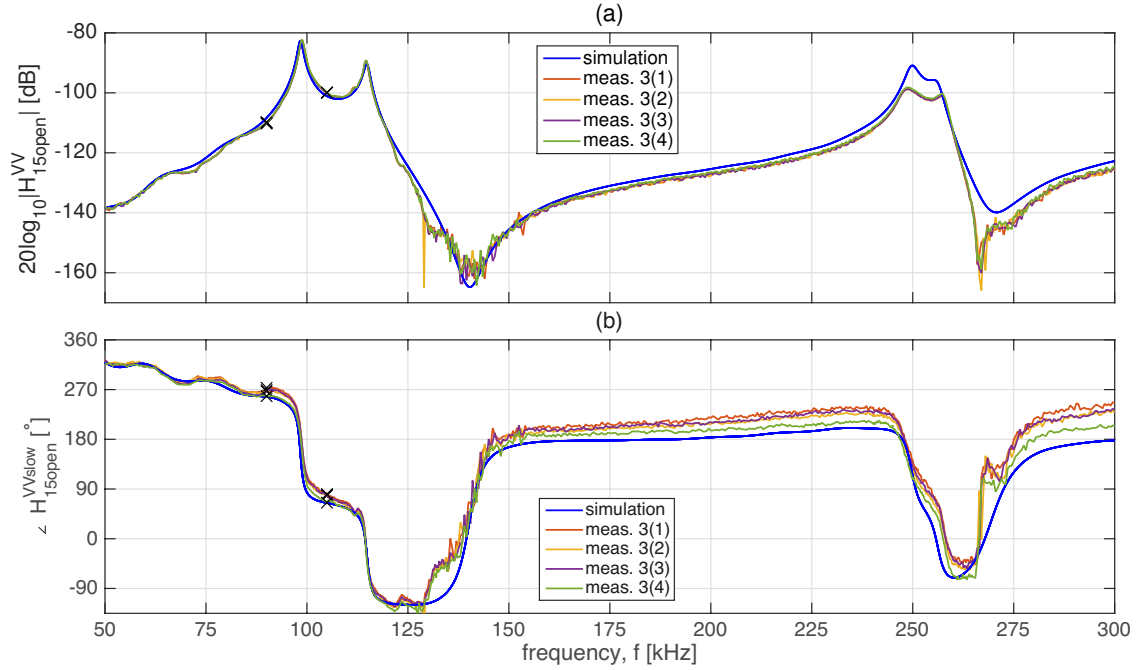


Figure 6.26: (a) magnitude of the transfer function  $|H_{15open}^{VV}|$  for transmitter and receiver pair nr. 3, for measurement 1–4. (b) same as (a) but for phase of the transfer function  $\angle H_{15open}^{VV}$ .

are shifted up in frequency with 0.5 kHz while a negligible increase in magnitude is observed. Comparing the magnitude measurements among themselves, no noticeable deviations are observed throughout the frequency range.

In Fig. 6.27 (b) a fair overall agreement between all measurements and simulation are observed. The best agreement between a measurement and simulation is observed for the measurement 4, where a deviation of  $14^\circ$  is observed given  $f = 200$  kHz. The greatest deviation between measurements and simulation is experienced for measurement 1 and 2, where a deviation of  $36^\circ$  is observed.

Comparing the measurements among themselves, it is observed that measurements 1 and 2, as well as 3 and 4, corresponds best with each other. The deviation between the two pairs are approximately  $20^\circ$  at 200 kHz.

### Determining what measurement to use in the calibration

The measurements to be used in the calibration equations are determined by the measurements on the phase. The mean of the four phases for each transmitter and receiver pair is calculated and the measurement that is closes in value to the mean is selected. The selected measurements are: 1(1), 2(2), 3(2) and 4(3).

### Comparison of the selected measurements

The four selected measurements of the previous section are compared against each other for both magnitude and phase. In Fig. 6.28 the comparisons are given for (a) magnitude, (b) phase. An overall agreement between the magnitudes and phases are observed.

However, to better appreciate the possible deviations around the R1-mode in Fig. 6.29 (a) the frequency range 90–120 kHz of Fig. 6.28 (a) is given, and in Fig. 6.29 (b) the frequency range 96–102 kHz of Fig. 6.28 (b) is given. In Fig. 6.29 (a), for the first peak, the three measurements 1(1), 2(2) and 4(3) are nearly indistinguishable, while a deviation is observed for measurement 3(2). This deviation is thought to be due to the disk 07 exhibiting a different transmitting response than the disks 11 and 04.

For the second peak, the measurements 1(1) and 3(2) exhibits a fair agreement, while measurements 2(2) and 4(3) exhibits a fair agreement. For 1(1) and 3(2) the disk 04 is used as a

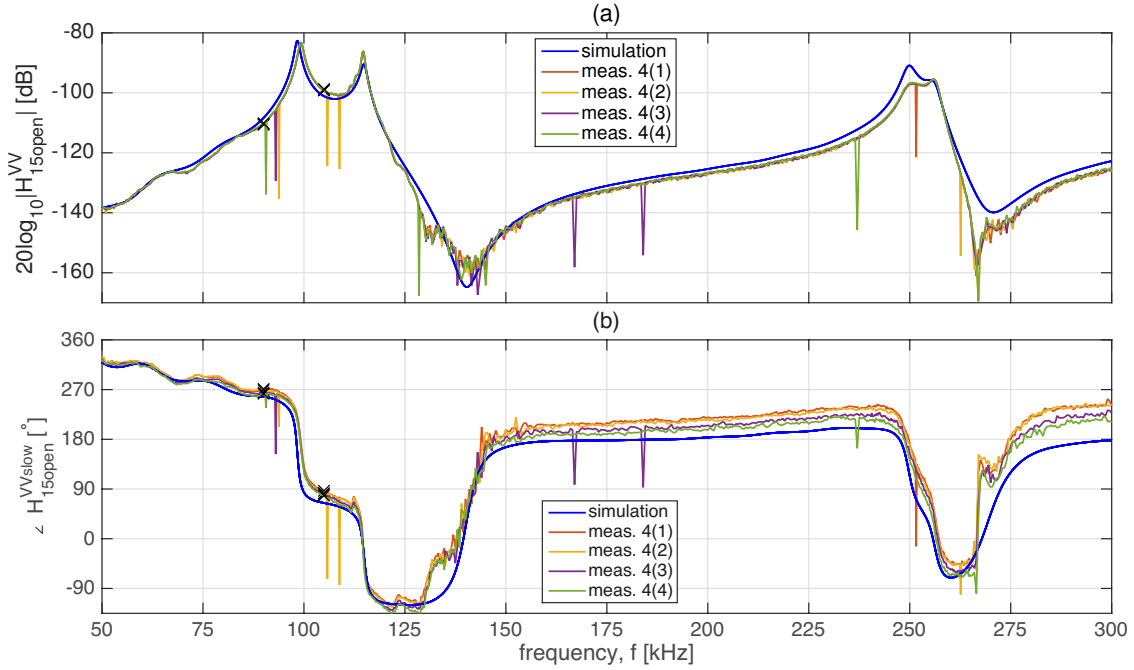


Figure 6.27: (a) magnitude of the transfer function  $|H_{15open}^{VV}|$  for transmitter and receiver pair nr. 4, for measurement 1–4. (b) same as (a) but for phase of the transfer function  $\angle H_{15open}^{VV}$ .

receiver, and for 2(2) and 4(3) the disk 07 is used as a receiver. In Fig. 6.29 (b) the same tendency and conclusion can be made. It is recognized that the disks 04 and 07 exhibits slightly different transmitting and receiving properties.

For the frequency range 112–114 kHz deviations are also observed, both between measurements and between the measurements and simulation. This deviation is not fully understood. It was hypothesized that this could stem from slightly wrong cable parameters such that the correction  $H_{5open5'}^{VV}$ , c.f. Sec.6.4.2, could take on a wrong value. However, the measurements on the cable parameters, c.f. Sec.3.10, and how they influence  $H_{5open5'}^{VV}$ , do not suggest this. It should be noted that this deviation is also seen in [3]. However, in [1,2] this deviation is almost indistinguishable.

### 6.5.3 Reciprocity check

A check for reciprocity is performed on the transmitter and receiver pair 04 and 07, and pair 04 and 11, c.f. Sec.8.9, for the frequency range 50–300 kHz. The reciprocity check is performed for both magnitude and phase and are presented as the differences defined as

$$\begin{aligned} \text{difference [dB]} &= 20 \log_{10} |H_{15open}^{VV(04 \rightarrow 07)} \cdot Z_T^{04}| - 20 \log_{10} |H_{15open}^{VV(07 \rightarrow 04)} \cdot Z_T^{07}|, \\ \text{difference [}^\circ\text{]} &= \angle [H_{15open}^{VV(04 \rightarrow 07)} \cdot Z_T^{04}] - \angle [H_{15open}^{VV(07 \rightarrow 04)} \cdot Z_T^{07}], \end{aligned} \quad (6.1)$$

where  $H_{15open}^{VV(04 \rightarrow 07)}$  denotes the transfer function  $H_{15open}^{VV}$  given that disk 04 is used as a transmitter and disk 07 is used as a receiver, and  $Z_T^{04}$  denotes the impedance of the disk 04 being used as a transmitter. When the other disks are used as either transmitter or receiver, the superscripts change accordingly.

In Fig.6.30 the results are given for both magnitude (a) and phase (b). The red curve corresponds to the transmitter and receiver pair 04 and 07, referred to as the "first pair", while the black curve corresponds to the transmitter and receiver pair 04 and 11, referred to as the "second pair".

In Fig.6.30 (a) it is observed that the frequency range 50–125 kHz is associated with a low decibel value, approximately  $\pm 1$  dB, which signifies a good overall reciprocal behavior of the two disk pairs. However, at 100 kHz the red curve shows significant fluctuations. This fluctuation

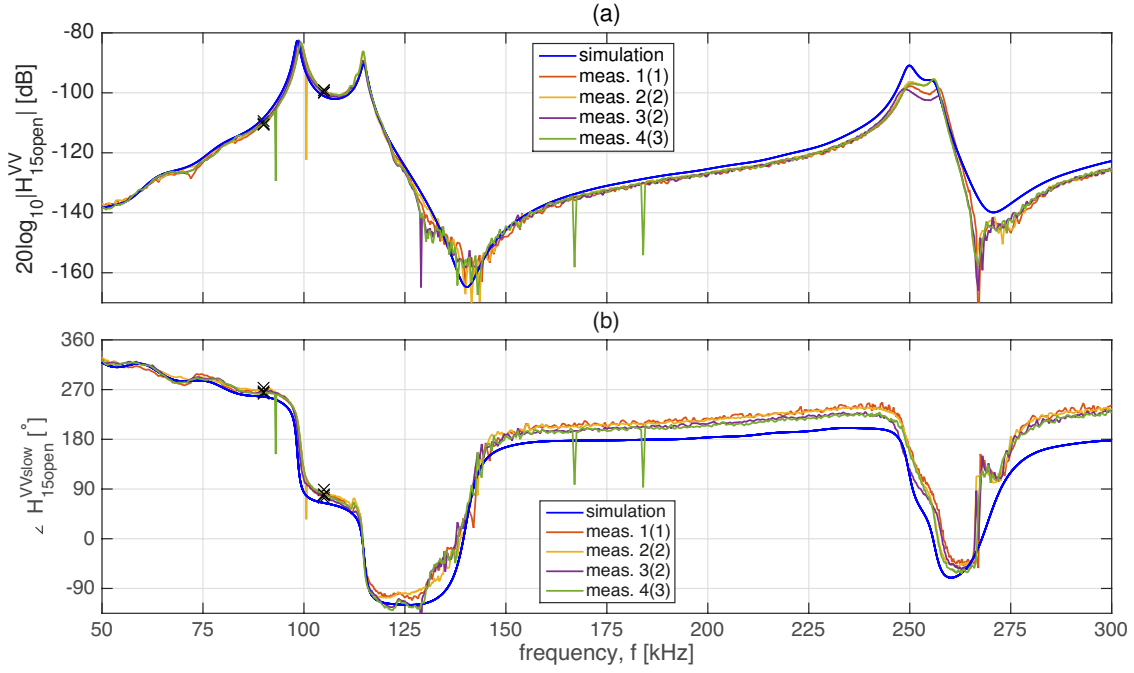


Figure 6.28: (a) magnitude of the transfer function  $|H_{15open}^{VV}|$  for the selected measurements given in the previous section. (b) same as (a) but for phase of the transfer function  $\angle H_{15open}^{VV}$ .

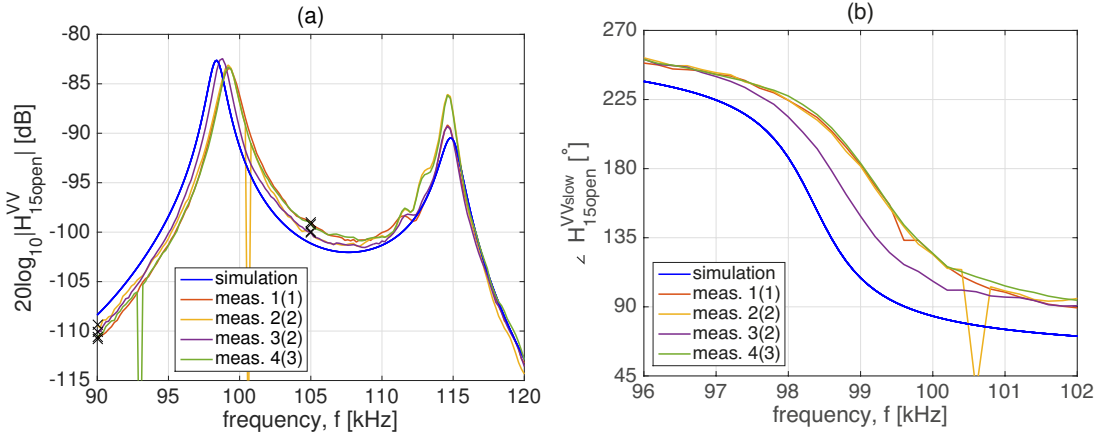


Figure 6.29: (a) close up of Fig. 6.28 (a). (b) close up of Fig. 6.28 (b).

corresponds to the deviation observed in Fig.6.29, and it is observed that for the second pair, only a small fluctuation is observed for the same frequency. The significance of this is that the second pair exhibits a higher degree of mutual reciprocity than the first pair for the given frequency.

For the frequency range 125–160 kHz the observed fluctuations are mainly due to noise. For the frequency range 160–245 kHz a difference of  $\pm 1$  dB is observed for both pairs. For the R2-mode, the first pair again fluctuates more than the second pair, and peak differences of 4 dB and -3 dB are observed. The second pair has a peak difference of 1 dB. From 260 kHz the fluctuations are again due to noise.

In Fig.6.30 (b) a difference of less than  $\pm 5^\circ$  is mainly observed for the frequency range 50–125 kHz. The first pair exhibits fluctuations around 98.5 kHz where it drops in value to  $-28^\circ$ , and another fluctuation is observed at 112.8 kHz where it increases in value to  $12^\circ$ . At 112.8 kHz the second pair also exhibit a fluctuations of  $-10^\circ$ . From 150–245 kHz some fluctuations are observed, and at the R2-mode the first pair exhibit fluctuations of  $-30$  to  $+25^\circ$ , and an increase of  $+10^\circ$  is observed for the second pair at 250 kHz.

It is observed that the second pair tends to be more reciprocal than the first pair. <sup>4</sup>

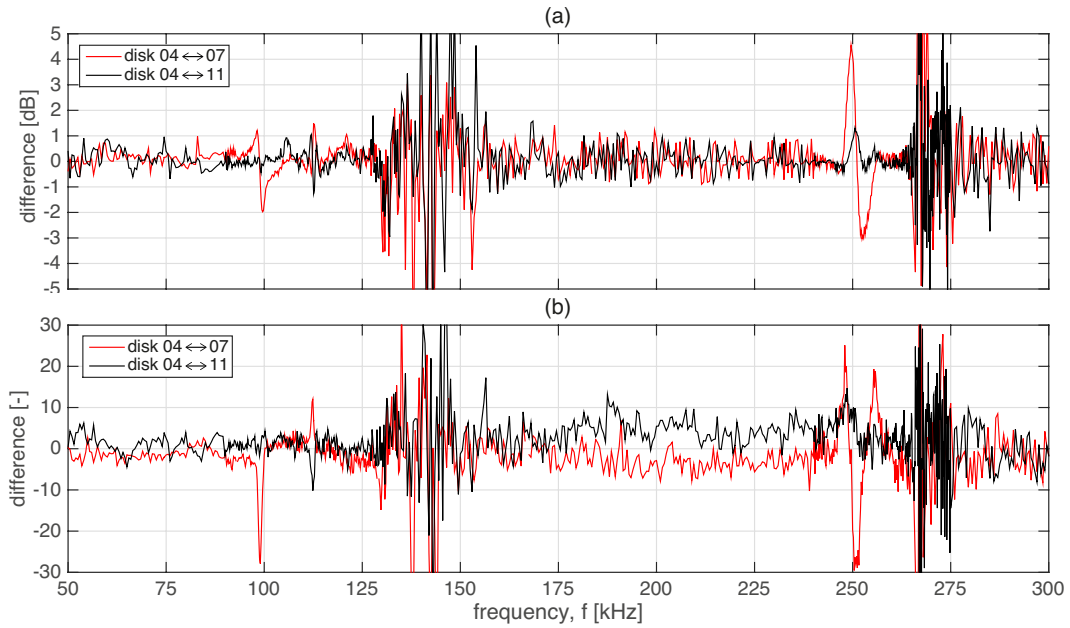


Figure 6.30: Difference of the reciprocity check for the disk pairs 04 ↔ 07, and 04 ↔ 11 for (a) magnitude, and (b) phase.

#### 6.5.4 Three transducer reciprocity calibration obtained at $d = 0.50$ m

In the current section the calibration of disk 04 and disk 07 obtained at  $d = 0.50$  m will be presented. The calibration is performed as described in Sec.2.5, and the results are compared with FE-simulations. First the full frequency range will be shown for the quantities  $M_V$  and  $S_V$  for both magnitude and phase, thereafter the frequency range 50–140 kHz will be shown. The latter frequency range is the frequency range where one can expect to perform calibration with the greatest signal-to-noise ratio, thus it is of interest to examine this in detail.

Given the four transmitter and receiver pairs defined in Sec.6.5 both disks 04 and 07 can be calibrated. In Table 6.2 the corresponding transmitter and receiver pairs with selected measurement numbers in parenthesis are given. The measurements 1(1) and 2(2) are identical for the two calibrations. The notation  $M_V^{04}$  is adopted to specify the receiving sensitivity,  $M_V$ , of disk 04, and a similar notation is used for  $S_V$ .

Table 6.2: Transmitter and receiver pairs with measurement number in parenthesis as used in the reciprocity calibrations.

disk 04			disk 07		
tr. and rec. pairs (meas. nr.)	tr.	rec.	tr. and rec. pairs (meas. nr.)	tr.	rec.
1(1)	11	04	2(2)	11	07
2(2)	11	07	1(1)	11	04
3(2)	07	04	4(3)	04	07

#### Receiving sensitivity, $M_V$

In Fig.6.31 the receiving sensitivity,  $M_V$ , of disk 04 and 07 are given for (a) magnitude and (b) phase. The crosses at 90 kHz and 105 kHz indicate where the 1 V measurements have been spliced

<sup>4</sup>Note that the reciprocity check presented in [1] are wrong. The admittance, rather than the impedance have been multiplied with  $H_{15open}^{VV}$ , such that the values are lower than expected.

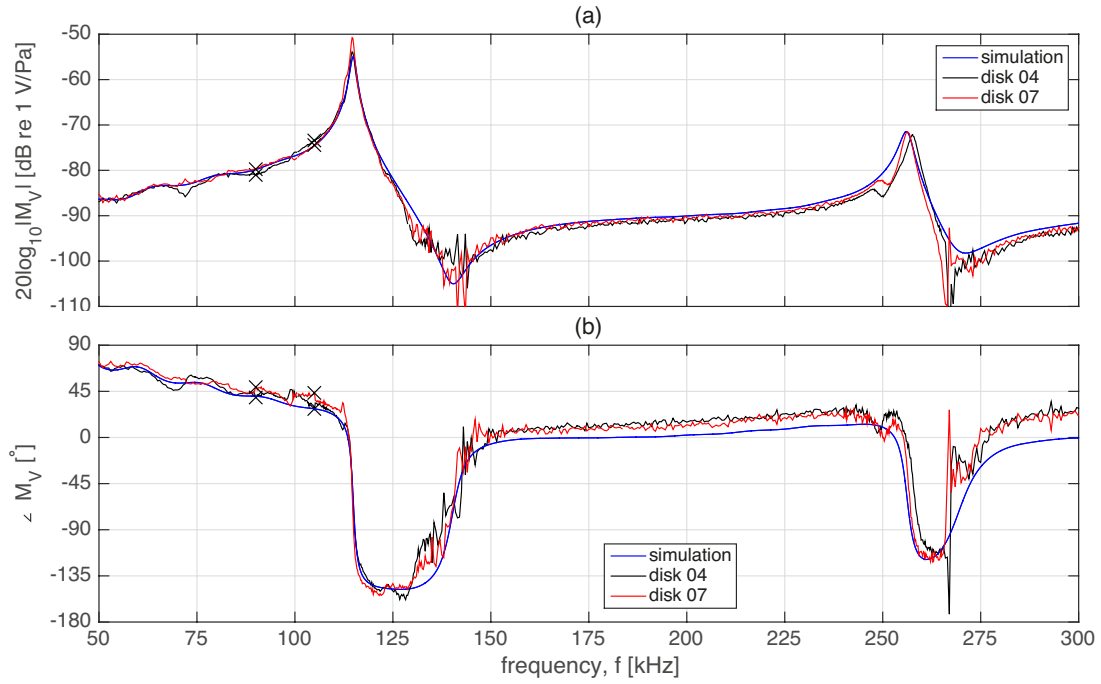


Figure 6.31: Receiving voltage sensitivity obtained by the reciprocity calibration method for (a) magnitude,  $|M_V|$ , and (b) phase,  $\angle M_V$ . The calibration is performed for disk 04 (black), and disk 07 (red), and are compared to FE-simulation (blue).

onto the 10 V measurements.

In Fig.6.31 (a) a good overall agreement in-between both measurements, and between both measurements and the simulation are observed. For the peak at the R1-mode (114.6 kHz)  $M_V^{04}$  is approximately 3 dB lower in value than  $M_V^{07}$ , and the simulation is approximately 1 dB lower in value than  $M_V^{04}$ . The simulation is approximately 4 dB lower in value than  $M_V^{07}$ . A slight frequency shift is also observed, where the simulation is shifted upwards in frequency with approximately 0.1 kHz, compared to both measurements.

After the dip at 140 kHz, the three curves tend to agreement until  $\approx 245$  kHz, where the non-linearity of the piezoelectric disks are observed, this is discussed in Sec.6.5.1, and it should suffice to state that this deviation would be lower if measurements with a lower voltage had been performed. However, the deviations stemming from non-linearity are expected to be concentrated around the frequencies 245–255 kHz, such that the observed peak at the R2-mode is not associated with deviations due to non-linearity. Thus, one-to-one comparisons of the simulation and the two measurements should be valid for 256–257 kHz. It is observed that for the peak at the R2-mode the magnitude of  $M_V^{07}$  is nearly indistinguishable from the simulation and  $M_V^{04}$  is shifted 0.4 kHz up in frequency compared to the simulation. The magnitude of  $M_V^{04}$  and the simulation is also comparable, however  $M_V^{04}$  is shifted 1.7 kHz up in frequency compared to the simulation.

In Fig.6.31 (b) a good overall agreement between the two measurements is observed. From 50–90 kHz deviation of  $5^\circ$  are observed between the two measurements and simulation. In the range 90–105 kHz, the largest deviation between the two measurements and simulation is approximately  $15^\circ$ . A deviation at approximately 112 kHz is observed. This deviation is discussed in Sec.6.5.2, and it should suffice to state that the deviation observed in  $H_{15open}^{VV}$  propagates to the calibrated quantities. In the range 113–125 kHz  $\angle M_V^{04}$  and the simulation show fair agreement, with deviations lower than  $10^\circ$ . For the same frequency range, the simulation and  $\angle M_V^{07}$  exhibits larger deviations than  $\angle M_V^{04}$  for the same comparison. For the frequency range 175–225 kHz a constant deviation between  $M_V^{07}$  and the simulation of  $9^\circ$  is observed. The deviation between the two measurement in this frequency range is approximately  $1\text{--}3^\circ$ , where  $\angle M_V^{04} \geq \angle M_V^{07}$ . In the frequency range 245–255 kHz the non-linearity of the disks are again observed, and for the frequency 267 kHz the jump in value as discussed in Sec.6.5.2 is observed.



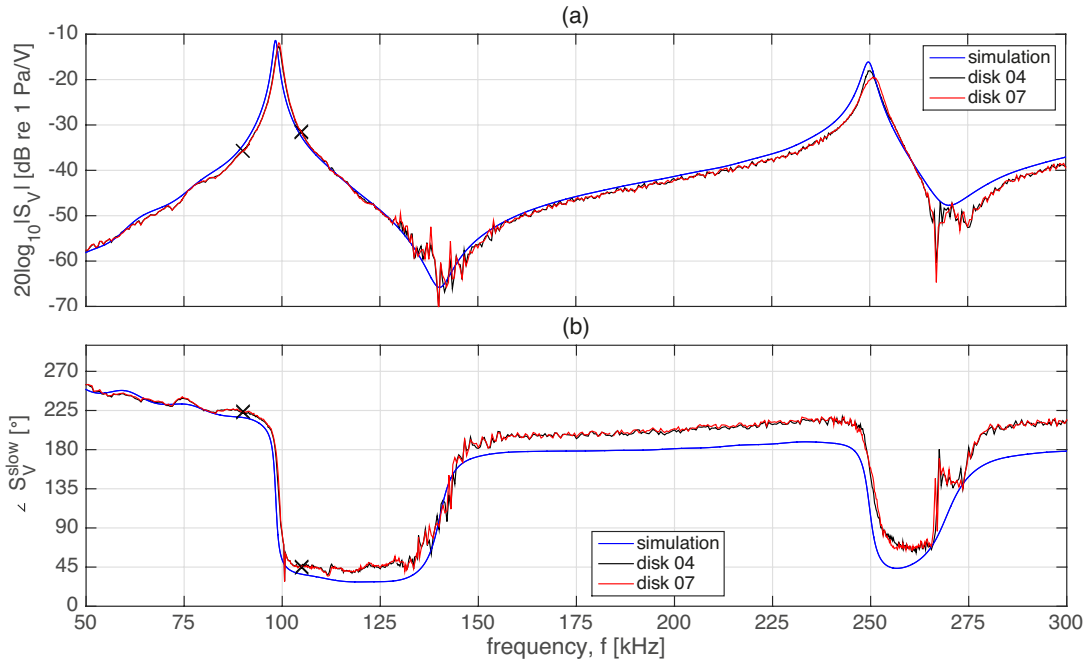


Figure 6.32: Transmitting voltage response obtained by the reciprocity calibration method for (a) magnitude,  $|S_V|$ , and (b) phase,  $\angle S_V$ . The calibration is performed for disk 04 (black), and disk 07 (red), and are compared to FE-simulation (blue).

### Transmitting response, $S_V$

In Fig.6.32 the transmitting response,  $S_V$ , of disk 04 and 07 are given for (a) magnitude and (b) phase. The crosses at 90 kHz and 105 kHz indicate where the 1 V measurements have been spliced onto the 10 V measurements.

In Fig.6.32 (a) a good overall agreement in-between the two measurements and between the two measurements and the simulation is observed. For the peak at the R1-mode  $S_V^{07}$  is 0.8 dB larger in value than  $S_V^{04}$  and the frequency shift between them are negligible. Comparing the measurements and simulation, it is observed that the measurements are shifted up in frequency with 0.9 kHz. A deviation in magnitude between the simulation and  $S_V^{04}$  and  $S_V^{07}$  of 1.3 dB and 0.5 dB is observed, where the measurements are lower in value. After the dip at 140 kHz both measurements are slightly lower in value than the simulation and the deviation tends to increase with frequency. At 200 kHz the deviation is 0.8 dB. Comparisons between the simulation and measurements at the peak of the R2-mode are not readily observed as the measurements do exhibit non-linearity for this specific frequency. Thus, this will be omitted. However, comparison between the two measurements are readily available.  $S_V^{04}$  peaks 1.2 kHz earlier than  $S_V^{07}$ , and the peak value of  $S_V^{04}$  is 1.5 dB higher than the peak value of  $S_V^{07}$ .

In Fig.6.32 (b) a good overall agreement between both measurements is observed. Comparing both measurements with the simulation, a downwards frequency shift of the simulation of 0.8 kHz is observed. In the range 90–105 kHz a constant deviation of  $6.5^\circ$  between both the measurements and the simulation is observed. This deviation tends to grow with frequency, and at 200 kHz the measurements are  $21.5^\circ$  larger in value than the simulation. The comparison at the resonance frequency of the R2-mode is omitted here, too. The jump at 267 kHz is discussed in Sec.6.5.2.

### Further examination of the frequency range 50–140 kHz for $M_V$ and $S_V$

In Fig.6.33 the close ups of Fig.6.31 and Fig.6.32 are given. In all figures, the frequency range where one can expect to perform calibration with a signal-to-noise ratio larger than 40 dB is indicated as the grey area. This frequency range is determined in Sec.6.3.1. To appreciate the non-linear tendency of the R1-mode, this has been plotted as the black and red dots, for disk 04 and 07, respectively.



The same discussion as above is still valid, and it should suffice to state that a good overall agreement is observed for the measurements and between the measurements and the simulations.

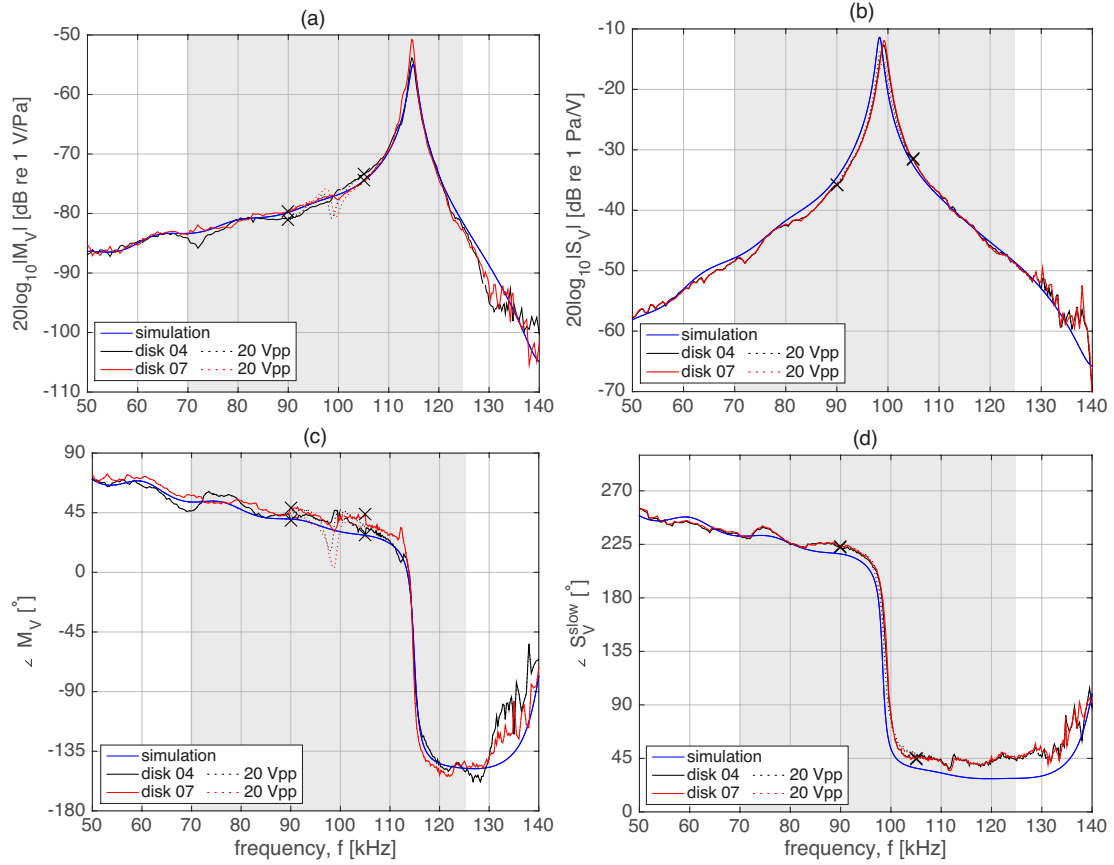


Figure 6.33: (a) close up of Fig.6.31 (a). (b) close up of Fig.6.31 (b). (c) close up of Fig.6.32 (a). (d) close up of Fig.6.32 (b). For all figures the grey area indicate where the calibration can be expected to be performed with a signal-to-noise ratio larger then 40 dB.

### 6.5.5 Measurements performed at $d = 0.85$ m

In the current section the measurements on the transfer function  $H_{15open}^{VV}$  given  $d = 0.85$  m will be presented for both magnitude and phase. The measurements will be compared to FE-simulations of the same transfer function and are presented in Fig.6.34 for both magnitude (a) and phase (b).

Four transmitter and receiver pairs have been investigated, where the same transmitter and receiver pairs as defined in Table 6.1 is still used. However, the repeated measurements will not be shown, such that the notation  $1(1) \rightarrow 1$  is used to denote the first transmitter and receiver pair.

Note that in the current section measurements with 1 V voltage were performed. The 1 V measurements have been used in the frequency range 240–260 kHz, indicated as before with black crosses. The frequency range spans over the second peak of the R2-mode, where it has before been assumed that we should not experience non-linearity. However, deviations at  $\approx 255$  kHz, which is assumed to stem from non-linearity, are observed such that to avoid these deviations a larger frequency range is chosen as to where the 1 V measurements are used.

In Fig.6.34 (a) a good overall agreement between the four measurements is observed, though there are deviation at the first and second peak of both the R1- and R2-mode. The deviations at the R1-mode are discussed in Sec.6.5.2 and will not be repeated here as it is assumed that the deviations are independent of distance. However, the R2-mode deserves a little attention. For the first measurement the first peak occurs at 251.4 kHz, approximately 1.4 kHz larger in frequency than the simulation, and the measurement is 1.7 dB is lower than the simulation. For the second peak, the measurement is shifted up in frequency with 1.6 kHz and a decrease in value of 0.9 dB

is observed, both compared to the simulation.

For the first peak, the second measurement is shifted up in frequency with 1.9 kHz compared to the simulation, and a negligible deviation in magnitude is observed. The second peak of the measurement is shifted up in frequency with 0.7 kHz, and an increase of 2.4 dB is observed for the measurement compared to the simulation.

For the first peak, the third measurement shows negligible shift in frequency, but a decrease of 2.8 dB is observed for the measurement compared to the simulation. The second peak of the third measurement is shifted up in frequency with 1.7 kHz, and a decrease of 2.6 dB is observed for the measurement compared to the simulation.

The second and fourth measurement are similar enough to be treated as identical, such that the discussion regarding the second measurement is deemed valid for the fourth measurement.

In Fig.6.34 (b) a good overall agreement between the four measurements is observed, however the third measurement tends to be lower in value than the other measurements. For 200 kHz, the third measurement is 30° lower in value than the other three measurements. Measurement 1, 2 and 4 tends to agree throughout the entire frequency range, though measurement 2 deviates slightly at 240 kHz, where the 1 V measurements are used.

An important aspect in (b) and (a) is the frequency range 260–275 kHz, and especially 267 kHz, where a jump (b) and (dip) (a) in value was observed for the measurements at  $d = 0.50$  m, c.f. e.g. Fig.6.24. This jump and dip is difficult to distinguish in Fig.6.34 (b) or (a). Thus, it is claimed that the jump and dip are distance dependent, and a hypothesis as to its origin is given in Sec.6.5.2.

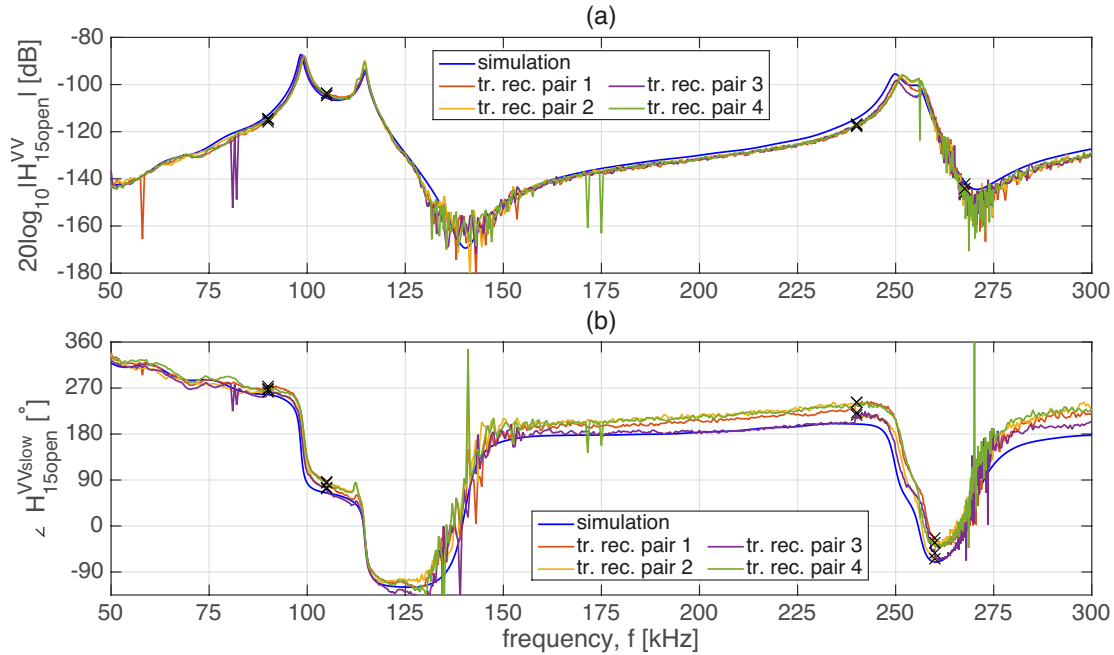


Figure 6.34: Transfer function  $H_{15open}^{VV}$  for (a) magnitude and (b) phase. Four measurements on four transmitter and receiver pairs, abbreviated tr. rec. pair, are juxtaposed with FE-simulation (blue).

### 6.5.6 Three transducer reciprocity calibration obtained at $d = 0.85$ m

In the current section the calibration of disk 04 and disk 07 obtained at  $d = 0.50$  m will be presented. The calibration is performed as described in Sec.2.5, and the results are compared with FE-simulations. The measurements that are used in the calibration are given in the previous section, and the same transmitter and receiver pairs defined in Table 6.2 are used in the current section.

### Receiving sensitivity, $M_V$

In Fig.6.35 the receiving sensitivity,  $M_V$ , of disk 04 and 07 are given for (a) magnitude and (b) phase. The black crosses at 90 kHz and 105 kHz, as well as 240 kHz and 260 kHz, indicate where the 1 V measurements have been spliced onto the 10 V measurements.

In Fig.6.35 (a) a good overall agreement in-between the two measurements, and between the two measurements and the simulation, are observed. At the R1-mode, the  $|M_V^{07}|$  is 3.7 dB larger in magnitude than  $|M_V^{04}|$  and 4.4 dB larger in magnitude than the simulation. Both measurements peak at the same frequency, approximately 0.3 kHz before the simulation. At the R2-mode there is a negligible deviation in the frequency where  $|M_V^{07}|$  and the simulation peak, however  $|M_V^{07}|$  is 1.5 dB larger in magnitude.  $|M_V^{04}|$  is shifted up in frequency with 1.7 kHz, and  $|M_V^{04}|$  is 0.1 dB higher in magnitude than the simulation and 1.4 dB lower than  $|M_V^{07}|$ .

At 65–80 kHz  $M_V^{04}$  deviates from both the simulation and  $|M_V^{07}|$ . This deviation is sometimes observed in  $|H_{15open}^{VV}|$  and is thought to stem from either the soldering process or the solder itself. It could also be due to the stiffness of the wires. However, this is strictly hypothetical and are not investigated. And, it is observed that for the upper frequency bound, 300 kHz, both measurement agrees well and both measurements also agree well with the simulation. In [1] generally a higher deviation was observed at this frequency.

In Fig.6.35 (b) a good overall agreement between the three curves are observed. However, there are some fluctuations for both measurements that require some attention. First, the dip and peak at 98–100 kHz is due to non-linearity, this even so that measurements with 1 V has been performed in this range. For both frequency ranges where the 1 V measurements are used, jump in value are observed. The reason behind these jumps are difficult to pin down exactly, but could be due to small movements in the measurement set-up in-between the 10 and 1 V measurement. Such jumps are also observed in e.g. Fig.6.31 (b) at 90 kHz and 105 kHz, however the magnitude of the jumps are lower than what is observed in the current section. Moreover, these jumps are observed in  $\angle H_{15open}^{VV}$  in Fig.6.34 that are intrinsic to both  $\angle M_V^{04}$  and  $\angle M_V^{07}$ .

At 112 kHz a jump is observed for  $\angle M_V^{07}$  and a slight dip for  $\angle M_V^{04}$ . These deviations are discussed earlier and are not fully understood, but are thought to stem from the correction  $H_{5open5}^{VV}$ , c.f. Secs.6.4.2 6.5.2.

Comparing  $\angle M_V^{04}$  and the simulation hardly any deviation is observed for 200 kHz, while a deviation of about  $22^\circ$  is observed between  $\angle M_V^{04}$  and  $\angle M_V^{07}$  at 200 kHz. Also worth taking notice of is the jump discussed earlier at 267 kHz, which is practically not possible to distinguish.

### Transmitting response, $S_V$

In Fig.6.36 the transmitting response,  $S_V$ , of disk 04 and 07 are given for (a) magnitude and (b) phase. The black crosses at 90 kHz and 105 kHz, as well as 240 kHz and 260 kHz, indicate where the 1 V measurements have been spliced onto the 10 V measurements.

In Fig.6.36 (a) a good overall agreement in-between the two measurements, and between the two measurements and the simulation, are observed. For the R1-mode the two measurements show negligible deviations, while both measurements are shifted up in frequency compared to the simulation with 0.8 kHz and a decline in magnitude of 1.5 dB is observed. At the R2-mode the two measurements agree well, and both measurements are shifted up in frequency compared to the simulation with 1.8 kHz.

In Fig.6.36 (b) a good overall agreement in-between the two measurements, and between the two measurements and the simulation, are observed. As in Fig.6.35 (b) jump are observe where the 1 V measurements have been used, though the jumps are lower in Fig.6.36 (b) than in 6.35 (b).

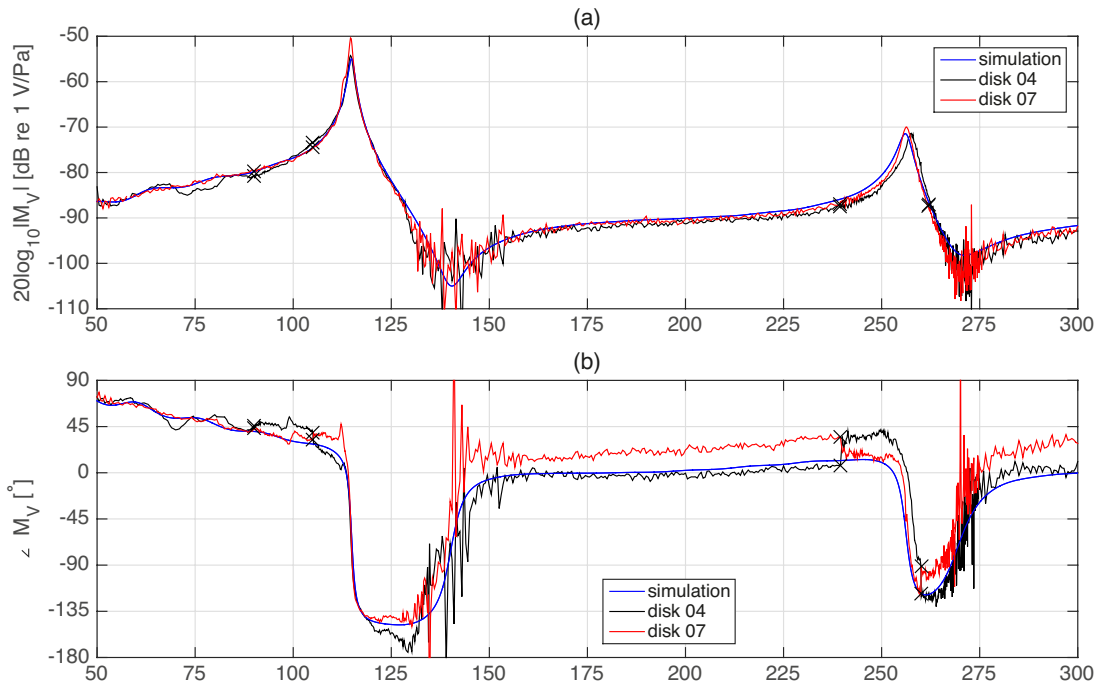


Figure 6.35: Receiving voltage sensitivity obtained by the reciprocity calibration method for (a) magnitude,  $|M_V|$ , and (b) phase,  $\angle M_V$ . The calibration is performed for disk 04 (black), and disk 07 (red), and are compared to FE-simulation (blue).

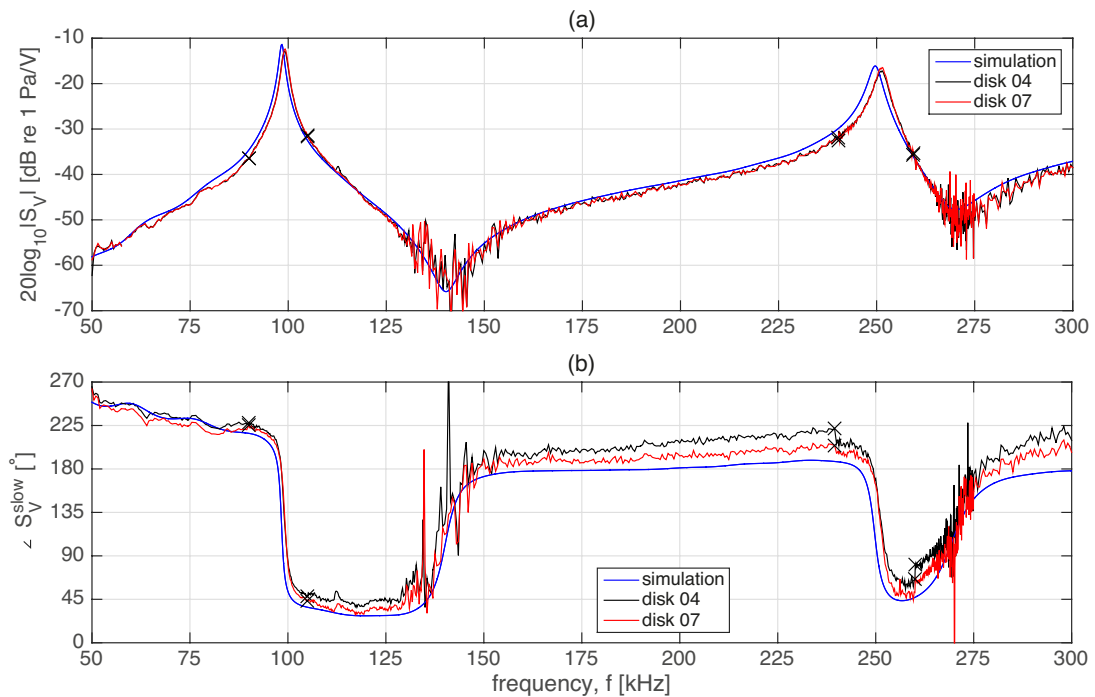


Figure 6.36: Transmitting voltage response obtained by the reciprocity calibration method for (a) magnitude,  $|M_V|$ , and (b) phase,  $\angle M_V$ . The calibration is performed for disk 04 (black), and disk 07 (red), and are compared to FE-simulation (blue).

# Chapter 7

## Measurement uncertainties

Whenever a measurement is performed the obtained result will be associated with a certain quantifiable amount of uncertainty. A measurement is therefore not complete without a statement about the uncertainty [92]. Without such an indication, measurement results cannot be compared, either among themselves or with reference values provided in specifications or various standards [92]. It is therefore of interest, if not of necessity, to evaluate the uncertainties associated with the measurement set-up and associated system model.

The current chapter is devoted to the measurement uncertainties experienced in the measurement set-up. The development of the measurement uncertainties follow the Guide to the expression of uncertainty in measurement (GUM). In Appendix A an introduction to the GUM is presented <sup>1</sup>.

It is of interest to investigate the measurement uncertainties associated with the calibrated quantities,  $M_V$  and  $S_V$ . However, to evaluate these uncertainties, it is necessary to first obtain an estimate for the uncertainty associated with the loss-free open circuit transfer function,  $H_{15open}^{VV}$ , since the associated uncertainty of the transfer function will propagate to  $M_V$  and  $S_V$ .

$H_{15open}^{VV}$  is a complex quantity, and the uncertainty for magnitude and phase have to be evaluated separately. Except in Sec. 7.8 where the repeatability of the measurement set-up is evaluated for magnitude and phase, and in Sec. 7.2 where the uncertainty of the impedance of a piezoelectric disk is evaluated, only the uncertainties associated with the magnitude have been evaluated.

Although, it is of interest to investigate the uncertainties associated with the slowly varying phase of  $H_{15open}^{VV}$ , and investigate how this uncertainty propagates to the phase of  $M_V$  and  $S_V$ , however, due to time limitation this has not been performed.

Throughout the section, all input quantities are assumed uncorrelated. This is regarded as an approximation which by Eq.(A.10) can be expanded on by using the results obtained in the current section. In Secs. 7.5.7 and 7.6.1 a discussions regarding this approximation are given. All uncertainties are stated as standard uncertainties with a 68.3% level of confidence.

### Chapter outline

In Sec. 7.1 the combined standard uncertainty associated with the measurement distance,  $d$ , will be developed. In Sec. 7.2 the combined standard uncertainties for the impedance measurements of a piezoelectric disk will be evaluated. In Sec. 7.3 the combined standard uncertainties associated with the correction for propagation losses,  $C_\alpha$ , will be given. In Sec. 7.5 the combined standard uncertainties associated with the open circuit loss-free transfer function  $H_{15open}^{VV}$  will be investigated for magnitude. This is deemed an important evaluation as the uncertainties associated with  $H_{15open}^{VV}$  will propagate to the calibrated quantities,  $M_V$  and  $S_V$ . In Secs. 7.7 and 7.7 the combined standard uncertainties associated with the magnitude of the calibrated quantities  $M_V$  and  $S_V$  are given, respectively. In Sec. 7.8 the repeatability of the measurement set-up is evaluated.

---

<sup>1</sup>The notation  $u_c(Y)$  will be used whenever the combined uncertainty of a quantity,  $Y$ , is under investigation. However, the input quantities  $X_i$  to  $Y$  can also be functions depending on other input quantities, e.g.  $X_1 = X_1(a_1, a_2)$ . To assess the combined uncertainty of e.g.  $X_1$  the proper notation should be  $u_c(X_1)$ . However, in the appendix H.1 [92], where an example is presented, GUM only use the subscript  $c$  for the combined uncertainty of the final quantity, i.e.  $u_c(Y)$ . The combined uncertainties of the input quantities are e.g. denoted  $u(X_1)$ , although  $X_1$  is itself a function of several quantities. This notation is followed in the current thesis.

## 7.1 Combined standard uncertainty of the measurement distance, $u_c(d)$

An important quantity to be determined in the uncertainty analysis is the uncertainty associated with the measurement distance,  $d$ . From Eq. (3.1) the measurement distance,  $d$ , can be determined:

$$d = d_{rel} + d_{xe} + d_1 + d_2, \quad (7.1)$$

where  $d_{rel}$ ,  $d_{xe}$ ,  $d_1$ , and  $d_2$  are defined in Sec.3.4. The combined standard uncertainty associated with  $d$  is then

$$u_c(d) = \sqrt{u^2(d_{rel}) + u^2(d_{xe}) + u^2(d_1) + u^2(d_2)}. \quad (7.2)$$

### Standard uncertainty, $u(d_{rel})$

The standard uncertainty  $u(d_{rel})$  associated with the movement of the transmitter, is estimated by measurements on the repeatability of the z-axis translation stage. The measurements and results are given in Sec. 3.4.1. The greatest values in Table 3.8 are used, such that

$$u(d_{rel}) = \sqrt{u^2(d_{rel}^{L_1}) + u^2(d_{rel}^{L_2})} = 11 \cdot 10^{-6} \text{ m}, \quad (7.3)$$

where  $u(d_{rel}^{L_1}) = 9.6 \cdot 10^{-6} \text{ m}$  and  $u(d_{rel}^{L_2}) = 4.5 \cdot 10^{-6} \text{ m}$  are the measured repeatabilities of laser 1 and 2, respectively. The values are given with a 68.3% confidence level.

### Standard uncertainty, $u(d_{xe})$

The standard uncertainty associated with the calibrated distance  $d_x$  corrected for possible thermal expansion  $d_{xe}$  is denoted  $u(d_{xe})$ . The associated uncertainty is found to be mainly due to the uncertainty associated with  $d_x$ , such that  $u(d_{xe}) \approx u(d_x)$ , where  $u(d_x) = 2.9 \text{ }\mu\text{m}$  was obtained in Sec. 5.6.3.

### Standard uncertainty, $u(d_1)$ and $u(d_2)$

The uncertainties,  $u(d_1)$  and  $u(d_2)$ , associated with the measured distances  $d_1$  and  $d_2$ , respectively, will be investigated in the current section. However, because it is assumed that the uncertainties  $u(d_1)$  and  $u(d_2)$  are equal, only the investigation of  $u(d_1)$  will be shown.

In Sec. 5.16 the uncertainty of the measured distance  $d_1$  was under investigation. There it was found that the standard uncertainty,  $u(d_1)$ , could be approximated by the uncertainty of the linearity of the laser sensors, i.e.  $u(d_1) \approx u(d_{lin}) \approx 1.4 \text{ }\mu\text{m}$ .

This result is still valid, and will be employed. However, since we are now discussing the distance measurement performed prior to an acoustical measurement, the laser sensors have to be elevated to the appropriate measurement height by the translation pole. Thus, the possible uncertainties associated with this translation have to be taken into account. The expression for the standard uncertainty is

$$u(d_1) = \sqrt{u^2(d_{lin}) + u^2(d_{pole})}, \quad (7.4)$$

where  $u(pole)$  is the standard uncertainty associated with the translation pole. In Sec. 5.7 measurements on the repeatability of the translation pole were performed. The greatest values of Fig. 5.8 (right) are selected to represent the standard uncertainty of the translation pole, i.e.  $u(pole) = 27 \text{ }\mu\text{m}$ . Recognizing that  $u(d_{pole}) \gg u(d_{lin})$ , the standard uncertainty  $u(d_1) = u(d_2) \approx u(d_{pole}) \approx 27 \text{ }\mu\text{m}$ .

### 7.1.1 Numerical result, $u_c(d)$

Combining the obtained values, in accordance with Eq. (7.2), yields a combined standard uncertainty  $u_c(d) = 40 \text{ }\mu\text{m}$ , at a 68.3% level of confidence. It is recognized that the greatest contributor to this value is  $u(pole)$ . In the discussion, Sec. 8.6, the implication of this uncertainty is evaluated for the slowly varying phase  $\angle H_{15open}^{VVslow}$ .

## 7.2 Combined standard uncertainty of the impedance of a piezoelectric disk

It is of interest to investigate the uncertainties associated with the measurements on the impedance of the piezoelectric disks used in the current thesis. The investigation is performed on disk 12. The diameter and thickness of disk 12 is  $20.23 \pm 0.04$  mm and  $2.0357 \pm 0.0006$  mm, respectively.

For the disk 12 and the R1-mode, the series resonance frequency,  $f_s$ , and the frequency for maximum admittance,  $f_m$ , are concurrent at 98.75 kHz. The parallel resonance frequency,  $f_p$ , and the frequency for maximum impedance,  $f_n$ , are also concurrent at 114.7 kHz. For the R2-mode these frequencies differ slightly. For the R2-mode,  $f_s$  is at 250.2 kHz,  $f_m$  is at 250.2 kHz,  $f_p$  is at 256.6 kHz, and  $f_n$  is at 256.9 kHz.

The notation  $Z_R = Z_R^{re} + iZ_R^{im} = |Z_R| \angle Z_R$  will be used to denote the complex impedance of a piezoelectric disk, where the subscript  $R$  denotes *receiver*<sup>2</sup>, the superscripts  $re$  and  $im$  denotes the real and imaginary part of the complex impedance, respectively,  $|Z_R|$  and  $\angle Z_R$  denotes the magnitude and phase of the complex impedance, respectively.

The standard uncertainty is evaluated as a type A and type B uncertainty. The type A uncertainty, denoted  $u(|\bar{Z}_R|)$  and  $u(\angle \bar{Z}_R)$ , is estimated as the experimental standard deviation about the mean, c.f. Eq. (A.5), obtained by ten repeated measurements. The measurements have been conducted in the frequency range 50–300 kHz, with a minimum frequency step of 50 Hz in the frequency ranges 90–120 kHz and 225–275 kHz, and a frequency step of 100 Hz elsewhere.

The type B standard uncertainty is calculated assuming a basic accuracy of 0.1% [69], where this value is valid for magnitude and phase measurements or resistance and reactance measurements. This basic accuracy is an approximation to the uncertainty. Available in [69] are tables with specified measurement accuracy as function of impedance and dissipation, and it is believed, but not investigated, that utilizing these tables will result in a more accurate statement about the uncertainty.

The type B standard uncertainty is calculated by

$$\begin{aligned} u(|Z_R^B|) &= \frac{|Z_R| \cdot 0.001}{2\sqrt{3}}, \\ u(\angle Z_R^B) &= \frac{\angle Z_R \cdot 0.001}{2\sqrt{3}}, \end{aligned} \quad (7.5)$$

where the superscript  $B$  denotes the type B evaluation, dividing on  $\sqrt{3}$  is performed assuming a rectangular distribution, and dividing on two is to obtain the half-width of the distribution.

The combined standard uncertainty,  $u_c(|Z_R|)$ , associated with the magnitude of the impedance of the piezoelectric disk, and the combined standard uncertainty,  $u_c(\angle Z_R)$ , associated with the phase of the impedance of the piezoelectric disk, are estimated by

$$\begin{aligned} u_c(|Z_R|) &= \sqrt{u^2(|\bar{Z}_R|) + u^2(|Z_R^B|)}, \\ u_c(\angle Z_R) &= \sqrt{u^2(\angle \bar{Z}_R) + u^2(\angle Z_R^B)}. \end{aligned} \quad (7.6)$$

In Fig. 7.1 (a) the relative standard uncertainty  $u_r(|Z_R|) = u_c(|Z_R|)/|Z_R|$  is given in percent and as a function of frequency. It is observed that the largest relative uncertainties are associated with the R1- and R2-modes, and that the relative uncertainty tends to 0.03% outside of the resonance modes. The largest uncertainties are observed for 99.1 kHz and for 114.8 kHz where relative standard uncertainties of 0.28% and 0.38% are observed. The frequency range 250–260 kHz is associated with a relative uncertainty in the range 0.04–0.24%, with peak values of 0.24% and 0.23% occurring at 251.7 and 255.1 kHz, respectively.

In Fig. 7.1 (b) the standard uncertainty,  $u_c(\angle Z_R)$ , is given as a function of frequency. It is observed that for most frequencies the standard uncertainty tends to  $0.05^\circ$ . However, for the R1-mode, the standard uncertainty increases rapidly and peaks at both 98.7 kHz and 114.5 kHz, with

<sup>2</sup>The notation  $R$  for receiver is adopted here to conform with the notation in Sec. 7.5.4. The results obtained in the current section are valid for a transmitting disk as well.

standard uncertainties of  $0.22^\circ$  and  $0.26^\circ$ , respectively. At the R2-mode, the standard uncertainty exceeds  $0.15^\circ$  for the frequencies 250.2 kHz and 256.6 kHz.

For both magnitude and phase, it is observed that the frequencies where the uncertainties peaks are at slightly different frequencies than the respective resonance frequencies.

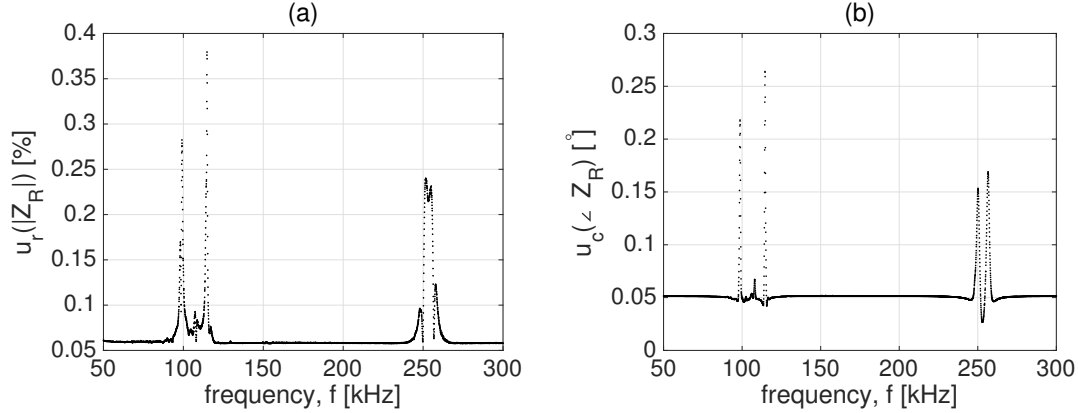


Figure 7.1: (a) relative standard uncertainty,  $u_r(|Z_R|)$ , associated with the magnitude of the impedance of a piezoelectric disk,  $|Z_R|$ . (b) standard uncertainty,  $u_c(\angle Z_R)$ , associated with the phase of the impedance of a piezoelectric disk,  $Z_R$ .

### 7.3 Standard uncertainty associated with the correction term accounting for attenuation in air, $u(C_\alpha)$

In [48] the accuracy of the attenuation coefficient,  $\alpha$ , is estimated to be  $\pm 10\%$ . This value is valid if 1) the molar concentration of water vapor is in the range 0.05–5%, 2) the air temperature is in the range  $-20$  to  $+50$  °C, 3) the atmospheric pressure is less than 200 kPa, and 4) the frequency-to-pressure ratio is in the range 40 Hz/atm – 1 MHz/atm.

Typical values obtained at the laboratory for the criterion are 1) 0.5–2%, 2) 24 °C, 3) 90–120 kPa, and 4) (for a frequency range 50–300 kHz) 50–300 kHz/Pa. It is appreciated that all criterion are fulfilled.

The standard uncertainty associated with the correction term  $u(C_\alpha)$ , c.f. Sec. 2.9, is

$$u(C_\alpha) = 0.1151 C_\alpha \sqrt{d^2 u^2(\alpha) + \alpha^2 u^2(d)}, \quad (7.7)$$

where  $u^2(\alpha)$  is the standard uncertainty associated with the attenuation coefficient  $\alpha$ ,  $u(d) \approx 40$   $\mu\text{m}$  (c.f. Sec. 7.1) is the standard uncertainty associated with the measurement distance  $d$ ,  $C_\alpha$  and the constant 0.1151 are defined in Sec. 2.9. In Fig. 7.2 (a) the standard uncertainty,  $u(C_\alpha)$ , is given in the frequency range 10–300 kHz for two distances:  $d = 0.50$  m (circles) and  $d = 0.85$  m (crosses). In (b) the relative uncertainty,  $u_r(C_\alpha) = u(C_\alpha)/C_\alpha$  is given for the same frequency range and distances as in (a). For both figures the following settings have been used: pressure 101325 Pa, relative humidity 40%, temperature 24° C.

### 7.4 Standard uncertainty associated with FFT-subroutine

A possible recurring source of uncertainty is the FFT-subroutine, c.f. Sec. 3.5. The FFT-subroutine is a numerical algorithm that estimates the frequency spectra, which in general could be associated with uncertainties. However, to assess this, transformations of simulated sinusoids have been performed. The transformations have yielded results with negligible deviations (not shown). Thus, throughout the thesis the FFT-subroutine is considered not to be associated with any uncertainties.



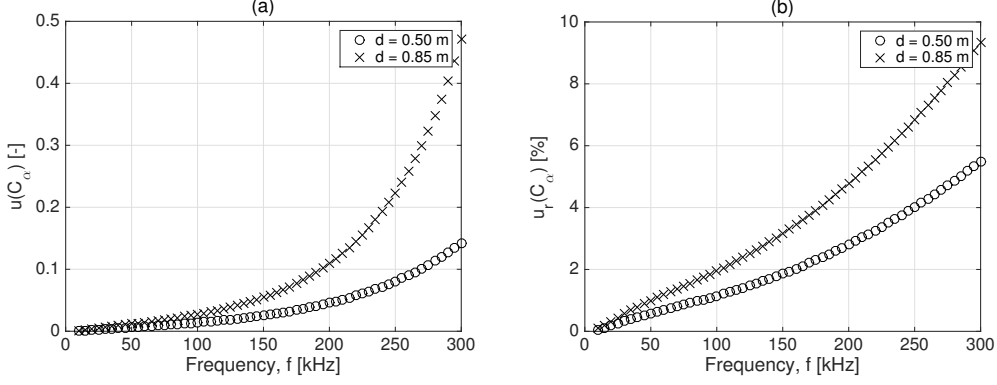


Figure 7.2: (a) standard uncertainty,  $u(C_\alpha)$ , associated with the correction term  $C_\alpha$ , (b) relative uncertainty,  $u_r(C_\alpha)$ .

## 7.5 Combined standard uncertainty, $u_c(|H_{15open}^{VV}|)$

The combined standard uncertainty,  $u_c(|H_{15open}^{VV}|)$ , c.f. Sec. 2.1.2, associated with the magnitude of the transfer function,  $|H_{15open}^{VV}|$ , obtained by measurements, will be dealt with in the following section. The evaluation will be given for a separation distance of 0.50 m, and is valid for approximately 24° C, a relative humidity of 35–40%, and an ambient pressure of approximately 100 kPa.

From Eq. (2.10) the magnitude of the transfer function can be expressed as the magnitude of each input quantity, i.e.

$$\begin{aligned} |H_{15open}^{VV}| &= \frac{|V_6|}{|V_{0m}|} \frac{1}{|H_{0m1}^{VV}| |H_{5open5'}^{VV}| |H_{5'6open}^{VV}| |H_{6open6}^{VV}|} C_\alpha |C_{dif}^{SFDC}| \\ &\approx \frac{|V_6|}{|V_{0m}|} \frac{1}{|H_{5open5'}^{VV}| |H_{5'6open}^{VV}|} C_\alpha |C_{dif}^{SFDC}| = \beta_1, \end{aligned} \quad (7.8)$$

where the assumption that  $|H_{0m1}^{VV}| \approx |H_{6open6}^{VV}| \approx 1$  has been made, c.f. Fig. 6.14, where it is observed that this approximation is valid since both corrections tend to one.  $\beta_1$  is used for simplicity of notation, and the subscript  $_1$  is used to separate subsequent  $\beta$ 's. This expression for the magnitude contains all the necessary corrections, as well as acoustical measurements, to obtain the loss-free, open circuit transfer function  $|H_{15open}^{VV}|$ .

The combined standard uncertainty can then be expressed as (c.f. Eq. (A.9))

$$\begin{aligned} u_c(|H_{15open}^{VV}|) &= \beta_1 \left[ \frac{1}{|V_6|^2} u^2(|V_6|) + \frac{1}{|V_{0m}|^2} u^2(|V_{0m}|) + \frac{1}{|H_{5open5'}^{VV}|^2} u^2(|H_{5open5'}^{VV}|) + \dots \right. \\ &\quad \left. \frac{1}{|H_{5'6open}^{VV}|^2} u^2(|H_{5'6open}^{VV}|) + \frac{1}{C_\alpha^2} u^2(C_\alpha) + \frac{1}{|C_{dif}^{SFDC}|^2} u^2(|C_{dif}^{SFDC}|) \right]^{1/2}. \end{aligned} \quad (7.9)$$

The uncertainties associated with each input quantity to Eq. (7.9) will be dealt with in the subsequent sections: Sec.7.5.1:  $u(|V_6|)$ , Sec.7.5.2:  $u(|V_{0m}|)$ , Sec.7.5.3:  $u(|H_{5'6open}^{VV}|)$ , Sec.7.5.4:  $u(|H_{5open5'}^{VV}|)$ , and the standard uncertainty  $u(C_\alpha)$  has been dealt with in Sec.7.3.<sup>3</sup>

### 7.5.1 Standard uncertainty, $u(|V_6|)$

The standard uncertainty associated with the recorded voltage  $|V_6|$  of Eq. (7.9) is determined as a type A and type B uncertainty. The type A uncertainty, denoted  $u(|\bar{V}_6|)$ , is estimated as

<sup>3</sup>Note that in Sec.7.5.3 there are two variables denoted  $|V_{6'}|$  and  $|V_{0'm}|$ . These should not be confused with the variables  $|V_6|$  and  $|V_{0m}|$  in Secs.7.5.1 and 7.5.2, respectively. To distinguish these variables, a ' is imposed on the variables in Sec.7.5.3, although this notation is not used in Sec. 2.10.3.

the experimental standard deviation about the mean, c.f. Eq. (A.6) [92], and is estimated by 6 repeated measurements. The bar over  $\bar{V}_6$  signifies mean. The standard uncertainty  $u(|\bar{V}_6|)$  is dependent on distance, and excitation voltage. Only the separation distance 0.50 m is considered. The frequency ranges 90–105 kHz, and 240–265 kHz utilizes an excitation voltage of 1 V, while for the remaining frequencies 10 V is used.

The type B standard uncertainty associated with  $|V_6|$  is the vertical resolution of the oscilloscope, denoted  $u(osc.res)$ . During measurement the vertical scaling of the oscilloscope changes dynamically depending on the magnitude of the received voltage. The Type B standard uncertainty is therefore frequency dependent, as well as dependent on the excitation voltage. Let  $V_{res}$  denote the full scale vertical resolution of the oscilloscope, then  $V_{res} = 10 \cdot V_{div}$  where  $V_{div}$  is the voltage per division, and multiplication with 10 is performed since there are 10 divisions on the oscilloscope. Given an 8-bit resolution, and a rectangular distribution, the Type B standard uncertainty is

$$u(osc.res) = \frac{(V_{res}/2^8)/2}{\sqrt{3}} \quad (7.10)$$

where dividing on 2 is performed to obtain the half width of the distribution. The standard uncertainty associated with  $|V_6|$  is then

$$u(|V_6|) = \sqrt{u^2(|\bar{V}_6|) + u^2(osc.res)}. \quad (7.11)$$

In Fig. 7.3 (a) the relative standard uncertainty,  $u_r(|V_6|) = u(|V_6|)/|V_6|$  is given in decibel. The red crosses indicate the frequency ranges where the 1 V measurements are used.

In Fig. 7.3 (a)  $u_r(|V_6|)$  decreases from 50 kHz to 90 kHz with -25 to -45 dB. The jump in value at 90 kHz is due to the change of excitation voltage from 10 V to 1 V. In the range 90–100 kHz,  $u_r(|V_6|)$  decreases from -30 to -45 dB and  $u_r(|V_6|)$  is fairly constant at -36 to -40 dB in the range 105–120 kHz. At 125 kHz the uncertainty increases rapidly, peaking at 140 kHz with a magnitude exceeding 0 dB. This frequency range is associated with noise, such that the signal is at times lost. Thus a large uncertainty is expected. The uncertainty decreases from 0 to -30 in the range 140–240 kHz. At 240 kHz a second jump is observed, due to the change of excitation voltage from 10 V to 1 V. In the range 240–250 kHz the uncertainty decreases rapidly from -24 to -40 dB. Between 250–265 the uncertainty increases, and peaks with a value larger than 0. This frequency range is also associated with noise.

### 7.5.2 Standard uncertainty, $u(|V_{0m}|)$

The standard uncertainty associated with the recorded voltage  $|V_{0m}|$  of Eq. (7.9) is determined as a type A and type B uncertainty, and is estimated by equal means as  $u(|V_6|)$  Sec.7.5.1, where the type A uncertainty, denoted  $u(|\bar{V}_{0m}|)$ , is estimated as the experimental standard deviation about the mean, c.f. Eq. (A.6) [92], and is estimated by 6 repeated measurements.

The standard uncertainty associated with  $|V_{0m}|$  is

$$u(|V_{0m}|) = \sqrt{u^2(|\bar{V}_{0m}|) + u^2(osc.res)}. \quad (7.12)$$

In Fig. 7.3 (b) the relative standard uncertainty,  $u_r(|V_{0m}|) = u(|V_{0m}|)/|V_{0m}|$  is given in decibel. The red crosses indicate the frequency ranges where the 1 V measurements are used.

Generally, it is observed that  $u_r(|V_{0m}|) < u_r(|V_6|)$ , where  $u_r(|V_{0m}|)$  has a largest uncertainty of -42 dB. This is explained by  $V_{0m}$  being an electrical signal with an expected greater signal-to-noise ratio than  $V_6$ .

The jumps of approximately  $\pm 8$  dB are due to the type B uncertainty, i.e. the uncertainty associated with the vertical resolution of the oscilloscope. For example, at 92 kHz, the excitation voltage is 1 V, and the vertical resolution has changed from 0.5 V/div to 0.2 V/div. This corresponds to a factor of 2.5, and a value of approximately 8 dB. The vertical resolution of the oscilloscope has changed since the impedance of the disk decreases as the frequency approaches 100 kHz c.f. Fig. 3.4, and the excitation voltage is gradually shifted from the disk to the internal output impedance of the function generator. In the range 92–105 the uncertainty first increases rapidly, then decreases rapidly. Remembering that  $u_r(|V_{0m}|)$  is a relative standard uncertainty,

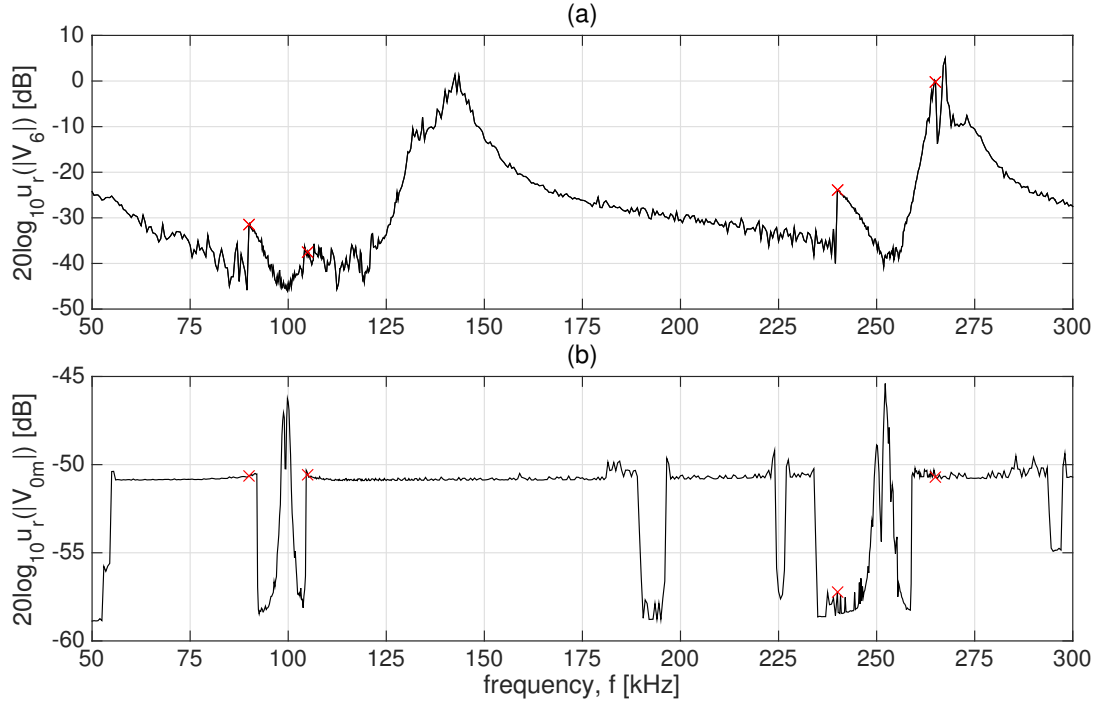


Figure 7.3: (a) relative standard uncertainty,  $u_r(|V_6|)$ , associated with the magnitude of the recorded voltage,  $|V_6|$ , (b) relative standard uncertainty,  $u_r(|V_{0m}|)$ , associated with the magnitude of the recorded voltage,  $|V_{0m}|$ .

where the normalization is performed with respect to the voltage at the terminals of the disk, then an increase in  $u_r(|V_{0m}|)$  is expected when  $|V_{0m}|$  decreases.

c.f. Sec. 2.1.2,

### 7.5.3 Standard uncertainty, $u(|H_{5'6open}^{VV}|)$

The standard uncertainty,  $u(|H_{5'6open}^{VV}|)$ , associated with the magnitude of the transfer function,  $|H_{5'6open}^{VV}|$ , c.f. Secs. 2.1.2 and 2.10.3, is estimated utilizing the simplification:

$$|H_{5'6open}^{VV}| = \frac{|V_{6'}|}{|V_{0'm}|} \frac{1}{|H_{6open6}^{VV}| |H_{05'}^{VV}| |H_{0m0}^{VV}|} \approx \frac{|V_{6'}|}{|V_{0'm}|} \frac{1}{|H_{05'}^{VV}|} = \beta_2, \quad (7.13)$$

where the assumption  $|H_{0m0}^{VV}| \approx |H_{6open6}^{VV}| \approx 1$  has been made.  $|H_{6open6}^{VV}|$  is commented on in Sec. 7.5, and  $|H_{0m0}^{VV}| \approx 1$ , such that both assumptions are valid.  $\beta_2$  is used for short to denote the magnitude of the transfer function. The standard uncertainty, is then

$$u_c(|H_{5'6open}^{VV}|) = \beta_2 \sqrt{\frac{1}{|V_{6'}|^2} u^2(|V_{6'}|) + \frac{1}{|V_{0'm}|^2} u^2(|V_{0'm}|) + \frac{1}{|H_{05'}^{VV}|^2} u^2(|H_{05'}^{VV}|)}. \quad (7.14)$$

The uncertainties associated with  $|V_{6'}|$ ,  $|V_{0'm}|$  and  $|H_{05'}^{VV}|$  are dealt with in the following three sections.

#### Standard uncertainty, $u(|V_{6'}|)$

The standard uncertainty associated with  $|V_{6'}|^4$  is determined as a type A and type B uncertainty, and is estimated by equal means as  $u(|V_6|)$  Sec.7.5.1. The type A uncertainty, denoted  $u(|\bar{V}_{6'}|)$ , is estimated as the experimental standard deviation about the mean, c.f. Eq. (A.6) [92], and is estimated by 10 repeated measurements.

<sup>4</sup>Note that  $|V_{6'}|$  in the current section is different from  $|V_6|$  in Sec.7.5.1

The vertical scaling of the oscilloscope was constant at 2 V/div, such that a voltage range of 20 V was realized during measurements. The type B standard uncertainty is then

$$u(osc.res) = \frac{(20/2^8)/2}{\sqrt{3}} \approx 22.6 \cdot 10^{-3} V, \quad (7.15)$$

and the standard uncertainty associated with  $|V_{6'}|$  is

$$u(|V_{6'}|) = \sqrt{u^2(|\bar{V}_{6'}|) + u^2(osc.res)}. \quad (7.16)$$

In Fig. 7.4 (a) the relative standard uncertainty  $u_r(|V_{6'}|) = u(|V_{6'}|)/|V_{6'}|$  is given in decibels. It is observed that the values tend to be in the range -75 to -70 dB, with some fluctuations at the upper frequency range.

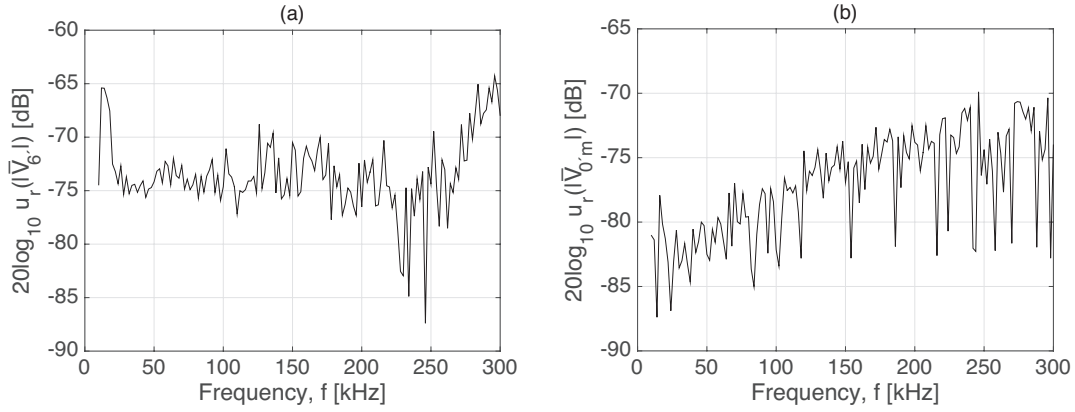


Figure 7.4: (a) relative standard uncertainty,  $u_r(|V_{6'}|)$ . (b) relative standard uncertainty,  $u_r(|V_{0'm}|)$ . For both (a) and (b) the uncertainties are associated with measurements on the transfer function  $u(|H_{5'6open}^{VV}|)$ .

### Standard uncertainty, $u(|V_{0'm}|)$

The standard uncertainty associated with  $|V_{0'm}|$ <sup>5</sup> is determined as a type A and type B uncertainty, and is estimated by equal means as  $u(|V_{6'}|)$  Sec.7.5.1. The type A uncertainty, denoted  $u(|\bar{V}_{0'm}|)$ , is estimated as the experimental standard deviation about the mean, c.f. Eq. (A.6) [92], and is estimated by 10 repeated measurements.

The vertical scaling of the oscilloscope was constant at 0.1 V/div, such that a voltage range of 1 V was realized during measurements. The type B standard uncertainty is then

$$u(osc.res) = \frac{(1/2^8)/2}{\sqrt{3}} \approx 1.1 \cdot 10^{-3} V. \quad (7.17)$$

$$u(|V_{0'm}|) = \sqrt{u^2(|\bar{V}_{0'm}|) + u^2(osc.res)}. \quad (7.18)$$

In Fig. 7.4 (b) the relative standard uncertainty  $u_r(|V_{0'm}|) = u(|V_{0'm}|)/|V_{0'm}|$  is given in decibels. It is observed that the values tend to be in the range -85 to -70 dB.

### Standard uncertainty, $u(|H_{05'}^{VV}|)$

The standard uncertainty,  $u(|H_{05'}^{VV}|)$ , associated with the magnitude of the transfer function,  $|H_{05'}^{VV}|$ , (c.f. Sec. 2.10.3) is estimated by

$$|H_{05'}^{VV}| = \frac{1}{\left(\frac{1}{Z_{vd2}} + \frac{1}{Z_{amp,in}}\right)Z_{vd1} + 1} \approx \frac{1}{\frac{Z_{vd1}}{Z_{vd2}} + 1} = \frac{1}{\beta_3}, \quad (7.19)$$

<sup>5</sup>Note that  $|V_{0'm}|$  in the current section is different from  $|V_{0m}|$  in Sec.7.5.2

since  $|Z_{amp,in}| \gg Z_{vd2}$ . The absolute sign is omitted from both  $Z_{vd1}$  and  $Z_{vd2}$  since they are resistances with assumed negligible reactance. It is also assumed that  $Z_{vd1}$  and  $Z_{vd2}$  are independent of frequency. Both  $Z_{vd1}$  and  $Z_{vd2}$  are measured with the same HP-impedance analyzer [69], however they are assumed uncorrelated. The values and standard uncertainties for  $Z_{vd1}$  and  $Z_{vd2}$  are states in Table 7.1 and are calculated according to [69].

The standard uncertainty,  $u(|H_{05'}^{VV}|)$ , can be obtained by

$$u(|H_{05'}^{VV}|) = \frac{1}{\beta_3^2} \sqrt{\frac{1}{Z_{vd2}^2} u^2(Z_{vd1}) + \frac{Z_{vd1}^2}{Z_{vd2}^4} u^2(Z_{vd2})} \approx 1.0 \cdot 10^{-3}, \quad (7.20)$$

where the obtained value is given at a confidence level of 68.3%.

Table 7.1: Values for  $Z_{vd1}$  and  $Z_{vd2}$  with standard uncertainties at a confidence level of 68.3%.

Quantity	Resistance [ $\Omega$ ]	Standard uncertainty [68.3%] [69]
$Z_{vd1}$	1196	9.3
$Z_{vd2}$	42.98	1.3

### Result standard uncertainty, $u(|H_{5'6open}^{VV}|)$

In Fig. 7.5 (a) the transfer function  $|H_{5'6open}^{VV}|$  is given (blue) with errorbars (black) signifying the associated uncertainty at a level of confidence of 68.3%. It is observed that the uncertainties are approximately  $\pm 30$ , which corresponds to a deviation of less than  $\pm 0.3$  dB for the entire frequency range. In comparison, the manufacturer of the amplifier [82] gives the uncertainty to be  $\pm 0.5$  dB in the frequency range 1 Hz to 200 kHz. In (b) the relative uncertainty,  $u_r(|H_{5'6open}^{VV}|) = u(|H_{5'6open}^{VV}|)/|H_{5'6open}^{VV}|$ , is given in percentage. It is appreciated that the relative uncertainties are practically constant, equal to 3.0%.

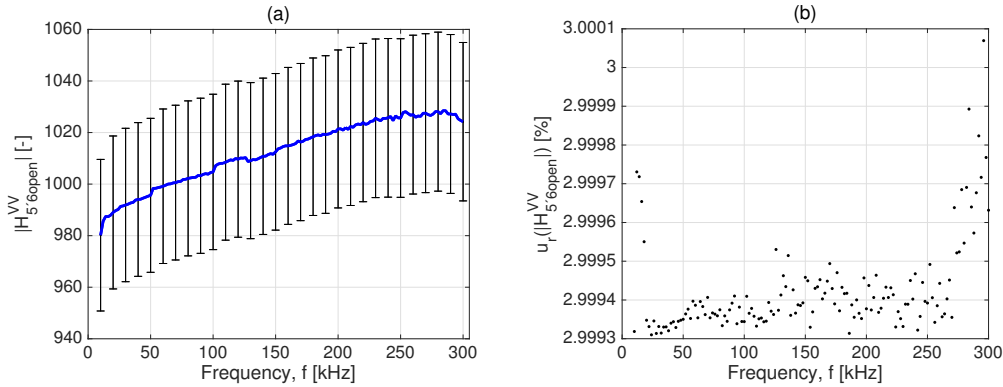


Figure 7.5: (a) standard uncertainty of the transfer function  $|H_{5'6open}^{VV}|$  (blue) given as errorbars (black). (b) relative uncertainty,  $u_r(|H_{5'6open}^{VV}|)$  of the transfer function  $|H_{5'6open}^{VV}|$ .

### 7.5.4 Standard uncertainty, $u(|H_{5open5'}^{VV}|)$

In the following section the standard uncertainty,  $u(|H_{5open5'}^{VV}|)$ , associated with the magnitude of the transfer function,  $|H_{5open5'}^{VV}|$ , c.f. Secs. 2.1.2 and 2.10.3, will be estimated. However, the estimation of  $u(|H_{5open5'}^{VV}|)$  requires a little subtlety as the input quantities to  $H_{5open5'}^{VV}$ , in general, are complex numbers. Although e.g.  $H_{15open}^{VV}$  is also a complex number with complex input quantities, for this transfer function an expression for the magnitude,  $|H_{15open}^{VV}|$ , expressed as a function of the magnitude of each input quantity was possible to obtain. However, this has not been possible to obtain for the magnitude  $|H_{5open5'}^{VV}|$ .

To overcome this, the input variables to  $|H_{5open5'}^{VV}|$  will be expressed as the real and imaginary parts of each input quantity, and the associated uncertainties will be expressed with respect to the real and imaginary parts.

From Eq. (2.70) we have

$$H_{5open5'}^{VV} = \frac{Z_{amp,in} Z_{b3}}{(Z_R + Z_{a3}) Z_{b3} + (Z_{a3} + Z_{amp,in}) \cdot (Z_R + Z_{a3} + Z_{b3})} \quad (7.21)$$

$$\approx \frac{1}{Z_R \left( \frac{1}{Z_{amp,in}} + \frac{1}{Z_{b3}} \right) + 1} = \frac{1}{Z_R Z_t + 1},$$

where the approximation is obtained by setting  $Z_{a3} = 0$ . The approximation is valid since  $|Z_{a3}| \ll |Z_{b3}|$  and  $|Z_{a3}| \ll |Z_{amp,in}|$ . The last expression is obtained by  $Z_t = \frac{1}{\frac{1}{Z_{amp,in}} + \frac{1}{Z_{b3}}}$ . All variables,  $Z_{amp,in}$ ,  $Z_{a3}$ ,  $Z_{b3}$  and  $Z_R$  are defined in Sec. 2.10.3.

The magnitude of Eq. (7.21) can be expressed as the real and imaginary part of each input quantity,  $Z_R = Z_R^{re} + iZ_R^{im}$ ,  $Z_{amp,in} = Z_{amp,in}^{re} + iZ_{amp,in}^{im}$ ,  $Z_{b3} = iZ_{b3}^{im}$  and  $Z_t = Z_t^{re} + iZ_t^{im}$ , i.e.

$$|H_{5open5'}^{VV}(Z_R^{re}, Z_R^{im}, Z_{amp,in}^{re}, Z_{amp,in}^{im}, Z_{b3}^{im})| = \sqrt{\frac{1}{(Z_R^{re} Z_t^{re} - Z_R^{im} Z_t^{im} + 1)^2 + (Z_R^{re} Z_t^{im} + Z_R^{im} Z_t^{re})^2}}, \quad (7.22)$$

where

$$Z_t^{re} = \frac{Z_{amp,in}^{re}}{(Z_{amp,in}^{re})^2 + (Z_{amp,in}^{im})^2}, \quad (7.23)$$

$$Z_t^{im} = - \left[ \frac{Z_{amp,in}^{im}}{(Z_{amp,in}^{re})^2 + (Z_{amp,in}^{im})^2} + \frac{1}{Z_{b3}^{im}} \right].$$

All input quantities to Eq. (7.22) are now real valued numbers, and the sensitivity coefficients can thus be obtained by partial derivation with respect to each input quantity.

### Sensitivity coefficients

The sensitivity coefficients are obtained by employing the symbolic derivation capability of MATLAB. To assess the expressions obtained by MATLAB, numerical partial derivation by central difference has been performed. In Fig. 7.6 (a) the sensitivity coefficient  $C_1 = \frac{\partial F}{\partial Z_R^{re}}$  obtained by analytic partial derivation (blue) and numerical partial derivation (stippled red) is given. Except small fluctuations in the numerical results it is appreciated that the two methods show good agreement. In Fig. 7.6 (b) the sensitivity coefficients,  $C_1 = \frac{\partial F}{\partial Z_R^{re}}$ ,  $C_2 = \frac{\partial F}{\partial Z_R^{im}}$ ,  $C_3 = \frac{\partial F}{\partial Z_{amp,in}^{re}}$ ,  $C_4 = \frac{\partial F}{\partial Z_{amp,in}^{im}}$ ,  $C_5 = \frac{\partial F}{\partial Z_{b3}^{im}}$ , are presented. The expressions for the analytic sensitivity coefficients are left out of the thesis, however, in Appendix B.1.3 the script used to generate the sensitivity coefficients is given.

### Standard uncertainties $u(Z_R^{re})$ and $u(Z_R^{im})$

The uncertainties associated with the impedance of the piezoelectric disk is estimated by similar method as in Sec. 7.2, though with respect to the real and imaginary part of the complex impedance. The derivation will therefore be omitted, however in Fig. 7.7 (a) the relative uncertainties  $u_r(Z_R^{re}) = u(Z_R^{re})/Z_R^{re}$  (blue), and  $u_r(Z_R^{im}) = u(Z_R^{im})/Z_R^{im}$  (red) is given. The large spikes for  $u_r(Z_R^{im})$  is due to the normalization with  $Z_R^{im}$  which for the frequencies 100 kHz, 115 kHz, 250 kHz and 256 kHz tends to zero.

### Standard uncertainties $u(Z_{amp,in}^{re})$ and $u(Z_{amp,in}^{im})$

The manufacturer [82] provides no information regarding the uncertainties of the input impedance of the amplifier. Therefore, the uncertainties associated with the real and imaginary part of

the complex input impedance of the amplifier, is determined using the results in Sec. ??, where measurements on the input impedance of the amplifier were performed. The difference between the adjusted values and the data-sheet values are used as an estimation of the uncertainties associated with the input resistance and input capacitance, which in turn is used to estimate  $u(Z_{amp,in}^{re})$  and  $u(Z_{amp,in}^{im})$ . The input impedance of the amplifier is the input resistance in parallel with the input capacitance, i.e.

$$Z_{amp,in} = \frac{R_{amp,in} \cdot \frac{1}{\omega C_{amp,in}}}{R_{amp,in} + \frac{1}{\omega C_{amp,in}}}, \quad (7.24)$$

where  $R_{amp,in}$  is the input resistance of the amplifier,  $C_{amp,in}$  is the input capacitance of the amplifier, and  $\omega = 2\pi f$ . The real and imaginary part of  $Z_{amp,in}$  can be expressed as

$$\begin{aligned} Z_{amp,in}^{re} &= \frac{R_{amp,in}}{(R_{amp,in} \cdot \omega \cdot C_{amp,in})^2 + 1}, \\ Z_{amp,in}^{im} &= \frac{(R_{amp,in})^2 \cdot \omega \cdot C_{amp,in}}{(R_{amp,in} \cdot \omega \cdot C_{amp,in})^2 + 1}. \end{aligned} \quad (7.25)$$

Four sensitivity coefficients are needed, which are defined as

$$\begin{aligned} C_1^{re} &\equiv \frac{\partial Z_{amp,in}^{re}}{\partial R_{amp,in}} = \frac{1 - (R_{amp,in} \cdot \omega \cdot C_{amp,in})^2}{([R_{amp,in} \cdot \omega \cdot C_{amp,in}]^2 + 1)^2}, \\ C_2^{re} &\equiv \frac{\partial Z_{amp,in}^{re}}{\partial C_{amp,in}} = -\frac{2(R_{amp,in}^3 \cdot \omega^2 \cdot C_{amp,in})}{([R_{amp,in} \cdot \omega \cdot C_{amp,in}]^2 + 1)^2}, \\ C_1^{im} &\equiv \frac{\partial Z_{amp,in}^{im}}{\partial R_{amp,in}} = \frac{2R_{amp,in} \cdot \omega C_{amp,in}}{([R_{amp,in} \cdot \omega \cdot C_{amp,in}]^2 + 1)^2}, \\ C_2^{im} &\equiv \frac{\partial Z_{amp,in}^{im}}{\partial C_{amp,in}} = -\frac{R_{amp,in}^2 \cdot \omega [(R_{amp,in} \cdot \omega \cdot C_{amp,in})^2 - 1]}{([R_{amp,in} \cdot \omega \cdot C_{amp,in}]^2 + 1)^2}. \end{aligned} \quad (7.26)$$

The standard uncertainties  $u(Z_R^{re})$  and  $u(Z_R^{im})$  can then be expressed by

$$\begin{aligned} u(Z_{amp,in}^{re}) &= \sqrt{C_1^{re2} u^2(R_{amp,in}) + C_2^{re2} u^2(C_{amp,in})}, \\ u(Z_{amp,in}^{im}) &= \sqrt{C_1^{im2} u^2(R_{amp,in}) + C_2^{im2} u^2(C_{amp,in})}, \end{aligned} \quad (7.27)$$

where the uncertainties associated with the input resistance,  $u(R_{amp,in})$ , and input capacitance,  $u(C_{amp,in})$ , are estimated as Type B uncertainties:

$$\begin{aligned} u(R_{amp,in}) &= \frac{5 \cdot 10^3 \Omega}{\sqrt{3}}, \\ u(C_{amp,in}) &= \frac{6 \cdot 10^{-12} \text{ F}}{\sqrt{3}}, \end{aligned} \quad (7.28)$$

assuming a rectangular distribution, and where the midpoint of the rectangular distribution is assumed to be the adjusted values obtained in Sec. ?? with the largest deviation of the distribution being the data-sheet value. In Fig. 7.7 (a) the relative uncertainties  $u_r(Z_{amp,in}^{re}) = u(Z_{amp,in}^{re})/Z_{amp,in}^{re}$  (orange), and  $u_r(Z_{amp,in}^{im}) = u(Z_{amp,in}^{im})/Z_{amp,in}^{im}$  (lilac) are given.

### Standard uncertainty $u_r(Z_{b3}^{im})$

The standard uncertainty,  $u_r(Z_{b3}^{im})$ , associated with the cable parameter  $Z_{b3}$ , is determined as a Type B uncertainty. Note that this quantity is purely imaginary. From Eq. (2.65)

$$Z_b = \frac{Z_0}{i \sin(k_{em} l)}, \quad (7.29)$$

where  $Z_0$  is the characteristic impedance of the the coaxial cable,  $k_{em}$  is the electromagnetic wave number and  $l$  is the cable length, the standard uncertainty can be derived:

$$u(Z_{b3}^{im}) = \sqrt{\frac{1}{\sin^2(k_{em} l)} u^2(Z_0) + \left[ \frac{Z_0 \cos(k_{em} l)}{\sin(k_{em} l)} \right]^2 u^2(k_{em})}, \quad (7.30)$$

where the uncertainty associated with the cable length has shown to be negligible. The manufacturer of the coaxial cable has given the uncertainty associated with the characteristic impedance to be  $\pm 2 \Omega$ , such that, assuming are rectangular distribution, the standard uncertainty is

$$u(Z_0) = \frac{2 \Omega}{\sqrt{3}}. \quad (7.31)$$

The electromagnetic wave number,  $u(k_{em})$ , was given in Eq. (2.66), as

$$k_{em} = \omega \sqrt{L_x C_x}, \quad (7.32)$$

where  $L_x$  is the inductance per meter, and  $C_x$  is the capacitance per meter of the coaxial cable, such that the standard uncertainty,  $u(k_{em})$ , is given by

$$u(k_{em}) = \frac{\omega \cdot \sqrt{L_x}}{2\sqrt{C_x}} u(C_x), \quad (7.33)$$

where the uncertainty associated with the inductance per meter has shown to be negligible for the cable lengths used in the current thesis. The standard uncertainty  $u(C_x)$  is determined from the measurements on the coaxial cable in Sec. ???. Assuming a rectangular distribution, and where the midpoint of the rectangular distribution is assumed to be the adjusted value, the uncertainty  $u(C_x)$  is therefore

$$u(C_x) = \frac{7 \cdot 10^{-12} \text{ F}}{\sqrt{3}}. \quad (7.34)$$

The uncertainty  $u(Z_{b3}^{im})$  is fully defined, and in Fig. 7.7 (a) the relative uncertainty  $u_r(Z_{b3}^{im}) = u(Z_{b3}^{im})/Z_{b3}^{im}$  is given in green.

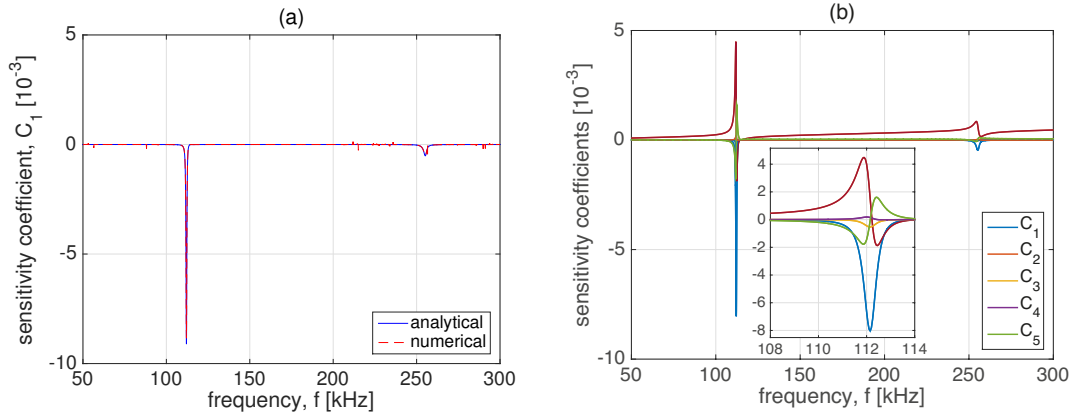


Figure 7.6: (a) sensitivity coefficient,  $C_1$ , obtained by analytic partial derivation (blue) and numerical partial derivation (stippled red). (b) the sensitivity coefficients,  $C_1, C_2, \dots, C_5$ . The frequency range 116–120 kHz is magnified.



### Final expression for the standard uncertainty $u(|H_{5open5'}^{VV}|)$

The final expression for the standard uncertainty,  $u(|H_{5open5'}^{VV}|)$ , is

$$u(|H_{5open5'}^{VV}|) = \sqrt{C_1^2 u^2(Z_R^{re}) + C_2^2 u^2(Z_R^{im}) + C_3^2 u^2(Z_{amp,in}^{re}) + C_4^2 u^2(Z_{amp,in}^{im}) + C_5^2 u^2(Z_{b3}^{im})}. \quad (7.35)$$

In Fig.7.7 (b) the relative uncertainty  $u_r(|H_{5open5'}^{VV}|) = u(|H_{5open5'}^{VV}|)/|H_{5open5'}^{VV}|$  is given as a function of frequency. The frequency range  $f = 108\text{--}116$  kHz is magnified. It is observed that the relative uncertainty is for most frequencies lower than 1%, however around the  $f = 110\text{--}116$  kHz the relative uncertainty increases rapidly, peaking around 5% for  $f = 111.8$  kHz and  $f = 112.5$  kHz.

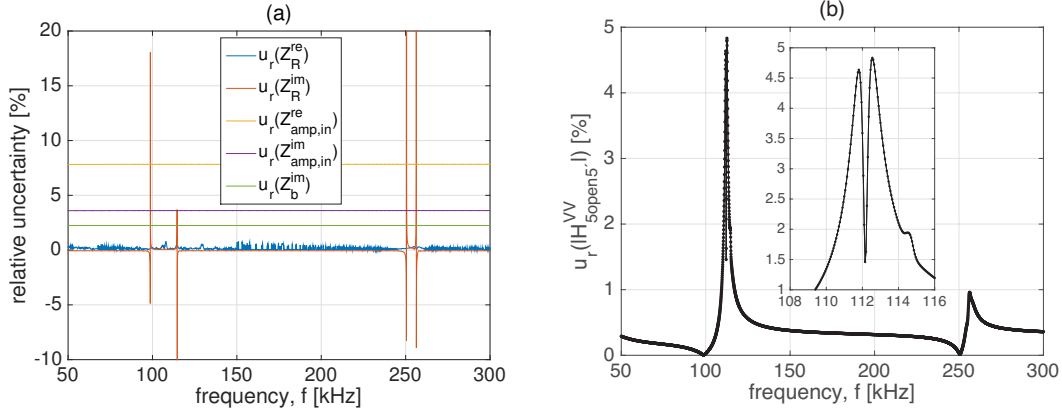


Figure 7.7: (a) relative uncertainties for the input quantities to Eq. (7.35). (b) relative uncertainty,  $u_r(|H_{5open5'}^{VV}|)$ , for the magnitude of the transfer function  $|H_{5open5'}^{VV}|$ . The frequency range  $f = 108\text{--}116$  kHz is magnified.

### 7.5.5 Standard uncertainty, $u(|C_{dif}^{SFDC}|)$

As an approximation, the uncertainty  $u(|C_{dif}^{SFDC}|)$  is set to zero, but not  $|C_{dif}^{SFDC}|$  itself. The uncertainty  $u(|C_{dif}^{SFDC}|)$  can be difficult to estimate since the validity of the model is still under investigation [49,107]. Although it is possible to estimate the uncertainty of  $C_{dif}$  using the GUM approach, it is believed that more investigation into the model is necessary. In an updated version of FEMP to be released during the autumn of 2015 a new functionality implemented by Storheim [49,108] will allow a user to define a receiver in the sound field. It is believed that this can aid in assessing the SFDC model, and possibly be used to estimate the uncertainty associated with the correction.

Excluding the uncertainty  $u(|C_{dif}^{SFDC}|)$  from the total uncertainty budget should, however, not be associated with too large deviations in the final uncertainty. For example, at 100 kHz and a separation distance of 0.50 m,  $|C_{dif}^{SFDC}|$  corrects the transfer function  $|H_{15open}^{VV}|$  with -1.4%. To compare this value with  $|C_{dif}^{BPDC}|$ , a correction of 1.1% is applied to  $|H_{15open}^{VV}|$ , and the difference between the two corrections is 2.5%. For both  $|C_{dif}^{SFDC}|$  and  $|C_{dif}^{BPDC}|$  the corrections are low in value, and the associated uncertainties relative to the total uncertainty budget is thus expected to be low.

### 7.5.6 Results for the standard uncertainty, $u_c(|H_{15open}^{VV}|)$

All input quantities and corresponding uncertainties to Eq. (7.9) have now been obtained. The final expression for the standard uncertainty,  $u_c(|H_{15open}^{VV}|)$ , where  $u(|C_{dif}^{SFDC}|) = 0$ , is

$$u_c(|H_{15open}^{VV}|) = \beta_1 \left[ \frac{1}{|V_6|^2} u^2(|V_6|) + \frac{1}{|V_{0m}|^2} u^2(|V_{0m}|) + \frac{1}{|H_{5open5'}^{VV}|^2} u^2(|H_{5open5'}^{VV}|) + \dots \right. \\ \left. \frac{1}{|H_{5'6open}^{VV}|^2} u^2(|H_{5'6open}^{VV}|) + \frac{1}{C_\alpha^2} u^2(C_\alpha) \right]^{1/2}. \quad (7.36)$$

In Fig. 7.8 the relative uncertainty  $u_r(|H_{15open}^{VV}|) = u_c(|H_{15open}^{VV}|)/|H_{15open}^{VV}|$  is given for (a) decibel, and (b) percent, and in (c) the positive deviation associated with  $u_c(|H_{15open}^{VV}|)$  calculated by

$$\text{deviation} = 20 \log_{10} \left[ 1 + \frac{u_c(|H_{15open}^{VV}|)}{|H_{15open}^{VV}|} \right]. \quad (7.37)$$

The deviation is useful when comparing the values obtained in the current thesis with e.g. data-sheet values of microphones and corresponding uncertainties. For (a), (b) and (c) the red crosses indicate where the 1 V measurements are used.

In Fig. 7.8 (a) the the relative uncertainty,  $u_r(|H_{15open}^{VV}|)$ , decreases in value from -23 to -29 dB in the range 50–90 kHz. A jump in value is observed at 90 kHz where the 1 V measurement is used. For the range 90–105 kHz  $u_r(|H_{15open}^{VV}|)$  decreases from -27 to -29 dB. In the range 110–115 kHz  $u_r(|H_{15open}^{VV}|)$  increases rapidly with 5 dB. This is due to the correction  $|H_{5open5'}^{VV}|$  which has a large impact for this frequency, c.f. Fig. 6.15 (a) for correction and Fig. 7.7 for associated relative standard uncertainty. From 125–160 kHz  $u_r(|H_{15open}^{VV}|)$  is large mainly due to noise. For this range,  $u_r(|H_{15open}^{VV}|)$  peaks at approximately +1 dB. In the range 175–240 kHz  $u_r(|H_{15open}^{VV}|)$  is fairly constant at -25 dB. A jump is observed where the 1 V measurement is used, at 240 kHz. In the range 240–255 the  $u_r(|H_{15open}^{VV}|)$  decreases with 5 dB, with a minimum value of -26 dB. The range 260–280 is associated with noise and large uncertainties are observed.

In Fig. 7.8 (b) the same observations as in (a) can be made, and these will not be repeated. However, it is worth noticing that for the R1-mode a relative standard uncertainty of less than 4% is achieved.

In Fig. 7.8 (c) the same observations as in (a) can be made. However, it is worth noticing that a deviation of less than 0.5 dB is achieved in the range 55–127 kHz, 180–240 kHz, and 245–257 kHz. For 100 kHz a deviation of 0.3 dB is achieved.

## 7.5.7 Comments on correlation and results

### Correlation

All input variables to Eq. (7.8) are assumed uncorrelated and Eq. (A.9), rather than Eq. (A.10), is used. It is assumed that this might lead to deviations in the uncertainty estimate. However, the results obtained in the current section are possible to expand on, when an investigation of the correlation of the input quantities have been made. Due to the complexity of the measurement set-up, it is difficult to assess if possible correlation will result in a decrease or increase in the combined uncertainty.

$|V_6|$  and  $|V_{0m}|$  are correlated since they are recorded with the same oscilloscope. However, the uncertainty associated with  $|V_{0m}|$  is found to be negligible. For example, excluding  $u(|V_{0m}|)$  from  $u_c(|H_{15open}^{VV}|)$  yields a deviation of -1.1%, thus the correlation between  $|V_6|$  and  $|V_{0m}|$  can be neglected [92].

The measurement distance,  $d$ , is obtained by two distance measurements,  $d_1$  and  $d_2$ , where laser sensors of the same make are employed. However, the correlation between the measurements can be neglected as the largest contributor to  $u_c(d)$  is  $u(d_{pole})$ . However  $u(d_1)$  can still be correlated with  $u(d_2)$  as  $u(d_1) = u(d_2) \approx u(d_{pole})$ . The implication of this has not been investigated.

### Results

The discussion of the results are deferred to Sec. 7.6.1 as they are comparable to the results obtained for  $u_c(|M_V|)$

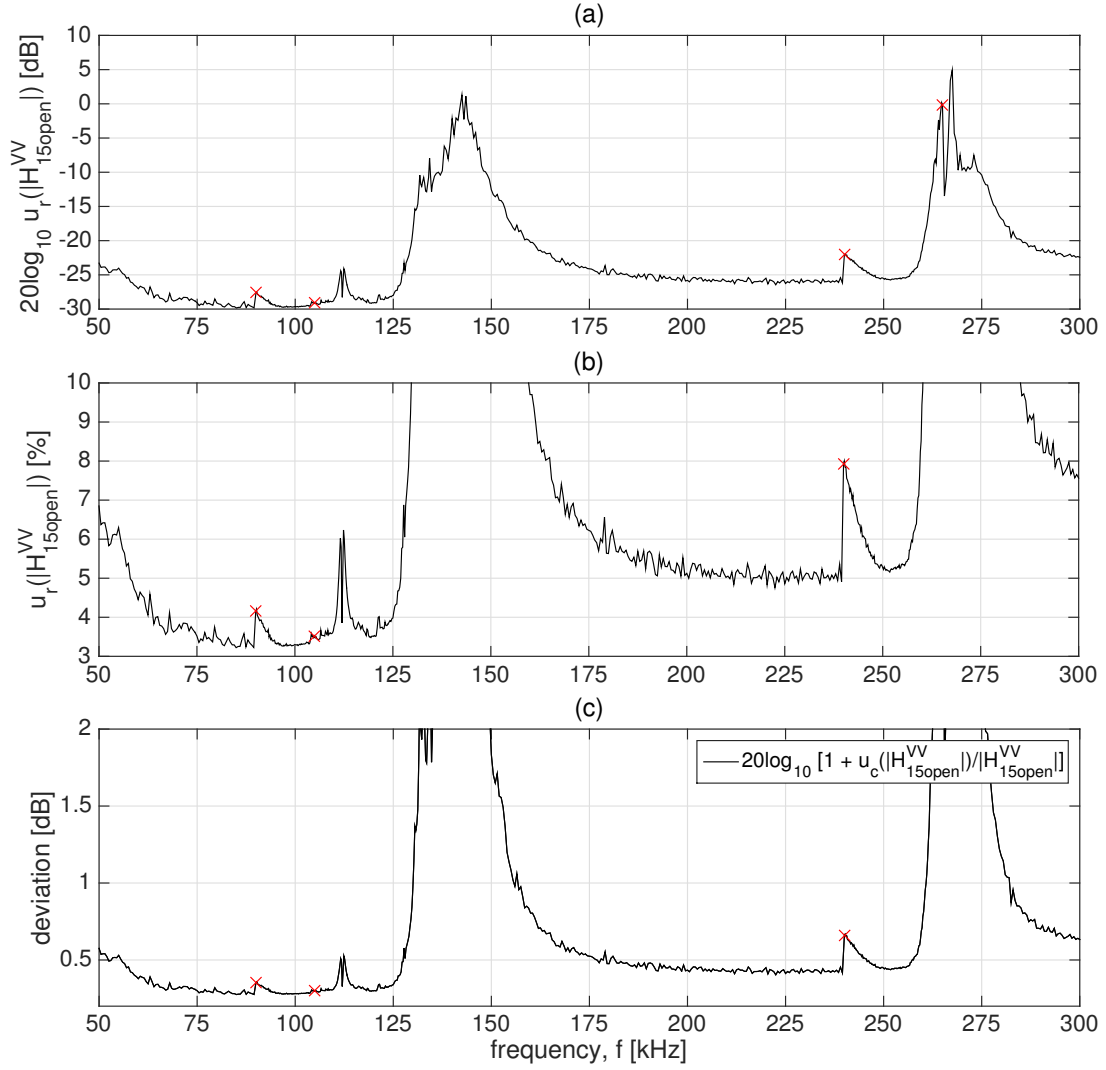


Figure 7.8: (a) and (b) relative uncertainty  $u_r(|H_{15open}^{VV}|)$  shown in decibel and percentage, respectively, and (c) deviation in decibels.

## 7.6 Combined standard uncertainty $u_c(|M_V|)$

In the current section the uncertainty of the magnitude of the receiving sensitivity  $u_c(|M_V|)$  obtained by the reciprocity method will be evaluated. The evaluation is valid for the same environmental conditions stated in Sec. 7.5.

From eq. (2.38) the magnitude of  $M_V$  is obtained, i.e.

$$|M_V| = \left[ |J^{(3)}| |Z^{T_3}| \frac{|H_{15open}^{VV(1)}| |H_{15open}^{VV(3)}| d_1 d_3}{|H_{15open}^{VV(2)}| d_0 d_2} \right]^{\frac{1}{2}} \quad (7.38)$$

where all input quantities have been defined in Sec. 2 and are expressed as magnitudes<sup>6</sup>. The combined standard uncertainty is

<sup>6</sup>Note that to conform with the notation in the current section  $|Z^{T_3}|$  will be denoted  $|Z_R|$ , and  $M_V^{T_2}$  will be denoted  $M_V$ .

$$u_c(|M_V|) = \frac{|M_V|}{2} \left[ \frac{1}{|J|^2} u^2(|J|) + \frac{1}{|Z_R|^2} u^2(|Z_R|) + \frac{1}{|H_{15open}^{VV(1)}|^2} u^2(|H_{15open}^{VV(1)}|) + \dots \right. \\ \left. \frac{1}{|H_{15open}^{VV(2)}|^2} u^2(|H_{15open}^{VV(2)}|) + \frac{1}{|H_{15open}^{VV(3)}|^2} u^2(|H_{15open}^{VV(3)}|) + \frac{1}{d_1^2} u^2(d_1) + \frac{1}{d_2^2} u^2(d_2) + \frac{1}{d_3^2} u^2(d_3) \right]^{\frac{1}{2}}, \quad (7.39)$$

where the assumption that all input quantities are uncorrelated has been made. The discussion regarding this assumption is deferred to Sec. 7.6.1. All input quantities, except  $|J|$ , have been dealt with in the previous sections, and the standard uncertainty associated with  $|J|$  is dealt with in next section.

### Standard uncertainty, $|J|$

The standard uncertainty associated with the magnitude of the reciprocity parameter,  $|J|$ , is estimated as a type B uncertainty. From eq. (2.26) the magnitude of  $J$  can be expressed as

$$|J| = \frac{2d_0}{\rho f}, \quad (7.40)$$

where  $\rho$  is the density of air,  $f$  is frequency and  $d_0 = 1$  m is a constant. Assuming no uncertainties are associated with  $f$ , the standard uncertainty,  $u(|J|)$ , is only a function of the density of the air, i.e.

$$u(|J|) = \sqrt{\left(\frac{2d_0}{\rho^2 f}\right)^2 u^2(\rho)}, \quad (7.41)$$

where  $u^2(\rho)$  is the standard uncertainty for the density of air. In [109–111] the relative standard uncertainty is given as  $u_r(\rho)/\rho = 22 \cdot 10^{-6}$  kg/m<sup>3</sup>. The uncertainty associated with  $|J|$ , given atmospheric pressure of 101325 Pa, a temperature of 24° C and a relative humidity of 35%, yields  $u(|J|) = 1.8 \cdot 10^{-10}$  m<sup>4</sup>/(kg·Hz).

### Results for the standard uncertainty, $u_c(|M_V|)$

In Fig. 7.9 the results of the uncertainty analysis of  $|M_V|$  is given: (a) relative standard deviation,  $u_r(|M_V|) = u_c(|M_V|)/|M_V|$  in decibel, (b) relative standard deviation,  $u_r(|M_V|)$ , in percent, and (c) deviation =  $20 \log_{10}[1 + u_r(|M_V|)]$  in decibel. In Fig. 7.9 the solid black lines represents the standard uncertainty associated with  $|M_V|$ . The dotted black lines are the standard uncertainty associated with  $|H_{15open}^{VV}|$ . These are juxtaposed to better appreciate the sameness of the two quantities.

In Fig. 7.9 (a), (b) and (c) the same trend is observed, the standard uncertainty associated with  $|M_V|$  is lower in value compared to  $|H_{15open}^{VV}|$ . In (a) for 100 kHz, a difference of 1.3 dB is observed between  $u_r(|M_V|)$  and  $u_r(|H_{15open}^{VV}|)$ , in (b) for 100 kHz, a difference of 0.5% is observed between  $u_r(|M_V|)$  and  $u_r(|H_{15open}^{VV}|)$ , and in (c) a difference of 0.04 dB is observed between  $u_r(|M_V|)$  and  $u_r(|H_{15open}^{VV}|)$ .

The standard uncertainty  $u_c(|M_V|)$  and  $u_c(|H_{15open}^{VV}|)$  corresponds fair when the deviations just pointed out are taken into account, thus the detailed description of the results in Fig. 7.9 will be omitted, and the detailed description given of the results in Sec. 7.5.6 is deemed valid for  $u_c(|M_V|)$ .

## 7.6.1 Comments on correlation and results

### Correlation

From Eq. (7.42) it is clear that the input quantities are correlated. For example, the magnitude of the transfer function,  $|H_{15open}^{VV}|$ , appears three times, each time representing a different transmitter and receiver pair. To obtain  $|H_{15open}^{VV}|$  measurements are performed, and the same equipment, except for the piezoelectric disks, are used for all three measurements. Sources of correlation that

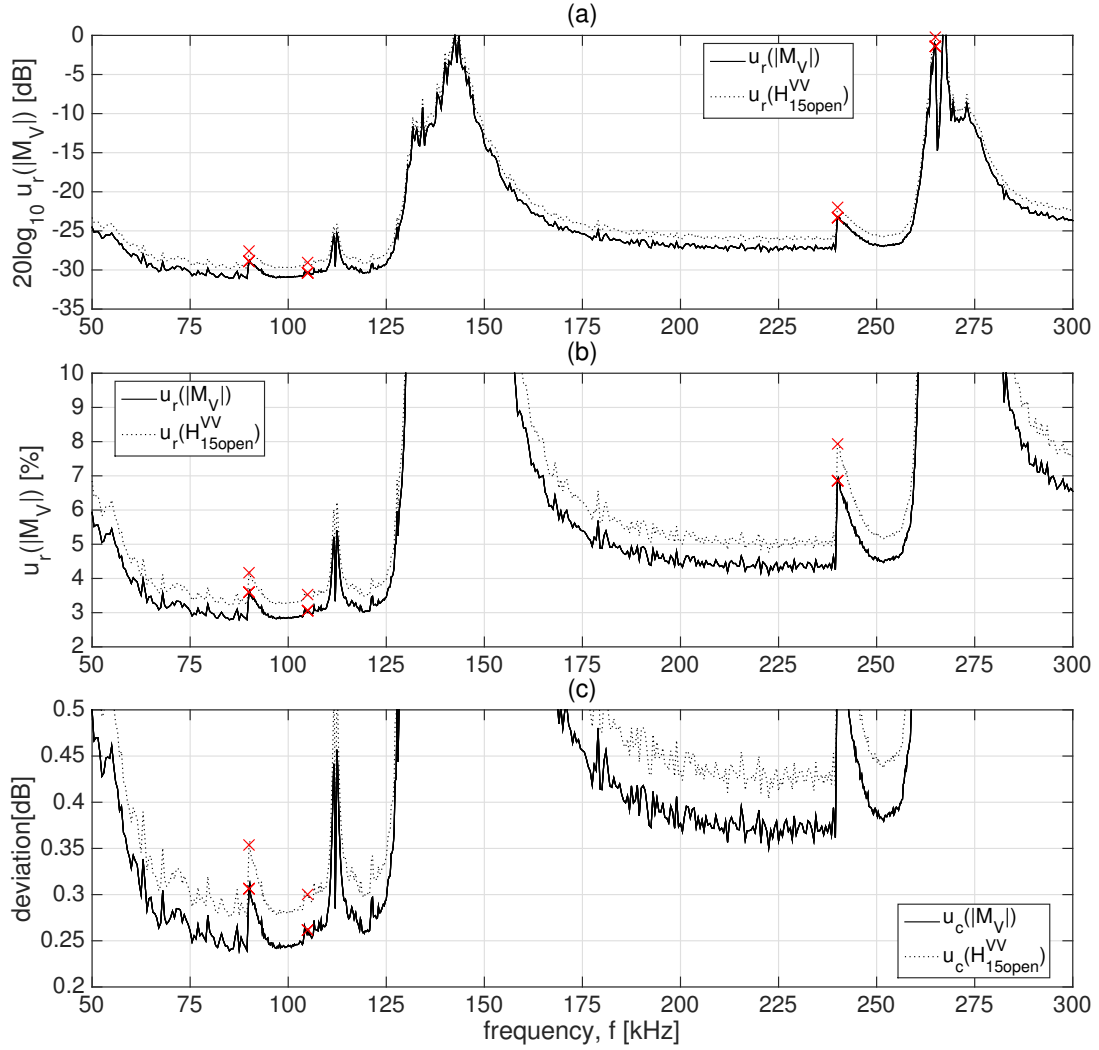


Figure 7.9: (a) and (b) relative uncertainty  $u_r(|M_V|)$  shown in decibel and percentage, respectively, and (c) deviation in decibels.

can be significant are the temperature measurements and the model used to calculate the speed of sound. Moreover, the corrections applied to obtain the loss-free open-circuit transfer function are similar, such that correlation is expected also here. However, it is difficult to estimate if the possible correlation will result in an increase or a decrease in the combined standard uncertainty, or if the transfer function are fully correlated.

Moreover, the three measurement distances are correlated. However, it is observed that the largest contributors to the combined standard uncertainty  $u_c(|M_V|)$  is  $u_c(H_{15open}^{VV})$ . Thus neglecting the correlation of the measurement distances seems fair.

## Results

The Brüel and kjaer Microphone Unit Type 4138-A-015 [85] available at UiB is calibrated with a corresponding uncertainty of 0.52 dB at a 95% confidence level [112], where this calibration is valid up to 100 kHz. This corresponds to a 0.26 dB uncertainty for 68.3% confidence level. However, to obtain the free-field response a free-field correction have to be applied to the microphone sensitivity, such that the overall uncertainty increases [113]. In Fig. 7.9 (c), for the range 65–125 kHz an uncertainty lower than 0.3 dB is observed, excluding the range 110–115 kHz. Moreover, in the range 95–105 kHz, an uncertainty of approximate 0.25 dB is observed. It is thus appreciated that the calibration performed at UiB yields uncertainties in the same order of magnitude as those performed by Brüel and kjaer.

## 7.7 Combined standard uncertainty $u_c(|S_V|)$

In the current section the uncertainty of the magnitude of the transmitting response  $u_c(|S_V|)$  obtained by the reciprocity method will be evaluated. The evaluation is valid for the same environmental conditions stated in Sec. 7.5.

From Eq. (2.41) the magnitude of  $S_V$  is obtained, i.e.

$$|S_V| = \left[ \frac{1}{|J^{(3)}||Z^{T_3}|} \frac{|H_{15open}^{VV(1)}||H_{15open}^{VV(2)}| d_1 d_0}{|H_{15open}^{VV(3)}| d_2 d_3} \right]^{\frac{1}{2}} \quad (7.42)$$

where all input quantities, defined in Sec. 2, are expressed as magnitudes<sup>7</sup>. The combined standard uncertainty is

$$u_c(|S_V|) = \frac{|S_V|}{2} \left[ \frac{1}{|J|^2} u^2(|J|) + \frac{1}{|Z_R|^2} u^2(|Z_R|) + \frac{1}{|H_{15open}^{VV(1)}|^2} u^2(|H_{15open}^{VV(1)}|) + \dots \right. \\ \left. \frac{1}{|H_{15open}^{VV(2)}|^2} u^2(|H_{15open}^{VV(2)}|) + \frac{1}{|H_{15open}^{VV(3)}|^2} u^2(|H_{15open}^{VV(3)}|) + \frac{1}{d_1^2} u^2(d_1) + \frac{1}{d_2^2} u^2(d_2) + \frac{1}{d_3^2} u^2(d_3) \right]^{\frac{1}{2}}, \quad (7.43)$$

where the assumption that all input quantities are uncorrelated has been made. The discussion regarding correlation in Sec. 7.6.1 are valid for  $S_V$ .

It is worth noticing that the expression for the uncertainties  $u_c(|S_V|)$  and  $u_c(|M_V|)$  are similar in form. The order of the transfer function are altered, as well as the order of the measurement distances, and Eq. (7.39) is multiplied with  $|M_V|$ , while Eq. (7.43) is multiplied with  $|S_V|$ . The implication of this is that the relative uncertainties  $u_r(|M_V|)$  and  $u_r(|S_V|)$  should be comparable.

In Fig. 7.10 the results of the uncertainty analysis of  $|S_V|$  is given: (a) relative standard deviation,  $u_r(|S_V|) = u_c(|S_V|)/|S_V|$  in decibel, (b) relative standard deviation,  $u_r(|S_V|) = u_c(|S_V|)/|S_V|$  in percent, and (c) deviation in decibel. The deviation is calculated by an equivalent expression as in Eq. (7.37). In Fig. 7.10 the solid black lines represents the standard uncertainty associated with  $|S_V|$ . The dotted black lines are the standard uncertainty associated with  $|H_{15open}^{VV}|$ .

It is appreciated that the standard uncertainties for  $|S_V|$  is comparable to the standard uncertainties for  $|M_V|$ , and the discussion regarding  $M_V$  in the previous section is valid for  $S_V$ .

## 7.8 Repeatability of the measurement set-up

In the current section the repeatability of the measurement set-up will be evaluated for magnitude and phase. The repeatability is evaluated by eight measurements where the measurement set-up has been dismantled in between each measurement, that is, for both transmitter and receiver, the screw holding the welding rod in place has been loosened and the welding rod has been moved in the suspension. The disks have thereafter been re-aligned using the method elaborated on in Sec. 3.3. Note that 6 measurements have been used for the frequency range 240–265 kHz, for both magnitude and phase.

In Fig. 7.11 the eight measurements are given for (a) magnitude and (b) phase. The eight measurements are given as the colored dash-dotted lines, and the mean of the eight measurements are given as the solid black line. For the magnitude only slight deviations are observed around the R1- and R2-mode. For the phase, frequency dependent deviations are observed, where the deviations increase with increasing frequency. For 90 kHz, a deviation between the largest and lowest value of 10.3° is observed. For 200 kHz a deviation of 36.4° is observed comparing the largest and lowest phase value. And at 300 kHz a deviation of 47.9° is observed comparing the largest and lowest phase value.

To quantify the results in Fig. 7.11 the Type A standard uncertainty is evaluated as the standard deviation about the mean [92], c.f. Appendix A.1. For the magnitude, the relative standard deviation about the mean will be used, i.e.

<sup>7</sup>Note that to conform with the notation in the current section  $S_V^{T_1}$  will be denoted  $S_V$ , and  $Z^{T_3}$  will be denoted  $Z_R$

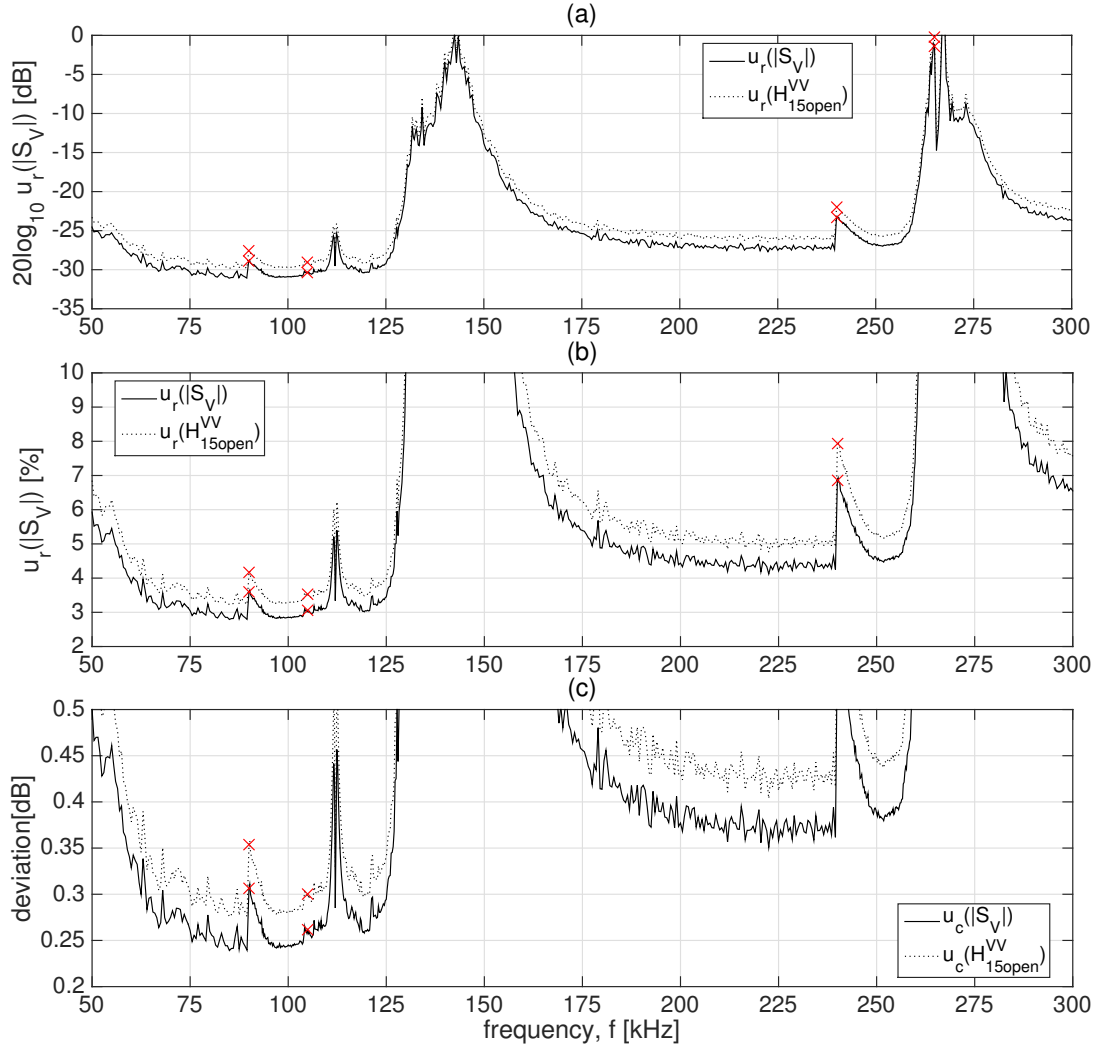


Figure 7.10: (a) and (b) relative uncertainty  $u_r(|S_V|)$  shown in decibel and percentage, respectively, and (c) deviation in decibels.

$$u_r(|\bar{H}_{15open}^{VV}|) = \frac{u(|\bar{H}_{15open}^{VV}|)}{|\bar{H}_{15open}^{VV}|}, \quad (7.44)$$

where the bar over  $H$  signifies the mean. For the phase, the standard deviation about the mean, denoted  $u(\angle \bar{H}_{15open}^{VV})$ , will be given.

In Fig. 7.12 (a)  $u_r(|\bar{H}_{15open}^{VV}|)$  is given in decibels, and in (b)  $u(\angle \bar{H}_{15open}^{VV})$  is given in degrees. In (a) for the R1-mode, the relative standard uncertainty is in the range -50– -40 dB, which corresponds to 0.3–1% relative standard uncertainty. In the frequency range 125–160 the relative standard uncertainty increases, and peaks at approximately -15 dB. However, this range is associated with a low signal to noise ratio and is not of primary interest. The frequency range 160–240 kHz is associated with a relative standard uncertainty of -40– -35 dB. For the R2-mode the relative uncertainty standard decreases rapidly, and is fairly constant at -45 dB for the frequency range 240–255 kHz. For the frequency range 255–300 kHz the relative standard uncertainty increases and peaks at -15 dB.

In Fig. 7.12 (b) the frequency dependent deviations observed in Fig. 7.11 (b) is again observed. Besides the frequency ranges 135–150 kHz, and 265–275 kHz, a fairly constant slope in the uncertainty is observed. A standard uncertainty lower than  $3^\circ$  is observed in the range 50–125 kHz, for the frequency range 160–265 kHz, a standard uncertainty of  $3$ – $6^\circ$  is observed, and for 300 kHz a standard uncertainty of  $5^\circ$  is observed.

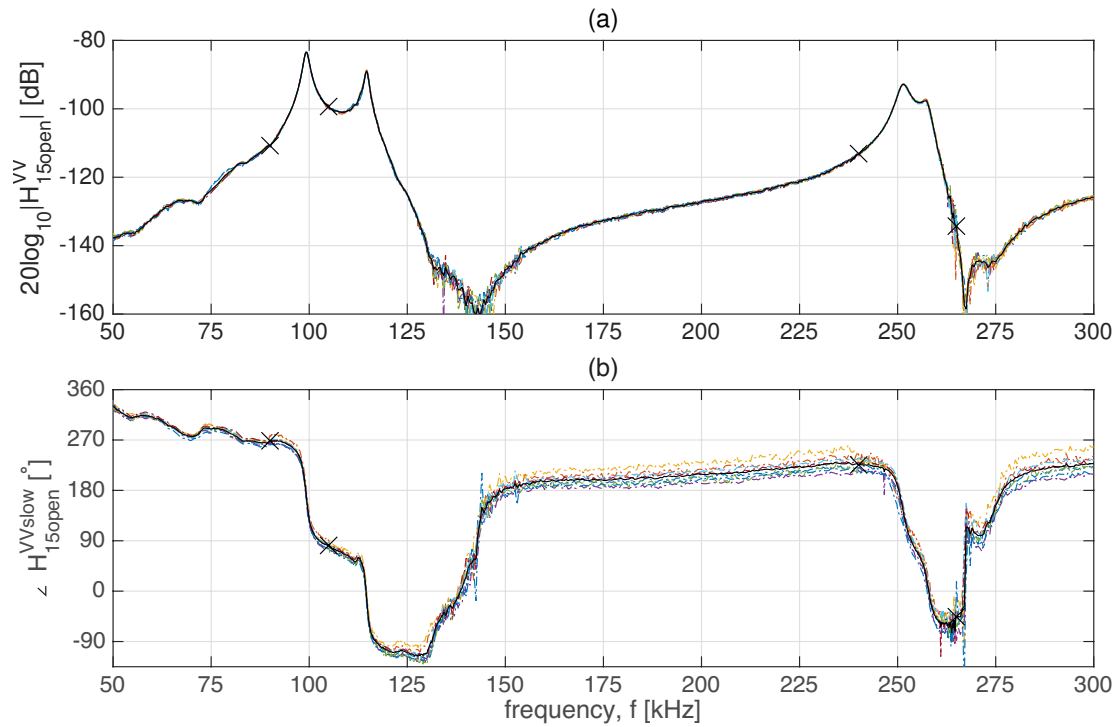


Figure 7.11: (a) magnitude and (b) slowly varying phase of eight measurements where the measurement set-up was dismantled in between each measurement. The colored dash-dotted lines are the measurements, and the mean of the eight measurements are represented as the solid black line. The black crosses indicates where the 2 V peak-to-peak measurements are used.

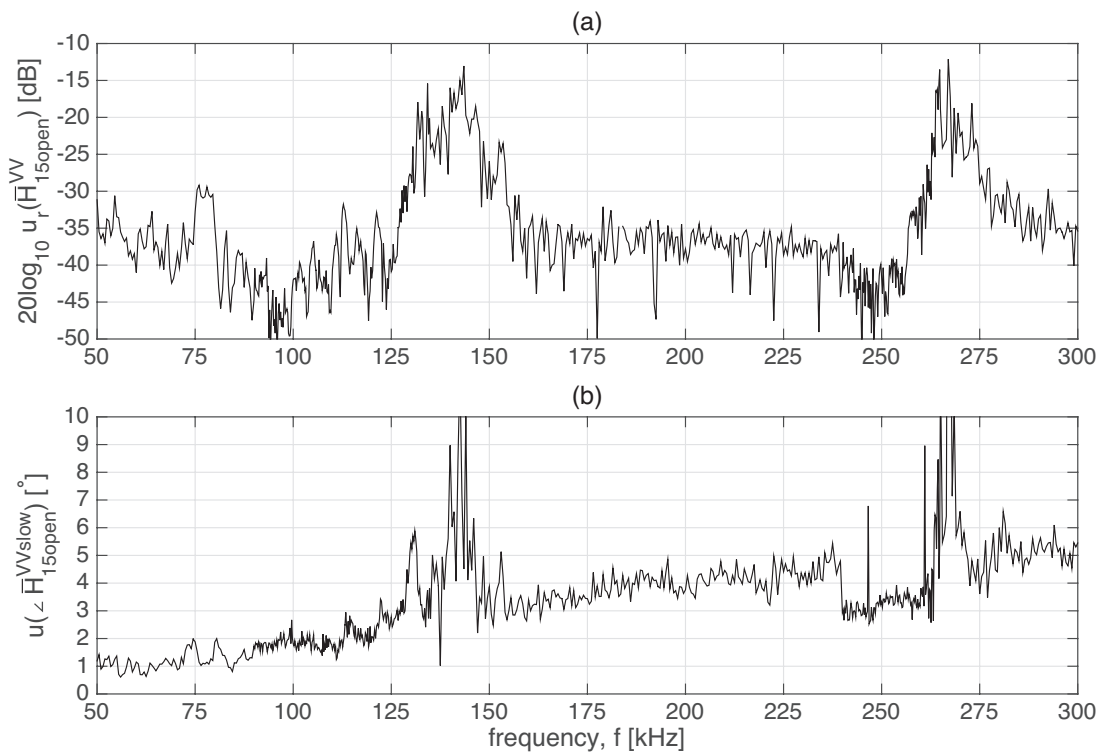


Figure 7.12: (a) relative standard deviation about the mean for  $|H_{15open}^{VV}|$ , in decibels. (b) standard deviation about the mean for  $\angle H_{15open}^{VVslow}$ .



# Chapter 8

## discussion

In the current chapter the discussion regarding the results and uncertainties presented in the previous chapters are given.

### 8.1 Measurements on non-linearity in piezoelectric disks

In Sec. 6.1.1 the results of the impedance measurements on a piezoelectric disk obtained with an oscilloscope were compared for two voltages.

The method presented were compared to the results obtained with a commercial impedance analyzer, the HP-impedance analyzer (HP). In Fig. 6.3 (a) the conductance, and (b) susceptance, and in Fig. 6.4 (a) the impedance and (b) corresponding phase angle were compared for the HP and the oscilloscope measurements. In both figures fair qualitative agreement, and for most frequencies, a fair quantitative agreement were observed. For both figures the greatest deviation were observed at the R1- and R2- modes for the series and parallel resonance frequencies. Two factors that might explain these deviations will now be presented:

1) The impedance measurements with the oscilloscope utilized an Agilent function generator [79] while the impedance measurement with the HP utilized the internal frequency generator of the HP. No measures have been performed to investigate if the two apparatuses outputs comparable frequencies. Due to the steep incline or decline of the slope around the resonance frequencies, a slight deviation in the actual frequency will lead to deviations.

2) The oscilloscope measurements have utilized a constant excitation voltage at the terminals of the piezoelectric disk. However, this is not the case with the HP-impedance analyzer. The HP is equipped with a  $50 \Omega$  output resistance, such that the excitation voltage at the terminals of the piezoelectric disk becomes a function of the impedance of the disk. Although the comparison between the HP and oscilloscope measurements are performed for a low excitation voltage ( $\approx 60$  mV) the disk is still believed to exhibit non-linear behavior. If it do exhibit non-linear behavior for this excitation voltage, then the slope of the two measurements should differ slightly around the resonance frequencies, and deviations between the two measurements can occur.

### 8.2 Piezoelectric disk properties and material constants used in FE-simulations

In Fig. 6.2 it is observed that the disks used in the current thesis exhibits slightly different frequency dependent behavior, where in (a, c) disk 07 stands out, and in (b) disk 04 stands out. The disks were chosen based on impedance measurements pre- and post soldering, and the disks that exhibited the most comparable frequency dependent properties were chosen. The impedance of a piezoelectric disk is related to the transmitting and receiving properties of the disks, and the differences in the impedance in Fig. 6.2 is to some extent also observed in e.g. Fig. 6.33, where the calibrated quantities,  $M_V$  and  $S_V$ , are given.

Although not shown, in Sec. 6.1 it was commented that simulations of the various disks in Table 3.6 yielded negligible deviations in the simulated impedance. In e.g. [2] Fig. 6.3, where

three simulations of three different disks are shown, a similar conclusion can also be drawn. It is therefore assumed that the deviations observed in Fig. 6.2, between the measurements and simulations, are due to the material constants used in the simulations. And it is further assumed that if the material constants used in the simulations were adjusted for each disk, these deviations would be less.

Since this has not been performed in the current thesis, care should be taken when quantitatively comparing the electrical, as well as the acoustical, measurements with the FE-simulations.

### 8.3 FE-simulation of phase

In the current thesis, the simulated phase response is obtained in FEMP by simulations of the sound pressure at 1000 m. In Fig. 3.13 it was shown that the use of a slightly different sound speed in the simulation versus the post-processing yielded large deviations. FEMP has been verified against other commercial FE-simulation programs with comparable results, [46, 47]. However, the implications of the slightly different sound speeds on phase simulations utilizing a far-field distance of 1000 m was first discovered by [49]. To the authors knowledge, simulations of the phase at 1000 m has not been verified against other simulation programs, e.g. COMSOL [114].

In the current thesis, a fair agreement is observed between the simulated and measured phase, however deviations are observed. The most noteworthy deviation is in the value of the measured phase compared to the simulated phase. Throughout, the measured phase has a larger value than the simulated phase. The origin of these deviations are not clear at present, and it would aid in future work to be able to attribute these deviations to either the simulations or the measurements. If e.g. COMSOL outputted a phase comparable to FEMP then the assumption that the deviations stems from the measurements seem fair.

### 8.4 Measured phase always higher in value than simulation

In e.g. Sec. 6.5.2 it is observed that all measured phases are larger in value than the simulated phases. The reason for this discrepancy is not understood, however, a couple of observations as to the origin of discrepancy will be pointed out.

1. At the time of writing it is not verified that the simulated phase as it is obtained in the current thesis is correct. As was pointed out in Sec. 8.3 the simulated phase should be verified.

2. The alignment of the piezoelectric disks might influence the measurement distance. That is, if the disks front faces are not parallel with the  $xy$ -plane then the measured distance might be larger or less than the actual distance between the front faces. However, if the parallelity is regarded as a random variable, then one would expect that the measured distance would sometimes be larger and sometimes less than the actual distance, yielding a distribution about a mean. However, the simulated phase do not seem to estimate this mean.

3. The calibration of  $d_x$  has only been performed by the current author. Since a possible deviation in  $d_x$  directly propagates to the phase, resulting in a constant deviation, verification of this distance is deemed important.

### 8.5 Uncertainties

In Sec. 7 the standard uncertainties were developed for the three quantities  $|H_{15open}^{VV}|$ ,  $|M_V|$  and  $|S_V|$ . For the range 65–125 kHz an uncertainty lower than 0.3 dB was observed, excluding the range 110–115 kHz. Moreover, in the range 95–105 kHz, an uncertainty of approximate 0.25 dB was observed. This number was compared to the calibrated uncertainty of the receiving sensitivity of a Brüel & Kjær Microphone Type 4138-A-015 [85], which was given to be 0.52 dB at a 95% confidence level [112], corresponding to a 0.26 dB uncertainty for a 68.3% confidence level. The calibration of the Brüel & Kjær Microphone is performed as a pressure calibration, which is often associated with a less uncertainties than a free-field calibration [10]. Moreover, to obtain the free-field response of the Brüel & Kjær Microphone, a free-field correction have to be applied to the stated receiving sensitivity. This correction is also associated with uncertainties [113].

The uncertainty obtained for  $|M_V|$  in Sec. 7 should be verified. However, if it turns out to be accurate, then calibrations performed at UiB are associated with uncertainties in the same order of magnitude as those performed by Brüel & Kjær.

## 8.6 Uncertainty in measurement distance influence on the slowly varying phase

In Sec. 7.1 the uncertainty associated with the measurement distance  $d$  was estimated to be  $u_c(d) = 40 \mu\text{m}$  given a 68.3% level of confidence. In Fig. 8.1 the effect of this uncertainty is exemplified on the simulated slowly varying phase  $\angle H_{15open}^{VVslow}$  given a separation distance,  $d = 0.50 \text{ m}$ . The blue curve corresponds to the phase at exactly  $0.50 \text{ m}$ , and the red dash-dotted curve corresponds to  $d = 0.50 \pm 40 \cdot 10^{-6} \text{ m}$ . At  $100 \text{ kHz}$ , a deviation of  $\pm 4.2^\circ$  is observed. At  $200 \text{ kHz}$ , a deviation of  $\pm 8.4^\circ$  is observed, and at  $300 \text{ kHz}$ , a deviation of  $\pm 12.6^\circ$  is observed.

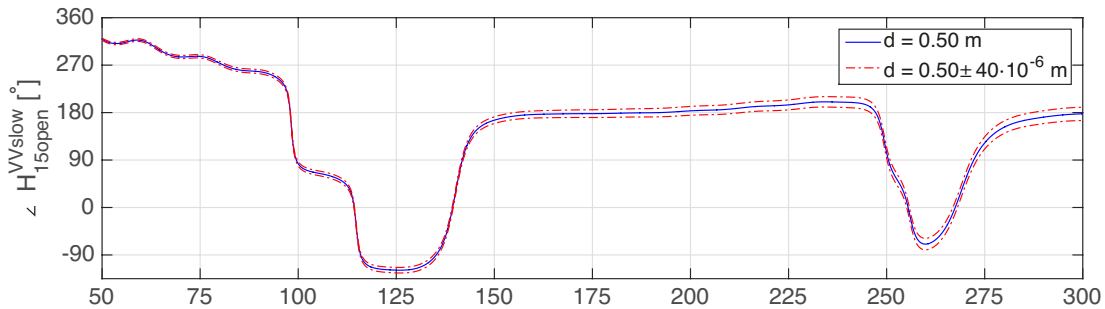


Figure 8.1: Effect of the uncertainty in the measurement distance,  $u_c(d)$ , on the slowly varying phase.

## 8.7 Alignment of piezoelectric disks

The alignment of the transmitting and receiving disk with the  $xy$ -plane is deemed one of the most important factors in obtaining repeatable measurements for both magnitude and phase. However, deviations in the alignment tends to be associated with larger deviations in the phase than in the magnitude.

Before the alignment techniques elaborated on in Sec. 3.3 was developed, the  $x$ - and  $y$ -axis translation stages were used to align the receiver with the  $xy$ -plane. However, the  $x$ - and  $y$ -axis translation stages are not perfectly aligned with the laser sensors, such that using the  $x$ - and  $y$ -axis translation stages mean that the receiver was not aligned with the same plane as the transmitter. Deviation in the parallelity was found to be no greater than  $100 \mu\text{m}$ , however, this lead to deviations between measurements on the same transmitter and receiver pair of approximately  $20\text{--}30^\circ$  for  $100 \text{ kHz}$ , and deviations of up to  $100^\circ$  for  $200 \text{ kHz}$ .

## 8.8 Atmospheric conditions influencing the measurements

In [3] a discussion was given regarding the influence of the atmospheric conditions on the slowly varying phase <sup>1</sup>. The discussion is highly applicable to the current work, and the most important observations made in [3] will be repeated here. The discussion is given with respect to the plane wave component,  $kd$ . All comparisons will be given for  $f = 100 \text{ kHz}$ , and all values are approximate.

1. A  $\pm 1 \text{ hPa}$  change in the atmospheric pressure is associated with a  $\pm 0.6^\circ$  change in  $kd$ . This is a negligible deviation.

2. A  $\pm 0.1^\circ \text{ C}$  change in the temperature is associated with a  $\pm 9^\circ$  change in  $kd$ . A  $\pm 0.1^\circ \text{ C}$  change in the temperature corresponds to the uncertainty of the Vaisala humidity and temperature transmitter HMT313 [81]. The Vaisala HMT313 is no longer used to estimate the temperature.

<sup>1</sup>The discussion is given in Sec. 6.1.4, page. 95–97.

3. A  $\pm 0.6\%$  change in the relative humidity is associated with a  $\pm 1.5^\circ$  change in  $kd$ . A  $\pm 0.6\%$  change in the relative humidity corresponds to the uncertainty of the Vaisala HMT313. The Vaisala HMT313 is used to estimate the relative humidity. A change of  $\pm 1.5^\circ$  is not regarded as negligible, however it is also not regarded as critical to the overall uncertainty.

4. An increase of 200 ppm in the  $\text{CO}_2$  concentration of air is associated with a  $3^\circ$  change in  $kd$ . When estimating the speed of sound, the  $\text{CO}_2$  concentration is assumed to be a constant, equal to that of outdoor air, set to 400 ppm. As of today, no equipment to measure the  $\text{CO}_2$  exist in the acoustic laboratory. Furthermore, no measurements attempting to indicate the  $\text{CO}_2$  concentration in the acoustic laboratory has been performed. Thus, it is difficult to assess whether or not an increase of 200 ppm is representative of the deviations in the  $\text{CO}_2$  concentration in the laboratory.

## 8.9 Reciprocity check

In Fig. 6.30 the results of the reciprocity check for (a) magnitude and (b) phase was given for the two transmitter and receiver pairs, disk 04 and 07, and disk 04 and 11. The second pair, 04 and 11, exhibited less fluctuations than the first pair, which had deviations around R1 of -2 to 1 dB. The first pair fluctuated around  $\pm 0.2$  dB. A deviation of 1 dB yields a deviation in percent of about 12%, while a 2 dB deviation corresponds to approximately 26%. This is regarded as large deviations, and it is quite surprising that such large deviations are observed for the R1 mode. The observed deviations for the second pair corresponds to approximately 2.3%.

Since the deviations for the first pair is so much larger than the second pair, it can not be excluded that something has gone wrong during the measurement of the first pair, and this should be investigated with new measurements to either conform or refute the findings.

# Chapter 9

## Conclusion and further work

### 9.1 Conclusion

A three transducer reciprocity calibration method is employed to calibrate two piezoelectric disks for both magnitude and phase. The disks are denoted 04 and 07. The calibrated quantities are the receiving voltage sensitivity of the receiver,  $M_V$ , and the transmitting voltage response of the transmitter,  $S_V$ . The calibration has been performed at two different distances, 0.50 m and 0.85 m. The frequency range of primary interest is 70–125 kHz. In this range a SNR larger than 40 dB is expected, and an uncertainty evaluation for the same frequency range indicates that the expected uncertainty for the magnitude of  $M_V$  and  $S_V$  is approximately 0.3 dB, corresponding to a relative uncertainty of 3-4%. However, a frequency range of 50–300 kHz is often discussed throughout the thesis as the upper frequency ranges indicate the accuracy of the measurement set-up and corresponding corrections.

The calibrated quantities are compared to FE-simulation, and the comparison has yielded fair agreement for most frequencies. For  $|M_V|$  a deviation between the measurement and simulation at 115 kHz of 1 dB is observed for disk 04, and a deviation of 4 dB is observed for disk 07. For the phase,  $\angle M_V$ , in the range 90–105 kHz, the largest deviation between the two measurements and simulation is approximately  $15^\circ$ , where the simulations is generally lower in value.

For  $|S_V|$  both measurements peak at the same frequency, 99.2 kHz, while the simulation peak at 98.4 kHz. The magnitude of the peaks are comparable for all three quantities. For the phase,  $\angle S_V$ , in the range 90–105 kHz a constant deviation of  $6.5^\circ$  between both the two measurements and the simulation is observed. The simulation is lower in value than the measurements.

For the magnitude, the deviations between measurements and simulations around the R1- and R2-modes are mostly attributed the material constants used in the FE-simulations and are assumed to be reduced if the material constants had been determined for each disk, or, at least, for the respective batch. For the phase, the deviations between measurements and simulations around the R1- and R2-modes are also attributed the material constants, however, the deviations are also likely to stem from the estimate of the separation distance between the transmitter and receiver, and the estimate of the speed of sound.

The measurement set-up was expanded by the current author to include laser distance sensors. The laser sensors are employed to determine the measurement distance between the transmitter and receiver prior to an acoustical measurement. The estimated uncertainty associated with the measurement distance has been found to be approximately 40  $\mu\text{m}$ , where the largest contributor to the uncertainty is the translation mechanism used to place the laser sensors in-between the transmitter and receiver.

The installation of the laser sensors has resulted in an improved knowledge about the measurement distance, compared to prior work at UiB [1–3]. Moreover, the laser sensors are deemed indispensable when it comes to aligning the transmitter and receiver with one another. Deviations in the parallelity of less than 20  $\mu\text{m}$  has been a criterion when aligning the disks, and this has been achieved using the laser sensors and a manual XYZ-translation stage to scan the surface of the disks.

Repeated measurements have been performed to evaluate the repeatability of the measurement

set-up. A total of eight measurements have been performed on one transmitter and receiver pair, where the measurement set-up has been dismantled in between each measurement. The experimental standard deviation about the mean has been calculated for the open circuit transfer function,  $H_{15open}^{VV}$ , for both magnitude and phase. For the magnitude, in the range 90–105 kHz, the relative experimental standard deviation about the mean has been found to be less than -40 dB. For the phase, in the range 90–105 kHz, the experimental standard deviation about the mean has been found to be approximately  $2^\circ$ .

The improvement to the repeatability of the measurement set-up is attributed the installation of the laser distance sensors, and corresponding new alignment techniques of the piezoelectric disks.

## 9.2 Further work

In [3] it was pointed out that the soldering and corresponding heat treatment that the disks are undergoing alters the piezoelectric properties of the disks. However, in neither [3] nor the current thesis, no attempts to find an alternative method of applying the wires to the electrodes of the disks were investigated. However, Sæther [115] has investigated various methods to fasten wires to the electrodes of piezoelectric disks using epoxy or silver lacquer, with promising results. It is believed that applying similar methods might reduce the deviations seen in the impedance of the disks before and after soldering.

The measurement distance is estimated with an uncertainty of 40  $\mu\text{m}$ . However, this uncertainty is mainly due to the translation mechanism used to place the laser sensors in-between the transmitter and receiver. It is believed that an investment in a linear stage could reduce this uncertainty.

An important factor that influences the phase is the measured temperature. Although a precision thermometer is used, this was calibrated in 1997. Due to the significant impact the temperature has on the speed of sound, which again has a significant impact on the phase, a re-calibration of the thermometer is recommended.

It is of interest to have independent verification of the results obtained in the current thesis. For example, in [27] a vibrometer is used to verify the phase response of hydrophones obtained by the reciprocity method. Several research groups have vibrometers, e.g. the Hangzhou Applied Acoustic Research Institute in China, used in [27]. A collaboration with a research group with a vibrometer, or a group with another method that can be used to obtain the phase response of piezoelectric disks, would be beneficial for the project.

The measurement uncertainties estimated in the current thesis should be verified, either by a different method, e.g. a Monte Carlo simulation, or using the GUM. Further more, the uncertainties should be developed for the phase response.

In the current thesis, the simulations utilize a piezoelectric disk as a transmitter, however no receiving disk is used. It is of interest to simulate the transmitter and receiver pair with a receiver present in the sound field. It is believed that this would present a more correct simulation set-up of the real world problem under investigation. Moreover, simulations as such can be used to investigate the baffled piston diffraction correction, and the simplified finite element diffraction correction, [49].

Moreover, it is of interest to investigate the measurement methods on a pre-calibrated microphone, to indicate if the measurement methods are reliable. However, the pre-calibrated microphones available at UiB are not provided with accurate phase data. There are typical data available, and these should be used, however with care.

### Method to improve uncertainty in phase calibration

Luker and Van Buren [28] (1981) proposed a method to reduce the phase errors resulting from uncertainty in measured distances and sound speed. The method relies on a transducer arrangement where the three distances between the transducers, or disks, exactly cancel each other out. In Fig. 9.1 the arrangement is shown for piezoelectric disks. Note that this differs slightly from [28], where hydrophones were used, due to the thickness of the  $T_2$  disk. In the arrangement,  $T_1$  is the transmitting disk,  $T_2$  is the disk to be calibrated, and  $T_3$  is the reciprocal disk.  $d_1$ ,  $d_2$  and  $d_3$  are

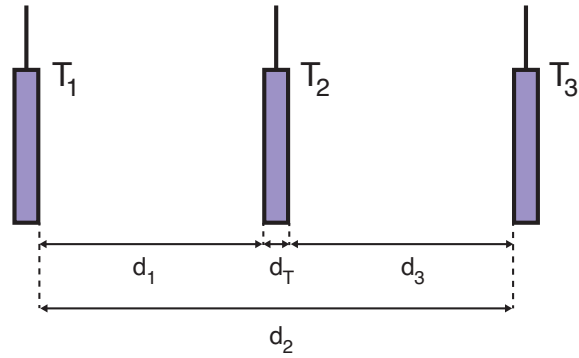


Figure 9.1: Transducer arrangement as proposed by Luker and Van Buren to reduce the dependency on the measured distance and sound speed, shown for piezoelectric disks.  $T_1$  is the transmitting disk,  $T_2$  is the disk to be calibrated, and  $T_3$  is the reciprocal disk.  $d_1$ ,  $d_2$  and  $d_3$  are the distances between the respective disk pairs, and  $d_T$  denoted the thickness of the  $T_2$  disk.

the distances between the respective disk pairs, and  $d_T$  denoted the thickness of the  $T_2$  disk. Three measurements are needed, 1)  $T_1$  to  $T_2$ , 2)  $T_1$  to  $T_3$ , and 3)  $T_3$  to  $T_2$ .

A challenge with this method, using hydrophones, is that the hydrophone in the middle have to be turned  $180^\circ$  in between measurement 1 and measurement 2, leading to challenges with the distances and possible alignment. Using piezoelectric disk, one do not need to turn the disk in the middle  $180^\circ$ , however, one would need to correct the phase for an offset of  $180^\circ$ , due to the polarization direction. Moreover, the exponent will not exactly cancel due to the thickness of the disk. But accurate measurements on the thickness of the disk can be performed with e.g. a micrometer [116].

It is believed that this method could be implemented in the measurement cage with some changes, and that this can reduce the overall uncertainty in the phase measurements.

# Bibliography

- [1] E. Mosland, “Reciprocity calibration method for ultrasonic piezoelectric transducers in air,” Master’s thesis, Department of Physics and Technology, University of Bergen, Norway, June 2013.
- [2] R. Hauge, “Finite element modeling of ultrasound measurement systems for gas. Comparison with experiments in air,” Master’s thesis, Department of Physics and Technology, University of Bergen, Norway, June 2013.
- [3] A. A. Søvik, “Ultrasonic measurement system for gas. Finite element modelling compared with measurements in air.” Master’s thesis, Department of Physics and Technology, University of Bergen, June 2015.
- [4] *ANSI/ASA Procedures for Calibration of Underwater Electroacoustic Transducers*, ANSI/ASA Std. S1.20, 2012.
- [5] P. Lunde, K.-E. Frøysa, R. A. Kippersund, and M. Vestrheim, “Transient diffraction effects in ultrasonic meters for volumetric, mass and energy flow measurement of natural gas,” in *Proc. 21st International North sea flow Measurement Workshop*, Tønsberg, Norway, 28-31 October 2003.
- [6] K.-E. Frøysa, P. Lunde, G. Lied, and A. Hallanger, “Natural gas quality measurements using ultrasonic flow meters. Development of a prototype gas analyzer with results from testing on North Sea gas field data,” in *Proc. 30th Scandinavian Symp. on Physical Acoust.*, Geilo, Norway, 28-31 January 2007, Norwegian Physics Soc., <http://www.norskfysikk.no>.
- [7] D. Reilly and G. Hayward, “Through air transmission for ultrasonic nondestructive testing,” in *Proc. Ultrasonics Symp.*, Dec 1991, pp. vol. 2 763–766.
- [8] K. K. Park and B. T. Khuri-Yakub, “3-D airborne ultrasound synthetic aperture imaging based on capacitive micromachined ultrasonic transducers,” *Ultrasonics*, vol. 53, no. 7, pp. 1355–1362, 2013. [Online]. Available: <http://dx.doi.org/10.1016/j.ultras.2013.04.003>
- [9] J. F. Figueroa, “A method for accurate detection of time of arrival: Analysis and design of an ultrasonic ranging system,” *The Journal of the Acoustical Society of America*, vol. 91, no. 1, p. 486, 1992.
- [10] G. S. K. Wong, *Primary Pressure Calibration by Reciprocity*, In *AIP Handbook of Condenser Microphones: Theory, Calibration, and Measurements*. New York, American Institute of Physics, 1995, (Edited by G. S. K. Wong and T. F. W. Embleton).
- [11] K. R. Erikson, “Tone-Burst Testing of Pulse-Echo Transducers,” *IEEE Transactions on Sonics and Ultrasonics*, vol. SU-26, no. 1, pp. 7–14, 1979.
- [12] P. C. Pedersen, P. A. Lewin, and L. Bjørnø, “Application of time-delay spectrometry for calibration of ultrasonic transducers.” *IEEE Transactions on Ultrasonics, Ferroelectrics, and Frequency Control*, vol. 35, no. 2, pp. 185–205, 1988.
- [13] J. A. Simmons, C. D. Turner, and H. N. G. Wadley, “Vector calibration of ultrasonic and acoustic emission transducers,” *J. Acoust. Soc. Am.*, vol. 82, no. 4, pp. 1122–1130, 1987.



- [14] J. P. Damion, "Means of Dynamic Calibration for Pressure Transducers," *Metrologia*, vol. 30, no. 6, pp. 743–746, 1994.
- [15] M. Almqvist, A. Holm, H. Persson, and K. Lindström, "Characterization of air-coupled ultrasound transducers in the frequency range 40 kHz–2 MHz using light diffraction tomography," *Ultrasonics*, vol. 37, no. 8, pp. 565–575, Jan. 2000. [Online]. Available: <http://www.sciencedirect.com/science/article/pii/S0041624X99001687>
- [16] O. Bou Matar, L. Pizarro, D. Certon, J. Remenieras, and F. Patat, "Characterization of airborne transducers by optical tomography," *Ultrasonics*, vol. 38, pp. 787–793, Mar. 2000. [Online]. Available: <http://www.sciencedirect.com/science/article/pii/S0041624X99000943>
- [17] W. Galbraith and G. Hayward, "Development of a PVDF membrane hydrophone for use in air-coupled ultrasonic transducer calibration," *IEEE Transactions on Ultrasonics, Ferroelectrics, and Frequency Control*, vol. 45, no. 6, pp. 1549–1558, 1998.
- [18] A. Gachagan, G. Hayward, S. Member, S. P. Kelly, and W. Galbraith, "Characterization of Air-Coupled Transducers," vol. 43, no. 4, pp. 678–689, 1996.
- [19] *ANSI Measurement Microphones - Part 2, Primary Method for Pressure Calibration of Laboratory Standard Microphones by the Reciprocity Technique*, ANSI Std. S1.15/2, 2005.
- [20] H. G. Diestel, "Reciprocity calibration of microphones in a diffuse Sound Field," *J. Acoust. Soc. Am.*, vol. 33, no. 4, p. 514, 1961.
- [21] S. Barrera-Figueroa, K. Rasmussen, and F. Jacobsen, "A note on determination of the diffuse-field sensitivity of microphones using the reciprocity technique." *The Journal of the Acoustical Society of America*, vol. 124, pp. 1505–1512, 2008.
- [22] *ANSI method for the calibration of microphones*, ANSI Std. S1.10, 1966 (R1976).
- [23] *IEC Measurement microphones - Part 3: Primary method for free-field calibration of laboratory standard microphones by the reciprocity technique*, IEC Std. 61 094-3 ed1.0, 1995.
- [24] V. Nedzelnitsky, "Brief review of primary methods applicable to key comparisons in acoustics," *Metrologia*, vol. 36, no. 4, pp. 257–263, 2003.
- [25] E. Frederiksen, "Acoustic metrology – an overview of calibration methods and their uncertainties," *International Journal of Metrology and Quality Engineering*, vol. 4, no. 2, pp. 97–107, 2013. [Online]. Available: <http://www.metrology-journal.org/10.1051/ijmqe/2013045>
- [26] R. J. Jackett and R. G. Barham, "Phase sensitivity uncertainty in microphone pressure reciprocity calibration," *Metrologia*, vol. 50, no. 2, pp. 170–179, 2013. [Online]. Available: <http://stacks.iop.org/0026-1394/50/i=2/a=170?key=crossref.c6f5a2e2c48c5f239be23ee6a1b7c48>
- [27] G. Hayman and S. P. Robinson, "NPL Report AC 1 Phase calibration of hydrophones by the free-field reciprocity method in the frequency range 10 kHz to 400 kHz," Tech. Rep. September, 2007.
- [28] L. D. Luker and A. L. Van Buren, "Phase calibration of hydrophones," *The Journal of the Acoustical Society of America*, vol. 70, no. 2, p. 516, 1981.
- [29] R. J. Bobber, *Underwater Electroacoustic Measurements*. Naval Research Laboratory Washington D.C., 1970.
- [30] W. R. MacLean, "Absolute measurement of sound without a primary standard," *J. Acoust. Soc. Am.*, vol. 12, no. 1, pp. 140–146, 1940.
- [31] R. K. Cook, "Absolute Pressure Calibrations of Microphones," *J. Acoust. Soc. Am.*, vol. 12, pp. 415–420, 1941.
- [32] S. Ballantine, "Reciprocity in electromagnetic, mechanical, acoustical, and interconnected systems," *Proc. of the Inst. of Radio Engineers*, vol. 17, no. 6, pp. 929–951, 1929.

- [33] W. Wathen-Dunn, "On the reciprocity free-field calibration of microphones," *J. Acoust. Soc. Am.*, vol. 21, no. 5, pp. 542–546, 1949.
- [34] H. F. Olsen, "Calibration of microphones by the principles of similarity and reciprocity," *J. Acoust. Soc. Am.*, vol. 12, no. 3, pp. 415–420, 1941.
- [35] P. Ebaugh and R. E. Mueser, "The Practical Application of the Reciprocity Theorem in the Calibration of Underwater Sound Transducers," *J. Acoust. Soc. Am.*, vol. 19, no. 4, pp. 695–700, 1947.
- [36] A. L. DiMattia and F. M. Wiener, "On the Absolute Pressure Calibration of Condenser Microphones by the Reciprocity Method," *J. Acoust. Soc. Am.*, vol. 18, no. 2, pp. 341–344, 1946.
- [37] I. Rudnick and M. N. Stein, "Reciprocity free field calibration of microphones to 100 Kc in air," *J. Acoust. Soc. Am.*, vol. 20, no. 6, pp. 818–825, 1048.
- [38] K. Matsuzawa, "Condenser Microphones Having Flat Frequency Response up to 500 kHz," *Japanese Journal of Applied Physics*, vol. 17, pp. 451–452, 1978.
- [39] M. J. Anderson, "Use of reciprocity to characterize ultrasonic transducers in air above 100 kHz," *J. Acoust. Soc. Am.*, vol. 103, no. 1, pp. 446–453, 1998.
- [40] —, "Broadband electrostatic transducers: Modeling and experiments," *J. Acoust. Soc. Am.*, vol. 97, no. 1, p. 262, 1995.
- [41] N. Bouaoua, "Free-field Reciprocity Calibration of Condenser Microphones in the Low Ultrasonic Frequency Range," Ph.D. dissertation, Universität Oldenburg, Germany, 2008.
- [42] S. B. Figueroa, "New methods for transducer calibration: Free-field reciprocity calibration of condenser microphones," Ph.D. dissertation, Technical University of Denmark Ørsted Denmark, 2003.
- [43] S. Barrera-Figueroa, K. Rasmussen, and F. Jacobsen, "A time-selective technique for free-field reciprocity calibration of condenser microphones," *J. Acoust. Soc. Am.*, vol. 114, no. 3, pp. 1467–1476, 2003.
- [44] P. L. van Neer, H. J. Vos, and N. de Jong, "Reflector-based phase calibration of ultrasound transducers," *Ultrasonics*, vol. 51, no. 1, pp. 1–6, 2011. [Online]. Available: <http://linkinghub.elsevier.com/retrieve/pii/S0041624X10000806>
- [45] E. G. D. Oliveira, R. P. B. Costa-felix, and J. a. C. Machado, "Reciprocity-based method for magnitude and phase calibration of hydrophone sensitivity," *Ultrasonics Symp. (IUS), 2013 IEEE International*, pp. 465–468, 2013.
- [46] J. Kocbach, "Finite Element Modeling of Ultrasonic Piezoelectric Transducers," Ph.D. dissertation, Department of Physics, University of Bergen, Norway, 2000.
- [47] J. Kocbach, P. Lunde, M. Vestrheim, and R. Kippersund, "Finite Element Modeling of Ultrasonic Piezoelectric Transducers: Extension of FEMP to 3D analysis," CMR Report no. CMR-06-A10046-RA-01, Christian Michelsen Research AS, Bergen, Norway, December, 2006.
- [48] *ANSI Method for calculation of the absorption of sound by the atmosphere*, ANSI Std. S1.26, 1995.
- [49] E. Storheim, "Diffraction effects in the ultrasonic field of transmitting and receiving circular piezoceramic disks in radial mode vibration," Ph.D. dissertation, University of Bergen, Department of Physics and Technology, Bergen, Norway, 2015.
- [50] Ø. S. Amundsen, "Material constants determination for piezoelectric disks, and influence on source sensitivity. Measurements and simulations," Master's thesis, University of Bergen, Department of Physics and Technology, Bergen, Norway, 2011.

- [51] *LK-G Series User's Manual*, Keyence Corporation, 1100 North Arlington Heights Road, Suite210, Itasca, IL 60143, United States, 2010, [www.keyence.com](http://www.keyence.com).
- [52] O. Cramer, "The variation of the specific heat ratio and the speed of sound in air with temperature, pressure, humidity, and CO<sub>2</sub> concentration," *J. Acoust. Soc. Am.*, vol. 93, pp. 2510–2516, 1993.
- [53] P. Lunde, R. A. Kippersund, and M. Vestrheim, "Signal modelling using the FLOSIM system model in ultrasonic instrumentation for industrial applications," in *Proceedings of Norwegian Signal Processing Symposium*, 2003.
- [54] P. Lunde, "Modeller for beskrivelse av elektroakustisk sender-mottaker målesystem, inkl. diffraksjonseffekter/-korreksjon (Norwegian) [Models for description of electro acoustic transmit-receive measurement systems, incl. diffraction effects/correction]," Unpublished note, Department of Physics and Technology, University of Bergen, Norway, Jan 2013.
- [55] E. N. Hauge, Rune and, E. Storheim, P. Lunde, M. Vestrheim, and J. Kocbach, "Finite element modeling of ultrasound measurement systems for gas. Comparison with experiments in air," in *Proc. 36th Scandinavian Symp. on Physical Acoust.*, Geilo, Norway, 3-6 February 2013, Norwegian Physics Soc., <http://www.norskfysikk.no>.
- [56] A. A. Søvik, K. K. Andersen, P. Lunde, M. Vestrheim, and J. Kocbach, "Characterization of ultrasound transmit-receive measurement systems in air. Comparison of finite element modelling and experimental measurements," in *Proc. 38th Scandinavian Symp. on Physical Acoust.*, Geilo, Norway, 1-4 February 2015, Norwegian Physics Soc., <http://www.norskfysikk.no>.
- [57] L. E. Kinsler, A. R. Frey, A. B. Coppers, and J. V. Sanders, *Fundamentals of Acoustics*, 4th ed. John Wiley & Sons, New York, 2000.
- [58] E. O. Brigham, *The Fast Fourier Transform and its application*. Prentice-Hall International Editions, 1988.
- [59] M. Vestrheim, "Phys272 - Akustiske transdusere," Lecture notes, Department of Physics and Technology, University of Bergen, Norway (in Norwegian), 2013.
- [60] —, "Phys373 - Akustiske målesystem," Lecture notes, Department of Physics and Technology, University of Bergen, Norway (in Norwegian), 2013.
- [61] C. L. Morfey and G. P. Howell, "Speed of sound in air as a function of frequency and humidity," *J. Acoust. Soc. Am.*, vol. 68, no. 5, pp. 1525–1527, 1980.
- [62] *ANSI Acoustical Terminology*, ANSI Std. S1.1, 1994.
- [63] L. L. Foldy and H. Primakoff, "A general theory of passive linear electrostatic transducers and the electroacoustic reciprocity theorem. I," *J. Acoust. Soc. Am.*, vol. 17, no. 2, pp. 109–120, 1945.
- [64] A. S. Khimunin, "Numerical calculation of the diffraction corrections for the precise measurement of ultrasound absorption," *Acustica*, vol. 27, no. 4, pp. 173–181, 1972.
- [65] P. David M., *Microwave and RF Wireless Systems*, 1st ed. John Wiley & Sons, inc., 2001.
- [66] V. John L., *Antenna Engineering Handbook*, 4th ed. Mc Graw Hill, 2007.
- [67] B. Kaltenbacher, M. Hofer, M. Kaltenbacher, R. Simkovic, and R. Lerch, "Identification of Material Nonlinearities in Piezoelectric Ceramics," *IEEE Ultrasonics Symposium*, vol. 00, no. 4, pp. 358–361, 2003.
- [68] R. Perez and a. Albareda, "Analysis of nonlinear effects in a piezoelectric resonator," *The Journal of the Acoustical Society of . . .*, vol. 100, no. May, pp. 3561–3569, 1996. [Online]. Available: <http://scitation.aip.org/content/asa/journal/jasa/100/6/10.1121/1.417221>

- [69] *Operation and Service Manual - Model 4192A LF Impedance Analyzer, Part No. 04192-90001*, Yokogawa- Hawlett Packard, Ltd, 9-1, Takakura-cho, Hachioji-shi, Tokyo, Japan, 1982.
- [70] *Christian Michelsen Research, CMR*, Fantoftvegen 38, 5072 Bergen, Norway.
- [71] *Instruction manual - TESA DIGIT-CAL SI*, TESA SA, CH-1020 Renens, Suisse, 1993.
- [72] Mitutoyo Corporation, “Product data - Mitutoyo MDH-25H digital micrometer,” Kawasaki, Japan, 2012.
- [73] —, “Certificate of inspection, issue No.: 11L16B0, serial No. 15229628,” Kawasaki, Japan, 2012.
- [74] *Product instruction MP 30 E, M-500, Linear position stage*, Physik Instrumente (PI) GmbH & Co., KG, Auf der Roemerstrasse 1, 76228 Karlsruhe, Germany, 1996.
- [75] *Operating manual MP 33E, M-501.xx Series, Linear position stage*, Physik Instrumente (PI) GmbH & Co., KG, Auf der Roemerstrasse 1, 76228 Karlsruhe, Germany, 2010.
- [76] *SMC hydra TT 2 axes Controller System*, PI miCos GmbH, Freiburger Strasse 30, 79427 Eschbach, Germany, 2014.
- [77] *Product data - PI M-037 rotational stage*, Physik Instrumente (PI) GmbH & Co., KG, Auf der Roemerstrasse 1, 76228 Karlsruhe, Germany, 1998.
- [78] *MS77E User Manual, C-843 Motor Controller Card*, Physik Instrumente (PI) GmbH & Co., KG, Auf der Römerstr. 1, 76228 Karlsruhe, Germany, 2009.
- [79] *User’s guide - Agilent 33220A 20 MHz Waveform generator*, Agilent technologies, Inc., Headquarters, 5301 Stevens Creek Blvd, Santa Clara, CA 95051, US, 2007.
- [80] *DPO3000 Series Datasheet*, Tektronix Inc., 14150 SW Karl Braun Drive, Beaverton, OR 97077, United States, 2013.
- [81] *User’s guide - Vaisala HUMICAP Humidity and Temperature Transmitter HMT310*, Vaisala, Oyj, Finland,, 2010.
- [82] Brüel & Kjær, “Product Data, Wide Range Measuring Amplifiers - Types 2610 and 2636,” Brüel & Kjær Sound & Vibration Measurement A/S, Nærum, Denmark, 1996.
- [83] *Product data - Krohn-Hite Model 3940*, Krohn-Hite Corporation, 15 Jonathan Drive, Unit 4, Brockton, MA 02301, 2014.
- [84] *F250 Mk II Precision Thermometer - Operator’s Handbook*, Automatic Systems Laboratories Ltd., Isotech North America, 158 Brentwood Drive, Unit 4, Colchester, VT 05404, 1997.
- [85] Brüel & Kjær, “Calibration data for Type 4138-A-015 microphone system serial no. 2795107,” Brüel & Kjær Sound & Vibration Measurement A/S, Nærum, Denmark, 2012.
- [86] —, “Product Data, Falcon Range 1/4-inch Microphone Preamplifier - Type 2670,” Brüel & Kjær Sound & Vibration Measurement A/S, Nærum, Denmark, 1982.
- [87] *Calibration Certificate - Humidity and Temperature Transmitter HMT310, certificate report no. H33-10490035*, Vaisala, Oyj, Finland,, 2010.
- [88] LappLimited, “Product Data, RG 178 Co-Axial Cable,” Unit 3 Perivale Park, Horsenden Lane South, Greenford, Middlesex UB6 7RL, UK.
- [89] *IEEE Standard on Piezoelectricity*, ANSI/IEEE Std. S176, 1987.
- [90] V. Knappskog, “Radiellmode svingninger i piezoelektriske ultralydstransdusere for luft. Målinger og endelig element analyse,” Master’s thesis, Department of Physics and Technology, University of Bergen, 2007, (in Norwegian).

- [91] *Product data - Mitutoyo MDH-25H digital micrometer*, Mitutoyo Corporation, Kawasaki, Japan, 2012.
- [92] *Evaluation of measurement data - Guide to the expression of uncertainty in measurement*, Std. JCGM 100:2008 (GUM 1995 with minor corrections), <http://www.bipm.org/en/publications/guides/gum.html>.
- [93] D. Havelock, S. Kuwano, and M. Vorländer, *Handbook of Signal Processing in Acoustics*. Springer Science & Business Media, 2008.
- [94] F. Harris, “On the use of windows for harmonic analysis with the discrete Fourier transform,” *Proceedings of the IEEE*, vol. 66, no. 1, pp. 51–83, 1978.
- [95] NI, National Instrument, “The Fundamentals of FFT-Based Signal Analysis and Measurement in LabVIEW and LabWindows/CVI,” Online tutorial, June 08, 2009, [www.ni.com](http://www.ni.com).
- [96] K. K. Andersen, A. A. Søvik, P. Lunde, M. Vestrheim, and J. Kocbach, “Reciprocity calibration method for ultrasonic piezoelectric transducers in air. Comparison of finite element modelling and experimental measurements,” in *Proc. 38th Scandinavian Symp. on Physical Acoust.*, Geilo, Norway, 1-4 February 2015, Norwegian Physics Soc., <http://www.norskfysikk.no>.
- [97] S. Kogan, *Electronic noise and fluctuations in solids*, 1st ed. Cambridge University Press, Ney York, United States, 1996.
- [98] J. Kocbach, P. Lunde, and M. Vestrheim, “Resonance frequency spectra with convergence tests of piezoceramic disks using the finite element method,” *Acustica*, vol. 87(2), pp. 271–285, 2001.
- [99] *Meggitt Sensing Systems*, Porthusvej 4, 3490 Kvistgård, Denmark, 2013.
- [100] K. D. Lohne, “Undersøkelse og utnyttelse av svingemoder i ultralyd transduserkonstruksjoner,” Master’s thesis, Department of Physics and Technology, University of Bergen, Norway, 2005, (in Norwegian).
- [101] *CMR Prototech*, Fantoftvegen 38 NO-5892 Bergen, Norway.
- [102] *Thorlabs, Inc.*, 56 Sparta Avenue, Newton, NJ, United States.
- [103] *CMM Calibration Certificate*, Messtech AS, Postboks 88, Oterveien 26, seksjon A, U18, 2211 Kongsvinger, Norway, 2015.
- [104] J. W. Jewett, Jr. and R. A. Serway, *Physics for scientists and engineers with modern physics*, 8th ed. BROOKS/COLE CENGAGE Learning, Kentucky, United States, 2011.
- [105] *Gitzo SA*, Via Valsugana 100, 36022 Cassola (VI) Italy.
- [106] L. Svilainis and V. Dumbrava, “Measurement of complex impedance of ultrasonic transducers,” *Ultragarsas*, vol. 62, no. 1, pp. 1392–2114, 2007.
- [107] P. Lunde, “Private conversation,” Department of Physics and Technology, University of Bergen, Norway, 2015.
- [108] J. Kocbach, “Private conversation,” Christian Michelsen Research, Fantoftvegen 38, 5072 Bergen, Norway, 2015.
- [109] P. Giacomo, “Errata: Equation for the Determination of the Density of Moist Air (1981),” *Metrologia*, vol. 18, no. 3, pp. 171–171, 1982. [Online]. Available: <http://stacks.iop.org/0026-1394/18/i=3/a=011?key=crossref.b3ebbb5876c09e238182a0d249419a61>
- [110] a. Picard, R. S. Davis, M. Gläser, and K. Fujii, “Revised formula for the density of moist air (CIPM-2007),” *Metrologia*, vol. 45, no. May 2002, pp. 149–155, 2008.

- [111] R. S. Davis, “Equation for the Determination of the Density of Moist Air (1981/91),” *Metrologia*, vol. 29, pp. 67–70, 1992.
- [112] *Certificate of Calibration, No.: C1201771*, Brüel Kjær, 2012.
- [113] S. Barrera-Figueroa, K. Rasmussen, and F. Jacobsen, “On experimental determination of the free-field correction of laboratory standard microphones at normal incidence,” *Metrologia*, vol. 44, pp. 57–63, 2007.
- [114] *COMSOL Multiphysics*, Tegnérgatan 23, SE-111 40 Stockholm, SWEDEN.
- [115] M. Sæther, Ph.D. dissertation, University of Bergen, Department of Physics and Technology, Bergen, Norway, In progress, 2015.
- [116] *Certificate of inspection, issue No.: 11L164B0, serial No. 15229628*, Mitutoyo Corporation, Kawasaki, Japan, 2012.
- [117] Stephanie Bell, “Measurement good practice guide. A beginner’s guide to uncertainty of measurement,” National Physical Laboratory No. 11 Issue 2, 1999.

# Appendix A

## GUM

### A.1 Evaluating standard uncertainty

In the following a short introduction to the Guide to the expression of Uncertainty in Measurement (GUM) [92] will be presented. The objective is to present the equations and models used in the thesis. The notation differs from [92].

### A.2 General statements

When performing a measurement the quantity that is being measured is hereby referred to as the measurand. The following distinction between error and uncertainty, as stated in GUM, will be used [92]: Error is an idealized concept and errors cannot be known exactly; Uncertainty (of measurement) is a parameter associated with the result of a measurement that characterizes the dispersion of the values that could reasonably be attributed to the measurand.

#### A.2.1 The measurand

The measurand,  $Y$ , is often not measured directly, but is determined by  $N$  other input quantities  $X_i$  through a functional relationship

$$Y = f(X_1, X_2, \dots, X_N) = f(X_i) \quad i = 1, 2, \dots, N, \quad (\text{A.1})$$

where the input quantities may themselves be determined from measurements. However, only an estimate of the measurand is practically realizable, thus the measurand  $Y$  is estimated by

$$Y \approx y = f(x_1, x_2, \dots, x_N) = f(x_i), \quad (\text{A.2})$$

where  $x_1, x_2, \dots, x_N$  are the estimates of the input quantities  $X_1, X_2, \dots, X_N$  respectively.

#### A.2.2 Type A evaluation of standard uncertainty

A type A standard uncertainty is an uncertainty statement that is obtained by statistical methods.

Often, the best estimate of the expectation value  $\mu_{X_i}$  of the input quantity  $X_i$ , that varies randomly, and for which  $n$  independent observations  $X_{i,k}$ , where  $k = 1, 2, \dots, n$ , have been made, is the arithmetic mean or average  $\bar{X}_i$ :<sup>1</sup>

$$\bar{X}_i = \frac{1}{n} \sum_{k=1}^n X_{i,k} \quad (\text{A.3})$$

The estimation of the  $i$ 'th input quantity in Eq. A.2 is therefore  $x_i \approx \bar{X}_i$ .

The experimental standard variance of  $n$  observations, which estimates the variance  $\sigma^2(X_i)$  of the probability distribution of  $X_i$ , is

---

<sup>1</sup>Note that the notation used in the current chapter might deviate from that in [92]

$$\sigma^2(X_i) \approx s^2(X_i) = \frac{1}{n-1} \sum_{k=1}^n (X_{i,k} - \bar{X}_i)^2 \quad (\text{A.4})$$

The experimental variance and its positive square root, the experimental standard deviation,  $s(X_i)$ , characterize the observed values' dispersion about their mean,  $\bar{X}_i$ .

To quantify how well  $\bar{X}_i$  estimates the expectation  $\mu_{X_i}$  of  $X_i$ , the experimental standard variance, or deviation, is used. The experimental standard variance is the best estimate of the variance about the mean,  $\sigma^2(\bar{X}_i)$ , given by

$$\sigma^2(\bar{X}_i) = \frac{\sigma^2(X_i)}{n} \approx s^2(\bar{X}_i) = \frac{s^2(X_i)}{n} \quad (\text{A.5})$$

Both the experimental standard variance and deviation may be used as a measure of the uncertainty associated with  $X_i$ . Such that, for an input quantity,  $X_i$ , determined from  $n$  independent repeated observations,  $X_{i,k}$ , the standard uncertainty,  $u(x_i)$ , of its estimate,  $x_i = \bar{X}_i$ , is  $u(x_i) \approx s(\bar{X}_i)$ , where  $s^2(\bar{X}_i)$  is calculated from Eq. A.5. The final expression for the standard uncertainty is:

$$u(x_i) \approx \sqrt{\frac{1}{n(n-1)} \sum_{k=1}^n (X_{i,k} - \bar{X}_i)^2} \quad (\text{A.6})$$

Note that the number of observations  $n$  should be large enough such that  $\bar{X}_i$  provides reliable estimate of the expectation  $\mu_{X_i}$  of the random variable  $X_i$  [92]. In the current thesis, when applicable,  $n = 10$  [117].

### A.2.3 Type B evaluation of standard uncertainty

A type B evaluation of standard uncertainties is a statement about the uncertainty of a quantity obtained by any other means than statistical analysis. This can be e.g. manufacturer's specifications of laboratory equipment, previous measurement data and/or uncertainties assigned to reference data taken from handbooks [92].

Two cases of a Type B evaluation is considered in slightly more detail: 1) If the manufacturer's specifications of the uncertainty  $u(x_i)$  of the estimate  $x_i$  is stated as a multiple of a standard deviation,  $\sigma$ , the standard uncertainty is the statement divided on the multiple, i.e.

$$\begin{aligned} u(x_i)|_{\sigma=3} &= \beta \\ \Rightarrow u(x_i)|_{\sigma=1} &= \frac{\beta}{3} \end{aligned} \quad (\text{A.7})$$

2) If the manufacturer's specifications of the estimate  $x_i$  is given as a lower,  $a_-$ , and upper,  $a_+$ , bounds, then the distribution is regarded as rectangular such that the probability that the value of  $X_i$  lies within the interval  $a_-$  to  $a_+$  is one, and zero that the value of  $X_i$  lies outside the interval. The expectation value  $x_i$  of  $X_i$ , is therefore the midpoint of the interval,  $x_i = (a_- + a_+)/2$ , such that the standard uncertainty can be stated as

$$u(x_i) = \frac{\sqrt{(a_- + a_+)^2}}{2\sqrt{3}} = \frac{a}{\sqrt{3}}, \quad (\text{A.8})$$

where  $a$  is the half-width of the rectangular interval.

### A.2.4 Determining combined standard uncertainty

#### Uncorrelated input quantities

If all input quantities to Eq. A.2 are uncorrelated, the combined standard variance, denoted  $u_c^2(y)$ , where  $y$  is the estimate of the measurand  $Y$ , is given by



$$u_c^2(y) = \sum_{i=1}^N \left( \frac{\partial f}{\partial x_i} \right)^2 u^2(x_i) \quad (\text{A.9})$$

where the partial derivatives are denoted the sensitivity coefficients, and the uncertainties,  $u^2(x_i)$ , can be determined by either Type A or B evaluation.

### correlated input quantities

If one or more input quantities to Eq. A.2 are significantly correlated then the correlations must be taken into account. When the input quantities are correlated, Eq. A.9 becomes

$$\begin{aligned} u_c^2(y) &= \sum_{i=1}^N \sum_{j=1}^N \frac{\partial f}{\partial x_i} \frac{\partial f}{\partial x_j} u(x_i, x_j) \\ &= \sum_{i=1}^N \left( \frac{\partial f}{\partial x_i} \right)^2 u^2(x_i) + 2 \sum_{i=1}^{N-1} \sum_{j=i+1}^N \frac{\partial f}{\partial x_i} \frac{\partial f}{\partial x_j} u(x_i, x_j) \end{aligned} \quad (\text{A.10})$$

where  $x_i$  and  $x_j$  are the estimates of the the input quantities  $X_i$  and  $X_j$ , respectively, and  $u(x_i, x_j) = u(x_j, x_i)$  is the estimated covariance associated with  $x_i$  and  $x_j$ . The correlation coefficient,  $r(x_i, x_j)$ , estimates the degree of correlation between  $x_i$  and  $x_j$ , and are given by

$$r(x_i, x_j) = \frac{u(x_i, x_j)}{u(x_i)u(x_j)} \quad (\text{A.11})$$

where  $r(x_i, x_j) = r(x_j, x_i)$ , and  $|r(x_i, x_j)| \leq 1$ . Thus, if the estimates  $x_i$  and  $x_j$  are independent,  $r(x_i, x_j) = 0$ .

An important observations is made from Eq. A.10, namely that if none of the input quantities are correlated, Eq. A.10 is identical to Eq. A.9.

# Appendix B

## Source code

In present section the MATLAB scripts used in the current thesis are given.

### B.1 MATLAB scripts, post-processing

#### B.1.1 findPeakToPeak\_FFT\_k.m

```
1 function [pp_FFT, angle_FFT] = findPeakToPeak_FFT_k(signal, signal_f, Fs, l_lim, u_lim, SigL, t)
2 % [pp_FFT, angle] = findPeakToPeak_FFT(signal, signal_f, Fs, l_lim, u_lim)
3 %
4 % findPeakToPeak_FFT calculates the fft of signal and returns 2 vectors:
5 %   pp_FFT: the peak to peak absolute values
6 %   angle: the corresponding angles in radians
7 %   Both vectors of length = length(signal_f)
8 %
9 % input parameters:
10 %   signal: input signal, matrix or vector
11 %   signal_f: frequency vector, vector
12 %   Fs: sample rate found from:
13 %       Fs = 100e3./(results.acoustic_timescale*10);
14 %       where results.acoustic_timescale is the timescale from the
15 %       oscilloscope
16 %   l_lim: lover limit of fft window
17 %   u_lim: uper limit of fft window
18
19 % author K. Andersen, february 2015
20 % based on work by Rune Hauge and Eivind Mosand
21
22 %% % empty vectors to store fft values
23 pp_FFT = ones(1,length(signal(:,1)));
24 angle_FFT = ones(1,length(signal(:,1)));
25
26 for nn = 1:size(signal,1)
27     % compensate for possible bias by removing mean from signal
28     sig_mean = mean(signal(nn,:));
29     signal(nn,:) = signal(nn,:) - sig_mean;
30     %% call script zeros to obtain list of zeros in signal vector
31     zro = crossing(signal(nn,:));
32     %% find local maximum within one period, use next zero crossing
33     T = 1/signal_f(nn); % period time
34     Ts = 1/Fs(nn); % time between samples
35     Ns = T/Ts; % number of samples per period
36     l_lim2 = ceil(l_lim + Ns + Ns/4); % making sure that we cover one full T
37     u_lim2 = ceil(u_lim + Ns + Ns/4); % making sure that we cover one full T
38     % find local max for l_lim and u_lim
39     [loc_l_lim_max_value, loc_l_lim_max] = max(signal(nn, l_lim:l_lim2));
40     l_lim_max = l_lim + loc_l_lim_max;
41     [loc_u_lim_max_value, loc_u_lim_max] = max(signal(nn, u_lim:u_lim2));
42     u_lim_max = u_lim + loc_u_lim_max;
43     % obtain all the zero crosses up until the limit
```

```

44     l_limx = find(zro <= l_lim_max);
45     u_limx = find(zro <= u_lim_max);
46
47     % select the last zero cross of the two vectors
48     try
49         l_limx = l_limx(end);
50         l_limt = zro(l_limx);
51     catch
52         l_limt = l_lim;
53     end
54
55     try
56         u_limx = u_limx(end);
57         u_limt = zro(u_limx);
58
59     catch
60         u_limt = u_lim;
61     end
62
63     % determine length of signal to be processed by FFT
64     signalx = signal(nn, l_limt:u_limt);
65     L = length(signalx);
66
67     % determine the length of the fft signal, the number of fft points
68     % needs to be an integer number of the length of the signal
69     % NFFT = pow2(nextpow2(20*L))
70     NFFT = SigL*L;
71     % compute FFT (finally :D )
72     sig_specter = fft(signalx, NFFT)/L;
73
74     % determine fft frequency vector
75     fFFT = Fs(nn)/2* linspace(0,1,NFFT/2+1);
76     % interpolate the fft values upon the measurement frequency
77     spect_meas = interp1(fFFT, sig_specter(1:NFFT/2+1), signal_f);
78     % store the modulus of peak2peak values and angles in vectors
79     pp_FFT(nn) = 2*2*abs(spect_meas(nn));
80     angle_FFT(nn) = angle(spect_meas(nn));
81
82     if mod(nn, 100) == 0
83         disp(['n = ', num2str(nn), ', NFFT = ', num2str(NFFT)])
84     end
85 end
86 end

```

## B.1.2 findPeakToPeak\_FFT\_phase\_k.m

```

1 function [pp_FFT, angle_FFT] = findPeakToPeak_FFT_phase_k(signal, signal_f, Fs, l_lim_tmp, u_lim, SigL)
2 [pp_FFT, angle] = findPeakToPeak_FFT(signal, signal_f, Fs, l_lim, u_lim)
3 %
4 % findPeakToPeak_FFT_phase_k calculates the fft of signal and returns 2 vectors:
5 % pp_FFT: the peak to peak absolute values
6 % angle: the corresponding angles in radians
7 % Both vectors of length = length(signal_f)
8
9 % This script uses the lower limit as given in input, but finds the zero
10 % crossing after the u_lim given in input
11 %
12 % input parameters:
13 % signal: input signal, matrix or vector
14 % signal_f: frequency vector, vector
15 % Fs: sample rate found from:
16 %     Fs = 100e3./(results.acoustic_timescale*10);
17 %     where results.acoustic_timescale is the timescale from the
18 %     oscilloscope
19 % l_lim: lover limit of fft window
20 % u_lim: uper limit of fft window
21
22 % author K. Andersen, february 2015
23 % based on work by Rune Hauge and Eivind Mosand
24

```

```

25 %% % empty vectors to store fft values
26 pp_FFT = ones(1,length(signal(:,1)));
27 angle_FFT = ones(1,length(signal(:,1)));
28
29 for nn = 1:length(signal_f)
30     % check if lower limit is a vector or scalar
31     if isscalar(l_lim_tmp)
32         l_lim = l_lim_tmp;
33     else
34         l_lim = l_lim_tmp(nn);
35     end
36     % compensate for possible bias by removing mean from signal
37     sig_mean = mean(signal(nn,:));
38     signal(nn,:) = signal(nn,:) - sig_mean;
39     %% call script zeros to obtain list of zeros in signal vector
40     zro = crossing(signal(nn,:));
41     %% find local maximum within one period, use next zero crossing
42     T = 1/signal_f(nn); % period time
43     Ts = 1/Fs(nn); % time between samples
44     Ns = T/Ts; % number of samples per period
45     % l_lim2 = ceil(l_lim + Ns + Ns/4); % making sure that we cover one full T
46     u_lim2 = ceil(u_lim + Ns + Ns/4); % making sure that we cover one full T
47     % find local max for l_lim and u_lim
48     % [loc_l_lim_max_value, loc_l_lim_max] = max(signal(nn, l_lim:l_lim2));
49     % l_lim_max = l_lim + loc_l_lim_max;
50     [loc_u_lim_max_value, loc_u_lim_max] = max(signal(nn, u_lim:u_lim2));
51     u_lim_max = u_lim + loc_u_lim_max;
52     % obtain all the zero crosses up until the limit
53     % l_limx = find(zro <= l_lim_max);
54     u_limx = find(zro <= u_lim_max);
55     % select the last zero cross of the two vectors
56     %l_limx = l_limx(end);
57     u_limx = u_limx(end);
58     if isempty(u_limx)
59         u_limx = length(zro); % obtain last index value
60     end
61     % convert temporary index value to true index value
62     % l_limt = zro(l_limx);
63     u_limt = zro(u_limx);
64
65     % overwrite l_limt with value given as input parameter
66     l_limt = l_lim;
67
68     % determine length of signal to be processed by FFT
69     signalx = signal(nn, l_limt:u_limt);
70     L = length(signalx);
71
72     % determine the length of the fft signal, the number of fft points
73     % needs to be an integer number of the length of the signal
74     NFFT = SigL*L;
75     % compute FFT (finally :D )
76     sig_specter = fft(signalx, NFFT)/L;
77
78     % determine fft frequency vector
79     fFFT = Fs(nn)/2* linspace(0,1,NFFT/2+1);
80     % interpolate the fft values upon the measurement frequency
81     spect_meas = interp1(fFFT, sig_specter(1:NFFT/2+1), signal_f);
82     % store the modulus of peak2peak values and angles in vectors
83     pp_FFT(nn) = 2*2*abs(spect_meas(nn));
84     angle_FFT(nn) = angle(spect_meas(nn));
85
86     if mod(nn,100) == 0
87         disp(['n = ', num2str(nn)]);
88     end
89 end
90 end

```

### B.1.3 compute\_sensitivity\_coefficients.m

```

1 %% script calculates the partial derivatives, or sensitivity coefficients,

```

```

2 % associated with the magnitude of the transfer function |HVV5open5m|
3
4 % written by Kenneth k. Andersen
5 % Oct. 2015 University of Bergen
6
7 %% function F = |HVV5open5m|
8 % symbolic variables
9 % ZR = [ZRr + i*ZRi], impedance of piezoelectric disk
10 % Zamp = [Zamp_r + i*Zamp_i], input impedance B&K amplifier
11 % Zb = [i*Zbi], cable parameter, only imaginary
12 syms ZRr ZRi Zamp_r Zamp_i Zbi
13 % real part of F
14 Ztr = (Zamp_r)/(Zamp_r.^2 + Zamp_i.^2);
15 % imaginary part of F
16 Zti = -1.*[ (Zamp_i)/(Zamp_r.^2 + Zamp_i.^2) + (1/Zbi) ];
17 % magnitude of F expressed by the real and imaginary parts
18 F = sqrt(1./(( ZRr.*Ztr - ZRi.*Zti + 1).^2 + (ZRr.*Zti + ZRi.*Ztr).^2 ));
19
20 %% partial derivation, sensitivity coefficients
21 dF_ZRr = simplify(diff(F, ZRr)); % C1
22 dF_ZRi = simplify(diff(F, ZRi)); % C2
23 dF_Zamp_r = simplify(diff(F, Zamp_r)); % C3
24 dF_Zamp_i = simplify(diff(F, Zamp_i)); % C4
25 dF_Zbi = simplify(diff(F, Zbi)); % C5

```

## B.1.4 Khimunin\_diffractioncorrection.m

```

1 % Khimunin_diffractioncorrection.
2 %
3 % Calculate the diffraction correction for uniformly vibrating piston in a
4 % rigid baffle of infinite extent according to the expression given by Khimunin in
5 % A. S. Khimunin, "Numerical calculation of the diffraction corrections
6 % for the precise measurement of ultrasound absorption", Acustica 27(4),
7 % 173-181 (1972).
8 %
9 % There is a slight modification in the present script compared to the
10 % article. The output here is  $K = |p/p_0| = A + iB$ , while the "output" in
11 % the article is  $|p/p_0| = \sqrt{A^2 + B^2}$ . This allows the user to
12 % calculate both the magnitude and phase.
13 %
14 % Note: This version is limited to a fixed axial distance, z.
15 %
16 % Input variables:
17 % k : The wavenumber.
18 % a : The radius of the piston.
19 % z : The axial distance.
20 % N : Number of trapezoids in the numerical integration. 1000 is typically OK.
21 %
22 % Output variables:
23 % K : The complex diffraction correction.
24 %
25 % Espen Storheim (2009-2012).
26
27 function K = Khimunin_diffractioncorrection(k,a,z,N)
28
29 theta = pi*[0:1:N]/(2*N); % Khimunins integration variable.
30 S = z/a^2*2*pi./k; % Scaled axial distance.
31 ka = k*a; % ka number.
32
33 % Calculate the diffraction correction for the frequencies specified.
34 for ii = 1:length(ka)
35
36 % Calculate the integrand for C and D in Eq. (3).
37 CC = cos(sqrt(S(ii)^2*ka(ii)^4/(2*pi)^2 + 4*ka(ii)^2.*(cos(theta)).^2)).*(sin(theta)).^2;
38 DD = sin(sqrt(S(ii)^2*ka(ii)^4/(2*pi)^2 + 4*ka(ii)^2.*(cos(theta)).^2)).*(sin(theta)).^2;
39
40 % Numerical integration of C and D with the trapezoidal rule.
41 C = theta(2)*(sum(CC(1:end)) - 0.5*(CC(1) + CC(end)));
42 D = theta(2)*(sum(DD(1:end)) - 0.5*(DD(1) + DD(end)));
43

```

```

44     % Calculate the real and imaginary part of the diffraction
45     % correction.
46     A = 1 - C*4/pi*cos(ka(ii)^2*S(ii)/(2*pi)) - D*4/pi*sin(ka(ii)^2*S(ii)/(2*pi));
47     B = D*4/pi*cos(ka(ii)^2*S(ii)/(2*pi)) - C*4/pi*sin(ka(ii)^2*S(ii)/(2*pi));
48     KK = A + 1i*B;
49
50     % Store the complex diffraction correction for each ka number.
51     K(ii) = KK;
52
53     % Clear temp variables.
54     clear CC DD C D A B
55
56 end
57
58
59 end

```

## B.1.5 SpeedOfSound.m

```

1  % SpeedOfSound.m
2  % Acoustics - Institute of Physics and Technology
3  % University of Bergen
4  % By Andre Adelsten Sovik, 2014/2015
5  function [c0,c,gamma] = SpeedOfSound(F,TC,p,RH,xc)
6  %Speedofsound Calculate speed of sound corrected for dispersion and
7  %specific heat ratio
8  %
9  %-----
10 % F: frequency array [Hz], TC: temperature [Celsius],
11 % p: atmospheric pressure [Pa], RH: relative humidity %,
12 % xc: molar fraction of CO2
13 %-----
14 %% Reference values
15 % Reference temperature T_r and pressure p_r
16 p_r = 101.325; % (1atm) [kPa]
17 T_r = 293.15; % (20 degC) [K]
18
19 %% Temperature
20 T = TC + 273.15; % Absolute temperature [K]
21
22 %% Pressure
23 % Conversion from Pa to kPa
24 p = p./1e3;
25
26 % Molar fraction of CO2
27 % Value according to CIPM-2007, and assumed to be constant
28 xc = 0.00040; % Default value
29
30 %% Humidity
31 % Conversion of relative humidity to molar concentration of water vapor
32 % Formula from ANSI S1.26-1995
33 T01 = 273.16; % Triplepoint isotherm temperature
34 V = 10.79586.*(1-(T01./T))-5.02808.*log10(T./T01)+1.50474*(1e-4).*(1-10.^(-8.29692.*((T./T01)-1)))+0.42873*
35 PP = 10.^V; % Ratio of saturation vapor pressure to reference pressure.
36 % Approximation to saturation vapor pressure ratio
37 C = -6.8346*(T01/T)^1.261 + 4.6151;
38 % PP = 10^C;
39 h_r = RH; % Relative humidity in percent
40 h = h_r.*PP.*((p./p_r).^(-1)); % Molar concentration of water vapor in percent
41 xw = h./100; % Molar concentration of water vapor
42 % h = RH; %test
43 % xw = h./100; %test
44 %% Vibration relaxaion frequencies [Hz]
45 f_rO = (p/p_r).*(24 + ((4.04.*1e4.*h.*(0.02 + h))./(0.391 + h))); % Oxygen
46 f_rN = (p/p_r).*((T./T_r).^(-0.5)).*(9 + 280.*h.*exp(-4.170.*((T./T_r).^(-1./3))-1)); % Nitrogen
47
48 %% Maximum absorption over one wavelength, use [Np/lambda] not [dB/lambda]
49 thetaO = 2239.1; % Characeristic vibrational temperature O2 [K]
50 thetaN = 3352.0; % Characeristic vibrational temperature N2 [K]
51 xO = 0.209390; % Fractional molar concentration ANSI 0.209

```

```

52 xN = 0.780848; % Fractional molar concentration ANSI 0.781
53 %alphaLO = 1.559*xO.*((thetaO.^2)./(T.^2)).*exp(-thetaO./T); % [dB/lambda]
54 %alphaLN = 1.559*xN.*((thetaN.^2)./(T.^2)).*exp(-thetaN./T); % [dB/lambda]
55 alphaLO = (2*pi/35)*xO.*((thetaO.^2)./(T.^2)).*exp(-thetaO./T); % [Np/lambda]
56 alphaLN = (2*pi/35)*xN.*((thetaN.^2)./(T.^2)).*exp(-thetaN./T); % [Np/lambda]
57
58 %% Coefficients [Speed of sound c0, Specific heat ratio \gamma]
59 % Cramer, 1992
60 a0 = [331.5024,      1.400822];
61 a1 = [0.603055,     -1.75e-5];
62 a2 = [-0.000528,    -1.73e-7];
63 a3 = [51.471935,    -0.0873629];
64 a4 = [0.1495874,    -0.0001665];
65 a5 = [-0.000782,    -3.26e-6];
66 a6 = [-1.82e-7,     2.047e-8];
67 a7 = [3.73e-8,      -1.26e-10];
68 a8 = [-2.93e-10,    5.939e-14];
69 a9 = [-85.20931,    -0.1199717];
70 a10 = [-0.228525,   -0.0008693];
71 a11 = [5.91e-5,     1.979e-6];
72 a12 = [-2.835149,   -0.01104];
73 a13 = [-2.15e-13,   -3.478e-16];
74 a14 = [29.179762,   0.0450616];
75 a15 = [0.000486,    1.82e-6];
76
77 %% Approximate equations
78 % Cramer, 1992
79 % Speed of sound [m/s]
80 f_c = a0(1).*ones(1,length(TC)) + a1(1).*TC + a2(1).*(TC.^2) + (a3(1)+a4(1).*TC+a5(1).*(TC.^2)).*xw + (a6(1)
81 % Correction for dispersion
82 % Howell, Morfey, (1980) 1987
83 beta = alphaLO./((f_rO.^2)+(F.^2)) + alphaLN./((f_rN.^2)+(F.^2));
84 c0 = f_c;
85 %c = c0./(1-((F.^2)./pi).*beta); % Assumption c = c0 [ANSI]
86 c = c0.*(((F.^2)./pi).*beta+1); % Assumption c = c\phi [ANSI]
87 %c = c0.*((alphaLO.*(F.^2)./((f_rO.^2)+(F.^2))).*(1/pi) + (alphaLN.*(F.^2)./((f_rN.^2)+(F.^2))).*(1/pi) + 1
88 %c = c0./(1-(F.^2).*beta); % Assumption c = c_0 [ANSI]
89
90 % Specific heat ratio
91 % Note: do not calculate
92 %f_gamma = a0(2).*ones(1,length(TC)) + a1(2).*TC + a2(2).*(TC.^2) + (a3(2)+a4(2).*TC+a5(2).*(TC.^2)).*xw +
93 gamma = 0;
94 end

```

## B.2 MATLAB scripts, data acquisition

### B.2.1 main\_acoustic.m

```

1  %%%%%%%%%%%%%%%%%%%%%%%%%%%%%%%%%%%%%%%%%%%%%%%%%%%%%%%%%%%%%%%%%%%%%%%%%
2  % main.m
3  % Main software for acoustic measurements in air.
4  % Espen Storheim, 2011
5  % Based on work by Vidar Knappskog and Magne Aanes.
6  %
7  % Modified by Rune Hauge and Eivind Mosland, 2012/2013 (v1.1)
8  % Modified by Kenneth Andersen and Andre S?vik 2014/2015
9  %%%%%%%%%%%%%%%%%%%%%%%%%%%%%%%%%%%%%%%%%%%%%%%%%%%%%%%%%%%%%%%%%%%%%%%%%
10
11 clear
12 close all
13
14 %% Version number.
15 airversion = '1.1';
16
17 %% Add the subfolders to MATLABs path, just in case.
18 % Change folder names to exclude spaces.
19 if (isunix || ismac)
20     addpath([pwd '/User input'])
21     addpath([pwd '/Kernel'])

```

```

22     addpath([pwd '/Instrument control etc']);
23 else
24     addpath([pwd '\User input'])
25     addpath([pwd '\Kernel'])
26     addpath([pwd '\Instrument control etc']);
27 end
28
29 % Load information about the measurement about to be performed.
30 measurement_parameters
31
32 % Initialization of the instruments prior to measurements.
33 init_instruments
34
35 % Adjust scaling according to input voltage.
36 voltage_scaling = [0.02 0.05 0.1 0.2 0.5 1 2 5 10];
37 for ii = 1:(length(voltage_scaling));
38     if (4*voltage_scaling(ii) >= meas.voltage_in)
39         fprintf(instrument.scope, ['CH2:SCA ' num2str(voltage_scaling(ii))]);
40         break;
41     end
42 end
43
44 tic
45
46 %% Read the acoustic pulses.
47 ch = 1;
48 pause(10) % If starting on acoustical signal, the thermometer needs time to connect
49 disp(' ')
50 disp('Start reading the acoustical pulses...')
51
52 for ii = 1:length(meas.f);
53     %% Adjust the bandwidth of the KH-filter, changed 21.04.2015
54     pause(0.1)
55     % Set channel 1 to high pass mode.
56     try
57         fprintf(instrument.filter, 'CH1.1;M2');
58     catch
59         pause(5)
60         fprintf(instrument.filter, 'CH1.1;M2');
61     end
62     pause(0.1)
63     % Set the cutoff frequency for channel 1.
64     try
65         fprintf(instrument.filter, ['F' num2str((meas.f(ii)/1000)/2) 'K']);
66     catch
67         pause(5)
68         fprintf(instrument.filter, ['F' num2str((meas.f(ii)/1000)/2) 'K']);
69     end
70     pause(0.1)
71     % Set channel 2 to low pass mode.
72     try
73         fprintf(instrument.filter, 'CH1.2;M1');
74     catch
75         pause(5)
76         fprintf(instrument.filter, 'CH1.2;M1');
77     end
78     pause(0.1)
79     % Set the cutoff frequency for channel 2.
80     try
81         fprintf(instrument.filter, ['F' num2str((meas.f(ii)/1000)*2) 'K']);
82     catch
83         pause(5)
84         fprintf(instrument.filter, ['F' num2str((meas.f(ii)/1000)*2) 'K']);
85     end
86
87     %% Record temperature from ASL F250 Mk II
88     try
89         % disp('Hello from try')
90         ASLF250A = fscanf(instrument.temperature);
91         results.temp_ASLF250A_acoustic(ii) = str2double(ASLF250A(3:8)); % 3 des
92         %disp('Adios from try')

```



```

93     catch
94         disp('Problems reading the ASL F250, trying again')
95         pause(0.1);
96         ASLF250A = fscanf(instrument.temperature);
97     end
98     results.temp_ASLF250A_acoustic(ii) = str2double(ASLF250A(3:8)); % 3 des
99     clear ASLF250A
100
101     %% record acoustic signal
102     pause(0.1)
103     % Number of cycles is adjusted according to the given frequency
104     disp([num2str(meas.f(ii)/1000) ' kHz'])
105     fprintf(instrument.generator,['BM:NCYC ', num2str(floor(meas.f(ii)*t))]);
106     fprintf(instrument.generator,['FREQ ', num2str(meas.f(ii))]);
107     % Record environmental data.
108     [Temp RH] = VaisalaHMT313(instrument.humidity);
109     results.temp_acoustic(ii) = Temp;
110     results.humidity_acoustic(ii) = RH;
111     results.acoustic_time(ii,:) = clock;
112     clear Temp RH ASLF250A
113     % Adjust time window.
114     adjustTime('acoustic',instrument,meas)
115     % Adjust amplitude scaling and read out signal.
116     [dum1 dum2 dum3] = adjustAmplitude(1,instrument,meas);
117
118     results.acoustic_t(ii,:) = dum1;
119     results.acoustic(ii,:) = dum2';
120     results.acoustic_timescale(ii) = dum3;
121     results.acoustic_Vscale(ii) = str2num(query(instrument.scope,['CH',num2str(ch),' :SCA?']));
122     results.acoustic_Termination(ii) = str2num(query(instrument.scope,['CH',num2str(ch),' :TER?']));
123     clear dum1 dum2 dum3
124 end
125
126 %% Read electrical signal
127 disp(' ')
128 disp('Finished reading the acoustical signal. Now readjusting the scope and continuing to electrical pulses')
129 ch = 2;
130
131 for ii = 1:length(meas.f)
132     disp([num2str(meas.f(ii)/1000) ' kHz'])
133     fprintf(instrument.generator,['BM:NCYC ', num2str(floor(meas.f(ii)*t))]);
134     fprintf(instrument.generator,['FREQ ', num2str(meas.f(ii))]);
135     % Record environmental data.
136     [Temp RH] = VaisalaHMT313(instrument.humidity);
137     results.temp_electric(ii) = Temp;
138     results.humidity_electric(ii) = RH;
139     results.electric_time(ii,:) = clock;
140     clear Temp RH
141     % store number of cycles per burst, from N_cyc = t*f
142     results.N_cyc(ii) = t.*meas.f(ii);
143     % Adjust time window.
144     adjustTime('electric',instrument,meas)
145     % Stop aquisition.
146     fprintf(instrument.scope,'ACQ:STATE STOP');
147     % Wait to ensure that the scope wipes its memory.
148     pause(1)
149     % Start aquisition.
150     fprintf(instrument.scope,'ACQ:STATE RUN');
151     % Wait for averaging.
152     pause(meas.wait_scaling)
153     % Read and save.
154     % Adjust amplitude scaling and read out signal.
155     [dum1 dum2 dum3] = adjustAmplitude(2,instrument,meas);
156     results.electric_t(ii,:) = dum1;
157     results.electric(ii,:) = dum2;
158     results.electric_timescale(ii) = dum3;
159     results.electric_Vscale(ii) = str2num(query(instrument.scope,['CH',num2str(ch),' :SCA?']));
160     results.electric_Termination(ii) = str2num(query(instrument.scope,['CH',num2str(ch),' :TER?']));
161     clear dum1 dum2 dum3
162 end
163

```

```

164 %% allocating data to new struct
165 meas.bt = t; % burst time
166 results.electric_f = meas.f;
167 results.acoustic_f = meas.f;
168
169 %% Storing data
170 % go to directory given in measurement_parameters
171 cd(folderName)
172 xx = strcat(meas.name, '_',datestr(now,'yyyymmddHHMMSS'),' .mat');
173 identity = whos('results');
174
175 if identity.bytes < 2e9
176     save(xx,'results', 'meas');
177 else
178     save(xx,'results', '-v7.3', 'meas');
179 end
180 % return to parent folder where script files are located
181 cd('D:\AndreOgKenneth\Kenneth\AcousticMeasurements')
182
183 %% Finishing touches.
184 % Close the instrument ports and clear device handles.
185 instrument_shutdown
186 toc

```

## B.2.2 instruments.m

```

1  %%%%%%%%%%%%%%%%%%%%%%%%%%%%%%%%%%%%%%%%%%%%%%%%%%%%%%%%%%%%%%%%%%%%%%%%%
2  % Instruments.m
3  % Part of the software for acoustic measurements in air.
4  % Espen Storheim, 2011
5  % Based on work by Vidar Knappskog and Magne Aanes.
6  %%%%%%%%%%%%%%%%%%%%%%%%%%%%%%%%%%%%%%%%%%%%%%%%%%%%%%%%%%%%%%%%%%%%%%%%%
7
8  % Initialization of the instrumens used in the measurement setup for air.
9  % Contains MATLAB-handles for the instruments used in the setup, both GPIB,
10 % serial, and the special functions used by the PI positioning equipment.
11 %
12 % This file contains information about many devices in the laboratory, many
13 % that are not in use on the setup for measurements in air. These are by
14 % default commented out in the code.
15 %
16 % Comment out instruments not in use!
17 %
18 % Notes about future updates.
19 % - Include a test to check for acoustic or impedance measurements.
20 % - Remove the _idn parameter since there is no common response.
21
22 instrument = {};
23
24 %% Signal generators.
25
26 % Signal Generator: Agilent 33220A. S/N:
27 instrument.generator = gpib('NI',0,10);
28 fopen(instrument.generator);
29 instrument.generator_name = 'Agilent 33220A. S/N: ';
30 instrument.generator_idn = query(instrument.generator,'*IDN?');
31 % Test the connection. Should be a command where the response can be
32 % verified.
33 if isempty(instrument.generator_idn)
34     disp('Warning: The signal generator is not connected or configured properly.')
35 else
36     disp('The signal generator is connected and appears to be working.')
37 end
38
39 %% Oscilloscopes.
40 % 14.09.2012 Rune Hauge: Include 'instrfind' for locating a GPIB object
41 instrument.scope = instrfind('Type', 'visa-usb', 'RsrcName', 'USB0::0x0699::0x0410::C010246::0::INSTR', 'Ta
42
43 if isempty(instrument.scope)
44     % Our oscilloscope

```

```

45     instrument.scope = visa('NI', 'USB0::0x0699::0x0410::C010246::0::INSTR');
46     % Magne Aanes's oscilloscope
47     % instrument.scope = visa('NI', 'USB0::0x0699::0x0410::C011044::0::INSTR');
48 else
49     fclose(instrument.scope);
50     instrument.scope = instrument.scope(1);
51 end
52 % 20.09.2012 Rune Hauge: Set scope InputBufferSize to high enough value.
53 % Trying 1000000.
54 instrument.scope.InputBufferSize = 2000000;
55
56 fopen(instrument.scope)
57 instrument.scope_name = 'Tektronix DPO3012. S/N: ';
58 instrument.scope_idn = query(instrument.scope, '*IDN?');
59 % Test the connection. Should be a command where the response can be
60 % verified.
61 if isempty(instrument.scope_idn)
62     disp('Warning: The oscilloscope is not connected or configured properly.')
63 else
64     disp('The oscilloscope is connected and appears to be working.')
65 end
66
67 %% Environmental parameters.
68 % Temperature sensor: ASL F250. S/N:
69 %instrument.temperature = gpib('ni',0,3);
70 % 14.09.2012 Rune Hauge: Include 'instrfind' for locating a GPIB object
71 instrument.temperature = instrfind('Type', 'gpib', 'BoardIndex', 0, 'PrimaryAddress', 3, 'Tag', '');
72
73 if isempty(instrument.temperature)
74     instrument.temperature = gpib('NI', 0, 3);
75 else
76     fclose(instrument.temperature);
77     instrument.temperature = instrument.temperature(1);
78 end
79 fopen(instrument.temperature)
80 pause(0.5)
81 set(instrument.temperature, 'EOSmode', 'read&write');
82 pause(0.5)
83 set(instrument.temperature, 'EOSCharCode', 10); % Set terminator to LF.
84 instrument.temperature_name = 'ASL F250 mk II. S/N: ';
85 pause(0.5)
86 fprintf(instrument.temperature, 'A0');
87 pause(0.5)
88 % 24.02.2015 Andre Adelsten Sovik: Set the F250 resolution to 3 decimal
89 % place. Initial State: 2 decimal place (for temp.)
90 fprintf(instrument.temperature, 'R1');
91 pause(5)
92 instrument.temperature_idn = fscanf(instrument.temperature);
93
94 % Test the connection. Should be a command where the response can be
95 % verified.
96 if isempty(instrument.temperature_idn)
97     disp('Warning: The thermometer is not connected or configured properly.')
98 else
99     disp('The thermometer is connected and appears to be working.')
100 end
101
102 % Pressure sensor: Paroscientific DigiQuartz 740. S/N:
103 %instrument.pressure = serial('COM2', 'Baudrate', 4800, 'Terminator', 'cr', 'Databit', 7, 'Parity', 'even');
104 instrument.pressure_name = 'Paroscientific DigiQuartz 740. S/N: ';
105
106 % Relative humidity and temperature sensor: Vaisala HMT313. S/N:
107 instrument.humidity = serial('COM5', 'Baudrate', 4800, 'Terminator', 'cr', 'Databit', 7, 'Parity', 'even');
108 instrument.humidity_name = 'Vaisala HMT313. S/N: ';
109 fopen(instrument.humidity);
110
111
112 %% Signal processing.
113 % Bandpass filter: Krohn-Hite 3940A. S/N: AM2626.
114 %instrument.filter = gpib('ni',0,25);
115 % 14.09.2012 Rune Hauge: Include 'instrfind' for locating a GPIB object

```

```

116 instrument.filter = instrfind('Type', 'gpib', 'BoardIndex', 0, 'PrimaryAddress', 25, 'Tag', '');
117
118 if isempty(instrument.filter)
119     instrument.filter = gpib('NI', 0, 25);
120 else
121     fclose(instrument.filter);
122     instrument.filter = instrument.filter(1);
123 end
124 fopen(instrument.filter)
125 instrument.filter_name = 'Krohn-Hite 3940A. S/N: AM2626';
126 instrument.filter_idn = query(instrument.filter, '*IDN?');
127
128 %% stage Z-direction
129 global s1
130 s1 = serial('COM1', 'BaudRate', 115200);
131 fopen(s1);
132 fprintf(s1, '1 init'); % "init": motor restart after failure. Why is this here?
133 PID(0, 0.001000, 0);
134 fprintf(s1, '2 1 sna'); % 2
135 fprintf(s1, '5 1 snv'); % hastighet. bruk 10 for store flytt, 5 ellers

```

### B.2.3 `init_instruments.m`

```

1  %%%%%%%%%%%%%%%%%%%%%%%%%%%%%%%%%%%%%%%%%%%%%%%%%%%%%%%%%%%%%%%%%%%%%%%%%
2  % init_instruments.m
3  % Initialize the instruments according to measurement_parameters
4  % Part of the software for acoustic measurements in air.
5  % Espen Storheim, 2011
6  % Based on work by Vidar Knappskog and Magne Aanes.
7  %%%%%%%%%%%%%%%%%%%%%%%%%%%%%%%%%%%%%%%%%%%%%%%%%%%%%%%%%%%%%%%%%%%%%%%%%
8
9  % This script is used to initialize the instruments to the proper settings.
10 % Most of the values are taken from the "meas" structure specified by the
11 % user in the m-file "measurement_parameters.m".
12
13 instruments;
14
15 %% Initialize the oscilloscope.
16 % Code for the Tektronix DPO3012.
17 if strcmp(instrument.scope_name, 'Tektronix DPO3012. S/N: ')
18     % Set the acquisition mode to averaging.
19     fprintf(instrument.scope, 'ACQ:MOD AVE');
20     % Set the number of cycles to average.
21     fprintf(instrument.scope, ['ACQ:NUMAV ' num2str(meas.average)]);
22     % Number of points which shall be read from the scope.
23     fprintf(instrument.scope, ['HOR:RECO ' num2str(meas.samples)]);
24     % Start point for the recorded signal
25     fprintf(instrument.scope, 'DAT:START 1');
26     % Stop point for the recorded signal
27     fprintf(instrument.scope, ['DAT:STOP ' num2str(meas.samples)]);
28     % Trigger specifications. Set to edge detection from external source.
29     fprintf(instrument.scope, 'TRIG:A:EDGE:SOU EXT');
30     % Set the trigger type to positive edge.
31     fprintf(instrument.scope, 'TRIG:A:TYP EDG');
32     % 2012.11.19 EM: Added additional initialization.
33     % CH1
34     % Set Offset to zero.
35     fprintf(instrument.scope, 'CH1:OFFS 0');
36     % Set position to zero.
37     fprintf(instrument.scope, 'CH1:POS 0');
38     % Set coupling to AC.
39     fprintf(instrument.scope, 'CH1:COUP AC');
40     % CH2
41     % Set Offset to zero.
42     fprintf(instrument.scope, 'CH2:OFFS 0');
43     % Set position to zero.
44     fprintf(instrument.scope, 'CH2:POS 0');
45     % Set coupling to AC.
46     fprintf(instrument.scope, 'CH2:COUP AC');
47 end

```

```

48
49 %% Initialize the bandpass filter.
50 % Code for Krohn-Hite 3940A filter.
51 if strcmp(instrument.filter_name, 'Krohn-Hite 3940A. S/N: AM2626')
52     % There seems to be an overflow when the commands are combined, so they
53     % have been separated and a pause of 100 ms is set between each
54     % command.
55     %
56     % Set the input and output gain on both channels to 0 dB.
57     pause(0.1)
58     fprintf(instrument.filter, 'AL;0IG;0OG;B');
59     pause(0.1)
60     % Set channel 1 to high pass mode.
61     fprintf(instrument.filter, 'CH1.1;M2');
62     pause(0.1)
63     % Set the cutoff frequency for channel 1.
64     fprintf(instrument.filter, ['F' num2str(meas.cutoff_1) 'K']);
65     pause(0.1)
66     % Set channel 2 to low pass mode.
67     fprintf(instrument.filter, 'CH1.2;M1');
68     pause(0.1)
69     % Set the cutoff frequency for channel 2.
70     fprintf(instrument.filter, ['F' num2str(meas.cutoff_2) 'K']);
71 end
72
73 %% Initialize the signal generator.
74 % This code is for the Agilent 33*** series signal generators
75 if strcmp(instrument.generator_name, 'Agilent 33220A. S/N: ')
76     fprintf(instrument.generator, 'OUTP OFF');
77     fprintf(instrument.generator, ['APPL:SIN ' num2str(meas.f(1)) ' HZ, ' num2str(meas.voltage_in) ' VPP']);
78     % Set the trigger to internal and positive slope.
79     fprintf(instrument.generator, 'TRIG:SOUR IMM');
80     fprintf(instrument.generator, 'TRIG:SLOP POS');
81     % Set the number of periods in one burst.
82     fprintf(instrument.generator, ['BURS:NCYC ' num2str(meas.burst_cycles)]);
83     fprintf(instrument.generator, 'BURS:STAT ON');
84     % Set the burst rate, i.e. the frequency of the bursts.
85     fprintf(instrument.generator, ['BM:INT:RATE ' num2str(meas.burst_rate)]);
86     % Set the peak voltage.
87     fprintf(instrument.generator, ['VOLT ' num2str(meas.voltage_in(1))]);
88     % Activate the output.
89     fprintf(instrument.generator, 'TRIG:SLOP POS');
90     fprintf(instrument.generator, 'OUTP ON');
91 end
92
93 %% Initialize the thermometer.
94 % This code is for the Automated System Laboratories F250 mk II
95 % thermometer.
96 if strcmp(instrument.temperature_name, 'ASL F250 mk II. S/N: ')
97     % Activate channel A.
98     fprintf(instrument.temperature, 'P0');
99     pause(0.1)
100     % Set the displayed unit to Celsius.
101     fprintf(instrument.temperature, 'U0');
102     pause(0.1)
103 end

```

## B.2.4 measurement\_parameters.m

```

1  %%%%%%%%%%%%%%%%%%%%%%%%%%%%%%%%%%%%%%%%%%%%%%%%%%%%%%%%%%%%%%%%%%%%%%%%%
2  % measurement_parameters.m
3  % Information about the calibration of the measurement microphone.
4  % Part of the software for acoustic measurements in air.
5  % Espen Storheim, 2011
6  % Based on work by Vidar Knappskog and Magne Aanes.
7  %
8  % Modified by Rune Hauge and Eivind Mosland, 2012/2013
9  %%%%%%%%%%%%%%%%%%%%%%%%%%%%%%%%%%%%%%%%%%%%%%%%%%%%%%%%%%%%%%%%%%%%%%%%%
10
11 % This file is designed to be tampered with prior to each measurement.

```

```

12
13 %% ambient pressure
14 % meas.amb_pressure_hPa = 1001;
15 meas.amb_pressure = 100000;
16
17 %% Define initial bandpass filter low and high cutoff frequency
18 meas.cutoff_1 = 20; % kHz
19 meas.cutoff_2 = 600; % kHz
20 % At present, cutoff_2 is adjusted for each measurement frequency in
21 % main.m. This is currently not done for cutoff_1.
22
23 %% General measurement info.
24 % Version of this software which was used to make the measurements. Should
25 % be taken from elsewhere.
26 % meas.version = 'Updated 20/7-2011.';
27
28 % Name of the person performing the measurement and date.
29 % meas.name = 'Hvv_B&K_and_KHfilter_250mV_f10k_1k_300kHz';
30 meas.name = 'elem11_to_elem04_f50_300kHz_Mixed_voltage_bt1.1ms_meas001x1';
31 folderName = 'acoustic_meas/distance_85cm_x2';
32
33 % meas.f = [50e3:500:90e3,...
34 %          90.2e3:200:120e3,...
35 %          120.25e3:250:135e3,...
36 %          135.5e3:500:240e3,...
37 %          240.2e3:200:260e3,...
38 %          260.1e3:100:275e3,...
39 %          275.5e3:500:300e3];
40
41
42
43
44 % insert values for the parallelity of the two disks
45 % L1 = laser 1, left
46 meas.L1a = 2.248e-3;
47 meas.L1b = 2.248e-3;
48 meas.L1c = 2.249e-3;
49 meas.L1d = 2.252e-3;
50 % L2 = laser 2, right
51 meas.L2a = -2.522e-3;
52 meas.L2b = -2.528e-3;
53 meas.L2c = -2.524e-3;
54 meas.L2d = -2.537e-3;
55
56
57 TT = clock;
58 meas.date = [date ' , ' num2str(TT(4)) ':' num2str(TT(5))];
59 clear TT
60
61 % Information about the transmitting transducer.
62 % meas.source = 'Pz27 disk, D = 20.0 mm, T = 2.0 mm, Element No. 12 in batch 9/12.';
63
64 % Information about the receiving transducer.
65 % meas.receiver = 'Element No. 07 in batch 9/12.';
66
67 % Additional notes regarding the specific simulation.
68 % meas.notes = '';
69 % Folder to store data in
70 %folderName = 'acoustic_meas\preliminary_meas\acoustic_center/meas002';
71
72
73 %% Distance from transmitter.
74 meas.distance = 0.85;
75 %meas.z
76
77 %% Frequency information [Hz]
78 % noise meas, 789 frequencies
79 % meas.f = [50e3:500:90e3,...
80 %          90.1e3:100:114.9e3,...
81 %          115e3:500:245e3,...
82 %          245.1e3:100:255.9e3,...

```

```

83 %     256e3:500:300e3];
84
85 meas.f = [50e3:500:90e3,...
86           90.2e3:200:120e3,...
87           120.25e3:250:135e3,...
88           135.5e3:500:240e3,...
89           240.2e3:200:265e3,...
90           265.5e3:500:300e3];
91
92 %% do not delete, Andres freq vector
93 % meas.f = [50e3:500:90e3,...
94 %     90.1e3:100:120e3,...
95 %     120.25e3:250:160e3,...
96 %     160.5e3:500:240e3,...
97 %     240.1e3:100:260e3,...
98 %     260.5e3:500:300e3];%
99
100 % meas.f = [50:1:300].*1e3;
101 %
102 %% long freq vector, 1200 freqs with low f at 10 kHz
103
104 % meas.f = [50e3:500:90e3,...
105 %     90.1e3:100:120e3,...
106 %     120.25e3:250:135e3,...
107 %     135.1e3:100:145e3,...
108 %     145.5e3:500:240e3,...
109 %     240.1e3:100:275e3,...
110 %     275.5e3:500:300e3];%
111
112 % meas.f = [ 200.5e3:500:240e3,...
113 %     240.1e3:100:275e3,...
114 %     275.5e3:500:300e3];
115
116 % meas.f = [80:0.5:85,...
117 %     175:0.5:180,...
118 %     225:0.5:230,...
119 %     295:0.5:300].*1e3;
120
121
122 %% tight freq. vector for 50-140 kHz
123 % meas.f = [10e3:500:90e3,...
124 %     90.1e3:100:120e3,...
125 %     120.25e3:500:140e3];%
126
127
128 % meas.f = 100e3;
129 %% use for acoustic center
130 % meas.f = [70e3:1e3:130e3];
131
132 %% use for amplifier and filter measurements
133 %meas.f = [10e3:0.5e3:300e3];
134
135 %% use for statistical measurements, increments of 1kHz
136 % meas.f = [10e3:2e3:300e3];
137
138 %% do not delete, Rune and Eivinds freq vector
139 % meas.f = [50e3:500:88e3,...
140 %     88.1e3:100:114.9e3,...
141 %     115e3:500:236e3,...
142 %     236.1e3:100:255.9e3,...
143 %     256e3:500:300e3];
144
145
146 %% used for SSPA
147 % meas.f = [50e3:500:90e3,...
148 %     90.1e3:100:130e3,...
149 %     130.5e3:500:140e3];
150
151
152 % meas.f = [112e3];
153 % meas.f = [98.5e3, 112e3];

```

```

154
155 %% Adjust the burst length to ensure temporal resolution.
156
157 %   t = 16*100e-6; % == 160 burst cycles for f = 100 kHz
158           % == 400 burst cycles for f = 250 kHz
159 %   t = 14*100e-6; % == 140 burst cycles for f = 100 kHz
160           % == 350 burst cycles for f = 250 kHz
161 %   t = 12*100e-6; % == 120 burst cycles for f = 100 kHz
162           % == 300 burst cycles for f = 250 kHz
163 %   t = 11*100e-6; % == 110 burst cycles for f = 100 kHz
164           % == 275 burst cycles for f = 250 kHz
165     t = 11*100e-6; % == 100 burst cycles for f = 100 kHz
166           % == 250 burst cycles for f = 250 kHz
167 %   t = 8*100e-6; % == 80 burst cycles for f = 100 kHz
168           % == 200 burst cycles for f = 250 kHz
169 %   t = 6*100e-6; % == 60 burst cycles for f = 100 kHz
170           % == 150 burst cycles for f = 250 kHz
171 %   t = 4*100e-6; % == 40 burst cycles for f = 100 kHz
172           % == 100 burst cycles for f = 250 kHz
173
174 %% distance from center of rod to rim of faraday cage
175
176 % meas.dist_Rod2FaradayCage_left = 0.05; % [m]
177 % meas.dist_Rod2FaradayCage_right = 0.04; % [m]
178
179 %% Input waveform data.
180 % Vpp voltage out from the signal generator [V]. This is the actual voltage
181 % level of the function generator
182 meas.voltage_in = 10;
183 % meas.voltage_noise = 10e-3;
184 % Number of periods in each burst [-]
185 % Only used in initialization of the generator. In main.m the number of
186 % cycles is adjusted to fit a certain burst length [ms] specified therein.
187 meas.cycles = 100;
188 meas.burst_cycles = meas.cycles;
189 % Burst repetition rate [Hz]
190 meas.burst_period = 40e-3;
191 meas.burst_rate = 1/meas.burst_period;
192
193 % Approximate time before the signal is steady after a voltage scaling change.
194 % meas.wait_scaling = 3.5; % for 64
195 % meas.wait_scaling = 7; % for 128 averages
196 % meas.wait_scaling = 21; % for 512 averages
197
198 % A note on the input voltage: The signal generator claims that the voltage
199 % specified above is the peak to peak voltage. This is the case when the
200 % generator is connected to a 50 Ohm load. However, the transmitting
201 % transducer typically has an electrical impedance in the kilo Ohm range and is connected
202 % directly to the generator. This causes a voltage division which depends
203 % of the impedance of the transducer, and hence an impedance mismatch.
204
205 %% Oscilloscope parameters.
206 % Number of pulses which the signal is averaged.
207 meas.average = 128;
208 % Number of data points recorded by the scope.
209 meas.samples = 1e5;
210 % Channel used for measurements.
211 %meas.channel = 1;
212
213 % Channel number where the signal generator is connected.
214 meas.channel_electrical = 1;
215 % Channel number where the oscilloscope is connected.
216 meas.channel_acoustical = 2;
217
218 %% Distance from transmitter to receiver [m].
219 %meas.distance = meas.z;
220
221 %% Total input gain in the B&K 2636 measurement amplifier [dB].
222 % Only recorded for later reference. Must be set manually.
223 meas.gain_in = 40;
224 meas.gain_out = 20;

```



```

225 meas.gain = meas.gain_in + meas.gain_out;
226
227 %% read dmove struct from distance measurement
228 PWD_d_meas = 'D:\AndreOgKenneth\Kenneth\AcousticMeasurements\distance measurement';
229 name = dir(fullfile((PWD_d_meas), '*.mat'));
230 load([PWD_d_meas, name.name]);
231 meas.dmove = dmove;

```

## B.2.5 adjustAmplitude.m

```

1  %%%%%%%%%%%%%%%%%%%%%%%%%%%%%%%%%%%%%%%%%%%%%%%%%%%%%%%%%%%%%%%%%%%%%%%%%
2  % adjustAmplitude.m
3  %
4  % [x wf timeDiv] = adjustAmplitude(ch,instrument,meas)
5  %
6  % Adjusts voltage scaling and records acoustic data.
7  %
8  % Rune Hauge & Eivind Mosland, 2012
9  % modified by Kenneth Andersend to prevent infinite loops, and unnecessary
10 % readjusting of oscilloscope scaling
11 %%%%%%%%%%%%%%%%%%%%%%%%%%%%%%%%%%%%%%%%%%%%%%%%%%%%%%%%%%%%%%%%%%%%%%%%%
12
13 function [x wf timeDiv] = adjustAmplitude(ch,instrument,meas)
14 % Stop aquisition.
15 fprintf(instrument.scope,'ACQ:STATE STOP');
16 % Wait to ensure that the scope wipes its memory.
17 pause(0.1)
18 % Start aquisition.
19 fprintf(instrument.scope,'ACQ:STATE RUN');
20 % Wait for averaging.
21 pause(meas.wait_scaling)
22 % Read waveform.
23 [x wf timeDiv] = DPO_les(ch,instrument.scope);
24 maxV = max(wf);
25 % Get current scaling.
26 Scaling = str2double(query(instrument.scope,['CH',num2str(ch),':SCA?']));
27 % A minimum scaling of 10 mV/div is used to ensure that the noise prior to
28 % averaging is within the voltage range.
29 verticalScalings = [10e-3, 20e-3, 50e-3, 100e-3, 200e-3, 500e-3 1 2 5 10];
30 ind = find(Scaling==verticalScalings);
31 if isempty(ind)
32     disp('ind er tom!')
33     ind = 1;
34     fprintf(instrument.scope,['CH',num2str(ch),':SCA ',num2str(verticalScalings(ind))]);
35
36     [x wf timeDiv] = DPO_les(ch,instrument.scope);
37     maxV = max(wf);
38 end
39
40 % Half the number of vertical division. 8 visible divisions on the screen
41 % and one additional above and below.
42 scrnRows = 5;
43
44 % Adjust vertical scaling and measure until no clipping.
45 finished = 0;
46 Sv = 0; % vector to keep the different vertical scalings
47 cnt = 0;
48 while ~finished
49     %disp(['Current volt/div: ',num2str(verticalScalings(ind))])
50     cnt = cnt + 1;
51     disp(['count = ', num2str(cnt)])
52     if maxV >= scrnRows*verticalScalings(ind)
53         if length(Sv) >= 3
54             % compare the end-2 and end entries in Sv for equality
55             if Sv(end-2) == Sv(end) % scaling is in loop, choose lowest scaling, i.e. highest value
56                 disp('Greetings from first if...')
57                 Scaling = max(Sv(end-1), Sv(end))
58                 fprintf(instrument.scope,['CH',num2str(ch),':SCA ',num2str(Scaling)]);
59                 % Wait for averaging to finish.
60                 pause(meas.wait_scaling)

```

```

61         [x wf timeDiv] = DPO_les(ch,instrument.scope);
62         finished = 1;
63     end
64 end
65
66     Scaling = verticalScalings(ind+1);
67     fprintf(instrument.scope,['CH',num2str(ch),':SCA ',num2str(Scaling)]);
68     ind = ind +1;
69
70     % Wait for averaging to finish.
71     pause(meas.wait_scaling)
72
73     %disp('Measuring')
74     [x wf timeDiv] = DPO_les(ch,instrument.scope);
75     maxV = max(wf);
76     Sv(cnt) = Scaling;
77
78 elseif ind ~= 1 && maxV < scrnRows*verticalScalings(ind-1)
79     if length(Sv) >= 3
80         % compare the end-2 and end entries in Sv for equality
81         if Sv(end-2) == Sv(end) % scaling is in loop, choose lowest scaling
82             disp('Greetings from second if...')
83             Scaling = max(Sv(end-1), Sv(end))
84             fprintf(instrument.scope,['CH',num2str(ch),':SCA ',num2str(Scaling)]);
85             % Wait for averaging to finish.
86             pause(meas.wait_scaling)
87             [x wf timeDiv] = DPO_les(ch,instrument.scope);
88             finished = 1;
89         end
90     end
91
92     %disp('Decreasing scaling')
93     Scaling = verticalScalings(ind-1);
94     fprintf(instrument.scope,['CH',num2str(ch),':SCA ',num2str(Scaling)]);
95     ind = ind -1;
96
97     % Wait for averaging to finish.
98     pause(meas.wait_scaling)
99
100    %disp('Measuring')
101    [x wf timeDiv] = DPO_les(ch,instrument.scope);
102    maxV = max(wf);
103    Sv(cnt) = Scaling;
104
105    if cnt > length(verticalScalings)
106        % banal method to brake eventual infinite loop between
107        % scalings,
108        finished = 1;
109    end
110
111 else
112     finished = 1;
113 end
114 end
115
116 end

```

## B.2.6 adjustTime.m

```

1  %%%%%%%%%%%%%%%%%%%%%%%%%%%%%%%%%%%%%%%%%%%%%%%%%%%%%%%%%%%%%%%%%%%%%%%%%
2  % adjustTime.m
3  %
4  % adjustTime(type,instrument,meas)
5  %
6  % Sets time scaling and adjusts window position.
7  %
8  % Rune Hauge & Eivind Mosland, 2012/2013
9  %%%%%%%%%%%%%%%%%%%%%%%%%%%%%%%%%%%%%%%%%%%%%%%%%%%%%%%%%%%%%%%%%%%%%%%%%
10
11 function adjustTime(type,instrument,meas)

```

```

12     import instrument
13     % Set scaling.
14     if ~strcmp(type,'noise')
15         % Get frequency and number of cycles.
16         freq = query(instrument.generator,'FREQ?');
17         cycles = query(instrument.generator,'BURS:NCYC?');
18         % Compute appropriate scaling.
19         SignalLength = 1/str2num(freq)*str2num(cycles);
20         minScaling = SignalLength/10;
21
22         if minScaling <= 40e-6
23             Scaling = 40e-6;
24         elseif minScaling <= 100e-6
25             Scaling = 100e-6;
26         elseif minScaling <= 200e-6
27             Scaling = 200e-6;
28         elseif minScaling <= 400e-6
29             Scaling = 400e-6;
30         elseif minScaling <= 1e-3
31             Scaling = 1e-3;
32         end
33         fprintf(instrument.scope,['HOR:SCA ',num2str(Scaling)]);
34     else
35         noise_Scaling = 40e-6;
36         fprintf(instrument.scope,['HOR:SCA ',num2str(noise_Scaling)]);
37     end
38     % Set window position.
39     if strcmp(type,'electric')
40         triggerDelay = Scaling*5 - 0.00001;
41     elseif strcmp(type,'acoustic')
42         % Ensures that the onset of the acoustic signal is recorded.
43         %triggerDelay = Scaling*5 + (meas.distance-0.01)/343;
44         triggerDelay = Scaling*5 + (meas.distance-0.04)/345;
45     elseif strcmp(type,'noise')
46         triggerDelay = (meas.distance+0.002)/343 - noise_Scaling*5;
47     end
48     fprintf(instrument.scope,['HOR:DEL:TIM ',num2str(triggerDelay)]);
49 end

```

## B.2.7 relative\_translation.m

```

1 %% script calculates the relative translation in the positive z-axis
2 % relative to the stages 0 position. Script uses the temperature obtained from
3 % the F250 thermometer.
4 % dm is the wanted measurement distance in meters, temperature is in
5 % degree celcius
6
7 % written by Kenneth Andersen, 2015
8
9 %%
10 clear
11 close all
12 delete(instrfindall)
13 pause(1)
14 %% define measurement distance, dm, in meters
15 dm = 0.5;
16
17 %% variables
18 alpha_A1 = 24e-6;
19 dx = 182.5692e-3; % given 24 degree celcius
20 Tcal = 24; %degree celcius; temperature during calibration of dx
21 dc = 30e-3; % constant distance between front face of laser sensors to the zeroth position
22
23 %% read temperature, and correct dxt to dx for thermal expansion/contraction
24 addpath('D:\AndreOgKenneth\Kenneth\AcousticMeasurements\Instrument control etc')
25 instruments
26 pause(5); % allow ASL to initialize
27 try
28     disp('Hello from try')
29     ASLF250A = fscanf(instrument.temperature);

```

```

30     T_F250 = str2double(ASLF250A(3:8)); % 3 des
31     disp('Adios from try')
32 catch
33     disp('Problems reading the temperature, trying again')
34     pause(0.1);
35     ASLF250A = fscanf(instrument.temperature);
36 end
37 T_F250 = str2double(ASLF250A(3:8)); % 3 des
38 clear ASLF250A
39
40 %% read the distances d1 and d2 from file
41 PWD_dm = 'D:\AndreOgKenneth\Kenneth\AcousticMeasurements\distance measurement';
42 name = dir(fullfile(PWD_dm, '*.csv'));
43
44 %% define struct to store means and relative movement
45 dmove = struct();
46 d1m = [];
47 d2m = [];
48 drel_move = [];
49 Nmeas = length(name)/2;
50
51 for ii = 1:length(name)/2
52     d_name1 = name(ii).name;
53     d_name2 = name(Nmeas+ii).name;
54     filename1 = ['D:\AndreOgKenneth\Kenneth\AcousticMeasurements\distance measurement\' , d_name1];
55     filename2 = ['D:\AndreOgKenneth\Kenneth\AcousticMeasurements\distance measurement\' , d_name2];
56
57     %% read from .csv
58     delimiter = ',';
59     formatSpec = '%f%s%[\n\r]';
60     fileID1 = fopen(filename1,'r');
61     fileID2 = fopen(filename2,'r');
62     dataArray1 = textscan(fileID1, formatSpec, 'Delimiter', delimiter, 'EmptyValue', NaN, 'ReturnOnError',
63     dataArray2 = textscan(fileID2, formatSpec, 'Delimiter', delimiter, 'EmptyValue', NaN, 'ReturnOnError',
64     fclose(fileID1);
65     fclose(fileID2);
66     d1 = dataArray1(:, 1);
67     d2 = dataArray2(:, 1);
68     % compute mean of N samples
69     d1 = mean(d1)./1000;
70     d2 = mean(d2)./1000;
71     % "adding" the reference distance, 30 mm, to the measured distances
72     d1cor = dc - d1;
73     d2cor = dc - d2;
74
75     %% compute distance, d0, distance between the elements
76     dT = T_F250 - Tcal; % difference in temperature for thermal expansion
77     dx = dx.*(1 + alpha_Al.*dT); % thermal expansion
78     d0 = dx + d1cor + d2cor; % distance between transducers
79
80     %% compute distance to move stage
81     z_rel = dm - d0;
82
83     %% allocate d1 and d2 to vector
84     d1m = [d1m, d1cor];
85     d2m = [d2m, d2cor];
86     drel_move = [drel_move, z_rel];
87
88     %% store variables in struct
89     dmove(ii).d1 = d1cor;
90     dmove(ii).d2 = d2cor;
91     dmove(ii).dx = dx;
92     dmove(ii).d0 = d0;
93     dmove(ii).drel_move = z_rel;
94
95 end
96
97 %% compute mean and std
98 d1mean = mean(d1m);
99 d2mean = mean(d2m);
100

```

```

101 d1std = std(d1m);
102 d2std = std(d2m);
103
104 dmove(1).d1m = d1m;
105 dmove(1).d2m = d2m;
106
107 dmove(1).d1std = d1std;
108 dmove(1).d2std = d2std;
109
110 dmove(1).d1mean = d1mean;
111 dmove(1).d2mean = d2mean;
112
113 %% recalculate the distance to move stage given the mean of the drel_move
114 drel_move_mean = mean(drel_move);
115 dmove(1).drel_move_mean = drel_move_mean;
116 dmove(1).drel_move_std = std(drel_move);
117 disp(['Distance to move stage is, in millimeter: ', num2str(drel_move_mean.*1000)])
118
119 %% save to file
120 save(fullfile([PWD_dm, '/dmove']), 'dmove')
121
122 %% display values
123 disp(['STD L1: ', num2str(d1std)])
124 disp(['STD L2: ', num2str(d2std)])
125
126 %% plot to check if everything looks OK
127 figure(1)
128 subplot(1,2,1)
129 plot(d1m.*1000, 'xk')
130 subplot(1,2,2)
131 plot(d2m.*1000, 'xk')
132
133 %% delete handles to instruments
134 % delete(instrfindall)
135 pause(0.1)

```

## B.3 FEMP structures and extension

### B.3.1 piezofluid

```

1 function [read]=read_inn_project(read,commands)
2 %%%%%%%%%%%%%%%%%%%%%%%%%%%%%%%%%%%%%%%%%%%%%%%%%%%%%%%%%%%%%%%%%%%%%%%%%
3 % Read .inn-file. Note that this function calls a project specific
4 % read_inn_project.m which should be in the working directory
5 %
6 % Part of FEMP (Finite Element Modeling of Piezoelectric structures)
7 % Programmed by Jan Kocbach (jan@kocbach.net)
8 % (C) 2000 Jan Kocbach. This file is free software; you can redistribute
9 % it and/or modify it only under the the terms of the GNU GENERAL PUBLIC
10 % LICENSE which should be included along with this file.
11 % (C) 2000-2010 Christian Michelsen Research AS
12 %%%%%%%%%%%%%%%%%%%%%%%%%%%%%%%%%%%%%%%%%%%%%%%%%%%%%%%%%%%%%%%%%%%%%%%%%
13
14 % Put a file read_inn_project.m in your project directory to define local
15 % FEMP input commands. Also include init_const_project.m in this directory
16 % and define the commands there.
17 global glob;
18 read=read;
19
20 if ~isempty(read.piezofluid)
21
22     read.points=[]; read.areas=[]; read.materials=[]; read.dof=[]; read.restraints=[];
23
24     r = read.piezofluid(1,1,:);
25     t = read.piezofluid(1,2,:);
26     elr = read.piezofluid(1,3,:);
27     elt = read.piezofluid(1,4,:);
28     matnumP = read.piezofluid(1,5,:);
29     rinf = read.piezofluid(1,6,:);

```

```

30     elfinr = read.piezofluid(1,7,:);
31     elfint = read.piezofluid(1,8,:);
32     elinfr = read.piezofluid(1,9,:);
33     elinft = read.piezofluid(1,10,:);
34     matnumfluid = read.piezofluid(1,11,:);
35
36     tott = t;
37
38     for s = 1:size(r,3)
39         theta_coord = [r(s) tott(s)/2 % pkt 4
40                       r(s) -tott(s)/2 % pkt 2
41                       ];
42         theta = atan(theta_coord(:,2)./theta_coord(:,1));
43
44
45         read.points(:, :, s) = [1, 0, -tott(s)/2
46                                 2, r(s), -tott(s)/2
47                                 3, 0, tott(s)/2
48                                 4, r(s), tott(s)/2
49                                 5, 0, rinf(s)
50                                 6, cos(theta(1))*rinf(s), sin(theta(1))*rinf(s)
51                                 7, cos(theta(2))*rinf(s), sin(theta(2))*rinf(s)
52                                 8, 0, -rinf(s)
53                                 9, 0, 2*rinf(s)
54                                 10, cos(theta(1))*2*rinf(s), sin(theta(1))*2*rinf(s)
55                                 11, cos(theta(2))*2*rinf(s), sin(theta(2))*2*rinf(s)
56                                 12, 0, -2*rinf(s)
57                                 99, 0, 0
58                                 ];
59
60
61         read.areas(:, :, s) = [1, 1, 2, 4, 3, elr(s), elt(s), 0, 0;
62                                 2, 3, 4, 6, 5, elfinr(s), elfint(s), 0, 99;
63                                 2, 4, 2, 7, 6, elfinr(s), elfint(s), 0, 99;
64                                 2, 2, 1, 8, 7, elfinr(s), elfint(s), 0, 99;
65                                 3, 5, 6, 10, 9, elinfr(s), elinft(s), 99, 99;
66                                 3, 6, 7, 11, 10, elinfr(s), elinft(s), 99, 99;
67                                 3, 7, 8, 12, 11, elinfr(s), elinft(s), 99, 99;
68                                 ];
69
70
71         read.materials(:, :, s) = [1, glob.globvariables.piezo, matnumP(s);
72                                     2, glob.globvariables.fluid, matnumfluid(s);
73                                     3, glob.globvariables.infinitefluid, matnumfluid(s)
74                                     ];
75
76     % use when the upper area of the disc is set to 1 Volt, and the lower area
77     % of the disc is set to 0, opposite of predefined structure 'piezodiskfluid'
78
79     %     read.dof(:, :, s) = [-1e-9, r(s)+1e-9, -tott(s)/2-1e-9, -tott(s)/2+1e-9, glob.free.ep];
80     %
81     %     read.restraints(:, :, s) = [-1e-9, r(s)+1e-9, tott(s)/2-1e-9, tott(s)/2+1e-9, glob.free.ep, 1];
82
83
84     % use when the upper area of the disc is set to 0 Volt, and the lower area
85     % of the disc is set to 1, equal to predefined structure 'piezodiskfluid'
86
87     read.dof(:, :, s) = [-1e-9, r(s)+1e-9, tott(s)/2-1e-9, tott(s)/2+1e-9, glob.free.ep];
88
89     read.restraints(:, :, s) = [-1e-9, r(s)+1e-9, -tott(s)/2-1e-9, -tott(s)/2+1e-9, glob.free.ep, 1];
90
91
92     end
93 end

```

### B.3.2 Extension to pressure receiver

```

1 %% Verification
2 % The following code has been verified for f = 100e3, 200e3 and 300e3 Hz
3 % with 3 distance, z = 0.3, 0.4 and 0.5 m from transmitter to receiver,

```

```

4 % against the original harmonic_analysis code as in FEMP 5.0. All
5 % comparable values has yielded identical results
6
7 %% usage
8 % in the .inn file, use following syntax to obtain a vector
9
10 % set
11 % ...
12 % r,10e-3      radius of disk
13 % ...
14 % fmin,100e3   frequency vector
15 % fmax,300e3   ...
16 % fstep,100e3  ...
17 % ...
18 % zmin,0.05    distance vector for calculation of pressure at receiver
19 % zstep,0.001  ...
20 % zmax,3       ...
21 % ...
22 % end
23
24 % ...
25
26 % pressureatreceiver
27 % fmin,fstep,fmax,r,zmin,zstep,zmax
28 % end
29
30 % ...
31
32 % save
33 % pressureatreceiver,pressureatreceiver_f,pressureatreceiver_r
34 % end
35
36 %% Part 1
37 % Replace complete if ~isempty(read.pressureatreceiver) in
38 % harmonic_analysis.m with the following code:
39 % (in FEMP 5.0 go to about line 643)
40
41 if ~isempty(read.pressureatreceiver)
42     % RAK 4 August 2003
43     fmin = read.pressureatreceiver(lnr,1,sim);%KDL 30.06.04 {}->()
44     fstep = read.pressureatreceiver(lnr,2,sim);%KDL 30.06.04 {}->()
45     fmax = read.pressureatreceiver(lnr,3,sim);%KDL 30.06.04 {}->()
46     pressureatreceiverfvvect=[fmin:fstep:fmax];
47     if isempty(pressureatreceiverfvvect), pressureatreceiverfvvect=fvect;end;
48
49     %distance to, and radius of receiver
50     a_receiver = read.pressureatreceiver(lnr,4,sim);
51
52     %KKA 23.04.2015 allowing distance vector to be defined in inn-file
53     pressureatreceiver_r_min = read.pressureatreceiver(lnr,5,:);
54     pressureatreceiver_r_delta = read.pressureatreceiver(lnr,6,:);
55     pressureatreceiver_r_max = read.pressureatreceiver(lnr,7,:);
56     pressureatreceiver_r_ax_vector = [pressureatreceiver_r_min:pressureatreceiver_r_delta:...
57                                     pressureatreceiver_r_max];
58
59     % applying correction for front of structure, mostly borrowed
60     % from prior modification done by RAK 25.08.2004
61     dispcoord=[ find(glob.EQN(:,glob.free.dz)~=0);...
62               find(glob.EQN(:,glob.free.dy)~=0)];
63     if isempty(dispcoord)
64         FrontOfStructure=0;
65     else
66         FrontOfStructure=max(glob.COORD(2,dispcoord));
67         disp(['Receiver distance is corrected due to front of structure at ', ...
68             num2str(FrontOfStructure), ' m']);
69     end
70     pressureatreceiver_r_ax_vector = pressureatreceiver_r_ax_vector + FrontOfStructure;
71
72     % KKA 23.04.2015 commented out
73     % -----
74     % RAK 25.08.2004 Replaced for vector r_ax spec. with parametric simulation

```

```

75 % pressureatreceiver_r_ax = read.pressureatreceiver(lnr,5,sim)';
76 % pressureatreceiver_r_ax(1:size(read.pressureatreceiver,3))=read.pressureatreceiver(lnr,5,:);
77 % pressureatreceiver_r_ax = unique(pressureatreceiver_r_ax)';
78 % %RAK 25.08.2004 End of replacement
79 % %correct distance due to front of structure
80 % dispcoord=[ find(glob.EQN(:,glob.free.dz)~=0) ; find(glob.EQN(:,glob.free.dy)~=0)];
81 % if isempty(dispcoord)
82 % FrontOfStructure=0;
83 % else
84 % FrontOfStructure=max(glob.COORD(2,dispcoord));
85 % disp(['Receiver distance is corrected due to front of structure at '...
86 % num2str(FrontOfStructure) ' m']);
87 % end
88 % pressureatreceiver_r_ax = pressureatreceiver_r_ax+FrontOfStructure;%vector
89 % -----
90
91 % KKA 23.04.2015 using outer for loop to obtain pressureatreceiver
92 % at several distances. Values will temporary be stored in struct with
93 % length equal to length(pressureatreceiver_r_ax_vector)
94
95 pressureatreceiver_struct = struct();
96
97 for kkk = 1:size(pressureatreceiver_r_ax_vector,2)
98 % KKA 23.04.2015: assigning value to
99 % pressureatreceiver_r_ax, no further change before next
100 % comment by KKA 23.04.2015
101 pressureatreceiver_r_ax = pressureatreceiver_r_ax_vector(kkk);
102
103 % no interpolation in radial direction, find infinite elements
104 % intersecting receiver plane
105 %[dum thetareceiver_index] = find(thetainfnodes>(pi/2-atan(a_receiver/pressureatreceiver_r_ax(1))))
106 [dum thetareceiver_index] = find(thetainfnodes>0);%RAK 30.08.2004
107 % regner ut interpolering for alle (n?r kilde) noder ved alle avstander
108 thetareceiver_nodes = thetainfnodes(thetareceiver_index);
109 receiver_nodes = infnodes(:,thetareceiver_index);
110
111 pressureatreceiver_r_nodes = zeros(length(pressureatreceiver_r_ax),length(thetareceiver_nodes));
112 r_receiver_map = zeros(length(pressureatreceiver_r_ax),length(thetareceiver_nodes));
113 TTreceivernodes = zeros(ordert,length(pressureatreceiver_r_ax),length(thetareceiver_nodes));
114 for ii = 1:length(thetareceiver_nodes)
115 pressureatreceiver_r_nodes(:,ii) = pressureatreceiver_r_ax./cos(pi/2-thetareceiver_nodes(ii));
116 r_receiver_map(:,ii)=1-2*(a./pressureatreceiver_r_nodes(:,ii));
117 TTreceivernodes(:,ii)=calc_TT(r_receiver_map(:,ii)',ordert);
118 end
119 y_receiver_nodes = fliplr(pressureatreceiver_r_nodes.*...
120 sin(repmat(pi/2-thetareceiver_nodes,...
121 size(pressureatreceiver_r_nodes,1),1)));
122 y_receiver = 0:a_receiver/1000:a_receiver;
123 h_receiver = a_receiver/(1000);
124 receiver_el_area = 2*pi/(pi*a_receiver^2)*(y_receiver*h_receiver);
125 receiver_el_area([1 end])=receiver_el_area([1 end])/2;
126
127 % KKA 23.04.2015: assigning values to struct
128 pressureatreceiver_struct(kkk).pressureatreceiver_r_nodes = pressureatreceiver_r_nodes;
129 pressureatreceiver_struct(kkk).r_receiver_map = r_receiver_map;
130 pressureatreceiver_struct(kkk).TTreceivernodes = TTreceivernodes;
131 pressureatreceiver_struct(kkk).y_receiver_nodes = y_receiver_nodes;
132 pressureatreceiver_struct(kkk).y_receiver = y_receiver;
133 pressureatreceiver_struct(kkk).h_receiver = h_receiver;
134 pressureatreceiver_struct(kkk).receiver_el_area = receiver_el_area;
135 end
136
137 end
138
139
140
141 %% Part 2
142 % Replace complete if ~isempty(read.pressureatreceiver) in
143 % harmonic_analysis.m with the following code:
144 % (in FEMP 5.0 go to about line 1248)
145

```



```

146 if ~isempty(read.pressureatreceiver)
147     % RAK 4 August 2003
148     c_medium=glob.inf_c;
149     k=omega/c_medium;i=sqrt(-1);
150     pressureatreceiver_temp = [];
151
152     %% KKA 23.04.2015 : using outer for loop to loop trough entries in struct
153
154     for kkk = 1:size(pressureatreceiver_struct, 2)
155         % KKA 23.04.2015 quick solution, reading out values from struct
156         pressureatreceiver_r_nodes = pressureatreceiver_struct(kkk).pressureatreceiver_r_nodes;
157         r_receiver_map = pressureatreceiver_struct(kkk).r_receiver_map;
158         TTreiceivernodes = pressureatreceiver_struct(kkk).TTreiceivernodes;
159
160         y_receiver_nodes = pressureatreceiver_struct(kkk).y_receiver_nodes;
161         y_receiver = pressureatreceiver_struct(kkk).y_receiver;
162         h_receiver = pressureatreceiver_struct(kkk).h_receiver;
163         receiver_el_area = pressureatreceiver_struct(kkk).receiver_el_area;
164         % KKA 23.04.2015 end of change
165
166         if find(pressureatreceiverfvect==f)
167             receiver_nodeval=sol(receiver_nodes);
168             vp_at_receivernodes = zeros(size(TTreiceivernodes,2),size(TTreiceivernodes,3));
169             for ii=1:size(TTreiceivernodes,3)
170                 %RAK 200803         vp_at_receivernodes(:,ii)=
171                 %(receiver_nodeval(:,ii).'*TTreiceivernodes(:, :,ii)'.*...
172                 %exp(-i*k*a*(1+r_receiver_map(:,ii))./(1-r_receiver_map(:,ii))); %
173                 vp_at_receivernodes(:,ii)= ...
174                 (receiver_nodeval(:,ii).'*...
175                 TTreiceivernodes(:, :,ii)'.*...
176                 exp(-i*k*a*(1+r_receiver_map(:,ii))./(1-r_receiver_map(:,ii)));
177             end
178             vp_at_receivernodes = fliplr(vp_at_receivernodes);
179             vp_interp=zeros(size(vp_at_receivernodes,1),1001);
180             for ii =1:size(vp_at_receivernodes,1)
181                 %vp_interp(ii,1:1001) = interp1(y_receiver_nodes(ii,:),vp_at_receivernodes(ii,:),',...
182                 % y_receiver, 'linear').*receiver_el_area;
183                 vp_interp(ii,1:1001) = interp1(y_receiver_nodes(ii,:),...
184                 vp_at_receivernodes(ii,:).',y_receiver, 'linear').*receiver_el_area;
185             end
186             % % % RAK 060104 line commented% % % eval(['save vprec',int2str(f),' f vp_at_receivernodes']);
187             %             Keep_vp_at_receiver_nodes = [Keep_vp_at_receiver_nodes vp_at_receivernodes];
188
189             % KKA 23.04.2015 commented out
190             % pressureatreceiver = [pressureatreceiver (-i*2*pi*f*glob.inf_density)*sum(vp_interp,2)];
191             % pressureatreceiver_f=[pressureatreceiver_f f];
192             % pressureatreceiver_r=pressureatreceiver_r_ax;
193
194             % KKA 23.04.2015 storing values in temporary varibale
195             pressureatreceiver_temp = [pressureatreceiver_temp,...
196                                     (-i*2*pi*f*glob.inf_density)*sum(vp_interp,2)];
197         end
198
199     end
200     % KKA 23.04.2015 concatenating variable values
201     pressureatreceiver = [pressureatreceiver pressureatreceiver_temp.'];
202     pressureatreceiver_f=[pressureatreceiver_f f];
203     pressureatreceiver_r = pressureatreceiver_r_ax_vector; % unnecessary to do every iteration
204 end

```


# Appendix C

## Data sheets

Keyence laser sensor LK-G3000 series

Permitted to open to outside

### LK-G3000 SERIES DATA SHEET

FILING No.	LKG-S3-D002	Typical example
TITLE	<b>Scanning Data [White Ceramic]</b>	
HEAD	LK-G30	 <p>White ceramic gauge</p>
CONTROLLER	LK-G3000V	
<ul style="list-style-type: none"> <li>■ Measurement Conditions</li> <li>• Measurement distance : Reference distance</li> <li>• Measurement mode : Normal mode</li> <li>• Sampling speed : 200 <math>\mu</math>s</li> <li>• Average number of times : 256 times</li> <li>• Alarm setting : 8 times/level 4</li> </ul>		

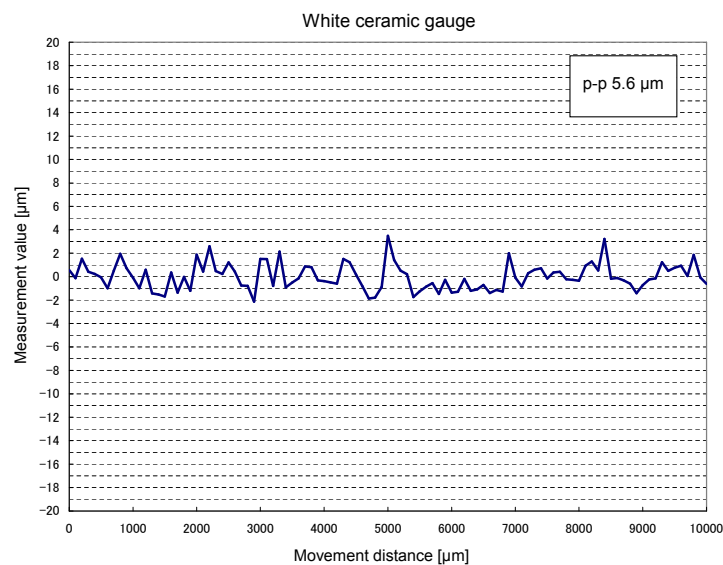
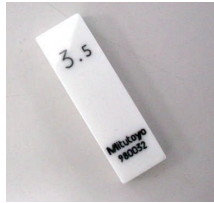


Figure C.1: Data sheet provided by Keyence showing an example measurement on a white ceramic material.

Permitted to open to outside

### LK-G3000 SERIES DATA SHEET

FILING No.	LKG-S3-D009	Typical example
TITLE	<b>Linearity Data [White Ceramic]</b>	
HEAD	LK-G30	 White ceramic gauge
CONTROLLER	LK-G3000V	
■ Measurement Conditions • Measurement mode : Normal mode • Sampling speed : 200 $\mu$ s • Average number of times : 256 times • Alarm setting : 8 times/level 4		

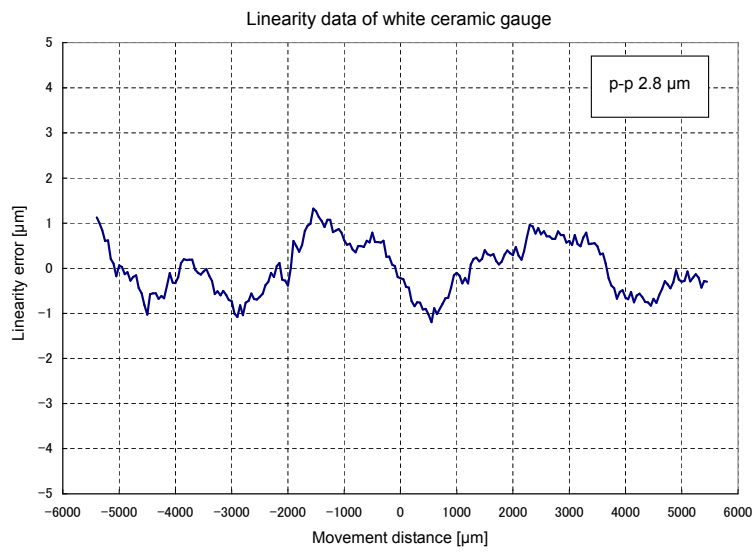


Figure C.2: Data sheet provided by Keyence showing the linearity error for a white ceramic material.

## PI miCos translation stage

# Measurement Protocol

Stage	LS-270 815mm SM Lia20	
Serial Number	12090049	
Customer	Universität Rostock	
Date	14.09.12	
Measurement Device	Laser-interferometer XL-80 Renishaw	
Measurement Base	Granit-base 1700x1050mm Quality LAB max error= 0.0016mm	
Environment	Temperature	22.9°C
	Humidity	62.3%
	Pressure	995 hPa
Hint	LS-270 mounted with 22xM6 (6,5Nm)	
Tester	Müller	

### Position-Error , absolute accuracy measured in a height 40 mm above the slider

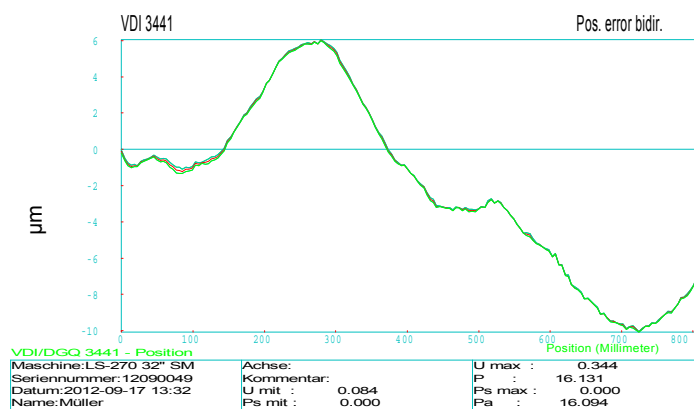


Figure C.3: Data sheet provided by PI miCos showing the position error of the translation stage LS-270.

# Appendix D

## SSPA

# Reciprocity calibration method for ultrasonic piezoelectric transducers in air. Comparison of finite element modelling and experimental measurements

Andersen, K. K.<sup>\*a</sup>, Søvik, A. A.<sup>a</sup>, Lunde, P.<sup>a,b,c</sup>, Vestrheim, M.<sup>a,c</sup>, and Kocbach, J.<sup>b,c</sup>

<sup>a</sup>University of Bergen, Department of Physics and Technology, Postboks 7803, NO-5020 BERGEN, Norway

<sup>b</sup>Christian Michelsen Research AS (CMR), P.O. Box 6031 Postterminalen, NO-5892 BERGEN, Norway

<sup>c</sup>The Michelsen Centre for Industrial Measurement Science and Technology, P.O. Box 6031, NO-5892 Bergen, Norway

## Abstract

*A modified free- and far-field three-transducer reciprocity calibration method has been utilized to determine the receiving voltage sensitivity,  $M_V$ , of a piezoelectric disc. The measurement results are compared to finite element modelling (FEM). A system model has been employed to give a theoretical description of the measurement system at hand, allowing corrections to be made accounting for laboratory instrumentation, diffraction and attenuation in air.*

*A technique to isolate different noise contributors has been utilised to obtain two different signal-to-noise ratio (SNR) analyses. It is shown that the SNR given coherent noise drops significantly, compared to that of random noise, for a certain frequency range when the piezoelectric discs are moved closer together.*

*All work is performed on piezoelectric discs radiating in air at room temperature at approximately 1 atm, with the first radial mode, R1, at about 100 kHz. The frequency range of interest is 100-300 kHz, though only a subset of this, 50-140 kHz, is investigated in the current work.*

## I. INTRODUCTION

The use of ultrasound in the industry motivates the study of calibration of precision measurement equipment operating in air in the frequency range 100-300 kHz. Industrial usages of ultrasound in this frequency range can be e.g. fiscal measurement of natural gas, therein multipath ultrasonic transit-time flow meters (USM) [1], measurements of the velocity of sound in the gas (VOS) [1], as well as quality measurements on natural gas [2] and air-coupled non-destructive testing (NDT) [3].

Although some techniques for the calibration of air microphones in the audio frequency range were developed before the 1940s [4], the calibration of electroacoustic transducers by the reciprocity method began shortly after 1940 with the independent work of MacLean [5] and Cook [6].

The free-field three-transducer reciprocity calibration method has since been adopted e.g. by the American National Standards (ANSI) [7], [8] and the International Electrotechnical Commission (IEC) [9].

In [10] the three-transducer reciprocity calibration technique was used over the frequency range 100-500 kHz for transducers operating in air. Broadband electrostatic transducers were employed [10], [11] to obtain the receiving voltage sensitivity,  $M_V$ , and the transmitting voltage response,  $S_V$ . Challenges related to the use of the three-transducer calibration technique at such high frequencies was with the use of corrections for diffraction and attention in air. Although, corrections for the signal filter were made, and it is stated [10] that parasitic current losses were less than 0.2 percent from the ideal open circuit conditions, no system model was employed.

\*E-mail: kan091@student.uib.no / kenneth.kirkeng.andersen@gmail.com

In [12] and [13] (both partly presented in [14], [15] and [16]) a finite-element (FE) based system model was employed, for calculations of correction terms to the measurements, and as an aid for improved control in evaluating the quality of the individual measurements constituting the three-transducer calibration method.

In [12] the three-transducer calibration method was employed to obtain  $M_V$  and  $S_V$  of piezoelectric discs and in-house built transducers, and the results were compared to FE simulations.

Although an adjusted material data set [17] was used in [12] and [13] to model the piezoelectric discs, the adjusted data set was not obtained for the specific piezoelectric discs used in the measurements. Contrary to this, the corrected measurements and the corresponding simulated quantities agreed fairly well.

Furthermore, for the piezoelectric discs, it was found that the corrections for absorption in air, on both  $M_V$  and  $S_V$  approached 6 dB at 300 kHz. And, around 112 kHz, the corrections for the receiving electronics approached 8 dB. The latter also introduced a frequency shift on the peak value of the receiving voltage sensitivity of up to several kHz.

In [12] this implementation of the three-transducer calibration method was also tested on a pre-calibrated B&K microphone system 4138-A-015 [18] and found to lie within 1 dB of the supplied calibration data for the frequency range 103-130 kHz [12], indicating that the corrections applied to the measurements are reasonable.

The phase response of  $M_V$ ,  $S_V$  or the involved voltage to voltage transfer function was not addressed in neither [10], [12] nor [13].

When modelling in a finite element environment, detailed knowledge about the material parameters for the materials involved in the modelled construction is necessary for accurate results. When using commercial transducers, little information regarding the different materials involved in the transducer construction is available [17]. When modelling in-house built transducers, lack of reliable and accurate material data for the materials involved, e.g. glue, metal housing, front- and back layer, can also pose challenges [19]. Prior work at the University of Bergen (UiB) on piezoelectric discs have shown fair agreement between measurements and simulations [17], while the same comparison on in-house built transducers has provided more challenges [12], [13].

Only piezoelectric discs are considered in the current work. The piezoelectric discs under investigation has a D/T-ratio of about 10, with the first radial mode,  $R_1$ , around 100 kHz. The lower radial modes in the piezoelectric discs are investigated since these modes are frequently used in transducers for gas operating in the frequency range 100-300 kHz. Other candidate modes, e.g. thickness-extension (TE) mode, become challenging at these frequencies, both due to dimensional consideration and possible interaction of different modes if the D/T-ratio is insufficiently large.

In the current work a free- and far-field three-transducer reciprocity calibration method has been modified to allow for corrections accounting for laboratory instrumentation, as well as corrections for attenuation in air and diffraction. The derivation of the three-transducer method, as well as the corrections, are based on [12]. It is the objective to investigate if the corrections applied to the measurements seem reasonable. The reliability of the corrections are given through juxtaposing the corrected measurements with a corresponding simulation.

Two separation distances,  $d$ , have been investigated in the current work, 0.40 m and 0.77 m. The latter for direct comparison with [12], and the former investigating the effects of moving the transmitter and receiver closer together.

In addition, due to the piezoelectric discs operating with the electrodes exposed there is a leakage of electromagnetic radiation (EMR) from the transmitter which is picked up by the receiver. The receivers sensitivity to this leakage is frequency dependent and increases with shorter spacing between the transmitter and receiver. The receivers sensitivity to this leakage could also in part be due to about 0.20 m of unshielded cable connecting the piezoelectric discs to the coaxial cable. An

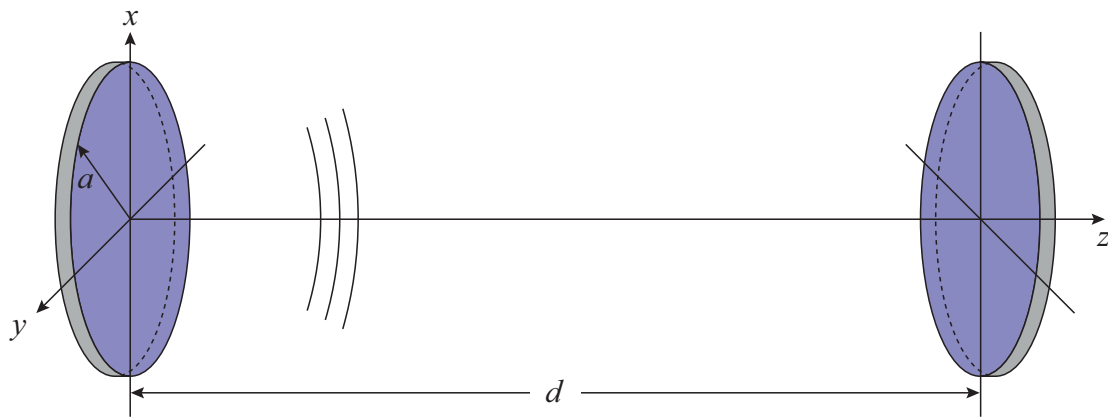
investigation of the effects the EMR has on the SNR is undertaken, yielding two different SNR analyses obtained for two separation distances and two generator voltages. The results from the SNR analysis are used to highlight the frequency range where calibration can be expected to be performed with a SNR > 40 dB.

## II. THEORY

### II.A. System model

A theoretical model, denoted system model, is introduced to describe the measurement system at hand. The system model is divided into several modules, represented by blocks. This division of the system model simplifies the theoretical description of the measurement system at hand.

In Fig. 1 the transmitting disc (left) and receiving disc (right) are shown in a coordinate system. The front face of the transmitting disc lies in the  $xy$ -plane at  $z = 0$ , centred at the  $z$ -axis. Similarly, the front face of the receiving disc lies in the  $xy$ -plane at  $z = d$ , centred at the  $z$ -axis. Both discs have radius  $a$ . The acoustic axis runs along the  $z$ -axis and  $d$  is the separation distance between the front faces of the transmitting and the receiving discs.

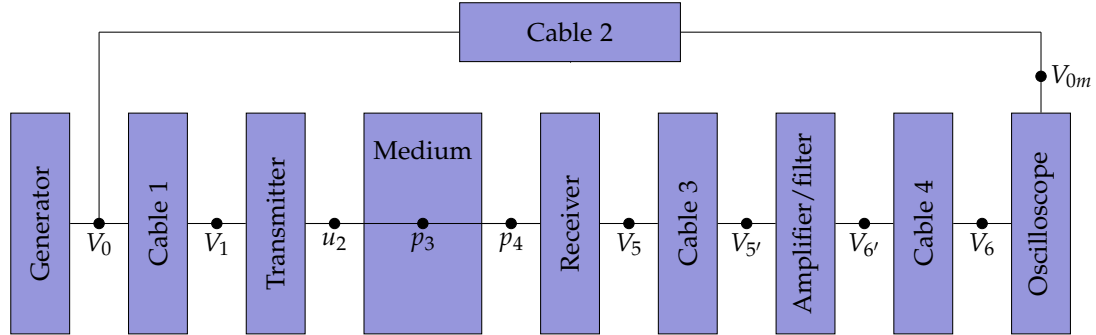


Figur 1: Schematics of coordinate system with transmitting disc (left) and receiving disc (right).

In Fig. 2 the block diagram of the system model is given. An explanation of the quantities involved are given below, and an explanation of the equipment represented by the individual blocks is given in Sec. III.A. All quantities in Fig. 2 are given as the Fourier transform of the time-domain equivalents, cf. Sec. III.B. Throughout, linear theory is used and the harmonic time dependency  $e^{i\omega t}$  is assumed and suppressed, where  $\omega = 2\pi f$ , and  $f$  is the frequency.  $f$  is also suppressed from the quantities given in Fig. 2, e.g.  $V_n = V_n(f)$ , where  $n$  is any integer between 0 and 6.

$V_0$  is the voltage delivered to cable 1 from the function generator.  $V_{0m}$  is the recorded voltage from the function generator through cable 2.  $V_1$  is the drive voltage over the terminals of the transmitting disc.  $u_2$  is the particle displacement at the center of the face of the transmitting disc.  $p_3 = p_3(d_0)$  is the on-axis free- and far-field sound pressure at a reference distance  $d_0 = 1$  m. If  $d_0$  is not in the far-field of the transmitting disc, the sound pressure is extrapolated back to the reference distance,  $d_0$ , from a pressure measured in the far-field [20].  $p_4 = p_4(d)$  is the on-axis free-field sound pressure at a separation distance  $d$  between the transmitting and receiving disc.





Figur 2: Functional block diagram of system model given in the frequency domain, i.e. all quantities are complex.

$V_5$  is the voltage delivered from the receiving disc to cable 3.  $V_5'$  is the input voltage across the terminals of the amplifier.  $V_6'$  is the voltage delivered to cable 4 by the amplifier.  $V_6$  is the recorded voltage given the path just described.

In addition,  $V_{5open}$ , the open-circuit output voltage at the terminals of the receiving disc,  $V_{6'open}$ ; the open-circuit output voltage at the terminals of the measurement amplifier; and,  $V_{gen}$ , the peak open-circuit generator voltage, corresponding to the peak electromotive force, are used.

## II.B. Derivation of the free-field spherical three-transducer reciprocity method

The derivation follows the approach in [12], though with some minor changes in the notation; the derivation is repeated in the current work for completeness.

The conventional three-transducer reciprocity method [7] is modified to account for the transmitting voltage response [21], [12] rather than the transmitting current response.

In the derivation, it is assumed 1) that the receiving transducer is in the far-field of the transmitting transducer, 2) that free-field conditions exist at the location of the receivers front face 3) that the open-circuit voltage is recorded, 4) that the medium is without losses and 5) that at least one of the transducers involved are reciprocal, i.e. one transducer needs to be both linear and reversible.

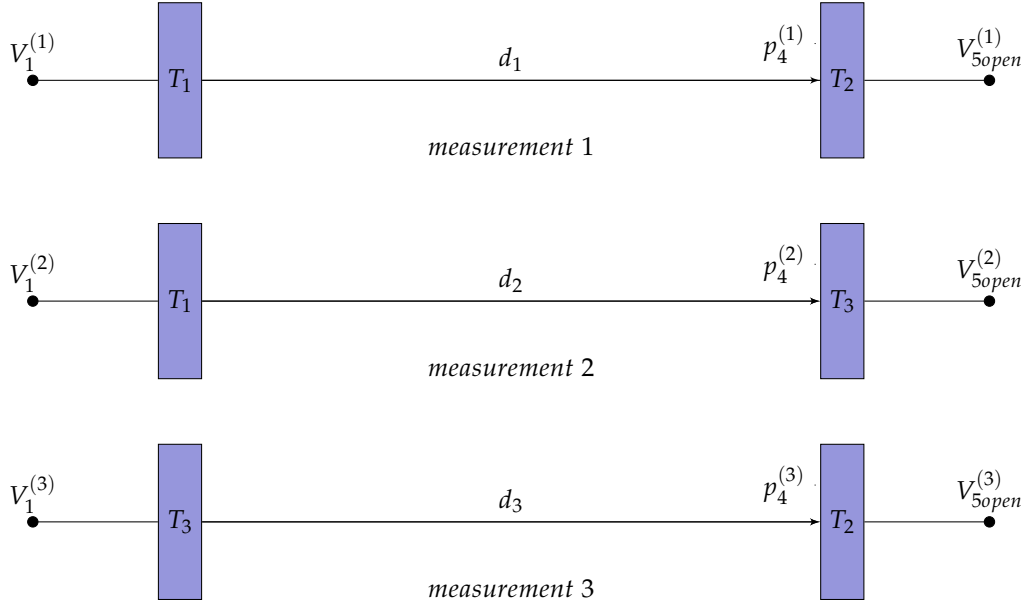
In Fig. 3 the schematics of the modified three-transducer calibration method is given.  $T_1$ ,  $T_2$  and  $T_3$  refers to the three transducers used, where  $T_1$  is the transmitting transducer,  $T_2$  is the transducer, or microphone, under investigation, and  $T_3$  is the reciprocal transducer, used as both receiver and transmitter. The superscripts (1), (2) and (3) refer to measurements 1, 2 and 3, respectively.  $d_1$ ,  $d_2$  and  $d_3$  are the separation distances between the transmitting transducers and the receiving transducers front faces, for the respective measurements.

The complex transmitting voltage response relates the on-axis, free- and far-field pressure at a reference distance  $d_0 = 1$  m, to the voltage over the transducers electrical terminals [22]

$$S_V \equiv \frac{p_3}{V_1} = |S_V| e^{i\phi_{S_V}} \quad (1)$$

where  $|S_V|$  is the magnitude and  $\phi_{S_V}$  is the phase of the transmitting voltage response.

If the sound pressure is obtained at a distance,  $d$ , different than the reference distance,  $d_0$ , the



Figur 3: Schematics of the modified three-transducer calibration method.

corresponding sound pressure at 1 m is obtained by extrapolation

$$p_3 = p_4 \frac{d}{d_0} e^{ik(d-d_0)} \quad (2)$$

where  $k = \omega/c$  is the wave number and  $c$  is the sound velocity of the medium at a frequency,  $f$ . Substituting  $p_3$  in Eq. 1, yields

$$S_V = \frac{p_4}{V_1} \frac{d}{d_0} e^{ik(d-d_0)} \quad (3)$$

The complex receiving voltage sensitivity is the quotient of the output open-circuit voltage at the terminals of the receiving transducer to the on-axis free- and far-field sound pressure, given as [8]

$$M_V \equiv \frac{V_{5open}}{p_4} = |M_V| e^{i\phi_{M_V}} \quad (4)$$

where  $|M_V|$  is the magnitude and  $\phi_{M_V}$  is the phase of the receiving voltage sensitivity.

The complex spherical reciprocity parameter is the quotient of the receiving voltage sensitivity to the transmitting current sensitivity [23]

$$J \equiv \frac{M_V}{S_I} = \frac{M_V}{S_V Z} = \frac{2d_0}{i\rho f} e^{ikd_0} \quad (5)$$

where  $S_I$  is the transmitting current response,  $Z$  is the input electrical impedance of the transmitting transducer and  $\rho$  is the density of the medium.

The complex voltage to voltage transfer functions is defined as

$$H_{15open}^{VV(i)} \equiv \frac{V_{5open}^{(i)}}{V_1^{(i)}} \quad (6)$$

where  $i = 1, 2$  and  $3$  refers to measurement 1 through 3, respectively.

From the above definitions the receiving voltage sensitivity of the transducer under investigation can be found as [12]

$$M_V^{T_2} = \left[ J^{(3)} Z^{T_3} \frac{H_{15open}^{VV(1)} H_{15open}^{VV(3)}}{H_{15open}^{VV(2)}} \frac{d_1 d_3}{d_0 d_2} e^{ik(d_1+d_3-d_0-d_2)} \right]^{\frac{1}{2}} \quad (7)$$

where  $J^{(3)}$  is the spherical reciprocity parameter for measurement 3, and  $Z^{T_3}$  is the complex input electrical impedance of the reciprocal transducer,  $T_3$ .

## II.C. Corrections

When performing measurements, the ideal conditions assumed in Sec. II.B are not generally fulfilled. Therefore, corrections have to be made on the recorded voltages to account for lack of ideal measuring conditions. Corrections are performed for 1) attenuation in air, 2) diffraction due to near-field effects, and 3) laboratory instrumentation, i.e. coaxial cables, signal amplifier and filter, termination of signal in oscilloscope and electrical impedance of the piezoelectric discs.

Correction 1) and 2) are theoretical corrections, while 3) is a mixture of theoretical corrections and corrections based on measurements. The corrections under 3) consist of voltage to voltage transfer functions relating the output voltage of a given block to the input voltage of the same block, cf. Fig. 2. Several blocks can be combined. The cables connecting the laboratory instruments are modelled as ideal transmission lines. For a supplementary discussion on the corrections, cf. [24], and [12], [13]

Measurement on the input impedance of a 2.97 m long coaxial cable connected to the input terminals of the B&K measurement amplifier has shown fair agreement with a simulation of the same combination. Though, some deviations were noticed, this did not transfer noticeably to the resulting quantity,  $M_V$ . All corrections for cables are in the current work obtained theoretically.

In [25] the absorption in air is given as

$$p_t = p_i e^{-0.1151 \cdot \alpha_{dB/m} \cdot z} \quad (8)$$

where  $p_i$  is an initial lossless sound pressure and  $p_t$  is the corrected sound pressure accounting for attenuation in air,  $\alpha_{dB/m}$  is the absorption coefficient given in decibels per meter and  $z$  is the distance the sound wave propagates in air. Rewriting Eq. 8, yields the correction factor for attenuation in air [12]

$$C_\alpha \equiv \frac{p_i}{p_t} = e^{0.1151 \cdot \alpha_{dB/m} \cdot z} \quad (9)$$

The correction term for diffraction,  $C_{dif}$ , is based on Khimunin's diffraction correction [26] for a uniformly vibrating piston source mounted in a rigid baffle of infinite extent. This is considered as a simplification with regard to the piezoelectric discs used in the current work. The measured pressure is extrapolated out to a far-field axial distance,  $z_{ff} = 1000$  m, before the corresponding on-axis far-field pressure is spherically extrapolated back to the measurement distance,  $d$ .

The correction term for diffraction is given in [12] as

$$C_{dif} = \frac{d_{ff} H^{dif}(d_{ff}, f)}{d H^{dif}(d, f)} \quad (10)$$

where  $H^{dif}$  is the Khimunin's diffraction correction, see [12] for complete derivation.

The complex voltage to voltage transfer function, obtained from measurements, with correction terms, is given as

$$H_{15open}^{VV} = \frac{V_6}{V_{0m}} \frac{1}{H_{0m1}^{VV} H_{5open5'}^{VV} H_{5'6'open}^{VV} H_{6'open6}^{VV}} C_\alpha C_{dif} \quad (11)$$

where  $H_{0m1}^{VV} \equiv V_{0m}/V_1$  is the transfer function relating the measured voltage,  $V_{0m}$ , to the voltage across the terminals of the transmitting disc,  $V_1$ ;  $H_{5open5'}^{VV} \equiv V_{5'}/V_{5open}$  is the transfer function relating the input voltage across the terminals of the signal amplifier,  $V_{5'}$ , to the open-circuit output voltage across the terminals of the receiving disc,  $V_{5open}$ ;  $H_{5'6'open}^{VV} \equiv V_{5'}/V_{6'open}$  is the transfer function relating the open-circuit output voltage of the signal amplifier,  $V_{6'open}$ , to the input voltage across the terminals of the signal amplifier,  $V_{5'}$ ;  $H_{6'open6}^{VV} \equiv V_{6'open}/V_6$  is the transfer function relating the recorded voltage,  $V_6$ , to the open circuit output voltage of the signal amplifier,  $V_{6'open}$ .

The expression for  $H_{15open}^{VV}$  from Eq. 11 is substituted in Eq. 7.

### III. METHODS

#### III.A. Experimental set-up

The current experimental set-up is based on [27], [28], [12] and [13]. Except for some modification it is the same experimental set-up as was used in [12] and [13], i.e the coaxial cables connecting the disc to the signal generator and signal amplifier are exchanged from type RG58 to RG-178, and a new set of piezoelectric discs are used.

The transmitter and receiver are Pz27 [29] piezoelectric discs of approximately radius 10 mm and thickness 2 mm. The discs have conducting wires soldered onto both electrodes and the wires are attached with shrinking plastic to a thin metal rod of diameter 1 mm and length 0.2 m, cf. Fig. 4 (b).

In Fig. 4 (a) the discs are shown suspended coaxially in the measurement cage with  $d = 0.77$  m. The measuring cage is surrounded by sheets of plastic preventing possibly airflow and ventilation currents from interfering with the measurements. On the right, two stages for linear translation in the x- and y-direction can be seen, and on the left a stage for rotation is shown. At the time of writing the translation in the z-direction is done manually.

When coaxially aligning the discs, the discs are first brought together with only a millimetre or two separating them. The discs are then aligned such that the front surfaces are parallel with each other and perpendicular to the z-axis. The discs are then moved apart to the measurement distance and a measurement on the separation distance,  $d$ , is made with a measuring tape. The final measurement position is obtained by employing the x- and y-axis stages to move either the transmitter or the receiver until the voltage reading on the oscilloscope is maximized.

An Agilent 33220A function generator is used to produce a sinusoidal tone burst. A burst time,  $b_t$  is defined as the time duration where  $V_{gen} \neq 0$ , i.e. the length of the burst given in seconds. Two burst times have been used,  $b_t = 0.8$  ms and  $b_t = 1.2$  ms, for the separation distances  $d = 0.40$  m and  $d = 0.77$  m, respectively. In addition, two peak open-circuit generator voltages  $V_{gen} = 1$  V

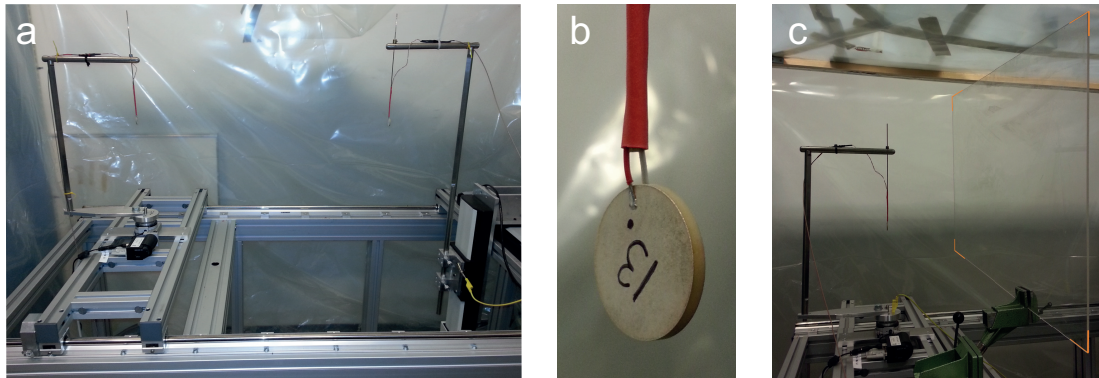


Figure 4: (a) Transmitting and receiving disc mounted in cage displaying how free-field conditions are approximately obtained. (b) Close up of Pz27 disc number 13 with polarization direction given as a black circle, cf. Fig. 1. (c) Acrylic plate mounted in front of the transmitter to block the acoustic energy from propagating.

and  $V_{gen} = 10$  V have been investigated. A peak generator voltage of 10 V corresponds to 20 V peak-to-peak used in [12] and [13].

A Brüel and Kjær 2636 measurement amplifier, gain set to 60 dB, is used to amplify the received acoustical signal. The amplifier is connected to an external Krohn-Hite 3940A digital filter. The two signals,  $V_{0m}$ , and  $V_6$ , are recorded by a Tektronix DPO3012 digital oscilloscope. Temperature and humidity measurements are done with a Vaisala humidity and temperature transmitter, HMT313, for each frequency, and one or several manual readings of a barometer during measurements yields the atmospheric pressure. All connections between the laboratory equipment are done using coaxial cables and Matlab [30] is used to control the function generator and to read out the recorded voltages.

### III.B. Signal processing

A fast Fourier transformation (FFT) [31] is utilized to obtain the peak-to-peak voltage of the transmitted and received bursts. From the recorded time-domain burst a shorter signal is obtained utilizing a rectangular window denoted FFT-window. The FFT-window is adjusted such that it will cut the signal in (or at the closest point to) zero for both the upper and lower frames, and it is applied towards the end of the transmitted and received bursts, where it is assumed that steady-state conditions are reached. The length of the FFT-window is determined from the number of sample points,  $N_{FFT}$ , approximately 20.000 and 30.000 samples given  $b_t = 1.2$  ms and  $b_t = 0.8$  ms, respectively; the total number of sample points in a recorded signal is 99.991. The windowed signal is zero-padded with an integer multiple of its own length, set to 10 times the windowed signal length. The transformation is given as

$$V_n(t) \xleftrightarrow{FFT} V_{nssp}(f) \quad (12)$$

where  $V_{nssp}(f)$  is the single-sided peak voltage spectrum obtained with Matlabs FFT-function and  $n$  is any integer between 0 and 6. From  $V_{nssp}(f)$  the complex valued center frequency is read out for each burst and multiplied with 2.2 to obtain the complex peak-to-peak voltage,  $V_n = V_n(f)$ .

### III.C. Finite element modelling

All finite element simulations are performed using FEMP 5.0, Finite Element Modelling of Ultrasonic Piezoelectric Transducers [32]. The simulation setup is defined in cylindrical coordinates and solved as a 2-dimensional, axisymmetric problem in the  $rz$ -plane, where  $r = \sqrt{x^2 + y^2}$ . The simulated piezoelectric disc is centred at the origin. All simulations are performed using infinite elements to represent the infinite fluid medium, where the infinite elements have been applied 30 mm radially from the origin in the  $rz$ -plane. 9 elements per shear wavelength,  $\lambda_s$ , have been used in the piezoelectric disc, while the medium, air, is simulated without losses using 9 elements per wavelength.

Since the material data obtained from Ferroperm comes with high uncertainty, an adjusted material data set have therefore been developed at UiB [17] and is used in the current work.

The derivation of the receiving voltage sensitivity obtained from a FE-based simulation model, is given in [24].

### III.D. Noise analysis

Due to the discs operating with the electrodes exposed, it is observed that the piezoelectric discs are rather susceptible to electric energy, as well as acoustic. The observed electric energy is either 1) random fluctuations, or 2) coherent sinusoidal signals.

The random electric energy stems from electromagnetic fluctuations present in the laboratory, possibly due to computers and wireless communication as well as electric noise generated inside the laboratory equipment, e.g. thermal noise, shot noise and  $1/f$  noise [33]. When recording the random electric energy,  $V_{gen}$  is set to zero. No coherent acoustic energy should therefore be present in the recording, though random acoustic energy might be present. Since no coherent signals are observed during the recording, this will be referred to as random noise.

The coherent sinusoidal signals stems from the transmitter which, when a sinusoidal voltage is superimposed across its terminals, sets up an electromagnetic field. This field is picked up by the receiver and will be referred to as EMR. This is an unwanted side effect of operating with discs rather than transducers, where an electromagnetic shield can be embedded in the design. It should be noted that no EMR is observed when recording with a Brüel and Kjær microphone system 4138-A-015.

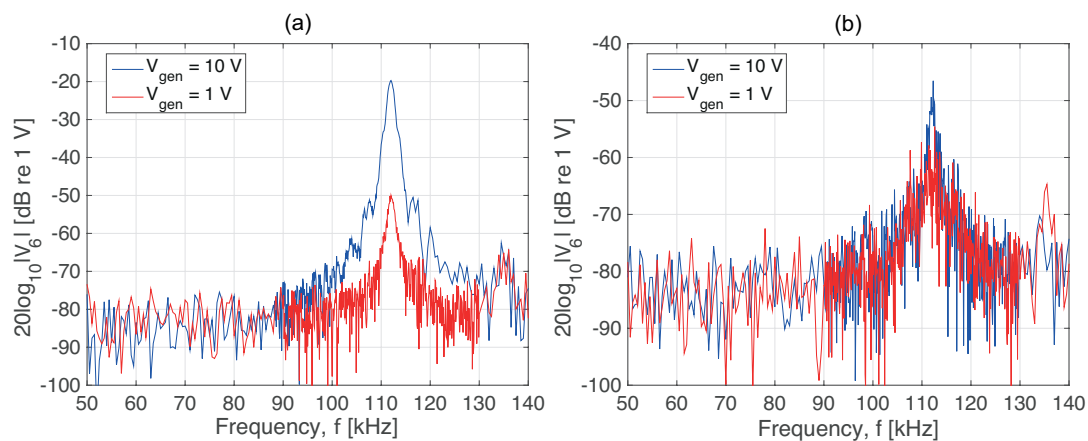


Figure 5: (a) Recorded coherent noise for  $d = 0.40$  m and two generator voltages,  $V_{gen}$ , denoted in legend, (b) same as (a) but for  $d = 0.77$  m.

To record the EMR an acrylic plate is mounted in front of the transmitter, cf. Fig. 4 (c). The recording of the EMR is then processed as in Sec. III.B, and in Fig 5 the results are given as a function of frequency for two separation distances and two voltages. Throughout the text, EMR recorded thus will be referred to as coherent noise. It should be noted that when recording the coherent noise, random noise is also present in the recording. Thus, in the absent of coherent noise e.g. for a large  $d$  or a low generator voltage, the recording of the coherent noise should converge to that of random noise.

In Fig. 5 (a) and (b) we see that from 50-90 kHz the voltage level for all curves flutters between -90 and -80 dB, corresponding to the voltage level of random noise. Exceeding 90 kHz, the coherent noise becomes significant when approaching 112 kHz, and increasingly so when the discs are positioned closer together. For  $V_{gen} = 10$  V measured at  $d = 0.40$  m, the voltage level at 112 kHz is about 1000 times larger than that of random noise, while the same comparison at  $d = 0.77$  m yields a factor of about 32. Beyond 112 kHz, the voltage level reduces to that of random noise.

During some preliminary investigations on the possibility of using a Faraday cage to attenuate the electric noise, the coherent noise was successfully attenuated with a factor of about 2 without compromising the acoustical signal too much. More work will have to be done regarding this before any final conclusions might be reached.

It has been investigated if the peaks at 112 kHz might, in part or fully, be due to acoustic energy propagating through the acrylic plate. A simulation of an incident plane wave on an acrylic plate of thickness 4 mm yields a transmission coefficient at 112 kHz of about -120 dB. Thus it is assumed that all of the coherent noise stems from the EMR produced by the transmitter.

## IV. PRELIMINARY RESULTS

### IV.A. Signal-to-noise ratio

In [7] it is stated that a SNR larger than 20 dB yields an error of about  $\pm 1$  dB in the calibrated quantity. This translates to about  $\pm 10$  percent error. In the context of calibration of measurement microphones, an error of about  $\pm 10$  percent is regarded as quite large, thus for the remainder of this work a criterion of SNR larger than 40 dB will be discussed. This corresponds to approximately  $\pm 1$  percent error. This does not guaranty that the final quantity,  $M_V^T$ , will be given with  $\pm 1$  percent error.

In Fig. 6 the SNR is plotted for two separation distances,  $d$ , and two generator voltages,  $V_{gen}$  for both coherent and random noise. Also, in the figures, are colour areas corresponding to the frequency range where the  $SNR_r$  for random noise (light blue area) and  $SNR_c$  for coherent noise (light red area) are greater then 40 dB. Due to the volatile behaviour of both  $SNR_r$  and  $SNR_c$ , the exact frequency where the SNR is larger than 40 dB is difficult to pin down. These colour areas are inherited to, and used to analyse the results in, Fig. 7.

In Fig. 6 (a) a  $SNR_r$  larger than 40 dB is observed for a frequency range 65-120 kHz, yielding a frequency range of 55 kHz, peaking around 100 kHz with a peak level just below 80 dB. The  $SNR_c$  follows the same path as  $SNR_r$  from 50-90 kHz. From 90-112 kHz the  $SNR_c$  drops significantly compared to that of  $SNR_r$ . Beyond 112 kHz the curves tend to converge, before at about 130 kHz they are overlapping. The frequency range where  $SNR_c > 40$  dB starts at 65 kHz ending at 105 kHz, yielding a frequency range of 40 kHz. The max deviation between the two curves, is observed at 112 kHz where  $SNR_r$  is 125 times larger than  $SNR_c$ . 112 kHz corresponds to the frequency where the receiving disc is at its most sensitive.

In Fig. 6 (b) the same trend as in (a) is observed, though in (b) both frequency ranges are significantly more narrow. A  $SNR_r$  larger than 40 dB is observed for a frequency range 90-115 kHz

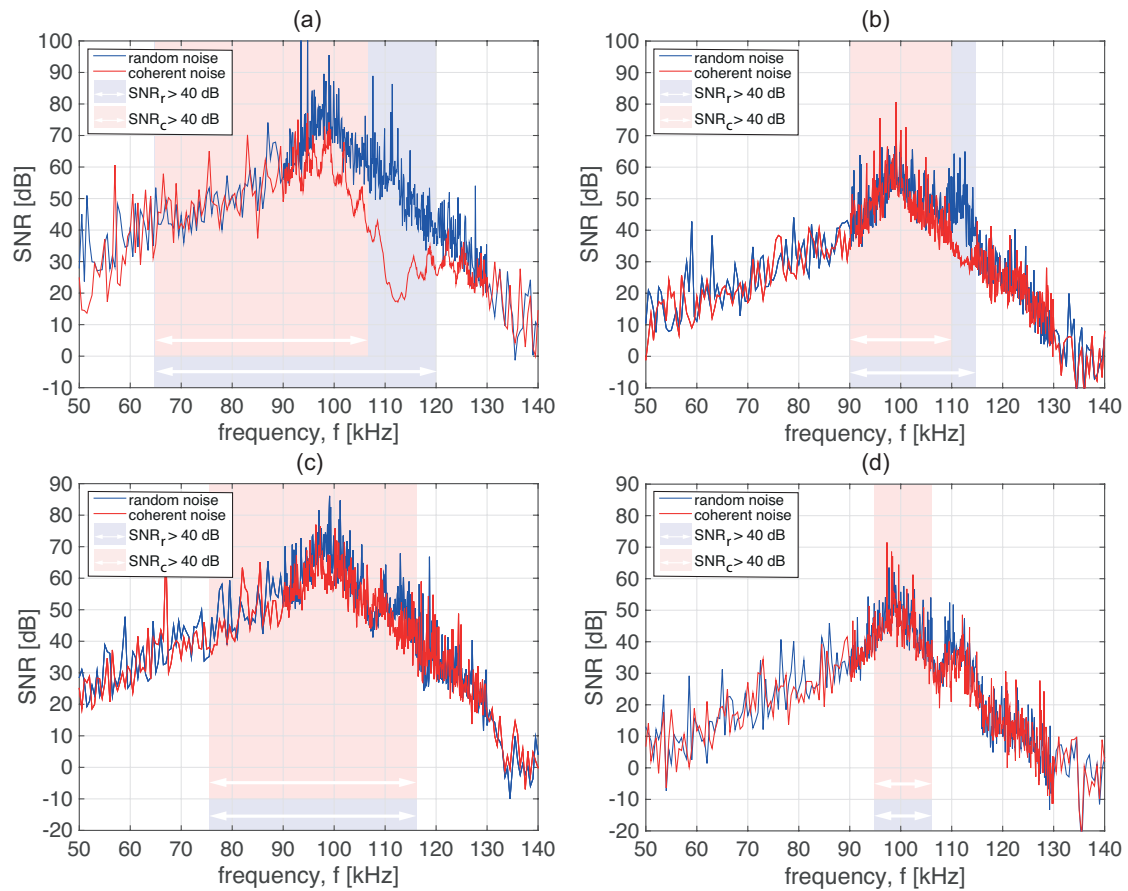


Figure 6: SNR for both random and coherent noise for two generator voltages and two separation distances. (a)  $V_{gen} = 10$  V,  $d = 0.40$  m. (b)  $V_{gen} = 1$  V,  $d = 0.40$  m. (c)  $V_{gen} = 10$  V,  $d = 0.77$  m. (d)  $V_{gen} = 1$  V,  $d = 0.77$  m. The color areas denote the frequency range where the SNR given random noise, SNR<sub>r</sub>, and SNR given coherent noise, SNR<sub>c</sub>, are greater than 40 dB. The white arrows indicate the start and end of both frequency ranges.

while for SNR<sub>c</sub> the frequency range is 90-100 kHz. Both curves are overlapping throughout the entire frequency range, except for 110-115 kHz. The peak SNR level, for both curves, is about 60 dB.

In (b) the upper limit of the SNR<sub>c</sub> > 40 dB is located at 110 kHz, while in (a) the same upper limit is located at 105 kHz. Additionally, the dip observed at 112 kHz in both (a) and (b) has a SNR<sub>c</sub> level of 18 dB and 30 dB, respectively. Both indicate that the effect of EMR relative to the received acoustic energy, is less for 1 V than 10 V.

In Fig. 6 (c) a SNR larger than 40 dB is observed for a frequency range 75-115 kHz for both SNR<sub>r</sub> and SNR<sub>c</sub>. Both curves are overlapping throughout the entire frequency range, with a slight deviation around 110-115 kHz. The peak SNR level, for both curves, is about 70 dB.

In Fig. 6 (d) a SNR larger than 40 dB is observed for a frequency range 95-105 kHz for both SNR<sub>r</sub> and SNR<sub>c</sub>. In (d) both curves are overlapping throughout the entire frequency range. The peak SNR level, for both curves, is around 50-55 dB.

Comparing the results from Fig. 6 (a) and (c), it is observed that the peak SNR<sub>r</sub> level has



dropped from just below 80 dB to about 70 dB. This is in agreement with the received voltage level which increase with a factor of about 2, or 6 dB, when the discs are moved from  $d = 0.77$  m to  $d = 0.40$  m. Also, comparing the effects of coherent noise in Fig. 6 (a) with (c) it is observed the upper frequency with a  $\text{SNR}_c > 40$  dB is shifted from 105 kHz to 115 kHz. The latter, indicating that the positive effect of an overall increased SNR is decreased due to the significant increase in EMR.

#### IV.B. Receiving voltage sensitivity, $M_V^{T_2}$

In Fig. 7 the measured receiving voltage sensitivity,  $M_V^{T_2}$ , for two separation distances,  $d$ , and two generator voltages,  $V_{gen}$ , are given as functions of frequency; the corresponding simulated receiving voltage sensitivity is given in red.

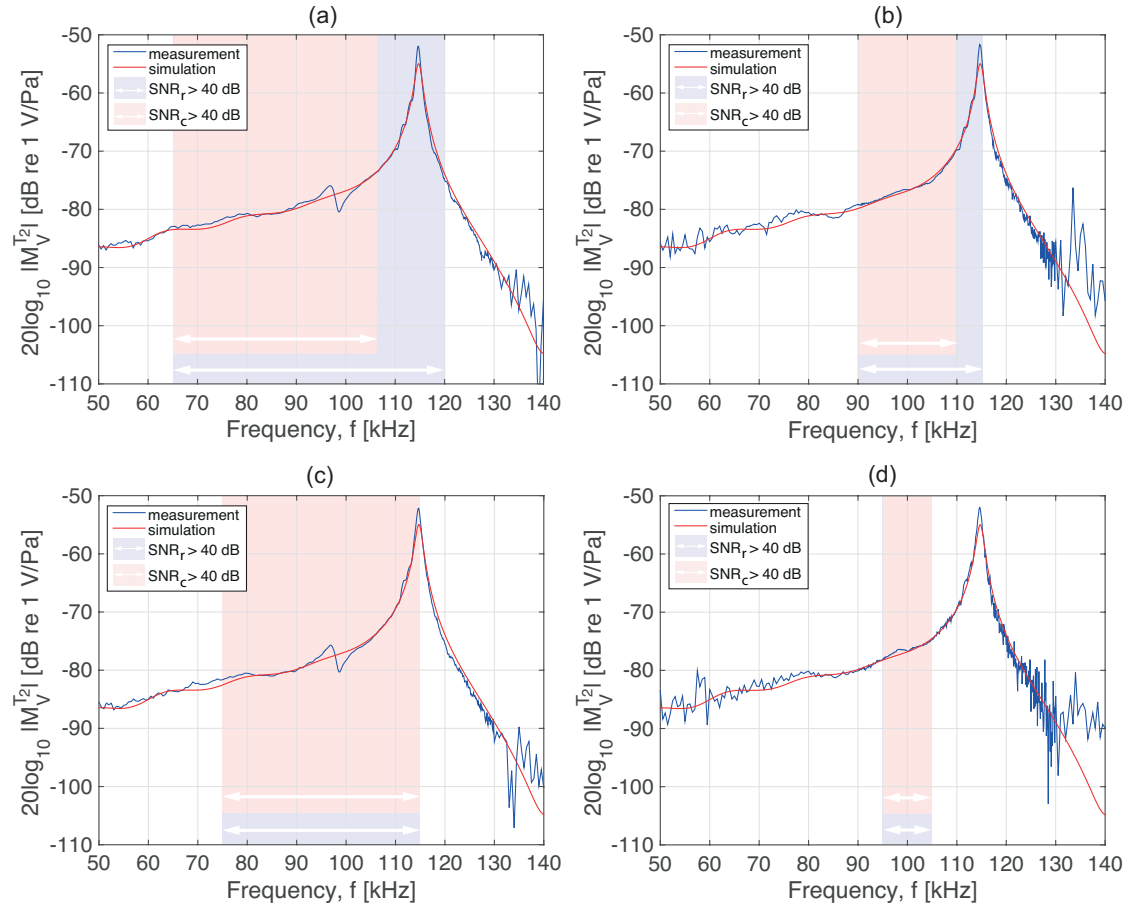


Figure 7: Receiving voltage sensitivity for two generator voltages and two separation distances. (a)  $V_{gen} = 10$  V,  $d = 0.40$  m. (b)  $V_{gen} = 1$  V,  $d = 0.40$  m. (c)  $V_{gen} = 10$  V,  $d = 0.77$  m. (d)  $V_{gen} = 1$  V,  $d = 0.77$  m. The colour areas are inherited from Fig. 6

In Fig. 7 (a) the measurement and the simulation show fair agreement throughout the frequency range except 1) at 112 kHz, where the measurement yield a value 3-4 dB higher than the simulation,

and 2) between 95-105 kHz where the non-linearity of the transmitting discs becomes evident [12], [13]. The first deviation is seen in all Figs. 7 (a) through (d). This deviation is thought to stem from the corrections for the receiving electronics. It is found that the correction for the receiving electronics depends largely on the electrical impedance of the receiving disc. It is not understood why the correction yields this deviation. The second deviation, due to the non-linearity of the transmitting disc, is seen only in Figs. 7 (a) and (c). The non-linearity of the piezoelectric disc becomes noticeable when approaching the series resonance frequency, approximately 100 kHz for  $R1$ , where the admittance of the disc increase.

The colour areas, inherited from Fig. 6, highlight the frequency ranges where we can expect to be able to perform calibration with a SNR > 40 dB. We clearly see how the coherent noise influence this frequency range, leaving the receiving voltage sensitivity peak of the  $R1$  mode, at 112 kHz, out of range.

In Fig. 7 (b) the same agreement and deviation between the measurement and simulation, as in (a), can be observed. Though, at 95-105 kHz there is no visible deviation due to non-linearity. In the frequency range 50-90 kHz there is noticeably more noise present in the signal than in (a) and from 130 kHz to the end of the frequency range, it is seen that the signal is lost in the noise. When performing calibration, the blue area indicates that the peak at 112 kHz will partly be omitted considering random noise, and the red area indicates that same peak will mostly be excluded considering coherent noise.

In Fig. 7 (c) both deviations, as well as the same agreement between measurement and simulation, observed in a) can be seen. Both colour areas indicate that the peak at 112 kHz will partly be omitted when performing calibration.

In Fig. 7 (d) the same observations as was made for (b) can be made. Clearly, considering a SNR > 40 dB, the peak at 112 kHz will be omitted, leaving only the frequency range 95-105 kHz subject to calibration.

## V. DISCUSSION

The preliminary results on the receiving voltage sensitivity yields fair comparison with the finite-element based model [24], and with prior results obtained at UiB [12]. Though, some experimental challenges not experienced in [12] or [13] exist: 1) the random noise level is greater, observed especially when measuring with a generator voltage of 1 V, and 2) the deviation between the measured and simulated receiving voltage sensitivity at 112 kHz was not observed in [12] or [13].

The correction for attenuation in air, at 100 kHz, is 0.59 dB and 1.06 dB for separation distances 0.40 m and 0.77 m, respectively. The correction for diffraction effects, at 100 kHz, is 0.59 dB and 0.021 dB for separation distances 0.40 m and 0.77 m, respectively. The correction term for attenuation in air becomes more significant at larger separation distances and higher frequencies, while the the correction term for diffraction becomes more significant when the discs are moved closer together.

Choosing a measurement distance to be used during calibration is thus seen as a compromise between 1) a larger separation distance with less near-field effects followed by a reduction in the overall SNR level, and 2) a shorter separation distance which yields a greater overall SNR compromised by a severe increase in coherent noise and possibly also near-field effects.

Considering the current use of narrowband piezoelectric discs, the frequency range where we can expect to perform calibration with a SNR > 40 dB is regarded as fairly large. Although only piezoelectric discs have been investigated in the current work, at later stages it is the objective to apply the techniques considered here to in-house built transducers. It is also of interest to assess the reliability of the corrections described here through measurements with a pre-calibrated B&K

microphone system [12].

Furthermore, the preliminary results regarding SNR yields a substantial improvement from what was reported in [12] or [13]. The reason for the rather large deviation in the SNR analysis in this work compared to [12] or [13], stems from where the latter recorded the noise. In [12] or [13] the noise was recorded just before the acoustic burst arrived at the receiver, and no distinction was made between the coherent and random noise. Around 112 kHz the coherent noise present when the acoustic burst arrive might still be quite large.

## VI. PRELIMINARY CONCLUSION

Except for the deviation between the measurement and simulation of  $M_V$ , observed at 112 kHz, all corrections performed seem reasonable and it appears justifiable to expand the three-transducer calibration method thus.

It may also be concluded that the effects of EMR need to be addressed when measuring with piezoelectric discs at shorter separation distances than 0.77 m.

## VII. ACKNOWLEDGEMENTS

The present work is part of the first authors master thesis, due in Nov. 2015 [34]. The work is supported by The Michelsen Centre for Industrial Measurement Science and Technology. Furthermore, the authors thank the following persona for guidance and aid: Eivind Nag Mosland, Rune Hauge and Espen Storheim, Christian Michelsen Research, Bergen.

## REFERENCES

- [1] P. Lunde, K.-E. Frøysa, R. A. Kippersund, and M. Vestrheim, "Transient diffraction effects in ultrasonic meters for volumetric, mass and energy flow measurement of natural gas," in *Proc. 21st International North sea flow Measurement Workshop*, Tønsberg, Norway, 28-31 October 2003.
- [2] K.-E. Frøysa, P. Lunde, G. Lied, and A. Hallanger, "Natural gas quality measurements using ultrasonic flow meters. Development of a prototype Gas Analyzer with results from testing on North Sea gas field data," in *Proc. 30th Scandinavian Symp. on Physical Acoust.*, Geilo, Norway, 28-31 January 2007, Norwegian Physics Soc., <http://www.norskfysikk.no>.
- [3] D. Reilly and G. Hayward, "Through air transmission for ultrasonic nondestructive testing," in *Proc. Ultrasonics Symposium, 1991.*, Dec 1991, pp. 763–766 vol.2.
- [4] R. J. Bobber, *Underwater Electroacoustic Measurements*. Naval Research Laboratory Washington D.C., 1970.
- [5] W. R. MacLean, "Absolute measurement of sound without a primary standard," *J. Acoust. Soc. Am.*, vol. 12, no. 1, pp. 140–146, 1940.
- [6] R. K. Cook, "Absolute Pressure Calibrations of Microphones," *J. Acoust. Soc. Am.*, vol. 12, pp. 415–420, 1941.
- [7] *ANSI/ASA Procedures for Calibration of Underwater Electroacoustic Transducers*, ANSI/ASA Std. S1.20, 2012.
- [8] *ANSI method for the calibration of microphones*, ANSI Std. S1.10, 1966 (R1976).

- [9] *IEC Measurement microphones - Part 3: Primary method for free-field calibration of laboratory standard microphones by the reciprocity technique*, IEC Std. 61 094-3 ed1.0, 1995.
- [10] M. J. Anderson, "Use of reciprocity to characterize ultrasonic transducers in air above 100 kHz," *J. Acoust. Soc. Am.*, vol. 103, no. August 1996, p. 446, 1998.
- [11] —, "Broadband electrostatic transducers: Modeling and experiments," *J. Acoust. Soc. Am.*, vol. 97, no. 1, p. 262, 1995.
- [12] E. Mosland, "Reciprocity calibration method for ultrasonic piezoelectric transducers in air," Master's thesis, Department of Physics and Technology, University of Bergen, Norway, 2013.
- [13] R. Hauge, "Finite element modeling of ultrasound measurement systems for gas. Comparison with experiments in air," Master's thesis, Department of Physics and Technology, University of Bergen, Norway, 2013.
- [14] E. N. Mosland, R. Hauge, E. Storheim, P. Lunde, M. Vestrheim, and J. Kocbach, "Reciprocity calibration method for ultrasonic, piezoelectric transducers in air, including finite element simulations," in *Proc. 36th Scandinavian Symp. on Physical Acoust.*, Geilo, Norway, 3-6 February 2013, Norwegian Physics Soc., <http://www.norskfysikk.no>.
- [15] E. N. Hauge, Rune and, E. Storheim, P. Lunde, M. Vestrheim, and J. Kocbach, "Finite element modeling of ultrasound measurement systems for gas. Comparison with experiments in air," in *Proc. 36th Scandinavian Symp. on Physical Acoust.*, Geilo, Norway, 3-6 February 2013, Norwegian Physics Soc., <http://www.norskfysikk.no>.
- [16] R. Hauge, E. N. Mosland, E. Storheim, P. Lunde, M. Vestrheim, and J. Kocbach, "Updated results on finite element modeling of a transmit-receive ultrasound measurement system. Comparison with experiments in air," in *Proc. 37th Scandinavian Symp. on Physical Acoust.*, Geilo, Norway, 2-5 February 2014, Norwegian Physics Soc., <http://www.norskfysikk.no>.
- [17] V. Knappskog, "Radiellmode svingninger i piezoelektriske ultralydstransdusere for luft. Målinger og endelig element analyse," Master's thesis, Department of Physics and Technology, University of Bergen, 2007, (in Norwegian).
- [18] *Certificate of Calibration, No.: C1201771*, Brüel Kjær, 2012.
- [19] M. Aanes, "Interaction of piezoelectric transducers excited ultrasound pulsed beams with a fluid-embedded viscoelastic plate," Ph.D. dissertation, Department of Physics, University of Bergen, Norway, 2014.
- [20] L. E. Kinsler, A. R. Frey, A. B. Coppens, and J. V. Sanders, *Fundamentals of Acoustics*, 4th ed. John Wiley & Sons, New York, 2000.
- [21] M. Vestrheim, "Phys272 - Akustiske transdusere," Lecture notes, Department of Physics and Technology, University of Bergen, Norway (in Norwegian), 2013.
- [22] *ANSI Acoustical Terminology*, ANSI Std. S1.1, 1994.
- [23] L. L. Foldy and H. Primakoff, "A General Theory of Passive Linear Electroacoustic Transducers and the Electroacoustic Reciprocity Theorem. I," *J. Acoust. Soc. Am.*, vol. 17, no. 2, pp. 109–120, 1945.

- [24] A. A. Søvik, K. K. Andersen, P. Lunde, M. Vestrheim, and J. Kocbach, "Characterization of ultrasound transmit-receive measurement systems in air. Comparison of finite element modelling and experimental measurements," in *Proc. 38th Scandinavian Symp. on Physical Acoust.*, Geilo, Norway, 1-4 February 2015, Norwegian Physics Soc., <http://www.norskfysikk.no>.
- [25] *ANSI Method for calculation of the absorption of sound by the atmosphere*, ANSI Std. S1.26, 1995.
- [26] A. S. Khimunin, "Numerical Calculation of the Diffraction Corrections for the Precise Measurement of Ultrasound Absorption," *Acustica*, no. 27, pp. 173–181, 1972.
- [27] Ø. S. Amundsen, "Material constants determination for piezoelectric disks, and influence on source sensitivity. Measurements and simulations," Master's thesis, University of Bergen, Department of Physics and Technology, Bergen, Norway, 2011.
- [28] E. Storheim, "Diffraction effects in the ultrasonic sound field of transmitting and receiving circular piezoceramic disks in radial mode vibration. FE modeling and comparison with measurements in air," Ph.D. dissertation, University of Bergen, Department of Physics and Technology, Bergen, Norway, In preparation, 2015.
- [29] *Meggitt Ferroperm Piezoceramics*, Hejreskovvej 18 A, DK-3490 Kvistgård, Denmark, 2013.
- [30] *The MathWorks, Inc.*, 3, Apple Hill Drive, Natick, Massachusetts 01760 USA.
- [31] E. O. Brigham, *The Fast Fourier Transform and its application*, 1st ed. Prentice-Hall International Editions, 1988.
- [32] J. Kocbach, "Finite Element Modeling of Ultrasonic Piezoelectric Transducers," Ph.D. dissertation, Department of Physics, University of Bergen, Norway, 2000.
- [33] S. Kogan, *Electronic noise and fluctuations in solids*. Cambridge University Press, 1996.
- [34] K. K. Andersen, "Working title: Reciprocity calibration method for ultrasonic piezoelectric transducers in air," Master's thesis, Department of Physics and Technology, University of Bergen, Norway, In preparation, 2015.